

STRUCTURE AND BONDING

123

Series Editor D. M. P. Mingos  
Volume Editor V. W. W. Yam

# Photofunctional Transition Metal Complexes

**123**

# **Structure and Bonding**

**Series Editor: D. M. P. Mingos**

**Editorial Board:**

**P. Day · X. Duan · T. J. Meyer**

**G. Parkin · H. W. Roesky · J.-P. Sauvage**

# Structure and Bonding

Series Editor: D. M. P. Mingos

Recently Published and Forthcoming Volumes

## High Energy Density Materials

Volume Editor: Klapötke, T. M.  
Vol. 125, 2007

## Ferro- and Antiferroelectricity

Volume Editors: Dalal, N. S.,  
Bussmann-Holder, A.  
Vol. 124, 2007

## Photofunctional Transition Metal Complexes

Volume Editor: V. W. W. Yam  
Vol. 123, 2007

## Single-Molecule Magnets and Related Phenomena

Volume Editor: Winpenny, R.  
Vol. 122, 2006

## Non-Covalent Multi-Porphyrin Assemblies

Synthesis and Properties  
Volume Editor: Alessio, E.  
Vol. 121, 2006

## Recent Developments in Mercury Science

Volume Editor: Atwood, David A.  
Vol. 120, 2006

## Layered Double Hydroxides

Volume Editors: Duan, X., Evans, D. G.  
Vol. 119, 2005

## Semiconductor Nanocrystals and Silicate Nanoparticles

Volume Editors: Peng, X., Mingos, D. M. P.  
Vol. 118, 2005

## Magnetic Functions Beyond the Spin-Hamiltonian

Volume Editor: Mingos, D. M. P.  
Vol. 117, 2005

## Intermolecular Forces and Clusters II

Volume Editor: Wales, D. J.  
Vol. 116, 2005

## Intermolecular Forces and Clusters I

Volume Editor: Wales, D. J.  
Vol. 115, 2005

## Superconductivity in Complex Systems

Volume Editors: Müller, K. A.,  
Bussmann-Holder, A.  
Vol. 114, 2005

## Principles and Applications of Density Functional Theory in Inorganic Chemistry II

Volume Editors:  
Kaltsoyannis, N., McGrady, J. E.  
Vol. 113, 2004

## Principles and Applications of Density Functional Theory in Inorganic Chemistry I

Volume Editors:  
Kaltsoyannis, N., McGrady, J. E.  
Vol. 112, 2004

## Supramolecular Assembly via Hydrogen Bonds II

Volume Editor: Mingos, D. M. P.  
Vol. 111, 2004

## Applications of Evolutionary Computation in Chemistry

Volume Editors: Johnston, R. L.  
Vol. 110, 2004

## Fullerene-Based Materials

Structures and Properties  
Volume Editor: Prassides, K.  
Vol. 109, 2004

## Supramolecular Assembly via Hydrogen Bonds I

Volume Editor: Mingos, D. M. P.  
Vol. 108, 2004

# Photofunctional Transition Metal Complexes

Volume Editor: Vivian W. W. Yam

With contributions by

A. L. Balch · E. Baranoff · F. Barigelletti · S. Bonnet  
J.-P. Collin · S. M. Contakes · L. Flamigni · E. C. Glazer  
D. B. Goodin · M. Grätzel · H. B. Gray · A.-M. Hays · S. Kume  
K. K.-W. Lo · P. Mobian · M. K. Nazeeruddin · Y. H. L. Nguyen  
H. Nishihara · J.-P. Sauvage

The series *Structure and Bonding* publishes critical reviews on topics of research concerned with chemical structure and bonding. The scope of the series spans the entire Periodic Table. It focuses attention on new and developing areas of modern structural and theoretical chemistry such as nanostructures, molecular electronics, designed molecular solids, surfaces, metal clusters and supra-molecular structures. Physical and spectroscopic techniques used to determine, examine and model structures fall within the purview of *Structure and Bonding* to the extent that the focus is on the scientific results obtained and not on specialist information concerning the techniques themselves. Issues associated with the development of bonding models and generalizations that illuminate the reactivity pathways and rates of chemical processes are also relevant.

As a rule, contributions are specially commissioned. The editors and publishers will, however, always be pleased to receive suggestions and supplementary information. Papers are accepted for *Structure and Bonding* in English.

In references *Structure and Bonding* is abbreviated *Struct Bond* and is cited as a journal.

Springer WWW home page: [springer.com](http://springer.com)

Visit the Struct Bond content at [springerlink.com](http://springerlink.com)

ISSN 0081-5993

ISBN 978-3-540-36809-0 Springer Berlin Heidelberg New York

DOI 10.1007/978-3-540-36810-6

This work is subject to copyright. All rights are reserved, whether the whole or part of the material is concerned, specifically the rights of translation, reprinting, reuse of illustrations, recitation, broadcasting, reproduction on microfilm or in any other way, and storage in data banks. Duplication of this publication or parts thereof is permitted only under the provisions of the German Copyright Law of September 9, 1965, in its current version, and permission for use must always be obtained from Springer. Violations are liable for prosecution under the German Copyright Law.

**Springer is a part of Springer Science+Business Media**

[springer.com](http://springer.com)

© Springer-Verlag Berlin Heidelberg 2007

The use of registered names, trademarks, etc. in this publication does not imply, even in the absence of a specific statement, that such names are exempt from the relevant protective laws and regulations and therefore free for general use.

Cover design: *Design & Production* GmbH, Heidelberg

Typesetting and Production: LE-TeX Jelonek, Schmidt & Vöckler GbR, Leipzig

Printed on acid-free paper 02/3180 YL – 5 4 3 2 1 0

---

## Series Editor

Prof. D. Michael P. Mingos

Principal  
St. Edmund Hall  
Oxford OX1 4AR, UK  
*michael.mingos@st-edmund-hall.oxford.ac.uk*

## Volume Editor

Prof. Vivian W. W. Yam

Chair of Chemistry  
Department of Chemistry  
The University of Hong Kong  
Pokfulam Road  
Hong Kong, PR China  
*wwyam@hku.hk*

## Editorial Board

Prof. Peter Day

Director and Fullerenic Professor  
of Chemistry  
The Royal Institution of Great Britain  
21 Albermarle Street  
London W1X 4BS, UK  
*pday@ri.ac.uk*

Prof. Xue Duan

Director  
State Key Laboratory  
of Chemical Resource Engineering  
Beijing University of Chemical Technology  
15 Bei San Huan Dong Lu  
Beijing 100029, P.R. China  
*duanx@mail.buct.edu.cn*

Prof. Thomas J. Meyer

Department of Chemistry  
Campus Box 3290  
Venable and Kenan Laboratories  
The University of North Carolina  
and Chapel Hill  
Chapel Hill, NC 27599-3290, USA  
*tjmeyer@unc.edu*

Prof. Gerard Parkin

Department of Chemistry (Box 3115)  
Columbia University  
3000 Broadway  
New York, New York 10027, USA  
*parkin@columbia.edu*

Prof. Herbert W. Roesky

Institut for Anorganic Chemistry  
University of Göttingen  
Tammannstr. 4  
37077 Göttingen, Germany  
*hroesky@gwdg.de*

Prof. Jean-Pierre Sauvage

Faculté de Chimie  
Laboratoires de Chimie  
Organo-Minérale  
Université Louis Pasteur  
4, rue Blaise Pascal  
67070 Strasbourg Cedex, France  
*sauvage@chimie.u-strasbg.fr*

---

## **Structure and Bonding**

### **Also Available Electronically**

For all customers who have a standing order to Structure and Bonding, we offer the electronic version via SpringerLink free of charge. Please contact your librarian who can receive a password or free access to the full articles by registering at:

[springerlink.com](http://springerlink.com)

If you do not have a subscription, you can still view the tables of contents of the volumes and the abstract of each article by going to the SpringerLink Homepage, clicking on “Browse by Online Libraries”, then “Chemical Sciences”, and finally choose Structure and Bonding.

You will find information about the

- Editorial Board
- Aims and Scope
- Instructions for Authors
- Sample Contribution

at [springer.com](http://springer.com) using the search function.

---

## Preface

Functional materials research is one of the high priority strategic areas of development in science and technology in the 21<sup>st</sup> century. Amongst the variety of functions, the interaction of matter with light to generate light-driven or photo-responsive properties has always been one of the most appealing and attractive areas. Recent advances in the exploitation of transition metal complexes in bringing about photo-induced functions have attracted growing attention, particularly in areas related to materials, energy, and biomedical research. Selected examples include the development of molecular triplet emitters for organic light-emitting devices (OLEDs), optical and photo-switches, photochemical energy storage, dye-sensitized solar cells, photochemical molecular devices (PMD) and machines, optical and luminescence probes and chemosensors, luminescent labels and tags for biomolecules, and luminescence signaling and imaging.

This volume serves to provide the readers with some fundamentals of luminescent transition metal complexes and the recent exciting developments of a selected variety of functions and potential applications that transition metal complexes can offer for the betterment of the society in areas related to materials, energy, and biomedical research.

The first chapter of this volume by Balch discussed the current progress in two-coordinate luminescent gold(I) complexes. This class of complexes is well-known to show weak metal-metal interactions that lead to the isolation of novel architectures and polymorphism from relatively simple building blocks and the appearance of unique electronic absorption and emission spectroscopic features. The effect of the environment, such as solvents and counter ions, on the luminescence behavior of a number of two-coordinate gold(I) complexes was discussed.

The ability to generate machines and devices at the molecular level and setting them into motion via light excitation has always been a fascinating topic of research. The second chapter by Sauvage highlighted the importance of generating long-lived charge-separated states through the harvesting of light to mimic the natural photosynthetic reaction centers, and the design and assembly of multi-component systems using metal complex building blocks for light-driven molecular machines and devices.

Photochromic transition metal complexes derived from photoisomerization represents another important branch of photofunctional materials. Sev-



eral classes of photochromic complexes with photoisomerizable moieties were presented in the chapter by Nishihara. The effect of the transition metal complex systems on the photochromic moieties and the corresponding changes in physical properties of these materials were discussed. The importance of the introduction of transition metal complexes into organic photochromic units was highlighted.

Apart from using light to drive molecular motions and switching in the desired fashion as well as to induce charge separation as demonstrated in the previous chapters, another important consequence of photo-induced charge separation is to harvest light for conversion into electrical energy. This area of research has attracted fast growing attention as a major global issue that the world is facing today is the upcoming depletion of fossil fuels, the energy crisis and the urgent need for clean and renewable sources of energy. The chapter by Grätzel began with a brief historical background and the working principles of dye-sensitized solar cells followed by the maximization of quantum efficiencies through rational design of transition metal complex sensitizers. The second part of this chapter presented some recent examples of luminescent iridium(III) complexes used in organic light emitting devices. Organic light-emitting devices (OLEDs) have been identified as a promising candidate for the generation of lighting systems that are more energy-efficient so as to reduce the energy and environmental cost. The tuning of emission color and luminescence quantum yields of these highly emissive cyclometalated iridium(III) complexes were emphasized.

Instead of redox- and light-driven molecular machines which generate mechanical motions, electron transfer through a “molecular wire” is also of prime interest. A number of wire-type metal diimine complexes that are capable of binding selectively to different enzymes through hydrophobic interactions were described in the chapter by Gray. This strategy not only provides a handle for the study of protein mechanism, photo-generation of reactive enzyme redox states and parameters controlling substrates binding, but also opens up a new avenue for the development of promising luminescent sensors, electrochemical probes, and crystallographic tools for enzyme study.

The last chapter by Lo described the luminescent properties of some recent examples of transition metal complexes that can be employed as luminescent labels and probes for bio-molecules. The structural design of the metal complexes, the labeling and probing strategies, the spectroscopic and luminescent properties of the complexes and their bio-conjugates as well as their biological and analytical applications were presented.

Last but not least, I am indebted to the authors for their immense contributions on these important and exciting topics and I hope that the readers will find this volume useful, stimulating and inspirational to their research. I would also like to acknowledge my coworker, Dr. C. H. Tao, for providing assistance in the preparation of this volume.

---

# Contents

<b>Remarkable Luminescence Behaviors and Structural Variations of Two-Coordinate Gold(I) Complexes</b> A. L. Balch . . . . .	1
<b>From Photoinduced Charge Separation to Light-Driven Molecular Machines</b> E. Baranoff · F. Barigelletti · S. Bonnet · J.-P. Collin · L. Flamigni · P. Mobian · J.-P. Sauvage . . . . .	41
<b>Metal-Based Photoswitches Derived from Photoisomerization</b> S. Kume · H. Nishihara . . . . .	79
<b>Transition Metal Complexes for Photovoltaic and Light Emitting Applications</b> M. K. Nazeeruddin · M. Grätzel . . . . .	113
<b>Conjugates of Heme-Thiolate Enzymes with Photoactive Metal-Diimine Wires</b> S. M. Contakes · Y. H. L. Nguyen · H. B. Gray · E. C. Glazer · A.-M. Hays · D. B. Goodin . . . . .	177
<b>Luminescent Transition Metal Complexes as Biological Labels and Probes</b> K. K.-W. Lo . . . . .	205
<b>Author Index Volumes 101–124 . . . . .</b>	247
<b>Subject Index . . . . .</b>	257

---

## Contents of Volume 107

### **Optical Spectra and Chemical Bonding in Transition Metal Complexes**

Volume Editor: Thomas Schönherr

ISBN: 978-3-540-00854-5

#### **Optical Transitions of Trivalent Neodymium and Chromium Centers in LiNbO<sub>3</sub> Crystal Host Material**

G. Boulon

#### **Recent Advances of Spin Crossover Research**

P. Gülich · P. J. van Koningsbruggen · F. Renz

#### **Ruthenium Complexes of Non-Innocent Ligands; Aspects of Charge Transfer Spectroscopy**

A. B. P. Lever · S. L. Gorelsky

#### **Photoluminescence and Excitation Energy Transfer of Rare Earth Ions in Nanoporous Xerogel and Sol-gel SiO<sub>2</sub> Glasses**

M. Morita · S. Buddhudu · D. Rau · S. Murakami

#### **Allowed and Forbidden d-d Bands in Octahedral Coordination Compounds: Intensity Borrowing and Interference Dips in Absorption Spectra**

M.-C. Nolet · R. Beaulac · A.-M. Boulanger · C. Reber

#### **The Angular Overlap Model and Vibronic Coupling in Treating s-p and d-s Mixing – a DFT Study**

D. Reinen · M. Atanasov

#### **Progress in Hole-Burning Spectroscopy of Coordination Compounds**

H. Riesen

#### **Elucidation of Ligand-Field Theory, Reformulation and Revival by Density Functional Theory**

C. Anthon · J. Bendix · C. E. Schäffer

# Remarkable Luminescence Behaviors and Structural Variations of Two-Coordinate Gold(I) Complexes

Alan L. Balch

Department of Chemistry, University of California, One Shields Avenue,  
Davis, CA 95616, USA  
*albalch@ucdavis.edu*

1	Introduction . . . . .	1
2	Aurophilic Interactions . . . . .	2
3	Absorption and Luminescence from Linear Two-Coordinate Complexes in Solution . . . . .	3
4	Tunable Luminescence from Dicyanoaurate, $[\text{Au}^{\text{I}}(\text{CN})_2]^-$ . . . . .	5
5	Effects of Crystalline Polymorphism on Luminescence . . . . .	6
5.1	Polymorphs of $[(\text{C}_6\text{H}_{11}\text{NC})_2\text{Au}^{\text{I}}](\text{PF}_6)$ . . . . .	7
5.2	Polymorphs of $(\text{Me}_2\text{PhP})\text{Au}^{\text{I}}\text{Cl}$ . . . . .	10
5.3	Polymorphs of the Cyclic Trimer $\text{Au}^{\text{I}}_3(n\text{-PentN}=\text{COMe})_3$ . . . . .	11
5.4	A Polymorphic Phase Change in the Cluster Complex, $[\mu_3\text{-S}(\text{Au}^{\text{I}}\text{CNC}_7\text{H}_{13})_3]_2(\text{SbF}_6)_2$ . . . . .	14
6	Solvoluminescence from the Crystalline Trimer, $\text{Au}^{\text{I}}_3(\text{MeN}=\text{COMe})_3$ . . . . .	16
7	Counter Ion Effects on the Luminescence of Ionic Au(I) Complexes . . . . .	25
8	Luminescence from Frozen Solutions . . . . .	31
9	Mechanical Effects that Alter Luminescence . . . . .	34
10	Ligand-Bridged Complexes . . . . .	36
11	Conclusions . . . . .	38
	References . . . . .	38

## 1 Introduction

This article will examine some remarkable luminescent properties of gold(I) complexes, with an emphasis on those with relatively simple ligands. The review will not be exhaustive but will cover particular topics that show the range of factors that can alter the luminescence from relatively simple,

two-coordinate complexes. In particular, this article will focus upon two-coordinate complexes that can, at the simplest level, exist as simple monomers. Thus, our focus will be on complexes where bridges between gold(I) ions are absent. Only a short section at the end discusses a few relevant examples from the extensive literature on ligand-bridged, bi- and poly-nuclear complexes. Several articles are available that examine the fundamental coordination chemistry of gold [1, 2]. Gold(I) complexes generally exhibit coordination numbers of two, three, or four, but two-coordinate complexes are particularly prevalent and are the focus of this article. Such two-coordinate complexes are usually colorless and are frequently non-luminescent when individual complexes are isolated from one another. However, in many cases, these two coordinate complexes can become luminescent due to self-association through the formation of short  $\text{Au} \cdots \text{Au}$  contacts known as aurophilic interactions (vide infra). Such contacts are particularly common in crystalline solids but may also occur in solutions.

Earlier articles that cover related information are available, and these form a background for the present contribution [3, 4]. As this article will demonstrate, gold(I) complexes display an interesting array of luminescent properties that are frequently difficult to anticipate. This reviewer believes that there are still many interesting discoveries to be made in this ever-surprising field.

## 2

### **Aurophilic Interactions**

Gold(I) complexes involve a closed-shell, diamagnetic  $d^{10}$  metal center and consequently there are no apparent valence electrons available to connect simple Au(I) centers. Nevertheless, many gold(I) complexes show a remarkable tendency to self-associate through weak  $\text{Au} \cdots \text{Au}$  interactions. These interactions occur not only in neutral complexes but also in cationic and anionic complexes where Coulombic factors would be expected to cause significant repulsion. Such attractive interactions (aurophilic interactions) between two or more of these closed-shell Au(I) centers are significant in determining the solid state structures of many gold(I) complexes [5–9]. Aurophilic interactions also can contribute to the properties of such complexes in solution, particularly at high concentrations [10–12]. In the solid state, two-coordinate Au(I) complexes experience attractive aurophilic interactions that can frequently result in short  $\text{Au} \cdots \text{Au}$  separations. Generally,  $\text{Au} \cdots \text{Au}$  separations less than 3.5 Å are indicative of significant interactions between the two metal centers, although the effects of such interactions can extend beyond this distance.

Numerous theoretical treatments of the fundamental causes of aurophilic interactions have appeared, and there are a number of important reviews that

examine the voluminous literature in this area [13–15]. Theoretical studies have shown that attractive aurophilic interactions are caused by a combination of correlation effects and relativistic effects [16–19]. Experimental studies of rotational barriers have shown that the strength of this attractive interaction is comparable to hydrogen-bond energies: ca. 7–11 kcal/mol [20, 21]. Such aurophilic interactions have been shown to be sufficiently strong to persist in solution and to play a role in guiding chemical reactions [22, 23].

### 3

#### Absorption and Luminescence from Linear Two-Coordinate Complexes in Solution

Linear, two-coordinate gold(I) complexes are generally colorless and are frequently non-emissive. The absorption and magnetic circular dichroism (MCD) spectra of a number of rather simple, colorless Au(I) complexes including  $[\text{Au}(\text{CN})_2]^-$  [24, 25],  $[\text{Au}(\text{CNMe})_2]^+$  [26],  $[\text{Au}(\text{PR}_3)_2]^+$  [27],  $[\text{AuCl}_2]^-$  [28],  $[\text{AuI}_2]^-$  [28],  $\text{AuCl}(\text{PR}_3)$  [29], and  $[\text{Au}(\text{NCMe})_2]^+$  [27], have been examined and analyzed in the context of relevant molecular orbital calculations. Figure 1 shows the absorption and MCD spectra of an aqueous solution of  $\text{K}[\text{Au}(\text{CN})_2]$  [24, 25]. Numerous absorptions occur in the UV below 250 nm. The spectra obtained from solid  $[(n\text{-Bu})_4\text{N}][\text{Au}(\text{CN})_2]$  at low temperature are even more complex, with 27 bands resolvable in the  $40\,000\text{--}54\,000\text{ cm}^{-1}$  region. These transitions have been assigned as resulting from metal to ligand charge transfer (MLCT) that involves the filled gold  $d$  orbitals and the empty cyanide  $\pi^*$  levels. Spin orbit interaction for the gold is particularly important in contributing to the complexity seen in the numerous spectral transitions that have been resolved. Similar spectroscopic features are seen for gold(I) complexes with other  $\pi$ -accepting ligands. For example, the absorption and MCD spectra of  $[\text{Au}(\text{CNEt})_2](\text{ClO}_4)$  are shown in Fig. 2 [26]. Note the marked similarity to the spectra of  $\text{K}[\text{Au}(\text{CN})_2]$  shown in Fig. 1.

Dilute solutions of linear, two-coordinate gold(I) complexes are frequently non-luminescent. Many two-coordinate gold(I) complexes, however, do become luminescent under conditions where they undergo self-association, a situation that is particularly favored in the solid state. Such self-association brings the filled  $d_{z^2}$  and the empty  $p_z$  orbitals along the direction of the aggregation into contact and results in the bonding scheme shown in the molecular orbital diagram in Fig. 3. As a consequence, a filled band of  $d_{z^2}$  orbitals and an empty band of  $p_z$  orbitals are created. The absorption process results in promotion of an electron from the filled  $d_{z^2}$  band to the empty  $p_z$  band. Since the  $d_{z^2}$  orbital involved is anti-bonding but the  $p_z$  orbital is bonding in nature, the interactions between the gold(I) ions are strengthened in the excited state.

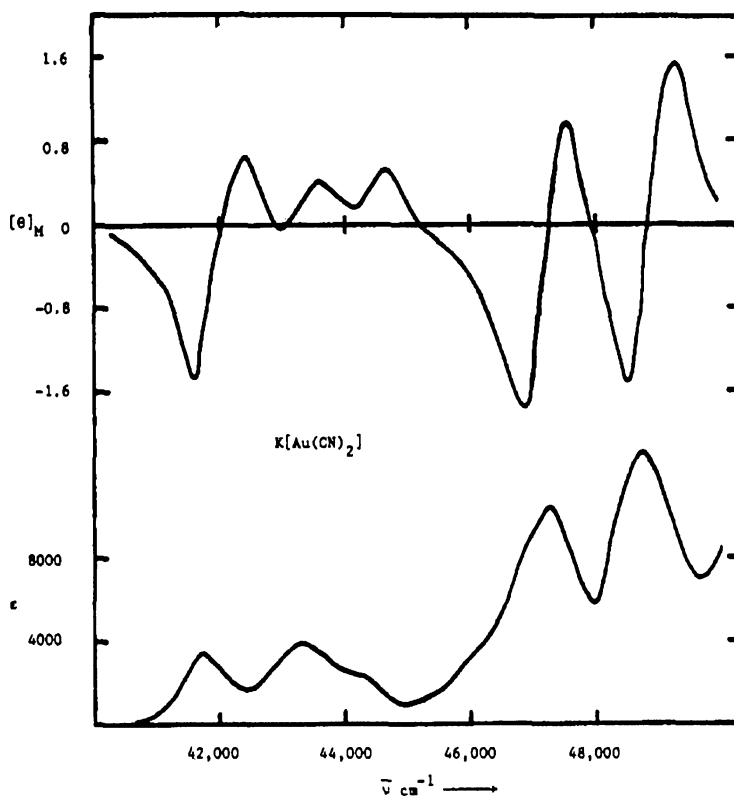


**Fig. 1** Electronic (*lower curve*) and MCD (*upper curve*) spectra of  $\text{K}[\text{Au}(\text{CN})_2]$  in water. From [24]

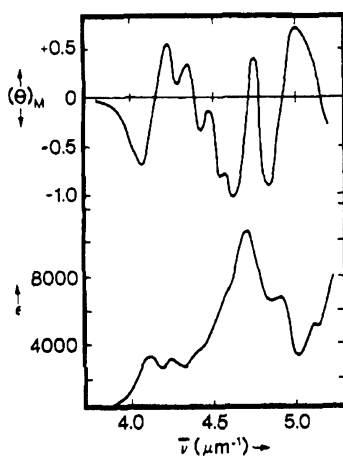


**Fig. 2** Electronic absorption (*lower curve*) and MCD (*upper curve*) spectra of  $[\text{Au}(\text{CN})_2]\text{ClO}_4$  in acetonitrile solution. From [26]

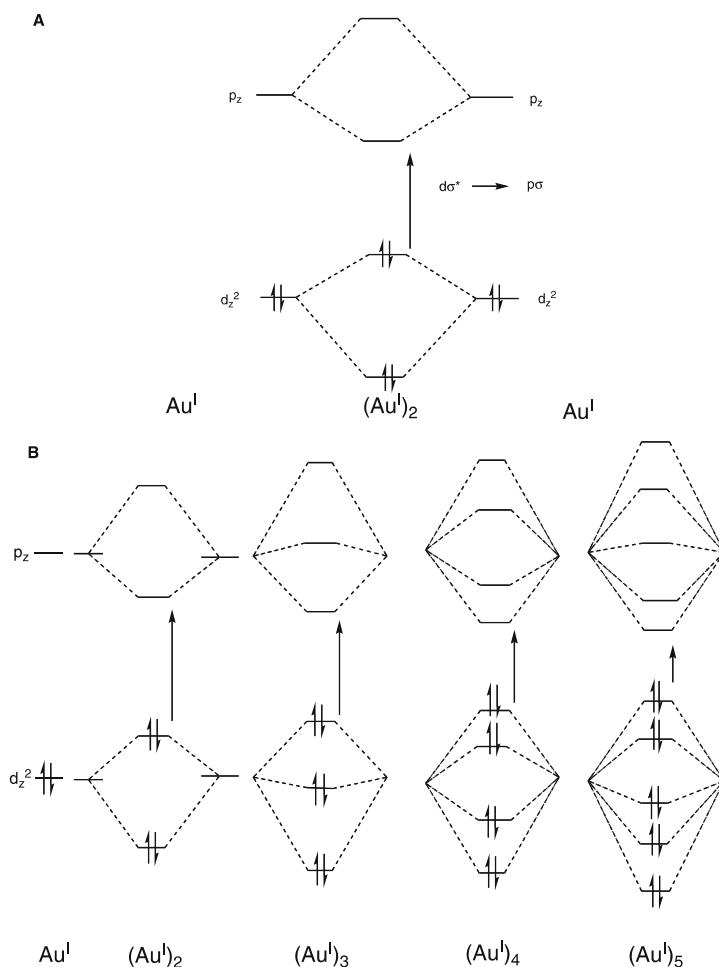


**Fig. 3** Molecular orbital diagrams showing the interactions between the filled  $d_{z^2}$  and the empty  $p_z$  orbitals for A, a dimer and B, for a chain of 2, 3, 4 and 5 gold(I) ions

#### 4

#### Tunable Luminescence from Dicyanoaurate, $[\text{Au}^{\text{I}}(\text{CN})_2]^-$

The simple, stable dicyanoaurate ion has considerable utility in electroplating processes, as a bactericide, in the recovery of gold from mineral deposits, and in the manufacture of gold-ruby glass [30–32]. The luminescence observed from the dicyanoaurate ion in a variety of media show a remarkable “tunability”, as demonstrated by a number of studies by Patterson, Omary, Fackler and coworkers [33–36]. Figures 4 and 5 show the luminescence obtained from the dicyanoaurate ion in various media. Figure 4 shows data collected from solutions of varying solvents and concentrations [36]. Figure 5 shows related



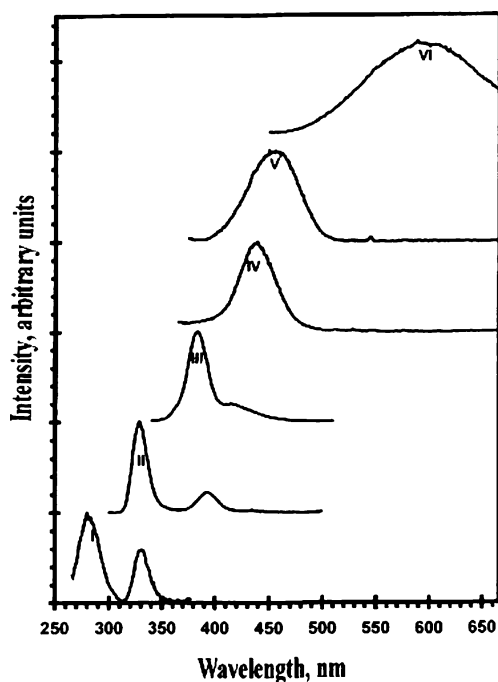


**Fig. 4** Exciplex tuning of the dicyanoaurate(I) emission in different media. Bands shown are *I*  $1.00 \times 10^{-5}$  M  $\text{K}[\text{Au}^{\text{I}}(\text{CN})_2]$  frozen solution in methanol (77 K,  $\lambda_{\text{ex}} = 250$  nm); *II*  $1.00 \times 10^{-4}$  M  $\text{K}[\text{Au}^{\text{I}}(\text{CN})_2]$  frozen solution in methanol (77 K,  $\lambda_{\text{ex}} = 260$  nm); *III*  $\text{K}[\text{Au}^{\text{I}}(\text{CN})_2]/\text{KCl}$  doped crystal (11 K,  $\lambda_{\text{ex}} = 265$  nm); *IV*  $\text{K}[\text{Au}^{\text{I}}(\text{CN})_2]/\text{KCl}$  doped crystal (120 K,  $\lambda_{\text{ex}} = 350$  nm); *V* 0.200 M  $\text{K}[\text{Au}^{\text{I}}(\text{CN})_2]$  aqueous solution (ambient temperature,  $\lambda_{\text{ex}} = 320$  nm); and *VI*  $\text{K}[\text{Au}^{\text{I}}(\text{CN})_2]$  pure crystal (ambient temperature,  $\lambda_{\text{ex}} = 330$  nm). From [36]

data [35], which arise from the dicyanoaurate ion in crystalline forms and in solution. As seen in these figures, the emission maxima for the simple  $[\text{Au}(\text{CN})_2]^-$  vary from 270 to 500 nm. The authors have attributed the luminescence to the formation of Au–Au bonded  $^*[\text{Au}(\text{CN})_2^-]_n$  excimers and exciplexes that differ in the number of anions in close proximity ( $n$  value) and in their geometry. The significant shortening of the Au–Au distance in the excited state is interpreted to cause the large Stokes' shifts seen for these excimers and exciplexes.

## 5

### Effects of Crystalline Polymorphism on Luminescence

Polymorphs have been defined by McCrone as “a solid crystalline phase of a given compound resulting from the possibility of at least two different ar-

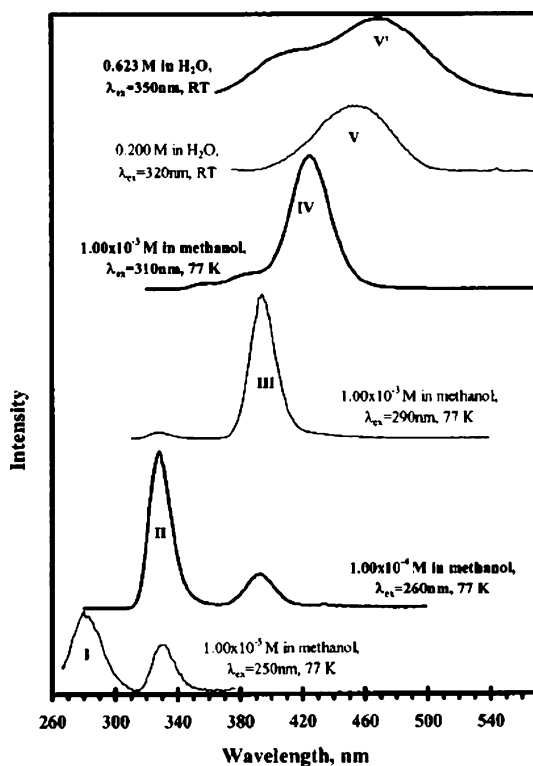


**Fig. 5** Tunable emission of  $K[Au^I(CN)_2]$  solutions by controlling the concentration, excitation wavelength, solvent, and temperature. From [35]

rangements of the molecules of that compound in the solid state” [37]. Several crystalline two-coordinate gold(I) complexes form different polymorphs that produce unique luminescence behavior for each form. These polymorphs can display varying degrees of aurophilic interactions, and hence the chemical bonding between the complexes can differ significantly in the disparate polymorphs. The differences in luminescence behavior frequently are correlated with ground state structures and the nature of the aurophilic interactions present.

## 5.1

### Polymorphs of $[(C_6H_{11}NC)_2Au^I](PF_6)$

Two polymorphs of the salt  $[(C_6H_{11}NC)_2Au^I](PF_6)$  have been found [38]. One of these is a yellow solid which displays a greenish emission, while the other forms colorless crystals that produce blue luminescence. Since both forms can be crystallized from a single solution, for example by adding diethyl ether to a dichloromethane solution of the complex, these are known as concomi-

tant polymorphs. Either polymorph melts over the 115–120 °C range to give a colorless, luminescent melt. Cooling the melt produces the yellow polymorph. Figure 6 shows the emission and excitation spectra from samples of each polymorph. Both polymorphs dissolve to give colorless solutions that produce identical absorption spectra. These solutions are non-emissive. This behavior indicates that the aggregation, due to aurophilic interactions, is responsible for the chemical bonding that produces the luminescence.

The structure of each polymorph has been determined by X-ray crystallography. The colorless polymorph crystallizes in the monoclinic space group  $P2_1/c$ , while the yellow polymorphs forms in the orthorhombic space group  $P2_12_12_1$ . Figure 7 shows a drawing of the chain of cations that are found in the colorless, monoclinic polymorph, and Fig. 8 presents a view of the more complex chains present in the yellow, orthorhombic polymorph. In these two

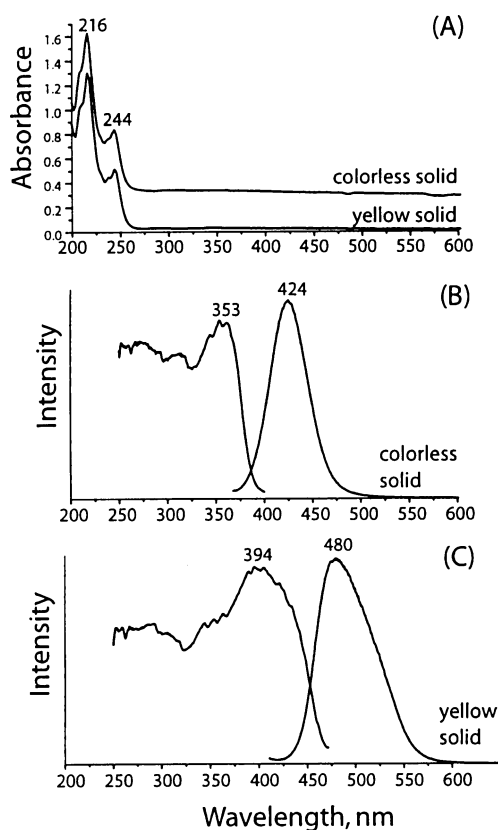


**Fig. 6** **A** The absorption spectra of acetonitrile solutions of the *yellow* (lower) and the *colorless* (upper, offset by 0.4 absorbance units) polymorphs of  $[(C_6H_{11}NC)_2Au^I](PF_6)$ . The emission (right side) and excitation (left side) spectra of **B** the *colorless* and **C** the *yellow* polymorphs of  $[(C_6H_{11}NC)_2Au^I](PF_6)$ . From [38]

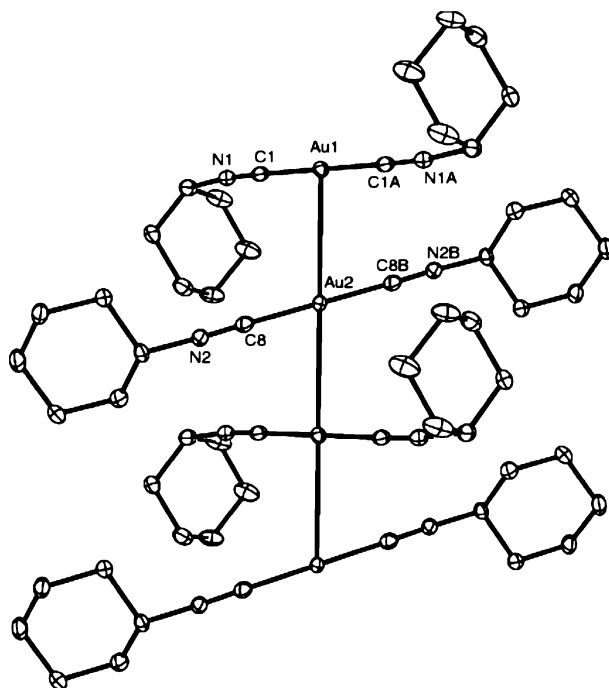


**Fig. 7** A view of a chain of cations within the colorless polymorph of  $[(C_6H_{11}NC)_2Au^I](PF_6)$ . The  $Au1 \cdots Au2$  distance is  $3.1822(3) \text{ \AA}$  and the  $Au1-Au2-Au1'$ ,  $Au2-Au1-Au2'$  angles are  $180^\circ$ . Anions are deleted for clarity. From [38]

figures the focus is on the cations and their interactions, while the anions, which are situated between the columns of cations, are not shown. The gold cations of the colorless polymorph form continuous linear chains. There are two gold ions in special positions in the solid. The  $Au \cdots Au$  distance along the chain is  $3.1822(3) \text{ \AA}$ , which suggests that there are strong aurophilic attractions.

The structure of the yellow polymorph of  $[(C_6H_{11}NC)_2Au^I](PF_6)$  is more complicated, as can be seen in Fig. 8. There are four cations in the asymmetric unit that are arranged to form a slightly helical chain. The  $Au \cdots Au$  contacts ( $2.9803(6)$ ,  $2.9790(6)$ ,  $2.9651(6)$ , and  $2.9643(6) \text{ \AA}$ ) between the cations are unusually short. Notice that these short contacts occur between cationic complexes where one might expect coulombic forces to keep the gold centers apart.

The bonding within the extended chains of gold atoms in the two polymorphs of  $[(C_6H_{11}NC)_2Au^I](PF_6)$  can be understood in the context of Fig. 3. The overlap of the occupied gold  $5d_{z^2}$  orbitals (where  $z$  is the axis along the  $Au \cdots Au \cdots Au$  chain) produces a filled band comprised of the  $d$  orbitals, while overlap of the empty gold  $6p_z$  orbitals produces a corresponding unoc-

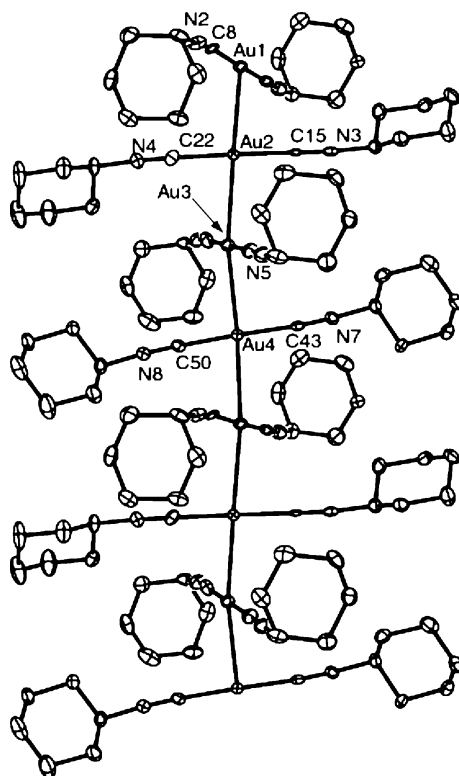


**Fig. 8** A view of a chain of cations within the *yellow* polymorph of  $[(C_6H_{11}NC)_2Au^I](PF_6)$ . The Au  $\cdots$  Au distances are as follows: Au1-Au2, 2.9803(6); Au1-Au4', 2.9790(6); Au2-Au3, 2.9651(6); and Au3-Au4, 2.9643(6) Å. And the angles are Au4'-Au1-Au2, 173.313(18); Au1-Au2-Au3, 152.129(17); Au2-Au3-Au4, 169.652(18); Au1'-Au4-Au3, 153.637(18). Anions are deleted for clarity. From [38]

cupied band of  $p$  orbitals as seen in Fig. 3. The absorption process involves an electronic transition from the filled  $5d_{z^2}$  band to the empty  $6p_z$  band, while emission results from the reverse process, transfer of an electron from the  $6p_z$  level back into the  $5d_{z^2}$  band.

## 5.2

### Polymorphs of $(Me_2PhP)Au^I Cl$

The linear, two-coordinate  $(Me_2PhP)Au^I Cl$  complex also forms two polymorphs [39]. One polymorph involves self-association of two molecules while the other involves association of three molecules. The structures of the dimer and trimer are shown in Fig. 9. In the dimer the Au  $\cdots$  Au contact is 3.230(2) Å, while in the trimer there are two slightly different, shorter Au  $\cdots$  Au separations, 3.091(2) and 3.120(2) Å.

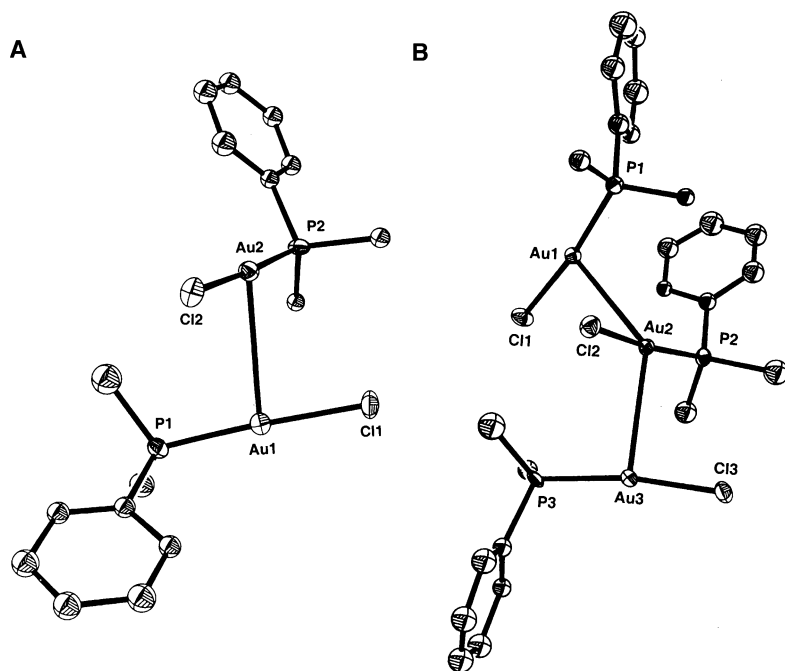


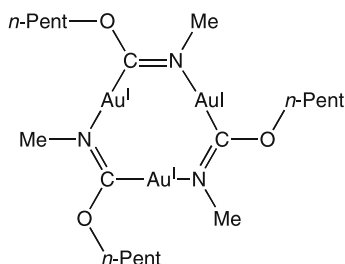
**Fig. 9** The structures of **A** the dimeric polymorph of  $(\text{Me}_2\text{PhP})\text{Au}^{\text{I}}\text{Cl}$  and **B** the trimeric polymorph of  $(\text{Me}_2\text{PhP})\text{Au}^{\text{I}}\text{Cl}$ . From [39]

Distinct emission spectra have been observed for the dimeric and trimeric forms of  $(\text{Me}_2\text{PhP})\text{Au}^{\text{I}}\text{Cl}$  [40]. Indeed the observation of varying emission was the key to identifying the presence of two different polymorphs in the colorless crystals of this compound. Each polymorph shows two emission bands from two excited states. Emission spectra collected at 77 and 1.2 K show that the higher energy emission with an origin at ca. 360 nm has the greater relative intensity at low temperatures. This emission has been assigned to intra-ligand phosphorescence from a phenyl localized  $^3\pi\pi^*$  state. The low energy emission has been assigned to a triplet state arising from a gold-based transition analogous to that seen for  $[(\text{C}_6\text{H}_{11}\text{NC})_2\text{Au}^{\text{I}}](\text{PF}_6)$  [38]. The two polymorphic forms of  $(\text{Me}_2\text{PhP})\text{Au}^{\text{I}}\text{Cl}$  differ in the intensity of this low-energy emission, which is absent in the 77 K spectrum of the dimeric polymorph, while the emission at 635 nm dominates the emission spectrum of the dimeric polymorph at that temperature.

### 5.3

#### Polymorphs of the Cyclic Trimer $\text{Au}_3^{\text{I}}(n\text{-PentN}=\text{COMe})_3$

Two different polymorphs appeared in the product, the cyclic trimer  $\text{Au}_3^{\text{I}}(n\text{-PentN}=\text{COMe})_3$  (whose structure is shown below in Scheme 1), that was ob-



$\text{Au}^{\text{I}}_3(\text{n-PentOC}=\text{NMe})_3$

### Scheme 1

tained from the reaction of a methanol solution of potassium hydroxide with  $(\text{Ph}_3\text{As})\text{Au}^{\text{I}}\text{Cl}$  and *n*-pentyl isocyanide [41]. Since these two types of crystals were obtained by evaporating a diethyl ether solution of the material, they are concomitant polymorphs. The two polymorphs differ in their morphologies and emissive behavior. No luminescence has been observed from the needle form, which is orthorhombic, while the block form, which is triclinic, shows a red emission with  $\lambda_{\text{max}}(\text{emission})$  at 654 nm and  $\lambda_{\text{max}}(\text{excitation})$  at 326 nm. The sizable Stokes' shift suggests that there is a significant distortion in the excited state of this compound.

Crystallographically, the two polymorphs differ in both their molecular configuration and in the intramolecular interactions present. Part A of Fig. 10 shows the structure of one of the four independent molecules in the triclinic blocks. The other three are similar and all have a planar core consisting of the three gold ions and the rest of the nine-membered ring that contains them. The peripheral substituents, the methoxy groups and the pentyl groups, lie very near to the plane of the nine-membered ring. The intramolecular  $\text{Au} \cdots \text{Au}$  distances are 3.315(3), 3.260(2), and 3.332(2) Å. These trimers are arranged into a complex fashion in the solid state as seen in Fig. 11. Each of the four independent molecules interacts with two adjacent molecules through  $\text{Au} \cdots \text{Au}$  contacts that range in distance from 3.3258(6) to 3.8125(6) Å as seen in Fig. 11.

In contrast, in the orthorhombic needles, there is only one molecule in the asymmetric unit and it has a different external shape. While the nine-membered ring at the core of this molecule is planar, one of the pentyl groups protrudes nearly vertically, as seen in Parts B and C of Fig. 10. The molecular packing involves a stair step arrangement of trimers with relatively long distances between them with the closest contact of 3.618(2) Å. The absence of strong aurophilic interactions between trimers may be responsible for the non-emissive nature of this polymorph.

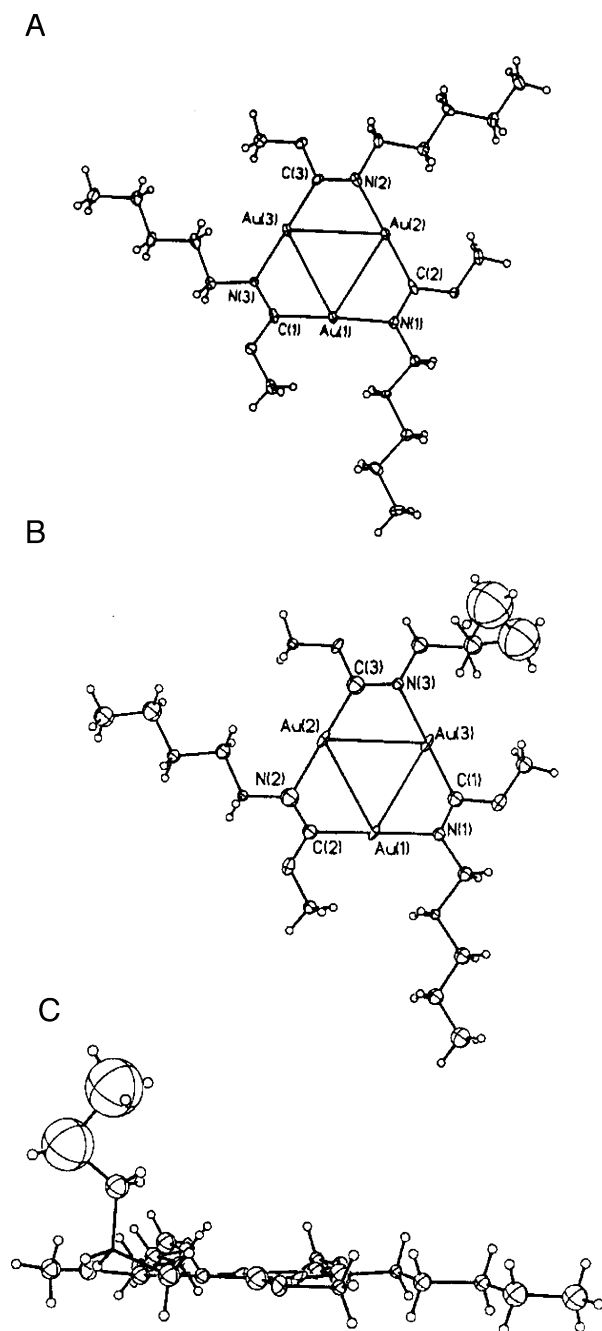


**Fig. 10** The structure of the cyclic trimer  $\text{Au}^{\text{I}}_3(n\text{-PentN}=\text{COMe})_3$ . Part **A** shows one of the four independent molecules in the triclinic blocks. The others are similar. Parts **B** and **C** show different views of the trimer in the orthorhombic needles. From [41]



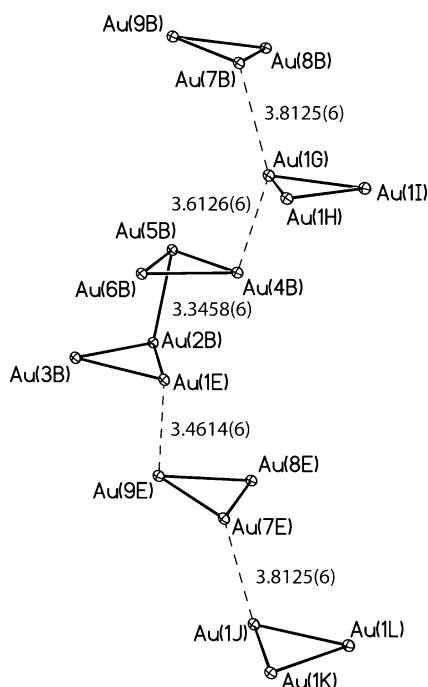


**Fig. 11** The Au...Au interactions in the triclinic blocks of  $\text{Au}^{\text{I}}_3(n\text{-PentN}=\text{COMe})_3$ . Only the positions of the gold(I) ions are shown. From [41]

## 5.4

### A Polymorphic Phase Change in the Cluster Complex, $[\mu_3\text{-S}(\text{Au}^{\text{I}}\text{CNC}_7\text{H}_{13})_3]_2(\text{SbF}_6)_2$

In the solid state,  $[\mu_3\text{-S}(\text{Au}^{\text{I}}\text{CNC}_7\text{H}_{13})_3](\text{SbF}_6)$  forms a dimeric unit that contains a pseudo-octahedral arrangement of gold ions that interact through both intra- and inter-ionic interactions as seen in Fig. 12 [42]. Remarkably, cooling the crystal results in a reversible polymorphic phase change that produces lengthening of the aurophilic interactions in one pair of cations while inducing shortening of those in a second pair of cations, as seen in Scheme 2 below. The phase change from orthorhombic to monoclinic occurs over a 5 degree range centered at 150 K. Crystallographic structure determinations have been conducted at 190 and 90 K. At 190 K there is only one cluster in the asymmetric unit and the inter-ionic Au...Au separations fall in the range 3.5421(9)–3.5826(8) Å. However, at 90 K there are two different cluster sites with the inter-ionic Au...Au separations in one cluster falling in the 3.3214(9)–3.4603(9) range, while in the other cluster, the inter-ionic Au...Au separations are much longer: 3.6545(9)–3.7707(10). At both temperatures, the Au – S distances fall in similar ranges: 2.281(6)–2.305(6) Å at 190 K, 2.283(4)–2.311(4) Å at 90 K.

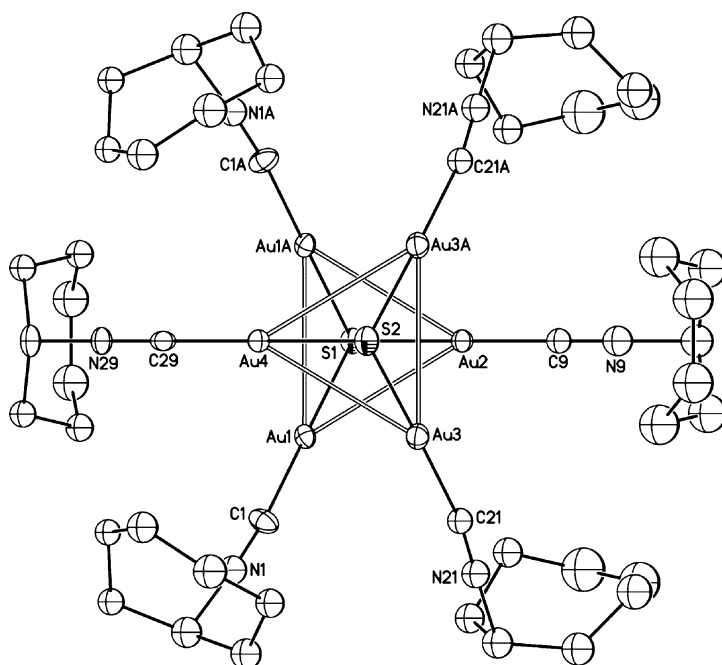
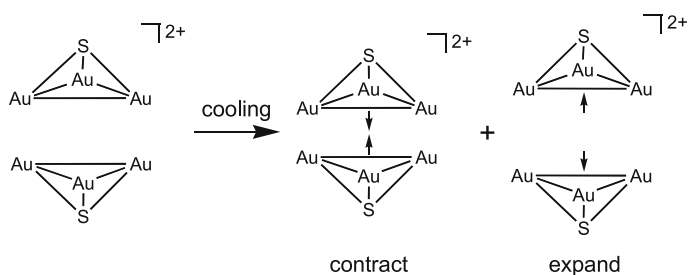


**Fig. 12** A view of the orientation of a pair of cations in the high temperature polymorph of  $[\mu_3\text{-S}(\text{AuCNC}_7\text{H}_{13})_3](\text{SbF}_6)$  with 10% thermal contours for all non-hydrogen atoms. From [42]



### Scheme 2

Crystals of  $[\mu_3\text{-S}(\text{Au}^1\text{CNC}_7\text{H}_{13})_3](\text{SbF}_6)$  produce an intense orange-red emission. The emission and excitation spectra at 298 K are shown in Fig. 13a. A single emission is seen at 667 nm with  $\lambda_{\text{max}}(\text{excitation})$  of 355 nm. Upon cooling, the emission spectrum changes (see in Fig. 13b). At 77 K, there are two emission maxima at 490 and 680 nm. The lifetimes of the two emissions have similar magnitudes: 25  $\mu\text{s}$  for the emission at 680 nm and 10  $\mu\text{s}$  for the emission at 490 nm. Thus, these emissions are both likely to result from phos-

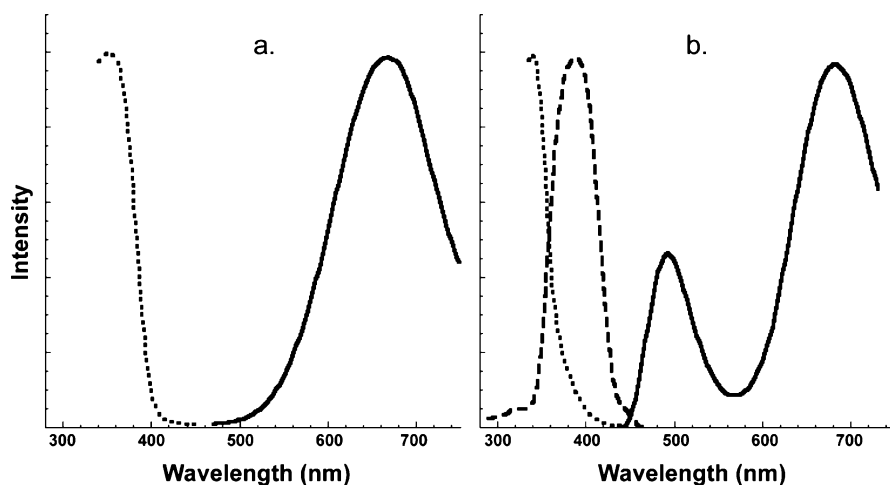


**Fig. 13** The emission and excitation spectra of a polycrystalline sample of  $[\mu_3\text{-S}(\text{AuCNC}_7\text{H}_{13})_3](\text{SbF}_6)$  at 298 K (a) and 77 K (b). At 77 K the dotted and dashed lines show the excitation spectra for emission at 680 and 490 nm, respectively. From [42]

phorescence. The emission at 680 nm has an excitation spectrum with a maximum at 340 nm, while the emission at 490 nm has an excitation maximum at 387 nm. In contrast, the emission spectrum of  $[\mu_3\text{-S}(\text{Au}^{\text{I}}\text{CNC}_6\text{H}_{11})_3](\text{PF}_6)$ , which does not undergo a phase change upon cooling but which has a structure similar to that shown in Fig. 12 for  $[\mu_3\text{-S}(\text{Au}^{\text{I}}\text{CNC}_6\text{H}_{11})_3](\text{SbF}_6)$ , does not change upon cooling from 298 to 77 K. These observations regarding  $[\mu_3\text{-S}(\text{Au}^{\text{I}}\text{CNC}_6\text{H}_{11})_3](\text{SbF}_6)$  have significant implications for understanding temperature-dependent changes from crystals of luminescent gold(I) complexes or other complexes where polymorphic phase changes can occur.

## 6

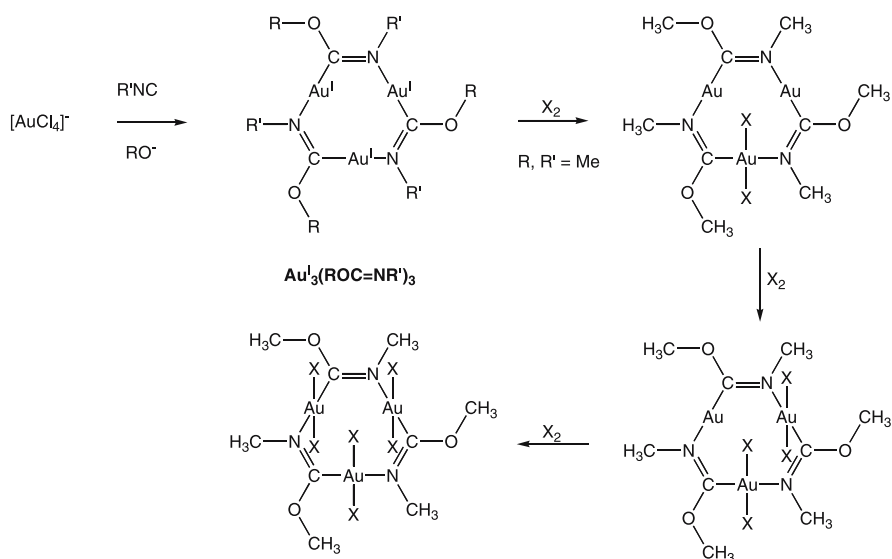
### Solvoluminescence from the Crystalline Trimer, $\text{Au}_3^{\text{I}}(\text{MeN}=\text{COMe})_3$

Solvoluminescence involves light emission that is triggered by contact of an organic solvent with crystals of the colorless, trimeric compound  $\text{Au}_3^{\text{I}}(\text{MeN}=\text{COMe})_3$  following photo-irradiation [43]. The preparation of  $\text{Au}_3^{\text{I}}(\text{MeN}=\text{COMe})_3$  and some related compounds is shown below in Scheme 3 [44, 45]. The emission from  $\text{Au}_3^{\text{I}}(\text{MeN}=\text{COMe})_3$  is sufficiently intense that it can be detected by the human eye under ambient lighting conditions. In fact, solvoluminescence from  $\text{Au}_3^{\text{I}}(\text{MeN}=\text{COMe})_3$  was initially detected during a routine filtration and washing of the compound as part of its preparation. Figure 14 shows spectra relevant to this unusual emission behavior of trimeric  $\text{Au}_3^{\text{I}}(\text{MeN}=\text{COMe})_3$ . Trace A shows the emission spectrum obtained from a solution of  $\text{Au}_3^{\text{I}}(\text{MeN}=\text{COMe})_3$  in chloroform.

Trace B shows the emission spectrum obtained from a sample of crystals of  $\text{Au}^{\text{I}}_3(\text{MeN} = \text{COMe})_3$  after pulsed irradiation, while Trace C shows the spectrum of the light emitted immediately after the addition of chloroform to a previously photo-irradiated sample of  $\text{Au}^{\text{I}}_3(\text{MeN} = \text{COMe})_3$  crystals. The spectrum shown in Trace C is that from solvoluminescence. Notice that the emitted light corresponds to the lower energy emission seen for the solid and does not correspond to that seen in solutions of the trimer. Similar emission spectra have been obtained with a number of different solvents including dichloromethane, toluene, methanol, hexane, and even water. In all cases the spectra of the emissions show a maximum at 550 nm. Thus, there is no solvent effect on the emission. However, the intensity of the emission is greatest with those liquids (chloroform, dichloromethane) that are good solvents for the complex and rather feeble in those that are not (hexane, water).

Crystals of  $\text{Au}^{\text{I}}_3(\text{MeN} = \text{COMe})_3$  that display solvoluminescence show dual emission as seen in Trace B of Fig. 14, which was obtained at room temperature. There is a structured, short-lived ( $\tau \sim 1 \mu\text{s}$ ) emission at 446 nm and a broad, long-lived emission at 552 nm. The later decay can be fit by three decay curves with  $\tau \sim 1.4, 4.4,$  and 31 sec. The yellow emission at 552 nm is readily detected by the human eye in a dark room for tens of seconds after photo irradiation of the crystalline solid. The extremely long lifetime of this yellow emission suggests that charge separation is occurring in the photo-irradiated solid.

In order to understand either of the two major issues involved in solvoluminescence—the nature of the energy storage process in the solid and



**Scheme 3**

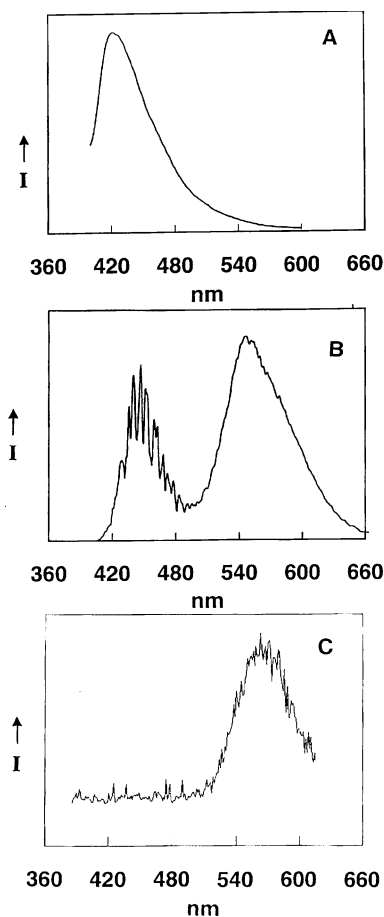


**Fig. 14** **A** The emission spectrum from a chloroform solution of  $\text{Au}^{\text{I}}_3(\text{MeN} = \text{COMe})_3$ . **B** The emission spectrum from a polycrystalline sample of  $\text{Au}^{\text{I}}_3(\text{MeN} = \text{COMe})_3$ . **C** The spectrum of the light emitted from a poly-crystalline sample of  $\text{Au}^{\text{I}}_3(\text{MeN} = \text{COMe})_3$  after UV irradiation and contact with a drop of chloroform. From [43]

the nature of the interaction of solvent with the solid to produce emission—it is necessary to understand the solid state structure of  $\text{Au}^{\text{I}}_3(\text{MeN} = \text{COMe})_3$ . Like a number of other Au(I) complexes,  $\text{Au}^{\text{I}}_3(\text{MeN} = \text{COMe})_3$  exists as different polymorphs. To date three polymorphs have been identified [41]. The hexagonal polymorph forms colorless needles with an intense yellow emission, while the triclinic and monoclinic polymorphs crystallize as colorless blocks. Crystals of the triclinic polymorph and monoclinic polymorphs show a bluish luminescence. Figure 15 shows the emission spectra of each polymorph taken with continuous excitation. Only the hexagonal polymorph is solvoluminescent, and that polymorph is the only one that exhibits the low energy emission at 520 nm.

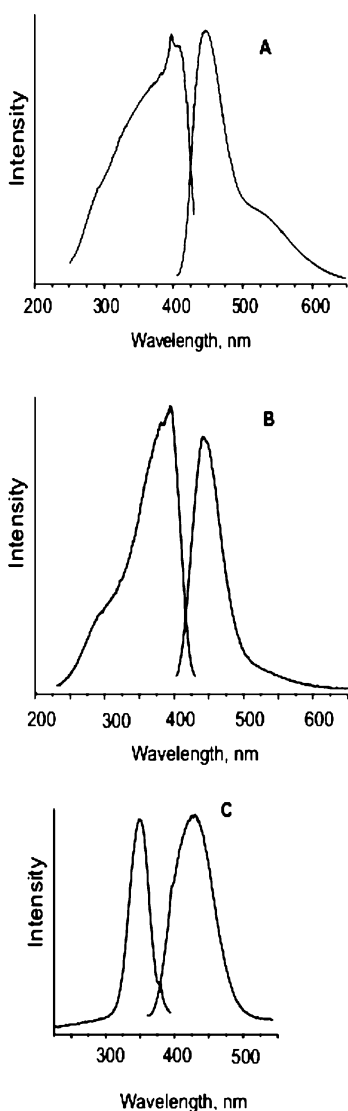


**Fig. 15** Comparisons of the emission and excitation spectra of the polymorphs of  $\text{Au}_3(\text{MeN}=\text{COMe})_3$  at 298 K: **A** hexagonal polymorph; **B** triclinic polymorph; and **C** monoclinic polymorph. From [41]

Aspects of the structures of these three polymorphs are shown in the following figures. Figure 16 shows the molecular structure of the trimer in the hexagonal polymorph and the flip disorder that results from the two positions for the methoxy methyl groups with 0.5 fractional occupancy for each group in the two alternate locations. This disorder results from a flipping of

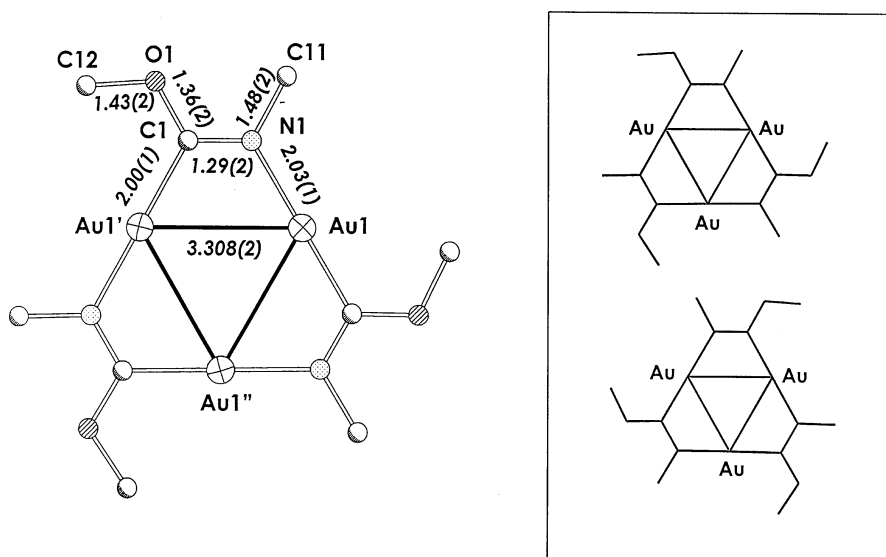


**Fig. 16** Drawings showing the molecular structure of the cyclic trimers in the hexagonal polymorph of  $\text{Au}_3(\text{MeN} = \text{COMe})_3$ . The drawing on the right illustrates the flip-disorder caused by interchange of the location of the peripheral substituents. From [43]

the molecule between the two orientations shown on the right side of the figure. Figures 17 and 18 show how these individual molecules are arranged into infinite columns or stacks in the crystal. There are two types of stacks. In the more ordered stacks, shown in Fig. 18, the molecules are aligned to form prismatic columns with an intermolecular  $\text{Au}^1 \cdots \text{Au}^1$  distance of 3.346(1) Å. In the other disordered stacks, there are two sets of positions for the triangles of gold atoms. Within the hexagonal polymorph, the molecules in each stack lie in common planes and the prismatic and disordered stacks occur in a 2 : 1 ratio as shown in Fig. 17.

The molecular structure of the trinuclear complex in the triclinic polymorph of  $\text{Au}_3(\text{MeN} = \text{COMe})_3$  is similar to that in the hexagonal polymorph but lacks the orientational disorder in the positions of the peripheral methoxy and methyl groups. Figure 19 shows the interactions between molecules in the triclinic polymorph. A pair of the cyclic trimers associate about a center of symmetry, which results in two equivalent  $\text{Au} \cdots \text{Au}$  interactions that involve Au1 in one molecule and Au2 in the adjacent molecule. This  $\text{Au1} \cdots \text{Au2A}$  distance is 3.2201(9) Å. Furthermore, these pairs of molecules interact with neighboring pairs through additional  $\text{Au} \cdots \text{Au}$  contacts that involve the other gold atom, Au3. The  $\text{Au3} \cdots \text{Au3A}$  distance (3.583(12) Å) is significantly longer than the  $\text{Au1} \cdots \text{Au2A}$  distance. Thus, each gold atom in the triclinic polymorph is involved in only one out-of-plane  $\text{Au} \cdots \text{Au}$  interaction. In contrast, in the ordered, prismatic stacks of the hexagonal polymorph each gold

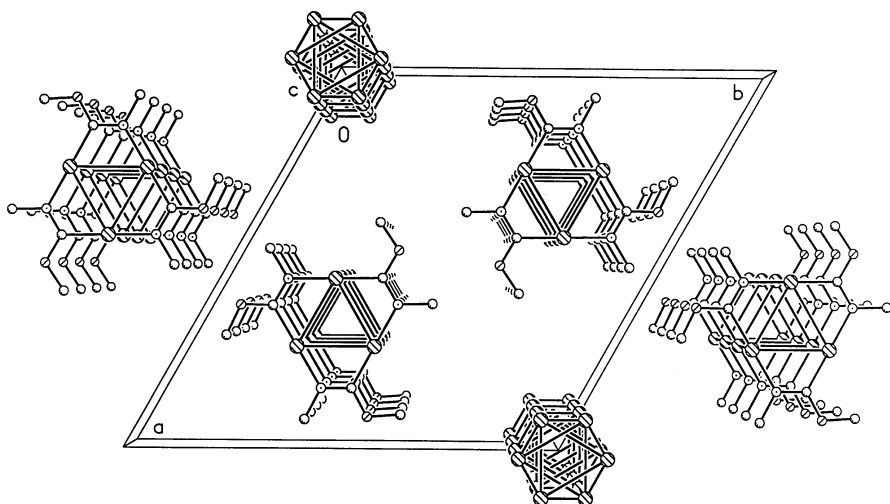


**Fig. 17** A view showing the stacking of the cyclic trimers in the hexagonal polymorph of  $\text{Au}^{\text{I}}_3(\text{MeN} = \text{COMe})_3$ . Only the locations of the gold ions in the disordered stacks were determined and these are shown only at two corners of the cell. From [43]

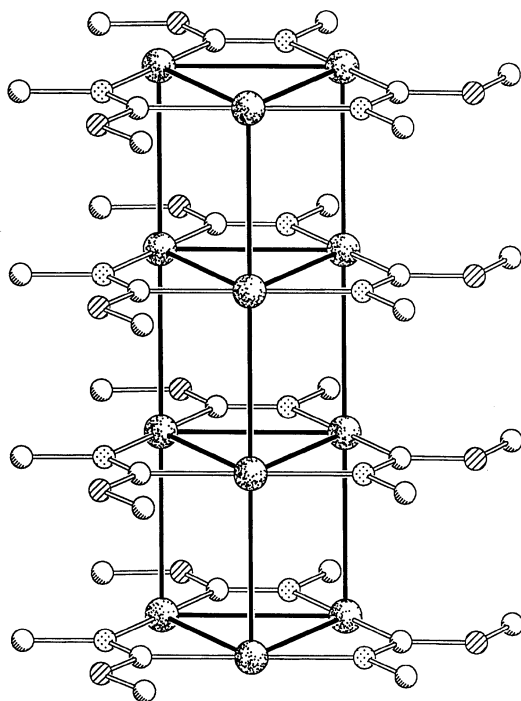


**Fig. 18** A view showing the ordered, prismatic stacks of the cyclic trimers in the hexagonal polymorph of  $\text{Au}^{\text{I}}_3(\text{MeN} = \text{COMe})_3$ . From [43]



atom is involved in two, out-of-plane Au  $\cdots$  Au interactions with neighboring molecules.

Only poorly diffracting crystals of the monoclinic polymorph of  $\text{Au}^{\text{I}}_3$  ( $\text{MeN} = \text{COMe}$ )<sub>3</sub> could be obtained [41]. These appear to contain a stacking fault and may have been twinned. The arrangement of these gold atoms within the unit cell is shown in Fig. 20. There are two crystallographically different prismatic stacks; each contains just three of the trinuclear molecules. The average out-of plane Au  $\cdots$  Au distance in these stacks is 3.28(3) Å. While there is stacking of the trimeric molecules in this polymorph, these stacks are

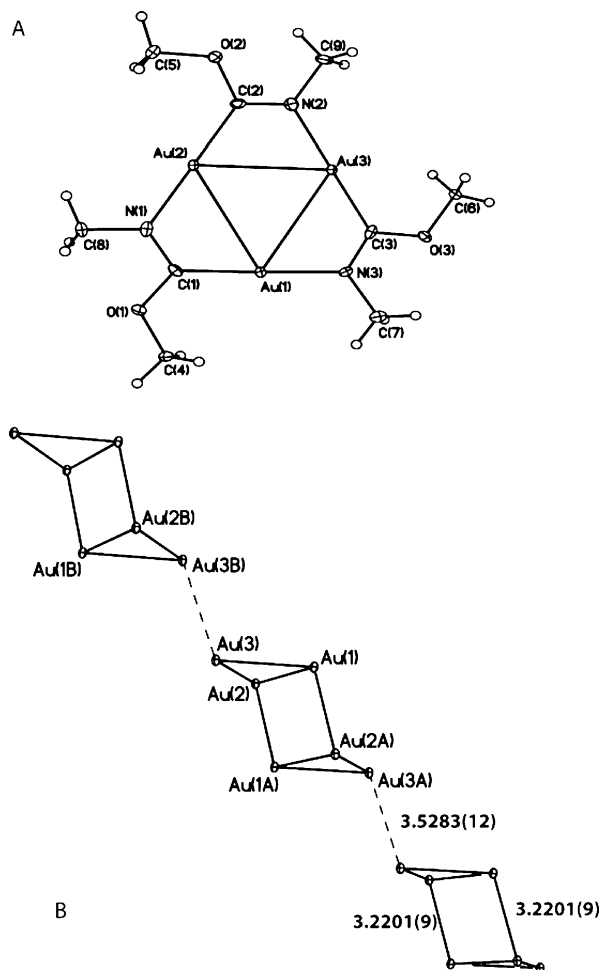


**Fig. 19** The structure of the trimeric polymorph of  $\text{Au}^{\text{I}}_3$  ( $\text{MeN} = \text{COMe}$ )<sub>3</sub> showing **A** the molecular structure and **B** the intermolecular contacts. Only the locations of the gold(I) ions are given in **B**. From [41]

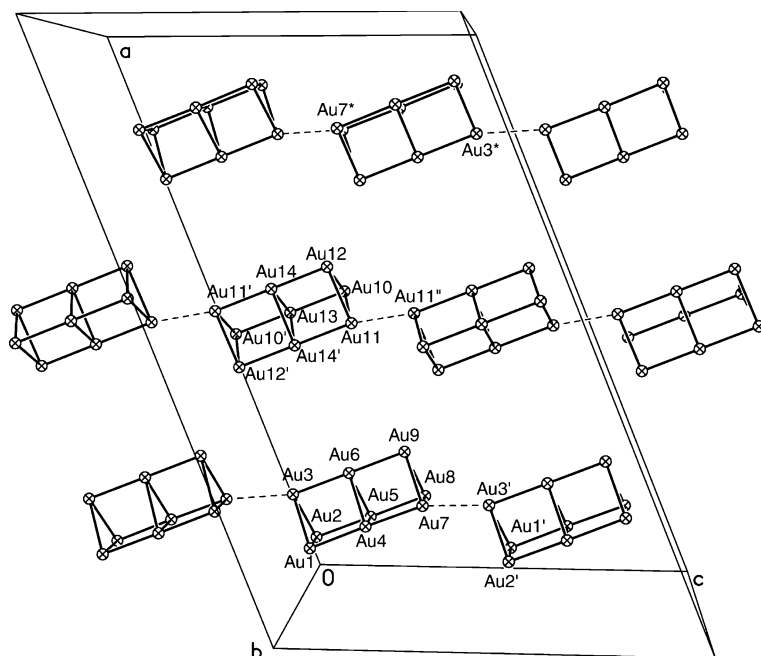


**Fig. 20** The structure of the monoclinic polymorph of  $\text{Au}^{\text{I}}_3(\text{MeN} = \text{COMe})_3$ . For clarity, only the positions of the gold(I) ions are shown. From [41]

short. The extended stacking seen in the hexagonal polymorph, which is believed to be important for its unique luminescence behavior, is absent in the monoclinic polymorph.

Thus, solvoluminescence is a property that is confined to the single hexagonal form of  $\text{Au}^{\text{I}}_3(\text{MeN} = \text{COMe})_3$ . A number of related molecules with different patterns of peripheral substituents have been made including  $\text{Au}^{\text{I}}_3(n\text{-PentN} = \text{COMe})_3$ ,  $\text{Au}^{\text{I}}_3(n\text{-BuN} = \text{COMe})_3$ ,  $\text{Au}^{\text{I}}_3(i\text{-Pr} = \text{COMe})_3$ ,  $\text{Au}^{\text{I}}_3(\text{benzylN} = \text{COMe})_3$ ,  $\text{Au}^{\text{I}}_3(\text{MeN} = \text{COEt})_3$  [41, 45], but none of these show the long-lived luminescence characteristic of the hexagonal polymorph of  $\text{Au}^{\text{I}}_3(\text{MeN} = \text{COMe})_3$ . None are solvoluminescent, and none display the extended columnar stacking and attendant disorder seen in the hexagonal polymorph of  $\text{Au}^{\text{I}}_3(\text{MeN} = \text{COMe})_3$ .

Similarly, chemical modification of  $\text{Au}^{\text{I}}_3(\text{MeN} = \text{COMe})_3$  also destroys its luminescent behavior. For example none of the oxidation products,  $\text{Au}_3\text{X}_n(\text{MeN} = \text{COMe})_3$  ( $n = 2, 4, \text{ or } 6$ ), shown in Scheme 3 are luminescent [45].  $\text{Au}^{\text{I}}_3(\text{MeN} = \text{COMe})_3$  and  $\text{Au}^{\text{I}}_3(\text{MeN} = \text{COMe})_3$  form several crystalline charge transfer complexes: deep yellow  $\{\text{Au}^{\text{I}}_3(\text{MeN} = \text{COMe})_3\} \cdot \{2,4,7\text{-trinitro-9-fluorenone}\}$ , red  $\{\text{Au}^{\text{I}}_3(\text{MeN} = \text{COMe})_3\} \cdot \{2,4,5,7\text{-tetranitro-9-fluorenone}\}$ , red  $\{\text{Au}^{\text{I}}_3(\text{MeN} = \text{COEt})_3\}_2 \cdot \{2,7\text{-dinitro-9-fluorenone}\}$  and red  $\{\text{Au}^{\text{I}}_3(\text{MeN} = \text{COEt})_3\}_2 \cdot \{2,4,7\text{-trinitro-9-fluorenone}\}$  [46]. The

structures of  $\{\text{Au}^{\text{I}}_3(\text{MeN} = \text{COMe})_3\} \cdot \{2,4,7\text{-trinitro-9-fluorenone}\}$ , and  $\{\text{Au}^{\text{I}}_3(\text{MeN} = \text{COMe})_3\} \cdot \{2,4,5,7\text{-tetranitro-9-fluorenone}\}$  consist of extended arrays in which the planar gold(I) trimers and the nearly planar nitro-9-fluorenones are interleaved. The gold trimers make face-to-face contact with the electron acceptors. Thus, these organic acceptors disrupt the aurophilic interactions present in crystalline  $\text{Au}^{\text{I}}_3(\text{MeN} = \text{COMe})_3$  itself. However, in  $\{\text{Au}^{\text{I}}_3(\text{MeN} = \text{COEt})_3\}_2 \cdot \{2,7\text{-dinitro-9-fluorenone}\}$  and  $\{\text{Au}^{\text{I}}_3(\text{MeN} = \text{COEt})_3\}_2 \cdot \{2,4,7\text{-trinitro-9-fluorenone}\}$ , dimers of  $\{\text{Au}^{\text{I}}_3(\text{MeN} = \text{COEt})_3\}$  are formed with nearly trigonal prismatic  $\text{Au}_6$  cores. These dimers are interleaved with the nitro-9-fluorenone molecules to form extended columns in which the components make face-to-face contact. None of these charge-transfer complexes are luminescent and so they cannot display solvoluminescence. Fackler and coworkers have also reported the formation of other related charge-transfer complexes of this type [47]. In particular they observed that, while crystalline  $\{\text{Au}^{\text{I}}_3(p\text{-MeC}_6\text{H}_4\text{N} = \text{COEt})_3\}_2$  shows a blue photoluminescence, this luminescence was lost when the compound was exposed to hexafluorobenzene vapor as shown in Fig. 21. The crystalline adduct,  $\{\text{Au}^{\text{I}}_3(p\text{-MeC}_6\text{H}_4\text{N} = \text{COEt})_3\} \cdot \text{C}_6\text{F}_6$ , was also found to be non-luminescent.

Thus, the presence of extended columns of  $\text{Au}^{\text{I}}_3(\text{MeN} = \text{COMe})_3$  molecules with close contacts between them and several types of disorder within the hexagonal polymorph offer a multiplicity of sites that may function as traps, and thus may be responsible for the energy storage that is needed for solvoluminescence.

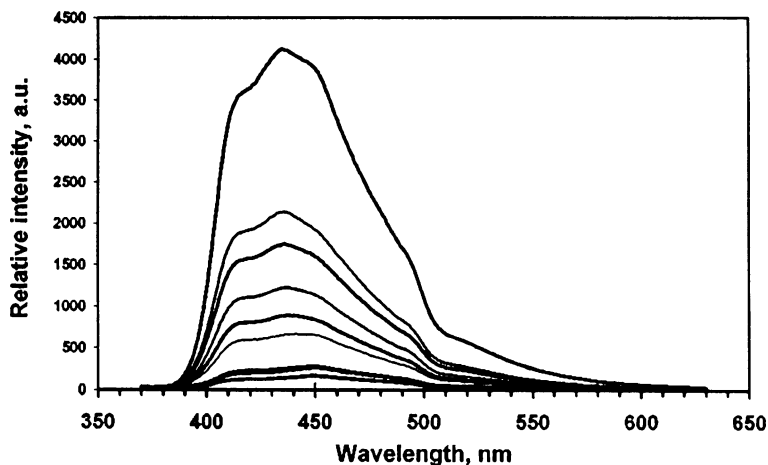


**Fig. 21** Emission spectra of  $\{\text{Au}^{\text{I}}_3(p\text{-MeC}_6\text{H}_4\text{N} = \text{COEt})_3\}$  during exposure of the crystalline solid to hexafluorobenzene. The exposure time was 0, 51, 65, 98, 148, 1322, 1439, 1439, and 1462 min from *top* to *bottom*. From [47]

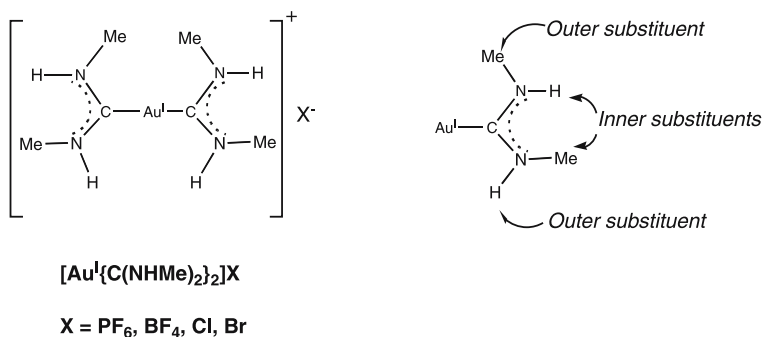
## 7

## Counter Ion Effects on the Luminescence of Ionic Au(I) Complexes

Aurophilic attractions can overcome the Coulombic factors which should serve to separate the cationic or anionic gold(I) complexes from one another. Consequently, self-association is common in both anionic and cationic gold(I) complexes. The structures and luminescence from these crystalline cationic or anionic gold(I) complexes can be altered by changing the counter anion or cation present. The luminescence of the two-coordinate gold(I) carbene cation,  $[\text{Au}^{\text{I}}\{\text{C}(\text{NHMe})_2\}_2]^+$ , whose structure is shown below in Scheme 4, offers a good example [48]. To date, four salts of this cation have been reported. The emission and excitation spectra of the hexafluorophosphate, tetrafluoroborate and chloride and bromide salts are shown in Figs. 22–24, respectively [49]. There are significant variations in the luminescence of these crystals, yet the same cationic species is the fundamental unit that is responsible for the emissions observed. All these salts dissolve to give colorless, non-luminescent solutions. Consequently, it is not the cation itself that is luminescent. Rather, the critical issue is how the cations interact in the solid state.

The solid state structures of various salts of  $[\text{Au}^{\text{I}}\{\text{C}(\text{NHMe})_2\}_2]^+$  show considerable variation. Figure 25 shows the structure of the chains of cations present in  $[\text{Au}^{\text{I}}\{\text{C}(\text{NHMe})_2\}_2](\text{PF}_6) \cdot 0.5(\text{acetone})$  [48]. The cations pack along a crystallographic screw axis with an  $\text{Au} \cdots \text{Au}$  separation of 3.1882(1) Å between planar complexes along the infinite linear chain. It is interesting to note that the hexafluorophosphate counter ions form hydrogen bonds to the N–H groups of the cations and may assist in holding these planar complexes in close proximity. In contrast, in  $[\text{Au}^{\text{I}}\{\text{C}(\text{NHMe})_2\}_2](\text{BF}_4)$  the cations pack in an offset, eclipsed fashion as seen in Fig. 26 [48]. In this case, the separation is somewhat longer (3.4615(2) Å).

As seen in Fig. 27, the cations in  $[\text{Au}^{\text{I}}\{\text{C}(\text{NHMe})_2\}_2]\text{X} \cdot \text{H}_2\text{O}$  ( $\text{X} = \text{Cl}$  or  $\text{Br}$ ) form simple dimers with  $\text{Au} \cdots \text{Au}$  separations of 3.1231(3) Å ( $\text{Cl}^-$  salt)



Scheme 4

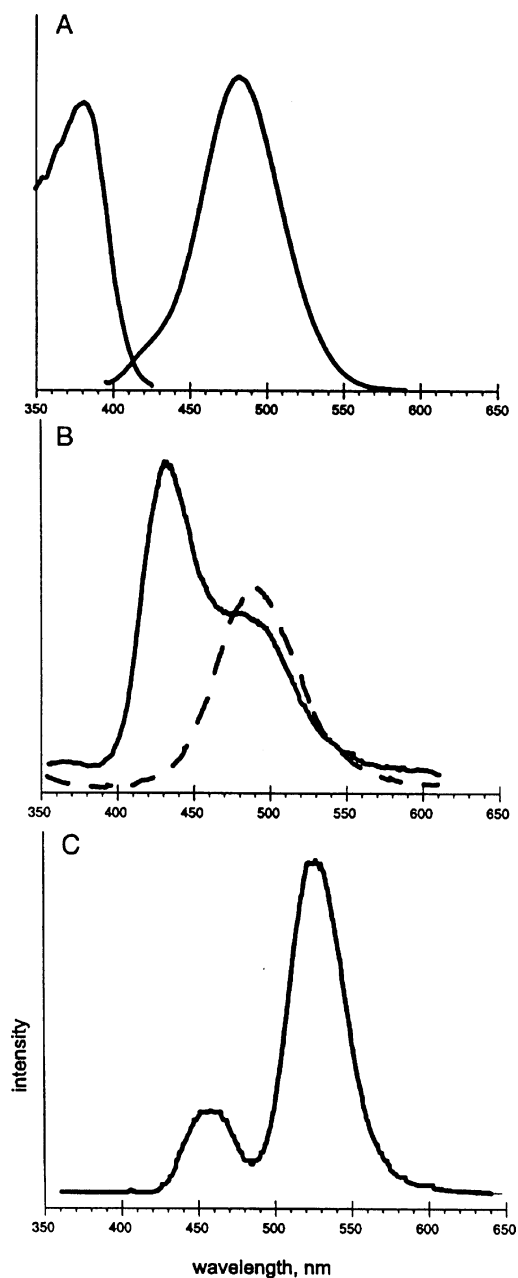


**Fig. 22** Emission spectra of polycrystalline  $[\text{Au}^{\text{I}}\{\text{C}(\text{NHMe})_2\}_2](\text{PF}_6) \cdot 0.5(\text{acetone})$ . **A** Emission ( $\lambda_{\text{excitation}}$ , 383 nm) and excitation ( $\lambda_{\text{emission}}$ , 482 nm) spectra at 300 K. **B** Time resolved emission spectra at 300 K; *solid line* emission acquired within 50 ns of a 337 nm laser pulse; *dotted line* emission acquired 200 ns after the laser pulse at 295 K. **C** Emission ( $\lambda_{\text{excitation}}$ , 365 nm) spectrum at 77 K. From [48]

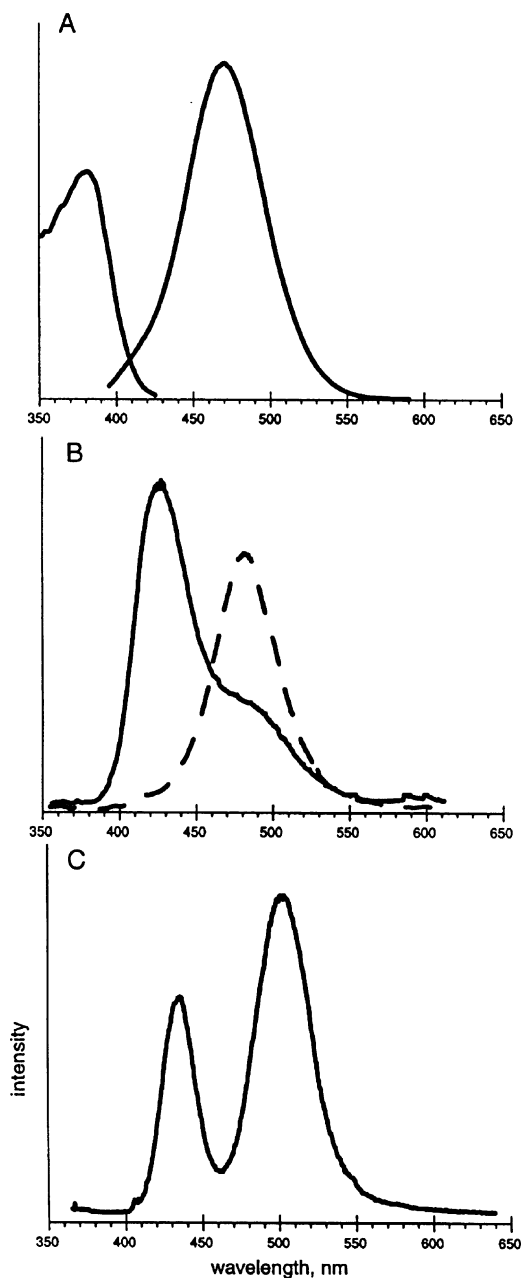


**Fig. 23** Emission spectra of polycrystalline  $[\text{Au}^{\text{I}}\{\text{C}(\text{NHMe})_2\}_2](\text{BF}_4)$ . **A** Emission ( $\lambda_{\text{excitation}}$ , 383 nm) and excitation ( $\lambda_{\text{emission}}$ , 482 nm) spectra at 300 K. **B** Time resolved emission spectra at 295 K: *solid line*, emission acquired within 50 ns of a 337 nm laser pulse; *dotted line*, emission acquired 200 ns after the laser pulse. **C** Emission ( $\lambda_{\text{excitation}}$ , 365 nm) spectrum at 77 K. From [48]

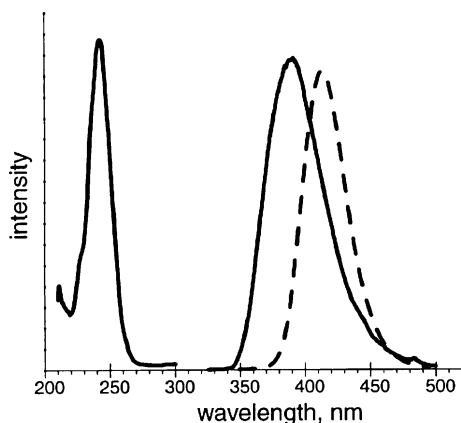


**Fig. 24** The emission (right) and excitation spectra of crystals of  $[\text{Au}^{\text{I}}\{\text{C}(\text{NHMe})_2\}_2]\text{Cl}\cdot\text{H}_2\text{O}$  at room temperature. The *dashed line* shows the emission spectrum from solid  $[\text{Au}^{\text{I}}\{\text{C}(\text{NHMe})_2\}_2]\text{Br}\cdot\text{H}_2\text{O}$ . From [49]

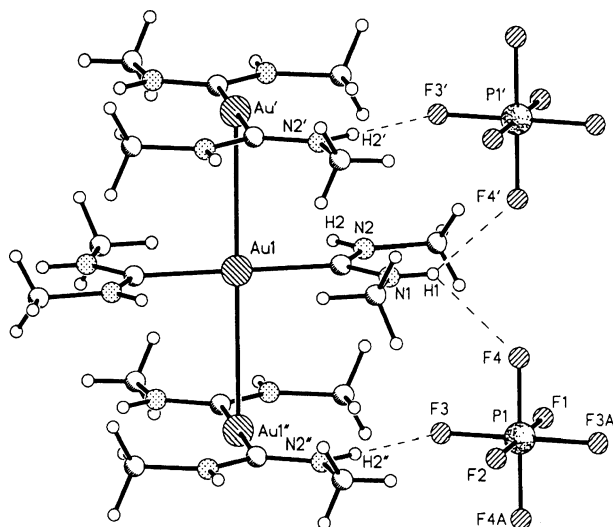


**Fig. 25** A portion of the structure of crystalline  $[\text{Au}^{\text{I}}\{\text{C}(\text{NHMe})_2\}_2](\text{PF}_6)\cdot 0.5(\text{acetone})$ , which emphasizes aurophilic interactions and the hydrogen bonding interactions between two cations and a hexafluorophosphate anion. The  $\text{Au}\cdots\text{Au}$  distance is  $3.1882(1)\text{ \AA}$ . From [48]

and  $3.1297(4)\text{ \AA}$  ( $\text{Br}^-$  salt) [49]. Despite the fact that potentially coordinating anions are present, the gold(I) ions choose aurophilic interactions over traditional binding of a simple Lewis base ligand. The halide ions are hydrogen bonded to ligand N–H groups of the cations and to water molecules as seen in Fig. 27. The luminescence of these dimers occurs at a higher energy than

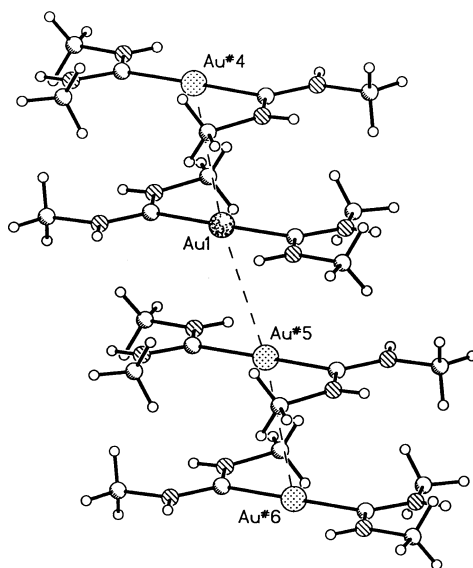


**Fig. 26** A view of the structure of  $[\text{Au}^{\text{I}}\{\text{C}(\text{NHMe})_2\}_2](\text{BF}_4)$  which shows the *offset* nature of the stacking of the cations. From [48]

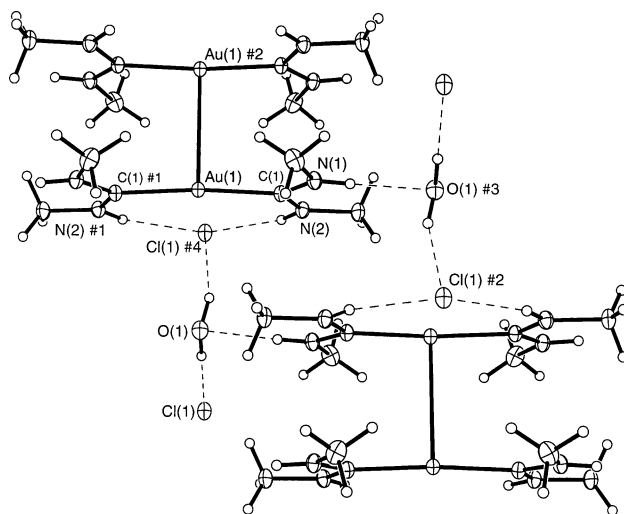


**Fig. 27** A view of the structure of  $[\text{Au}^{\text{I}}\{\text{C}(\text{NHMe})_2\}_2]\text{X} \cdot \text{H}_2\text{O}$  ( $\text{X} = \text{Cl}$  or  $\text{Br}$ ) which shows two dimers and their interactions with the anions and water molecules. From [49]

that observed in the extended chains of the same cation in the corresponding  $(\text{PF}_6)^-$  and  $(\text{BF}_4)^-$  salts and shows the important effects of aggregation on the observed luminescence.



Similar variations in structure are seen for the related cation  $[\text{Au}\{\text{C}(\text{OMe})\text{NMeH}\}_2]^+$  [50]. Colorless  $[\text{Au}\{\text{C}(\text{OMe})\text{NMeH}\}_2][\text{O}_2\text{CCF}_3]$  is luminescent ( $\lambda_{\text{max}}(\text{emission})$ , 520 nm;  $\lambda_{\text{max}}(\text{excitation})$ , 301 nm). In this salt the cations associate to form infinite, nearly linear ( $\text{Au}\cdots\text{Au}\cdots\text{Au}$  angle,  $172.209(7)^\circ$ ) chains that have the gold centers only 3.27797(15) Å apart. The cation in the chloroform solvate,  $[\text{Au}\{\text{C}(\text{OMe})\text{NMeH}\}_2][\text{C}_7\text{Cl}_2\text{NO}_3] \cdot \text{CHCl}_3$ , (where  $[\text{C}_7\text{Cl}_2\text{NO}_3]^-$  is an anion obtained by hydrolysis of 2,3-dichloro-4,5-dicyano-1,4-benzoquinone, DDQ) exists as an isolated monomer, while unsolvated  $[\text{Au}^{\text{I}}\{\text{C}(\text{OMe})\text{NMeH}\}_2][\text{C}_7\text{Cl}_2\text{NO}_3]$  contains pairs of cations that are linked through an  $\text{Au}\cdots\text{Au}$  interaction with a 3.1955(3) Å separation between the gold centers. Neither of the salts containing the red anion  $[\text{C}_7\text{Cl}_2\text{NO}_3]^-$  are luminescent.

Anionic gold(I) complexes can also show variations in emission and structure with changes in the cation present. Elder and coworkers have found an interesting set of variations for salts containing  $[\text{Au}^{\text{I}}(\text{SCN})_2]^-$  [51]. Structural variations include the following. The  $(\text{Ph}_4\text{P})^+$  salt is a monomer. The  $(\text{Bu}_4\text{N})^+$  salt forms a dimer with an  $\text{Au}\cdots\text{Au}$  distance of 3.07 Å. With  $\text{K}^+$ ,  $\text{Rb}^+$ , and  $\text{Cs}^+$  infinite linear chains with alternating long and short  $\text{Au}\cdots\text{Au}$  distances are found while the  $(\text{Me}_4\text{N})^+$  salt forms a kinked trimer with two different  $\text{Au}\cdots\text{Au}$  distances. These all show different emission maxima in the 450 to 750 nm range. As suggested previously [52], the  $\lambda_{\text{max}}(\text{emission})$  should correlate inversely with the  $\text{Au}\cdots\text{Au}$  distance. Figure 28 shows a plot of  $\lambda_{\text{max}}(\text{emission})$  versus the reciprocal of the shortest  $\text{Au}\cdots\text{Au}$  distance for these salts. On the basis of the agreement seen, the authors reached the important conclusion that a single pair of gold atoms acts as the emissive center regardless of whether the anions form a dimer, a trimer, or an extended chain.

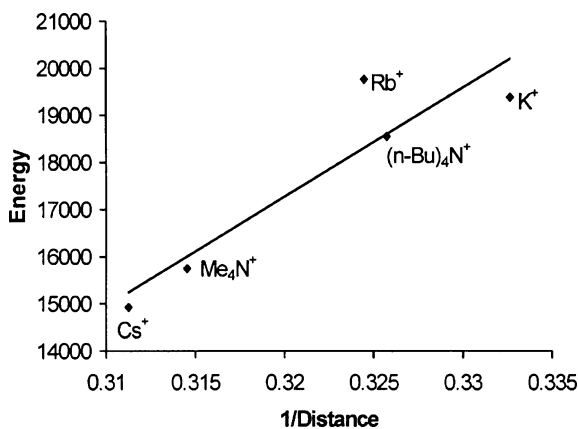


**Fig. 28** Emission energy ( $\text{cm}^{-1}$ ) versus  $1/d$  ( $\text{\AA}^{-1}$ ) for the short  $\text{Au}\cdots\text{Au}$  interactions in various salts of  $[\text{Au}^{\text{I}}(\text{SCN})_2]_n^{n-}$ . From [51]

## 8 Luminescence from Frozen Solutions

Colorless, non-luminescent solutions of  $[\text{Au}^{\text{I}}\{\text{C}(\text{NHMe})_2\}_2](\text{PF}_6) \cdot 0.5(\text{acetone})$  become intensely luminescent when they are frozen in a liquid  $\text{N}_2$  bath [48]. Strikingly, the colors of the emission vary in different solvents and appear only after the solvent has frozen. The frozen acetonitrile solution produces a green–yellow luminescence, with dimethyl sulfoxide and pyridine the emission is different shades of blue, with acetone it is orange, but with dimethylformamide no luminescence is observed. The process is entirely reversible;

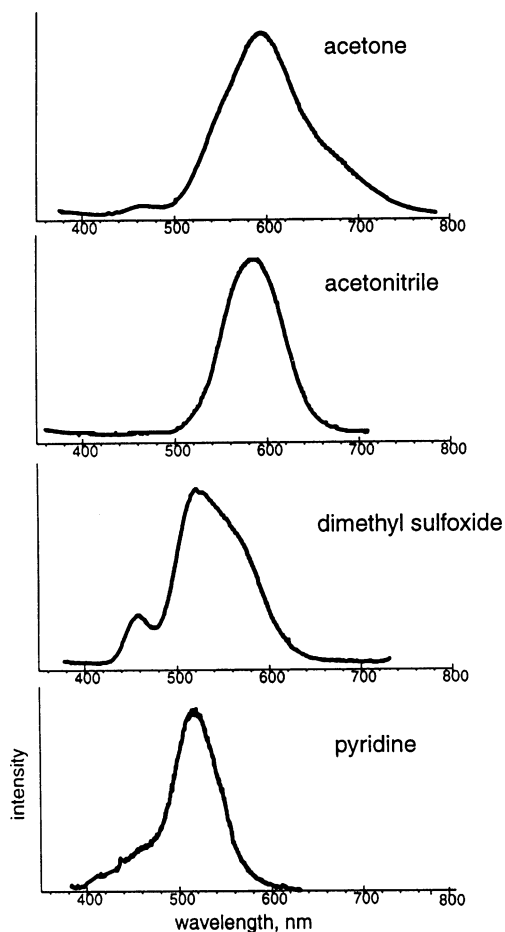


**Fig. 29** The emission spectra obtained from 6 mM solutions of  $[\text{Au}^{\text{I}}\{\text{C}(\text{NHMe})_2\}_2](\text{PF}_6) \cdot 0.5(\text{acetone})$ , **1**, in: acetone ( $\lambda_{\text{max}}$  498, 432 nm); acetonitrile ( $\lambda_{\text{max}}$  482, 426 nm); dimethyl sulfoxide ( $\lambda_{\text{max}}$  502, 432 nm); and pyridine, ( $\lambda_{\text{max}}$  475 nm) frozen at 77 K. From [48]

warming the samples results in the loss of the luminescence, while refreezing restores the colors. These colors are produced at different temperatures as each solvent freezes. Figure 29 shows the emission spectra obtained from frozen solutions of the complex at 77 K in acetone, acetonitrile, dimethyl sulfoxide, and pyridine. These effects are also concentration dependent and at lower concentrations the spectra of the frozen solutions are similar and rather like that of crystalline  $[\text{Au}^{\text{I}}\{\text{C}(\text{NHMe})_2\}_2](\text{PF}_6) \cdot 0.5(\text{acetone})$  as seen in Fig. 30.

The emission spectra obtained from these frozen solutions of  $[(\text{C}_6\text{H}_{11}\text{NC})_2\text{Au}^{\text{I}}](\text{PF}_6)$  also vary as the solvent is changed [38]. Visually the effect is not as striking as it is in the case of frozen solutions of  $[\text{Au}^{\text{I}}\{\text{C}(\text{NHMe})_2\}_2](\text{PF}_6) \cdot 0.5(\text{acetone})$ . Relevant spectra are shown in Fig. 31 for 6.0 mM solutions of  $[(\text{C}_6\text{H}_{11}\text{NC})_2\text{Au}^{\text{I}}](\text{PF}_6)$ . Dilution of the solutions of  $[(\text{C}_6\text{H}_{11}\text{NC})_2\text{Au}^{\text{I}}](\text{PF}_6)$  can also produce significant changes in the luminescence from some solutions as was the case with  $[\text{Au}^{\text{I}}\{\text{C}(\text{NHMe})_2\}_2](\text{PF}_6) \cdot 0.5(\text{acetone})$  as well.

The causes of the variations seen in Figs. 29, 30, and 31 are likely to result from a number of factors including the number of gold(I) ions involved in specific aggregates (dimers, trimers, extended chains, etc.), the distance between the gold(I) ions within any particular aggregate, the relative orientation

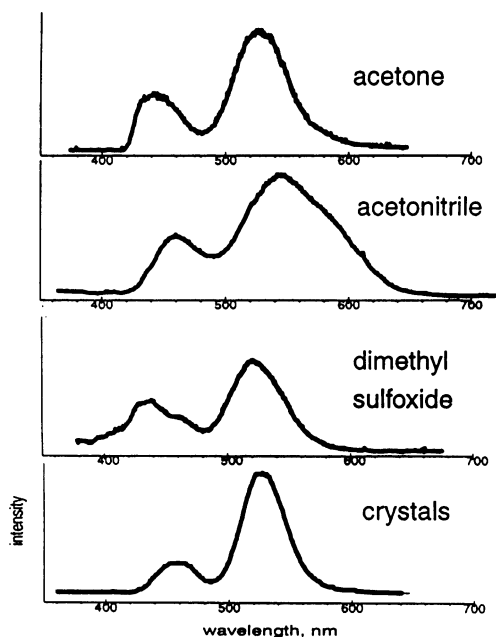


**Fig. 30** The emission spectra obtained from 0.06 mM solutions of  $[\text{Au}^{\text{I}}\{\text{C}(\text{NHMe})_2\}_2](\text{PF}_6) \cdot 0.5(\text{acetone})$  in acetone, dimethylsulfoxide, and acetonitrile frozen at 77 K and from crystalline  $[\text{Au}^{\text{I}}\{\text{C}(\text{NHMe})_2\}_2](\text{PF}_6) \cdot 0.5(\text{acetone})$ . From [48]

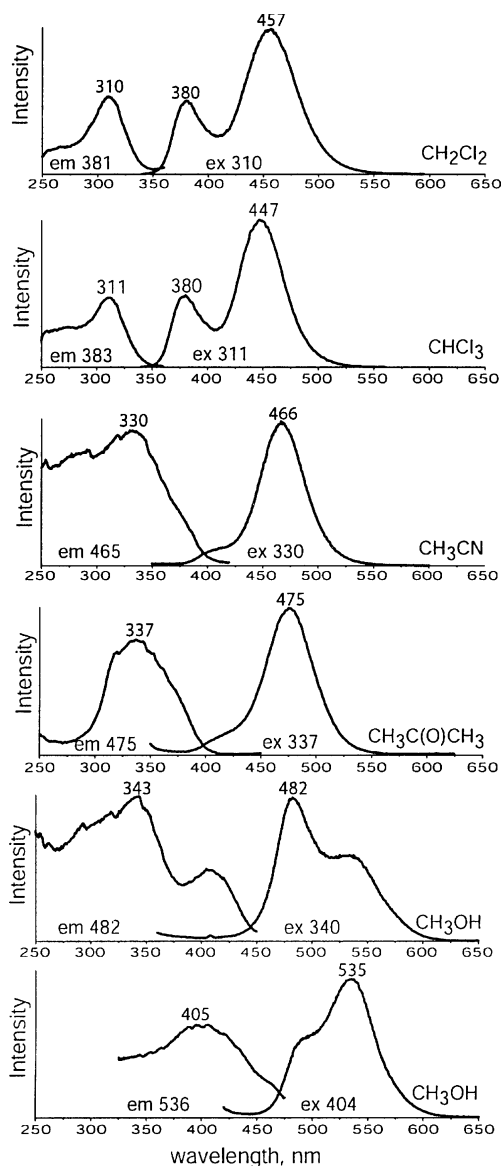


**Fig. 31** The emission (*right*) and excitation (*left*) spectra of frozen 6.0 mM solutions of  $[(C_6H_{11}NC)_2Au^1](PF_6)$  in various solvents at 77 K. The wavelength used to monitor the excitation profile is given below each excitation spectrum, and the wavelength used for excitation is shown below each emission spectrum. From [38]

of the ligands involved, hydrogen bonding interactions of the cation with the anion (hence the specific identity of the anion), hydrogen bonding interactions of the cation with the solvent, and coordination of the solvent to the

gold(I) ions in the aggregates. Solvent molecules might possibly cap the aggregates and constrain their sizes by coordination or by hydrogen-bonding with the ligands. Further work is certainly necessary to fully understand the range of aggregates that these gold complexes can form. However, the range of structures seen in the solid state with different anions presents models for the relevant structural variations. Understanding of the factors responsible for these luminescence changes should allow such complexes to be developed into sensors that are responsive to their chemical environments.

## 9

### Mechanical Effects that Alter Luminescence

It has been recognized for some time that grinding solid samples can alter the luminescence of certain metal complexes [53]. Thus, given the proclivity for the luminescence of two-coordinate gold(I) complexes to respond to various external factors, it is not entirely surprising to find that mechanical treatment of some gold(I) complexes alters their luminescent behavior.

One interesting example that is particularly pertinent to this review is the behavior of the salt  $[(\text{TPA})_2\text{Au}^{\text{I}}][\text{Au}^{\text{I}}(\text{CN})_2]$ , where TPA is 1,3,5-triaza-7-phosphaadamantane reported by Fackler and coworkers [54]. Crystallographically, the structure of the salt  $[(\text{TPA})_2\text{Au}^{\text{I}}][\text{Au}^{\text{I}}(\text{CN})_2]$  consists of an infinite column of alternating cations and anions with a  $\text{Au} \cdots \text{Au}$  separation of  $3.457(1) \text{ \AA}$  as seen in Fig. 32. The salt as prepared in crystalline form is not luminescent, but it becomes luminescent upon grinding as the data in Fig. 33 show. In this case it is important to note that grinding does not result in a polymorphic phase change. The powder X-ray diffraction of the ground sample is similar to that calculated on the basis of the single crystal X-ray diffraction data. However, a non-crystalline, but luminescent material could be produced during the grinding process that would not be detected by X-ray diffraction. The authors surmise that grinding creates trapping sites through exposing more chain ends, creating lattice defects, and increasing mosaic spread. The role of surface states in understanding the luminescence of solid inorganic phosphors has been recently reviewed [55].

Eisenberg and Lee have reported another case of a pressure-induced luminescence [56]. The thiouracil complex shown below in Scheme 5 contains a binuclear Au(I) complex with a short  $\text{Au} \cdots \text{Au}$  separation of  $2.8797(4) \text{ \AA}$  when the non-coordinated anion is trifluoroacetate. In crystalline form this complex displays a weak white luminescence, but upon grinding an intense blue luminescence is observed. This transformation is accompanied by liberation of acid vapor and the deprotonation of the uncoordinated nitrogen atom of the heterocycle. The resulting product has been independently prepared and crystallographically characterized. In this form a pair of the binuclear complexes are connected by a short ( $2.9235(4) \text{ \AA}$ )  $\text{Au} \cdots \text{Au}$  interaction.

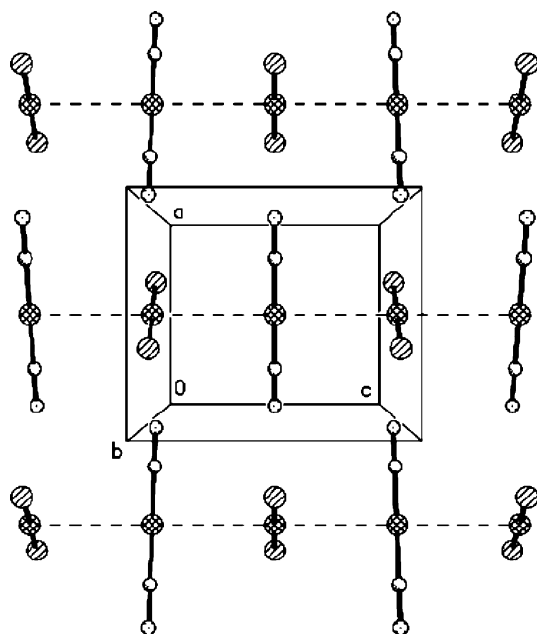


**Fig. 32** Packing diagram showing the linear chain structure of  $[(\text{TPA})_2\text{Au}^{\text{I}}][\text{Au}^{\text{I}}(\text{CN})_2]$ , (TPA is 1,3,5-triaza-7-phosphaadamantane). For clarity, only phosphorus atoms in the TPA ligand are shown. From [54]

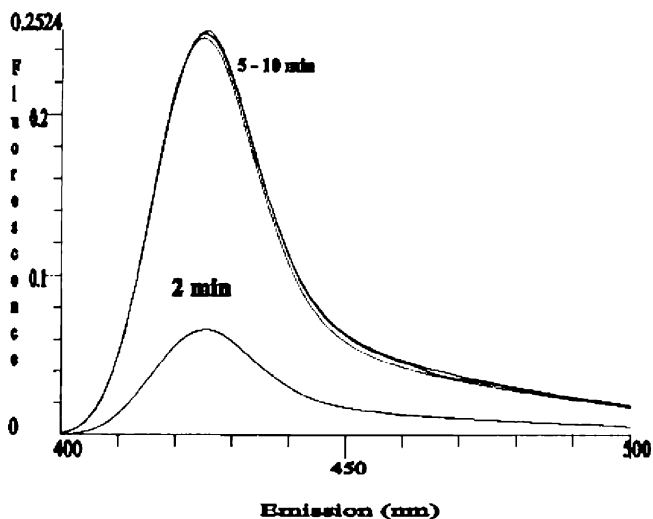
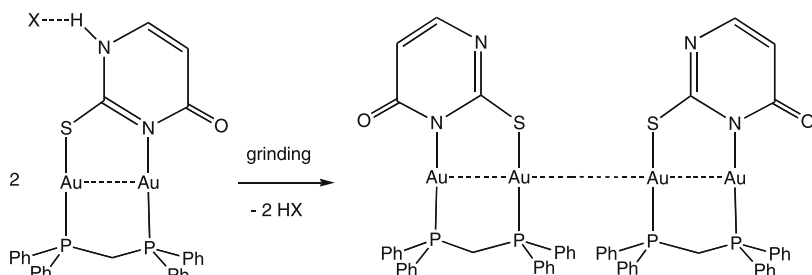


**Fig. 33** Relative emission intensity of  $[(\text{TPA})_2\text{Au}^{\text{I}}][\text{Au}^{\text{I}}(\text{CN})_2]$ , (TPA is 1,3,5-triaza-7-phosphaadamantane) with respect to grinding time. The spectra were recorded at 78 K with an identical PMT gain, slit width, and other instrumental setup. No emission is evident before grinding the crystalline sample. From [54]



Scheme 5

## 10 Ligand-Bridged Complexes

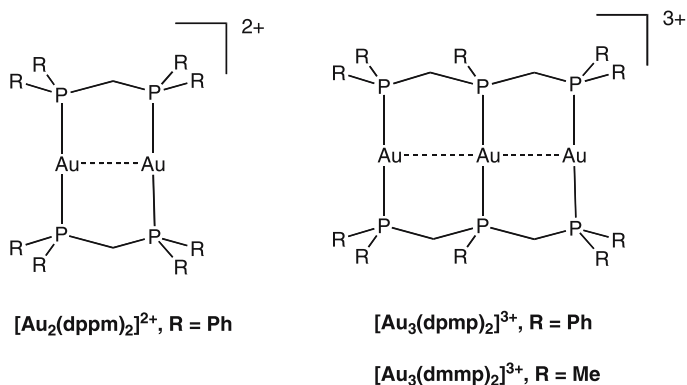
Bridging ligands can be utilized to hold and maintain two Au(I) ions in close proximity. Although a thorough review of such ligand-bridged complexes is beyond the scope of this article, it is useful to mention a few aspects of their spectroscopic properties. In particular, such ligand-bridged complexes provide models for the dimers that form from monomeric, two-coordinate Au(I) complexes. The prototypical complex of this class is the diphosphine-bridged dimer,  $[\text{Au}_2(\text{dppm})_2]^{2+}$ , whose structure is shown in Scheme 5 [57–59]. The electronic absorption spectrum of  $[\text{Au}_2(\text{dppm})_2]^{2+}$  in dilute solution at room temperature displays an absorption at 290 nm that has been assigned to transition from the filled  $5d_{z^2}(\sigma^*)$  to empty  $6p_z(\sigma)$  orbital and an emission at 570 nm, which was assigned as phosphorescence from a  $5d_{z^2}(\sigma^*)^1 6p_z(\sigma)^1$  state [58, 59]. The related complex  $[\text{Au}_2(\text{dcpm})_2](\text{ClO}_4)_2$ , with cyclohexyl groups in place of the phenyl groups, has a  $\text{Au} \cdots \text{Au}$  separation of 2.9263(9) Å, absorption at 277 and ca. 315 nm and emission at ca. 500 nm in acetonitrile solution [60]. The emission maxima from  $[\text{Au}_2(\text{dcpm})_2](\text{ClO}_4)_2$  shows variations in wavelength that depend upon the medium. These variations have been ascribed to exciplex formation of the  $5d_{z^2}(\sigma^*)^1 6p_z(\sigma)^1$  excited state with counter-ions or solvent [60]. The observation of emission from solutions of these dimeric complexes is particularly significant in the context of this review, because many of the monomeric, two-coordinate complexes discussed here are non-emissive in dilute solutions where no  $\text{Au} \cdots \text{Au}$  interactions are present.

The lowest energy dipole-allowed absorption band of  $[\text{Au}_2(\text{dcpm})_2](\text{ClO}_4)_2$  at 297 nm has been investigated by resonance Raman spectroscopy [61]. The characteristics of the spectrum are fully in accord with the assignment of the absorption band as transition from a filled  $5d_{z^2}(\sigma^*)$  orbital to an empty  $6p_z(\sigma)$  orbital. Analysis of the spectrum in terms of a pure  $\text{Au} \cdots \text{Au}$  stretch indicated that the  $\text{Au} \cdots \text{Au}$  distance is shortened by 0.11 Å in the excited state, a conclusion which is consistent with a situation in which an electron

moves from an anti-bonding orbital between the two Au<sup>I</sup> ions into an orbital that is bonding between the two Au<sup>I</sup> ions.

By using analogous tridentate triphosphine as a bridging ligand, we showed some time ago that a diverse variety of nearly linear trinuclear complexes could be obtained [62, 63]. This strategy has been applied to produce some nearly linear, trinuclear Au(I) complexes. The colorless ions, [Au<sub>3</sub>(dpmp)<sub>2</sub>]<sup>3+</sup> and [Au<sub>3</sub>(dmmp)<sub>2</sub>]<sup>3+</sup>, shown in Scheme 6 are prominent examples [64–67]. Colorless [Au<sub>3</sub>(dmmp)<sub>2</sub>](ClO<sub>4</sub>)<sub>3</sub> has been examined by single crystal X-ray diffraction and found to be significantly bent (Au⋯Au⋯Au angle of 136.26(2)°) with Au⋯Au separations of 2.981(1) and 2.962(1) Å [64]. The intense absorption band at 315 for [Au<sub>3</sub>(dmmp)<sub>2</sub>](ClO<sub>4</sub>)<sub>3</sub> and the corresponding band at 269 nm for the analogous di-gold complex [Au<sub>2</sub>(dmpm)<sub>2</sub>](ClO<sub>4</sub>)<sub>2</sub> have been assigned as the filled *d*<sub>z<sup>2</sup></sub>(σ\*) to empty *p*<sub>z</sub>(σ) transitions in each cation. The shift of the transition to lower energy in the trimer is consistent with the idea that an increase in the number of Au<sup>I</sup> ions involved in the complex narrows the gap between the filled *d*<sub>z<sup>2</sup></sub>(σ\*) level and the empty *p*<sub>z</sub>(σ) level. The emission spectrum of [Au<sub>3</sub>(dmmp)<sub>2</sub>](ClO<sub>4</sub>)<sub>3</sub> in acetonitrile solution shows two bands at 467 and 580 nm. The low energy feature has been associated with emission from a *d*<sub>z<sup>2</sup></sub>(σ\*)<sup>1</sup>*p*<sub>z</sub>(σ)<sup>1</sup> triplet, while the high energy band has been assigned to an intraligand transition of the phosphine [64]. A number of calculations have been performed that provide a theoretical background for understanding the absorption and emission processes and the effects of metal ion separation [68, 69]. The long-lived triplet excited state of [Au<sub>3</sub>(dmmp)<sub>2</sub>]<sup>3+</sup> has been utilized to induce cleavage of DNA [70].

A multitude of related polynuclear gold complexes have been prepared utilizing a range of bridging ligands, and their spectroscopic properties have been examined [71]. An example involving 16 individual Au(I) ions deserves mention because of its extreme complexity [72].



**Scheme 6**



## 11 Conclusions

As the examples shown above illustrate, the luminescence of many two-coordinate gold(I) complexes shows marked effects from the environment in which that complex finds itself. Thus, to understand the luminescence produced by such gold(I) complexes, one needs to know about the supramolecular structure. Self-association and the interactions produced by aurophilic interactions are particularly significant in contributing to the luminescent properties of many gold(I) complexes. In a few cases such as the luminescence from  $[\text{Au}^{\text{I}}(\text{SCN})_2]^-$  some trends like those seen in Fig. 28 are readily apparent [51], and the significance of localized pairs of emitting centers revealed [73]. In other cases such as solvoluminescence and the effects of grinding, further detailed understanding of the nature of the emitting sites would be welcome.

This review has been designed to cover a limited range of topics relevant to the luminescent properties of gold(I) in a two-coordinate situation. In any review of this sort, the author is bound to be guilty of the sin of omission and certainly that is the case here. The extensive work on polynuclear complexes of gold and of gold in combination with other transition metal ions has been specifically excluded. Time and space have not allowed us to review the luminescent properties of three- and four-coordinate gold [74]. Thus, the important work of Omary and coworkers on three-coordinate gold(I) has not been discussed [75, 76]. Interesting polymeric gold(I) complexes prepared by Puddephatt and coworkers have also not received their share of attention here [77–79]. Likewise, significant work on luminescent gold-alkynyl complexes of Yam and coworkers has not fallen into the purview of the work covered in this review [80, 81]. Nor have we been able to review the remarkable mixed-metal Au(I) complexes prepared by Catalano and others [82, 83].

**Acknowledgements** Work on luminescent gold(I) complexes at the University of California has been supported by the National Science Foundation (Grants CHE 9610507 and CHE-0413857) and by the Petroleum Research Fund (Grants Grant 40030-AC and 37056-AC). I thank them and my many wonderful students and postdocs for the opportunity to undertake some of the work reviewed here.

## References

1. Grohmann A, Schmidbaur H (1995) In: Abel EW, Stone FGA, Wilkinson G (eds) *Comprehensive Organometallic Chemistry II*. Elsevier, Oxford, 3:1
2. Schmidbaur H (1995) *Chem Soc Rev* 24:391
3. Forward JM, Fackler JP Jr, Assefa Z (1999) In: *Optoelectronic Properties of Inorganic Compounds*. Plenum Press, New York
4. Fackler JP Jr (2002) *Inorg Chem* 41:6959
5. Jones PG (1981) *Gold Bull* 14:102

6. Jones PG (1981) *Gold Bull* 14:159
7. Jones PG (1983) *Gold Bull* 16:114
8. Jones PG (1986) *Gold Bull* 19:4
9. Pathaneni SS, Desiraju GR (1993) *J Chem Soc Dalton Trans*, p 319
10. Schmidbaur H, Graf W, Müller G (1988) *Angew Chem Int Ed Engl* 27:417
11. Harwell DE, Mortimer MD, Knobler CB, Anet FAL, Hawthorne MF (1996) *J Am Chem Soc* 118:2679
12. Balch AL, Fung EY, Olmstead MM (1990) *J Am Chem Soc* 112:5181
13. Pyykkö P (1997) *Chem Rev* 97:597
14. Pyykkö P (2004) *Angew Chem Int Ed* 43:4413
15. Pyykkö P (2005) *Inorg Chim Acta* 358:4113
16. Pyykkö P, Runeberg N, Mendizabal F (1997) *Chem Eur J* 3:1451
17. Pyykkö P, Mendizabal F (1997) *Chem Eur J* 3:1458
18. Pyykkö P, Li J, Runeberg N (1994) *Chem Phys Lett* 218:133
19. Pyykkö P (2002) *Angew Chem Int Ed* 41:3573
20. Schmidbaur H, Graf W, Müller G (1988) *Angew Chem Int Ed Engl* 27:417
21. Harwell DE, Mortimer MD, Knobler CB, Anet FAL, Hawthorne MF (1996) *J Am Chem Soc* 118:2679
22. Balch AL, Fung EY, Olmstead MM (1990) *J Am Chem Soc* 112:5181
23. Zank J, Schier A, Schmidbaur H (1998) *J Chem Soc Dalton Trans*, p 323
24. Mason WR (1973) *J Am Chem Soc* 95:3573
25. Mason WR (1976) *J Am Chem Soc* 98:5182
26. Chastain SK, Mason WR (1982) *Inorg Chem* 21:3717
27. Fenske GP Jr, Mason WR (1974) *Inorg Chem* 13:1783
28. Koutek ME, Mason WR (1980) *Inorg Chem* 19:648
29. Savas MM, Mason WR (1987) *Inorg Chem* 26:301
30. Adams MD, Johns MW, Dew DW (1999) In: Schmidbaur H (ed) *Gold; Progress in Chemistry, Biochemistry and Technology*. Wiley, New York, p 65
31. Wagner FE, Haslbeck S, Stievano L, Calogero S, Pankhurst QA, Martlinek K-P (2000) *Nature (London)* 407:691
32. Shaw FS III (1999) *Chem Rev* 99:2589
33. Yersin H, Trümbach D, Strasser J, Patterson HH, Assefa Z (1998) *Inorg Chem* 37:3209
34. Rawashdeh-Omary MA, Omary MA, Patterson HH (2000) *J Am Chem Soc* 122:10371
35. Rawashdeh-Omary MA, Omary MA, Patterson HH, Fackler JP Jr (2001) *J Am Chem Soc* 123:11237
36. Hettiarachchi SR, Rawashdeh-Omary MA, Kanan SM, Omary MA, Patterson HH, Tripp CP (2002) *J Phys Chem B* 106:10058
37. McCrone WC (1965) In: Fox D, Labes MM, Weissberger (eds) *Polymorphism. Physics and chemistry of the organic solid state*. Wiley Interscience, New York 2:725
38. White-Morris RL, Olmstead MM, Balch AL (2003) *J Am Chem Soc* 125:1033
39. Toronto DV, Weissbart B, Tinti DS, Balch AL (1996) *Inorg Chem* 35:2484
40. Weissbart B, Toronto DV, Balch AL, Tinti DS (1996) *Inorg Chem* 35:2490
41. White-Morris RL, Olmstead MM, Attar S, Balch AL (2005) *Inorg Chem* 44:5021
42. Gussenhoven EM, Fettingner JC, Pham DM, Malwitz MA, Balch AL (2005) *J Am Chem Soc* 127:10838
43. Vickery JC, Olmstead MM, Fung EY, Balch AL (1997) *Angew Chem Int Ed Engl* 36:1179
44. Parks JE, Balch AL (1974) *J Organomet Chem* 71:453
45. Balch AL, Olmstead MM, Vickery JC (1999) *Inorg Chem* 38:3494
46. Olmstead MM, Jiang F, Attar S, Balch AL (2001) *J Am Chem Soc* 123:3260

47. Rawashdeh-Omary MA, Omary M, Fackler JP Jr, Galassi R, Pietroni BR, Brurini A (2110) *J Am Chem Soc* 123:9689
48. White-Morris RL, Olmstead MM, Jiang F, Tinti DS, Balch AL (2002) *J Am Chem Soc* 124:2327
49. White-Morris RL, Olmstead MM, Jiang F, Balch AL (2002) *Inorg Chem* 41:2313
50. Jiang F, Olmstead MM, Balch AL (2000) *J Chem Soc, Dalton Trans*, p 4098
51. Coker NL, Jeanette A, Krause Bauer JA, Elder RC (2004) *J Am Chem Soc* 126:12
52. Assefa Z, McBurnett B, Staples R, Fackler JP Jr, Assmann B, Angermaier K, Schmidbaur H (1995) *Inorg Chem* 34:75
53. Chandra BP, Majumdar B (1983) *Cryst Res Tech* 2:237
54. Assefa Z, Omary MA, McBurnett BG, Mohamed AA, Patterson HH, Staples RJ, Fackler JP Jr (2002) *Inorg Chem* 41:6274
55. Abrams BL, Holloway PH (2004) *Chem Rev* 104:5783
56. Lee AY, Eisenberg R (2003) *J Am Chem Soc* 125:7778
57. King C, Wang JC, Nazrul M, Khan I, Fackler JP Jr (1989) *Inorg Chem* 28:2145
58. Che CM, Kwong HL, Yam VWW, Cho KC (1989) *Chem Commun* 13:885
59. Che CM, Kwong HL, Poon CK, Yam VWW (1990) *J Chem Soc Dalton Trans* 11:3215
60. Fu WF, Chan KC, Miskowski VM, Che CM (1999) *Angew Chem Int Ed* 38:2783
61. Leung KH, Phillips DL, Tse MC, Che CM, Miskowski VM (1999) *J Am Chem Soc* 121:4799
62. Guimerans RR, Olmstead MM, Balch AL (1983) *J Am Chem Soc* 105:1677
63. Balch AL (1993) *Progr Inorg Chem* 41:239
64. Yam VWW, Lai TF, Che CM (1990) *J Chem Soc Dalton Trans*, p 3747
65. Li D, Che CM, Peng SM, Liu ST, Zhou ZY, Mak TCW (1993) *J Chem Soc Dalton Trans*, p 189
66. Bardaji M, Laguna A (2001) *Inorg Chim Acta* 318:38
67. Bardaji M, Laguna A, Vicente J, Jones PG (2001) *Inorg Chem* 40:2675
68. Zhang HX, Che CM (2001) *Chem Eur J* 7:4887
69. Pan QJ, Zhang HX, Fu HG, Yu HT (2006) *Eur J Inorg Chem* 5:1050
70. Yam VWW, Choi SWK, Lo KKW, Dung WF, Kong RYC (1994) *Chem Commun* 20:2379
71. Yam VWW, Lo KKW (1999) *Chem Soc Rev* 28:323
72. Yu SY, Zhang ZX, Cheng ECC, Li YZ, Yam VWW, Huang HP, Zhang R (2005) *J Am Chem Soc* 127:17994
73. Coker NL, Jeanette A, Krause Bauer JA, Elder RC (2004) *J Am Chem Soc* 126:12
74. Gimeno MC, Laguna A (1997) *Chem Rev* 97:511
75. Barakat KA, Cundari TR, Omary MA (2003) *J Am Chem Soc* 125:14228
76. Sinha P, Wilson AK, Omary MA (2005) *J Am Chem Soc* 127:12488
77. Brandys M-C, Puddephatt RJ (2001) *J Am Chem Soc* 123:4839
78. Hunks WJ, MacDonald M-A, Jennings MC, Puddephatt RJ (2000) *Organometallics* 19:5063
79. Irwin MJ, Vittal JJ, Puddephatt RJ (1997) *Organometallics* 16:3541
80. Yam VWW, Yip SK, Yuan LH, Cheung KL, Zhu N, Cheung KK (2003) *Organometallics* 22:2630
81. Yip SK, Cheng ECC, Yuan LH, Zhu NY, Yam VWW (2004) *Angew Chem Int Ed* 43:4954
82. Catalano VJ, Bennett BL, Kar HM, Noll BC (1999) *J Am Chem Soc* 121:10235
83. Catalano VJ, Malwitz MA, Noll BC (2001) *Chem Commun*, p 581

# From Photoinduced Charge Separation to Light-driven Molecular Machines

Etienne Baranoff<sup>1</sup> · Francesco Barigelletti<sup>2</sup> · Sylvestre Bonnet<sup>1</sup> ·  
Jean-Paul Collin<sup>1</sup> · Lucia Flamigni<sup>2</sup> · Pierre Mobian<sup>1</sup> ·  
Jean-Pierre Sauvage<sup>1</sup> (✉)

<sup>1</sup>Laboratoire de Chimie Organo-Minérale, UMR 7513 du CNRS, Institut Le Bel,  
Université Louis Pasteur, 4 rue Blaise Pascal, 67000 Strasbourg Cedex, France  
*sauvage@chimie.u-strasbg.fr*

<sup>2</sup>Istituto ISOF-CNR, Via P. Gobetti 101, 40129 Bologna, Italy

<b>1</b>	<b>Introduction</b> . . . . .	<b>43</b>
<b>2</b>	<b>Charge Separation on Derivatives of Ir(terpy)<sub>2</sub><sup>3+</sup> Used as Electron Relay or Photoactive Centre</b> . . . . .	<b>44</b>
2.1	Early Work on Systems Based on Ru(II) and Os(II) bis-Terpyridine Complexes . . . . .	45
2.2	Ir(terpy) <sub>2</sub> <sup>3+</sup> and Derivatives: Photophysical Properties . . . . .	53
2.3	Ir as Electron Relay: The Molecular Triads PH <sub>2</sub> -Ir(III)-PAu <sup>4+</sup> and PZn-Ir(III)-PAu <sup>4+</sup> . . . . .	56
2.4	Ir as Photoactive Centre . . . . .	59
2.5	Related Systems Reported by Other Groups . . . . .	62
<b>3</b>	<b>Ruthenium-based Light-driven Molecular Machine Prototypes</b> . . . . .	<b>64</b>
3.1	Use of Dissociative Excited States to Set Ru(II)-complexed Molecular Machines in Motion: Principle . . . . .	64
3.2	Photochemical and Thermal Ligand Exchange in a Ruthenium(II) Complex Based on a Scorpionate Terpyridine Ligand . . . . .	65
3.3	A Ru(terpy)(phen)-incorporating Ring and Its Light-induced Geometrical Changes . . . . .	67
3.4	Light-driven Unthreading Reaction in Rotaxane with a [Ru(diimine) <sub>3</sub> ] <sup>2+</sup> Core . . . . .	70
3.5	Photoinduced Decoordination and Thermal Reoordination of a Ring in a Ruthenium(II)-Containing [2]Catenane . . . . .	72
<b>4</b>	<b>Conclusion</b> . . . . .	<b>74</b>
	<b>References</b> . . . . .	<b>75</b>

**Abstract** The photochemical properties of transition metal complexes, such as those of iridium(III) or ruthenium(II), can be exploited in various ways to generate charge-separated (CS) states, in relation to the mimicry of the natural photosynthetic reaction centres, or to set multicomponent compounds or assemblies in motion. The first part of the present chapter summarizes the work carried out in our groups (Bologna and Strasbourg) in recent years with iridium(III)-terpy complexes (terpy: 2,2',6',6''-terpyridine). The synthesis of multicomponent iridium(III) complexes in reasonable yields has been

achieved and their photochemical properties have been investigated. Unexpectedly, the excited state lifetimes of some of these compounds are very long at room temperature (several microseconds) in fluid solution, making the Ir(terpy)<sub>2</sub><sup>3+</sup> fragment an interesting chromophore. Once attached to electron donor (D) groups, dyads of the Ir(terpy)<sub>2</sub><sup>3+</sup>-D type undergo fast photoinduced electron transfer. In addition Ir(terpy)<sub>2</sub><sup>3+</sup> in the ground state is a relatively good electron acceptor, displaying interesting properties as electron relay in porphyrinic triads. A triad, consisting of an Ir(terpy)<sub>2</sub><sup>3+</sup> central core, a Zn porphyrin as the primary donor on one side and a gold(III) porphyrin as the terminal acceptor on the other side, leads to a relatively long-lived CS state (close to the microsecond). The other section of the present chapter deals with light-driven molecular machines built around Ru(bpy)<sub>3</sub><sup>2+</sup> derivatives, including catenanes and rotaxanes. In order to set the system in motion, a dissociative ligand field (LF) state is generated from the light-absorbing metal-to-ligand charge transfer (MLCT) state, originating in the expulsion of a given ligand in a perfectly controlled fashion. This step is rapidly followed by coordination of another ligand to afford a kinetically stable new complex. The process can be inverted by thermal energy, so as to regenerate the starting state of the system.

**Keywords** Catenane · Ir/Ru · Light-driven molecular machine · Photoinduced Charge Separation · Rotaxane · Scorpionate

### Abbreviations

A	Acceptor
bpqpy	2,6-bis(4'-phenyl-2'-quinolyl)-pyridine
bpy	2,2'-bipyridine
CR	Charge Recombination
CS	Charge Separation or Charge Separated
CT	Charge Transfer
D	Donor
dmbp	6,6'-dimethyl-2,2'-bipyridine
dmp	2,9-dimethyl-1,10-phenanthroline
DPAA	di- <i>p</i> -anisylamine
dpbp	6,6'-diphenyl-2,2'bipyridine
DQ	<i>N,N'</i> -polymethylene bridged-2,2'-bipyridinium
HOMO	Highest Occupied Molecular Orbital
ILCT	Intra Ligand Charge Transfer
LC	Ligand Centered
LF	Ligand Field
LLCT	Ligand to Ligand Charge Transfer
LUMO	Lowest Unoccupied Molecular Orbital
MLCT	Metal to Ligand Charge Transfer
MV	1,1'-dimethyl-4,4'-bipyridinium, methyl viologen
OLED	Organic Light-Emitting Diode
PC	Photoactive Centre
phen	1,10-phenanthroline
PTZ	phenothiazine
py	pyridine
RCM	Ring Closing Metathesis
terpy	2,2' : 6',2''-terpyridine
tterpy	4'-( <i>p</i> -tolyl)-2,2' : 6',2''-terpyridine

## 1 Introduction

Several decades ago, inorganic photochemistry was mostly devoted to the photochemical reactivity of transition metal complexes: by shining light onto a transition metal complex, one or several photoproducts were obtained and analyzed. In this respect, inorganic photochemistry could be considered as an interesting *synthetic* method [1, 2].

The seventies have seen the triumph of  $\text{Ru}(\text{bpy})_3^{2+}$  and its numerous congeners, in relation to solar energy conversion [3, 4]. Gradually, the excited state became, in the photochemists' mind, a powerful energy or electron transfer agent instead of a molecular species to be converted to another one.

Many multicomponent transition metal complexes have been elaborated in the course of the last 15 to 20 years, with the aim of inducing charge separation under the action of light, so as to generate reasonably long-lived charge separated (CS) states. The first part of this review article relates to this active field of research.

One of the favourite generic arrangement is the molecular triad, consisting of a photoactive centre (PC), an electron donor (D) and an electron acceptor (A). In systems such as D-PC-A, the charge separated state  $\text{D}^+\text{-PC-A}^-$  is obtained in two consecutive-electron transfer processes after excitation of PC. Of course, several variants exist, depending on the electron transfer properties of PC and its excited state,  $\text{PC}^*$ , as well as on the precise arrangement of the various components ( $\text{PC-A}_1\text{-A}_2$  or  $\text{D}_2\text{-D}_1\text{-PC}$ , in particular, if  $\text{PC}^*$  is an electron donor or an electron acceptor, respectively).

$\text{Ir}(\text{III})$  complexes containing terpy type ligands (terpy = 2,2' : 6',2''-terpyridine) have been shown to behave as strong electron acceptors in their excited state and as interesting electron relays in their ground state. These unusual properties, distinctly different from those of their  $\text{Ru}(\text{II})$  analogues, have been exploited to construct molecular dyads and triads incorporating  $\text{Ir}(\text{terpy})_2^{3+}$  fragments.

The field of dynamic molecular systems, for which given parts of the compounds or assemblies can be set in motion in a highly controlled fashion, is most of the time referred to as "molecular machines". This new field of research seems to attract much interest from organic chemistry and coordination chemistry teams. Most of the molecular machines containing transition metal centres are driven using electrochemistry (reduction or oxidation of the metal centre). An alternative approach, reviewed in the second part of the present chapter, is based on photochemistry. The excited state is now considered, again, as a photoreagent whose function will be more complex than just exchanging energy or an electron. A real photochemical reaction will take place (expulsion of a ligand if light excitation generates a dissociative excited state), which will be at the origin of a large amplitude motion. Another stimulus will have to invert the motion and regenerate the starting state

of the complex. In this respect, this very recent aspect of the molecular machine area goes back to the previous work mentioned at the beginning of the introduction, dealing with preparative photochemistry. The main difference holds in the complexity of the ligand backbones now utilized to construct the molecular machines in question.

## 2

### Charge Separation on Derivatives of $\text{Ir}(\text{terpy})_2^{3+}$ Used as Electron Relay or Photoactive Centre

We will review here work wherein several types of species incorporate the Ir-bis-terpy unit and derivatives. The search for multicomponent arrays, including metal-based photoactive centres in combination with electron donor and acceptor components, was started a couple of decades ago, and one of the first systems, compound  $1^{4+}$ , was studied by Meyer et al. (Fig. 1) [5]. In this multicomponent system, the electron donor phenothiazine (PTZ) and the bridged 2,2'-bipyridinium (DQ) units are linked to the photoactive unit by flexible methylene connections. In this early example, excitation at the Ru-based chromophore ultimately yields a  $\text{PTZ}^+ \text{-DQ}^-$  CS state which lives 165 ns and for which the transiently stored energy is 1.29 eV.

We will see how our work extended such types of studies and gradually led to several types of Ru(II)- and Os(II)-based dyadic and triadic species and how the Ir(III)-bis-terpy-based photosensitizers emerged as convenient units to build up linearly arranged multicomponent arrays. It should be mentioned here that Ir(III)-cyclometalated complexes, both of bidentate and tridentate ligands, have proved to be convenient for use as singlet oxygen sensitizers [6, 7], as biological labelling reagents [8] and as efficient phosphors in

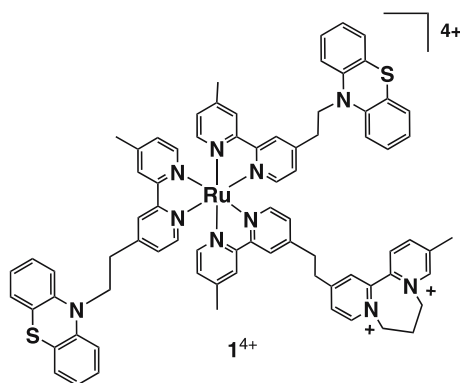


**Fig. 1** Chemical structure of compound  $1^{4+}$

the area of OLED fabrication [9–16]. For the last type of application, the research activity is expanding remarkably and several uncharged (neutral) Ir(III) species are being tested as phosphorescent dopant within these electroluminescent devices. The neutral character is a basic requirement to avoid the physical displacement of these luminophores upon application of the electric field to generate the electron and hole flux within the device. Ir(III) compounds featuring exceptionally high luminescent quantum yields (not far from unity) [9, 13] and tunable emission colours [14, 17–19] have been characterised and their incorporation within various types of OLEDs looks very promising. However, we shall restrict ourselves to applications aimed at the study of the photoinduced charge separation. For these, Ir-bis-terpyridine derivatives prove to be the basic unit of choice.

## 2.1

### Early Work on Systems Based on Ru(II) and Os(II) bis-Terpyridine Complexes

Compounds  $2^{4+}$ – $5^{4+}$  (Fig. 2) were the first systems studied by our groups with the aim of achieving charge separation over a nanometric array [20, 21]. The arrays are based on Ru(II) or Os(II) bis-terpyridine decorated with a methyl viologen (MV) electron acceptor and either a di-*p*-anisylamine (DPAA) or a phenothiazine (PTZ) as electron donors; the centre-to-centre separation between the terminal units can be evaluated to be ca. 1.7 nm. In comparison to other systems based on bidentate ligands [5], these structures have the advantage of a rigid, linear geometry well suited for the construction of wire-type arrays, without the possibility of different isomers. Excitation of the metal

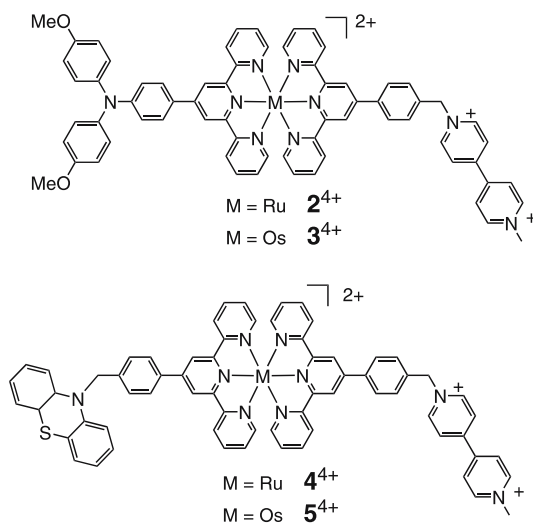


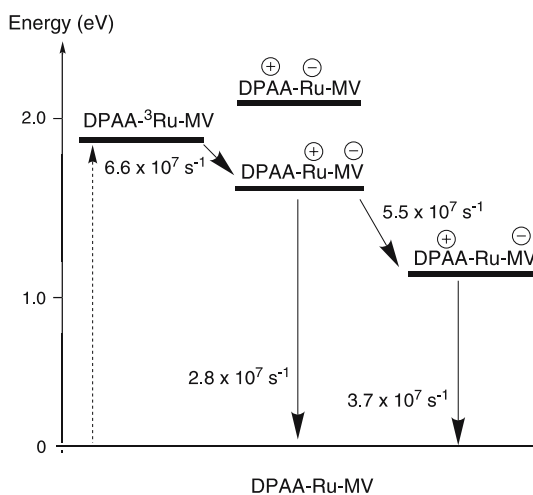
**Fig. 2** Chemical structures of compounds  $2^{4+}$ ,  $3^{4+}$ ,  $4^{4+}$  and  $5^{4+}$



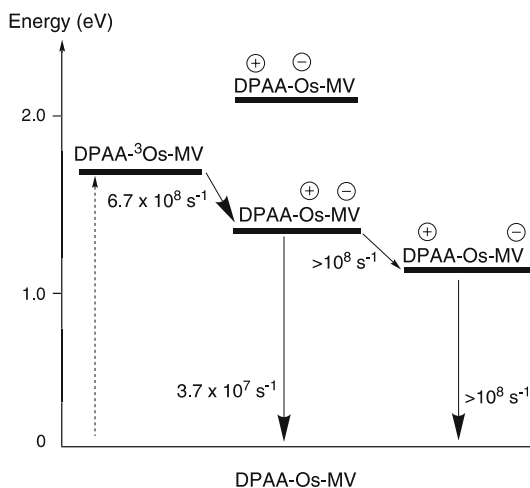
complex unit leads to population of the metal to ligand charge transfer triplet excited state ( $^3\text{MLCT}$ ) displaying lifetimes of 0.95 ns and 230 ns at room temperature for the complexes,  $\text{Ru}(\text{terpy})_2^{2+}$ , and  $\text{Os}(\text{terpy})_2^{2+}$  respectively. Due to the short lifetime of the former at room temperature, the determinations in the triads were performed in fluid solutions at low temperature (155 K) to increase the lifetime of the excited state. For comparison purposes the triads based on  $\text{Os}(\text{terpy})_2^{2+}$ , in addition to room temperature, were also studied at 155 K.

For the Ru-based DPAA-Ru-MV triad, the photoinduced processes are summarized in Scheme 1. In this approximate scheme, the excited state energy levels are derived from the luminescence data ( $\lambda_{\text{max}}$  at 77 K), and the energy of the charge separated states are derived from the redox potentials by simple addition of the energy necessary to oxidize the donor and the energy necessary to reduce the acceptor. The excitation of the Ru-based photosensitizer leads to a quenched luminescence lifetime of 15 ns as in the corresponding Ru-MV dyad which, compared to a lifetime of 800 ns for the model complex at 155 K [20], yields an electron transfer rate constant of  $6.6 \times 10^7 \text{ s}^{-1}$ . The transient spectrum obtained in the triad after excitation of the Ru complex consists of the DPAA $^+$  radical cation band, which is formed with a lifetime of 18 ns. Therefore after formation of the primary CS state, DPAA-Ru $^+$ -MV $^-$ , the fully CS state, DPAA $^+$ -Ru-MV $^-$ , is formed and subsequently decays with a lifetime of 27 ns.

For the Os-based triad, the primary electron transfer quenching process leading to DPAA-Os $^+$ -MV $^-$  takes place with  $k = 6.7 \times 10^8 \text{ s}^{-1}$  ( $\tau = 1.5 \text{ ns}$ ), Scheme 2. As can be seen from the energy level scheme, electron transfer



**Scheme 1** Energy level diagram and reaction rates for the photoinduced processes occurring in triad  $2^{4+}$  at 155 K. Excitation (*dashed arrow*) on the DPAA chromophore



**Scheme 2** Energy level diagram and reaction rates for the photoinduced processes occurring in  $3^{4+}$  at 155 K. Excitation (*dashed arrow*) on the DPAA chromophore

from the donor to the oxidized photosensitizer is thermodynamically feasible. Since neither  $\text{DPAA}^+$  nor  $\text{Os}^+$  absorption bands are detected in the transient spectra, it can be concluded that (i) the deactivation of  $\text{DPAA-Os}^+-\text{MV}^-$  via  $\text{DPAA}^+-\text{Os-MV}^-$  is faster than the rate of back electron transfer in the dyad  $\text{Os-MV}$  ( $k = 3.7 \times 10^7 \text{ s}^{-1}$ ) and that (ii) the subsequent CR of the fully CS state  $\text{DPAA}^+-\text{Os-MV}^-$  is faster than the experimental resolution (ca. 10 ns), placing for the last two reactions a lower limit of  $10^8 \text{ s}^{-1}$ . When PTZ is used as electron donor, the system displays chemical and photochemical instability [21].

In view of the higher energy content of the  $^3\text{MLCT}$  level of  $\text{Ru}(\text{ttrpy})_2^{2+}$  with respect to that of  $\text{Os}(\text{ttrpy})_2^{2+}$  (see Sect. 2.2), the former complex was preferred as a component for the subsequent development of the project, which involved the preparation of porphyrin-based dyads and triads. In this case both the ruthenium centre and the appended units can be excited in the visible region of the spectra. The synthetic strategy made use of the metal to act as a gathering centre for porphyrins, which were respectively either a zinc(II) porphyrin or a free-base porphyrin as donor groups (PZn or  $\text{PH}_2$ ) and a gold(III) porphyrin as acceptor unit (PAu). Whereas the gold porphyrin electron acceptor unit was a tetraphenyl porphyrin in all examined cases, the early attempts made use as an electron donor of the *ethio* zinc (II)- or free-base porphyrin,  $6^{3+}$  and  $7^{3+}$  (Fig. 3) [22].

Upon excitation of the metal complex centre, triplet energy transfer to the donor appended porphyrin rapidly quenches the excited state of the central ruthenium bis-terpyridyl unit, whereas excitation of the gold porphyrin, leads in less than 1 ps to the triplet-excited state [23], which is unreactive to-

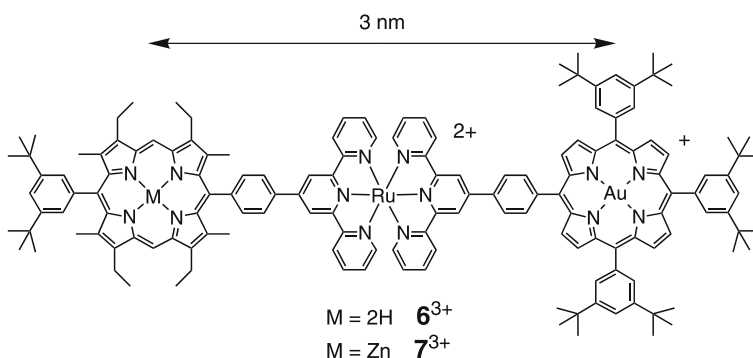
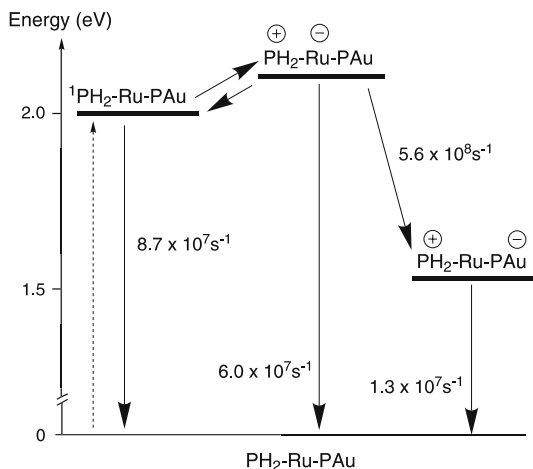


**Fig. 3** Chemical structures of compounds  $6^{3+}$  and  $7^{3+}$

ward electron or energy transfer processes. These experimental results have been explained as follows [22]. Excitation into the free base moiety of  $6^{3+}$  produces the corresponding excited singlet state  ${}^1\text{PH}_2 - \text{Ru} - \text{PAu}$ , which transfers an electron to the adjacent Ru-based unit, forming the charge separated state  $\text{PH}_2^+ - \text{Ru}^- - \text{PAu}$ . The two energy levels, Scheme 3, are very close, and consequently charge transfer is expected to be highly reversible. Competing processes for the deactivation of  $\text{PH}_2^+ - \text{Ru}^- - \text{PAu}$  will be: (i) back electron transfer leading directly to the ground state and (ii) further electron transfer to yield the fully CS state,  $\text{PH}_2^+ - \text{Ru} - \text{PAu}^-$ . This process occurs with a rate constant of  $5.6 \times 10^8 \text{ s}^{-1}$  at room temperature and the CS state exhibits a lifetime of

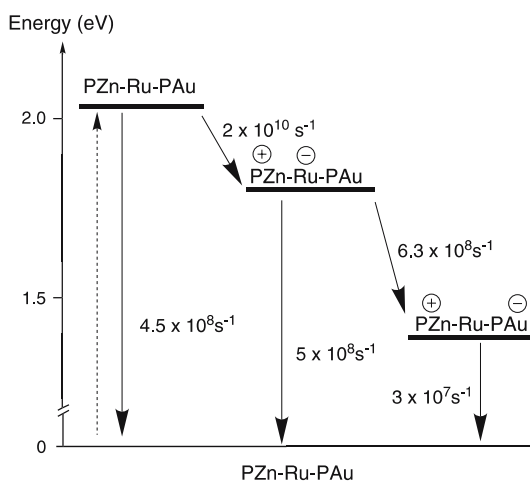


**Scheme 3** Energy level diagram and reaction rates for the photoinduced processes occurring in compound  $6^{3+}$ . The *dashed arrow* indicates excitation of the free-base porphyrin unit

75 ns in acetonitrile. On the basis of the rates reported on Scheme 3 a quantum yield of formation of charge separation ( $\Phi_{cs}$ ) of 0.27 can be calculated.

The triad  $7^{3+}$  containing the corresponding zinc porphyrin as a donor has a rather different energy level distribution (Scheme 4). Zinc porphyrin is, in fact, characterised by a higher energy level excited state (by ca. 0.1 eV) and a lower oxidation potential than the free-base counterpart by ca. 0.15–0.2 V [22]. The situation is favourable to the occurrence of electron transfer from the excited state localized on the zinc porphyrin unit,  $^1\text{PZn} - \text{Ru} - \text{PAu}$ , to the ruthenium centre to form the CS state  $\text{PZn}^+ - \text{Ru}^- - \text{PAu}$ , and subsequently the fully CS state  $\text{PZn}^+ - \text{Ru} - \text{PAu}^-$ . The latter has a lifetime of 33 ns and an overall yield of charge separation  $\phi_{cs} = 0.60$ . The shorter lifetime with respect to the free-base counterpart was explained by the fact that the charge recombination is not occurring so deep in the Marcus inverted region ( $\Delta G^0 = -1.23$  eV), as for the free-base porphyrin-containing triad ( $\Delta G^0 = -1.4$  eV).

In the subsequent development of the project, the *ethio*-type porphyrin was substituted by the more robust tetraaryl porphyrin, which could better stand the drastic conditions of the synthesis [24]. This has consequences also in the energy level diagram of the systems since the presence of meso-tetraaryl groups increases by ca. 0.05–0.1 V the oxidation potential of the porphyrin compared to the *ethio* derivatives with alkyl substitution on the tetrapyrrole, and decreases the excited state energy level by ca. 0.05–0.1 eV. In general, this means that in the meso-tetraaryl-based arrays there is a decrease of the driving force for charge separation and an increase in the driving force for charge recombination with rather important effects on the photoinduced processes.



**Scheme 4** Energy level diagram and reaction rates for the photoinduced processes occurring in compound  $7^{3+}$ . The *dashed arrow* indicates excitation of the Zn porphyrin unit

Another attempt that was tried in order to improve the performances of the arrays was the introduction of some change on the structure of the central  $\text{Ru}(\text{terpy})_2^{2+}$ , which could result in an increase of the lifetime of the complex at room temperature, while still maintaining the favourable geometry of the terpy ligand [25]. We reasoned that a longer lifetime of the excited metal complex unit would have allowed its use as a photosensitizer, in addition to its use as an electron relay, thus increasing the efficiency of CS upon excitation in the visible range at room temperature. To this aim a tridentate 2,6-bis(4'-phenyl-2'-quinoly)pyridine (bpqpy) was employed as ligand,  $\mathbf{8}^{2+}$  (Fig. 4) [25]. The use of this ligand with extended conjugation was expected to decrease the energy of the luminescent  $^3\text{MLCT}$  excited state, thus making more difficult its deactivation via the upper lying  $^3\text{MC}$  excited state (of  $d \rightarrow d$  origin and whose energy gap is governed by the ligand field strength [4]), and so increasing its lifetime [26]. The energy of the excited state of  $\mathbf{8}^{2+}$  was actually lower than that of  $\text{Ru}(\text{terpy})_2^{2+}$ , 1.83 eV vs. 1.97 eV respectively, and also the electrochemical properties were favourable, its reduction potential ( $E_{1/2} = -0.83$  V vs SCE) being less negative than that of  $\text{Ru}(\text{terpy})_2^{2+}$  ( $E_{1/2} = -1.18$  eV vs SCE) [22, 25]. Unfortunately, for  $\text{Ru}(\text{terpy})(\text{bpqpy})^{2+}$  steric crowding of the bpqpy ligand weakens the ligand field strength, resulting in an extremely short lifetime for the  $^3\text{MLCT}$  state, 90 ps compared to 0.95 ns of the  $\text{Ru}(\text{terpy})_2^{2+}$ . This leads to poor performances of this complex as a photosensitizer in the porphyrin dyads  $\mathbf{9}^{2+}$  and  $\mathbf{10}^{2+}$  (Fig. 4), in that its lifetime is too short to participate in the photoinduced

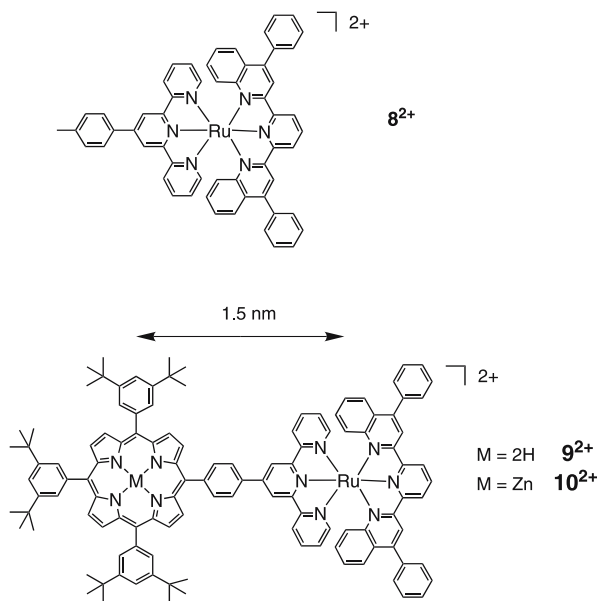
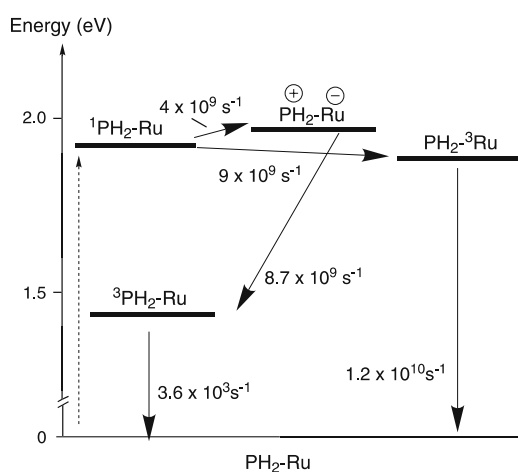


**Fig. 4** Chemical structures of compounds  $\mathbf{8}^{2+}$ ,  $\mathbf{9}^{2+}$  and  $\mathbf{10}^{2+}$

processes [25]. On the contrary, excitation of the porphyrin counterparts at room temperature led to charge separation, with an electron transferred from the excited state of the porphyrin to the ruthenium unit *and* energy transfer to the  $^3\text{MLCT}$  excited state localized on the complex. The energy transfer process is formally spin forbidden, and is made possible by the spin-orbit coupling induced by the heavy Ru(II) centre. From the results of the photoexcitation of these systems, summarized for  $9^{2+}$  in Scheme 5, we started to be aware of the possible occurrence of spin-forbidden energy transfer processes, which could efficiently compete with the desired electron transfer process whenever a low-lying excited state localized on the metal complex is present [26].

The confirmation of the importance of energy transfer processes in the  $\text{Ru}(\text{terpy})_2^{2+}$ -based triads came from the study of system  $11^{3+}$  (Fig. 5) [24].



**Scheme 5** Energy level diagram and reaction rates for the photoinduced processes occurring in compound  $9^{2+}$ . The *dashed arrow* indicates excitation of the free-base porphyrin unit

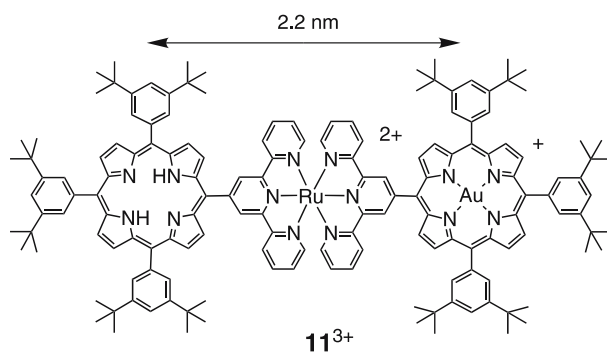
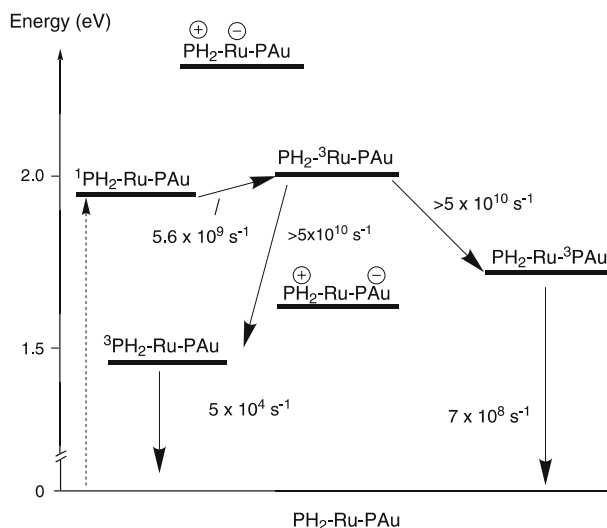


**Fig. 5** Chemical structure of compound  $11^{3+}$



**Scheme 6** Energy level diagram and reaction rates for the photoinduced processes occurring in compound  $11^{3+}$ . The dashed arrow indicates excitation of the free-base porphyrin unit

The energy level diagram of this system is reported in Scheme 6; the charge separated state with the oxidized porphyrin and the reduced ruthenium complex is high in energy and electron transfer from excited porphyrin to the metal complex unit cannot take place. The only thermodynamically feasible electron transfer reaction following excitation of porphyrin would be direct transfer of an electron to the gold porphyrin unit, but in spite of the coupling of the components in this array, with the phenyl spacer missing between the components, electron transfer across the metal complex does not occur. The experimental data in  $11^{3+}$  were explained as follows, see Scheme 6 [24].

After excitation into the free base porphyrin moiety, leading to  $^1\text{PH}_2 - \text{Ru} - \text{PAu}$ , an initial energy transfer occurs to the triplet state of the central metal complex,  $\text{PH}_2 - ^3\text{Ru} - \text{PAu}$  with a slightly endoergic process. This state deactivates rapidly ( $k > 5 \times 10^{10} \text{ s}^{-1}$ ) through two energy transfer pathways to either the triplet state of the free base,  $^3\text{PH}_2 - \text{Ru} - \text{PAu}$ , or to the triplet state localized on the gold porphyrin,  $\text{PH}_2 - \text{Ru} - ^3\text{PAu}$ . From the experimental ratio of the porphyrin triplet yields,  $\Phi_{\text{PAu}}^3 / \Phi_{\text{PH}_2}^3$ , the relative efficiencies of the energy transfer steps are estimated to be 4 in favour of the gold porphyrin triplet. The lifetime of the triplet localized on the gold porphyrin is the same as in the model PAu,  $\tau = 1.4 \text{ ns}$ , indicating that this state is inactive toward energy or electron transfer processes. The triplet lifetime of the free base porphyrin is slightly reduced with  $\tau = 20 \text{ } \mu\text{s}$  compared to the model  $\text{PH}_2$ , very likely for the effect of heavy ruthenium ion on the intersystem crossing rate [24]. At 77 K in glassy solvent, the lifetime of the gold porphyrin triplet

increases to 90  $\mu\text{s}$ , and in this condition it can transfer energy to the lower energy triplet state localized on the free base  ${}^3\text{PH}_2 - \text{Ru} - \text{PAu}$ , which becomes the final recipient of the light energy absorbed by the system [27].

The results here presented for the systems  $9^{2+}$ ,  $10^{2+}$  and  $11^{3+}$ , have clearly pointed out that the presence of a metal complex component with a low-lying excited state ( $\leq 2.0$  eV) can be detrimental to the efficiency of electron transfer.

## 2.2

### $\text{Ir}(\text{terpy})_2^{3+}$ and Derivatives: Photophysical Properties

The complexes of the Ir(III)-, Ru(II)-, and Os(II)- bis-terpy type have the nearly planar terpyridine systems perpendicularly arranged to each other. On this basis, a convenient linear arrangement for dyads and triads can be obtained by designing species having opposite groups appended at the 4' position of the two ligands, see Sect. 2.1; examples of Ru(II) and Os(II) cases are complexes  $2^{4+}$ ,  $3^{4+}$ ,  $4^{4+}$  and  $5^{4+}$ . This contrasts favourably with what happens with related complexes containing three bidentate ligands like bpy or phen, for example complex  $1^{4+}$  and derived molecular assemblies [5, 28]. Actually, Ru(II)- and Os(II)-tris-bpy (or phen) complexes exhibit good luminescence properties, both in terms of luminescence efficiency and lifetimes [4, 29]; however, the appended groups at the ligands give rise to dyads and triads that cannot exhibit a linear geometry [5, 30]; in addition, the presence of stereoisomers results in mixtures of species. In fact, only one case has been reported wherein the use of bidentate ligands might be amenable to the construction of the sought for linear arrangement of multicentre species; this occurs when a helical bis-phen ligand (which actually behaves as a tetradentate ligand) is coordinated to a Ru(II) centre,  $12^{2+}$  (Fig. 6) [31].

Unfortunately, most Ru(II)-bis-terpy type complexes are poor lumino-phores [26], even if several preparative approaches have afforded species with

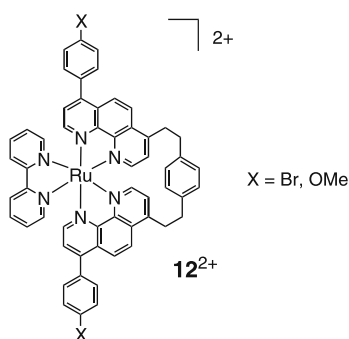


**Fig. 6** Chemical structure of compounds  $12^{2+}$



**Table 1** Photophysical parameters of Ir(III) tris-bpy and bis-terpy complexes; properties for related complexes of Ru(II) and Os(II) are also listed <sup>a</sup>

	$\lambda_{\text{abs}}$ (nm) <sup>b</sup> ( $\epsilon$ , M <sup>-1</sup> cm <sup>-1</sup> )	$\lambda_{\text{em}}$ (nm) <sup>c</sup>	$\phi_{\text{em}}$ <sup>d</sup>	$\tau$ <sup>d</sup> ( $\mu\text{s}$ )	$E_{0-0}$ (eV) <sup>e</sup>	Emitting state	Refs.
Ir(bpy) <sub>3</sub> <sup>3+</sup> <sup>f</sup>	344 (3300)	441	–	[2.4]	2.81		[32, 33]
Ir(terpy) <sub>2</sub> <sup>3+</sup> (13 <sup>3+</sup> ) <sup>f</sup>	352 (5800)	458	$2.5 \times 10^{-2}$	1.0 [1.2]	2.71	LC	[34]
14 <sup>3+</sup> <sup>f</sup>	372 (13200)	506	$2.6 \times 10^{-2}$	2.3		LC/MLCT	[34]
Ir(tterpy) <sub>2</sub> <sup>3+</sup> (15 <sup>3+</sup> ) <sup>f</sup>	373 (29000)	506	$2.9 \times 10^{-2}$	2.4 [9.5]	2.45	LC/MLCT	[34]
16 <sup>3+</sup>	372 (23800)	506	$2.2 \times 10^{-2}$ [ $9.3 \times 10^{-2}$ ]	1.6 [6.8]	2.55	LC/MLCT	[34] [35]
17 <sup>3+</sup>	380 (27000)	570	$0.21 \times 10^{-2}$ [ $0.55 \times 10^{-2}$ ]	0.49 [0.80]	2.43		[35]
18 <sup>3+</sup>	398 (45000)	566	$0.27 \times 10^{-2}$ [ $0.76 \times 10^{-2}$ ]	0.58 [2.0]	2.41		[35]
19 <sup>3+</sup>	377 (29200)	550	$0.2 \times 10^{-2}$	0.73	2.4	MLCT	[36]
20 <sup>3+</sup>	321 (53300), 504 (44800)	754 <sup>g</sup>	h	h	h	ILCT <sup>g</sup>	[17]
21 <sup>3+</sup>	321 (50600), 493 (35100)	784 <sup>g</sup>	h	h	h	ILCT <sup>g</sup>	[17]
22 <sup>3+</sup>	322 (31700), 476 (9400)	h	h	h	h	h	[17]
Ru(bpy) <sub>3</sub> <sup>2+</sup>	451 (13000)	610	$1.5 \times 10^{-2}$ [ $6.2 \times 10^{-2}$ ]	0.17 [0.90]	2.03	MLCT	[4, 37, 38]
Ru(terpy) <sub>2</sub> <sup>2+</sup> <sup>f</sup>	474 (14600)	~ 630	$< 5 \times 10^{-5}$	250 ps	2.07	MLCT	[39]
Ru(tterpy) <sub>2</sub> <sup>2+</sup>	490 (28000)	640	$3.2 \times 10^{-5}$	0.95 ns	1.98	MLCT	[26]
Os(bpy) <sub>3</sub> <sup>2+</sup>		718	$3.2 \times 10^{-3}$ [ $5 \times 10^{-3}$ ]	49 ns 60 ns	1.75	MLCT	[29, 38]
Os(terpy) <sub>2</sub> <sup>2+</sup>	477 (13800), 657 (3700)	718	$1.2 \times 10^{-3}$ [ $1.4 \times 10^{-2}$ ]	0.03 [0.27]	1.8	MLCT	Our results and [26]
Os(tterpy) <sub>2</sub> <sup>2+</sup>	490 (26000), 667 (6600)	734	$2.3 \times 10^{-3}$ [ $2.1 \times 10^{-2}$ ]	0.02 [0.22]	~ 1.8	MLCT	Our results and [26]

<sup>a</sup> Room temperature, in air-equilibrated acetonitrile unless otherwise indicated, PF<sub>6</sub><sup>-</sup> salts<sup>b</sup> Lowest energy band(s) with  $\epsilon > 1000$ <sup>c</sup> Highest energy peak maximum<sup>d</sup> In *square brackets*, values in degassed solvent<sup>e</sup> Energy content of the luminescent level estimated from fits of the luminescence profile at room temperature or from the luminescence band maximum at 77 K<sup>f</sup> Alcoholic solvent<sup>g</sup> The emission properties undergo changes in protic solvent<sup>h</sup> Not determined

significantly enhanced luminescence properties [40–43]. As for the Os(II)-bis-terpy complexes, these exhibit convenient luminescence properties, but the luminescent level can only store a low energy content,  $\sim 1.8$  eV, Table 1. A comparison of spectroscopic properties for representative iridium bis-terpyridine complexes, reported in Fig. 7, and related ruthenium and osmium complexes is provided in this table. Several iridium bis-terpyridine complexes are strongly luminescent at room temperature ( $\phi_{\text{em}} \sim 10^{-2}$ ), with lifetimes on the microseconds time scale. Importantly, the energy content of the emission level is high, in several cases larger than 2.5 eV, which contrasts favourably with that of the Ru(II) and Os(II) based counterparts, ca. 2 and 1.8 eV, respectively. For the Ir(III) complexes, the nature of the excited states responsible

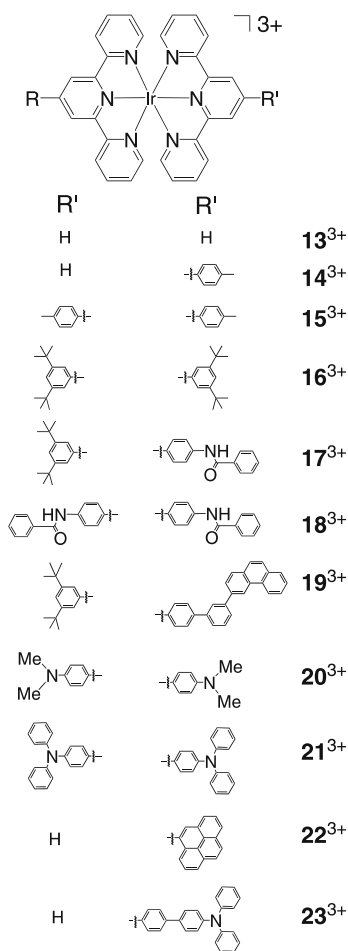


**Fig. 7** Chemical structures of compounds  $13^{3+}$  to  $23^{3+}$

for luminescence may vary from LC to MLCT and to ILCT depending on the electronic properties of the groups appended at the 4,4'-positions of the terpy ligands (Table 1). In some cases, the luminescence due to the Ir-bis-terpy unit appears substantially quenched, as it happens for the series of complexes  $20^{3+}$ - $23^{3+}$  (Fig. 7) [17]. This is due to the presence of low-lying levels, a consequence of the nature of the appended groups; for instance, the electron-donating properties of amino-benzene units may result in scarcely emitting low-lying levels of ILCT nature, cases of  $20^{3+}$ ,  $21^{3+}$ , and  $23^{3+}$  [17]. Nevertheless, the remarkable luminescence properties and the high energy content of the luminescent level for most of the Ir(III) bis-terpy complexes, in combination with their geometric properties, make them very attractive candidates as photosensitizers in dyadic and triadic schemes. In addition, their ease of reduction ( $E_{1/2}$  ca.  $-0.75$  V vs. SCE) compared to Os(II) and Ru(II) complexes, ( $E_{1/2}$  ca.  $-1.2$  V vs. SCE) makes them very promising electron acceptor or electron relay units in dyadic and triadic schemes for charge separation [26, 34].

### 2.3

#### Ir as Electron Relay: The Molecular Triads $\text{PH}_2\text{-Ir(III)-PAu}^{4+}$ and $\text{PZn-Ir(III)-PAu}^{4+}$

Having verified that the photophysical and electrochemical properties of the  $\text{Ir(terpy)}_2^{3+}$  derivatives were satisfying the characteristics we looked for, in that the excited state energy was well above 2 eV and that reduction was easier than for the related  $\text{Ru(terpy)}_2^{2+}$  derivatives, we decided to use  $\text{Ir(terpy)}_2^{3+}$  as assembling unit and as electron relay in the following evolution of the project. We then synthesized two triads based on the Ir(III) complex, using zinc or free base tetra-aryl-porphyrin as the donor and photoactive centre and a gold tetraarylporphyrin as the acceptor.

The energy level diagram for the triad containing the free base,  $24^{4+}$  (Fig. 8), is reported in Scheme 7 [44, 45].

Excitation of the free base porphyrin unit in  $24^{4+}$  leads to the excited state  ${}^1\text{PH}_2\text{-Ir-PAu}$ , which is quenched to a lifetime of 30 ps, compared to

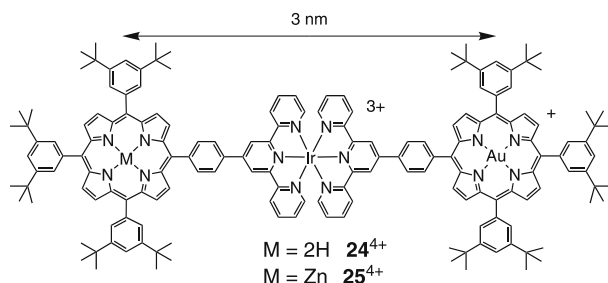
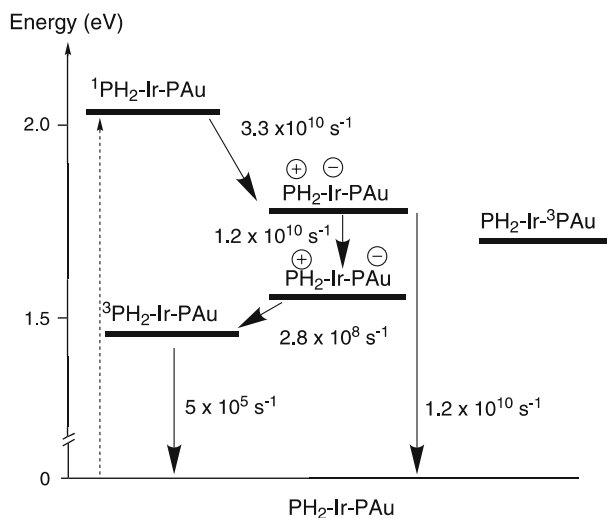


**Fig. 8** Chemical structures of compounds  $24^{4+}$  and  $25^{4+}$



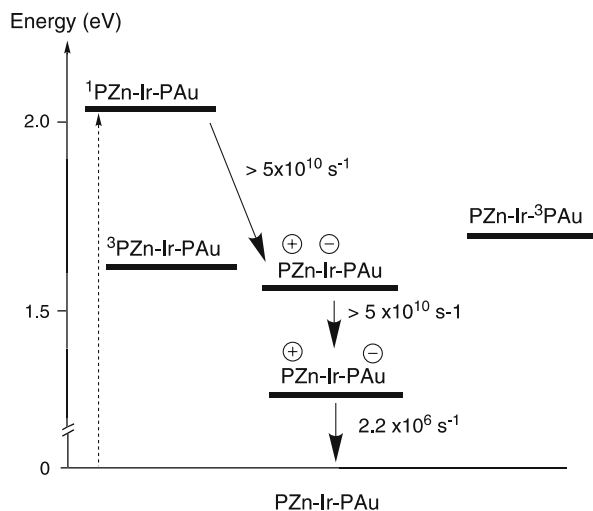
**Scheme 7** Energy level diagram and reaction rates for the photoinduced processes occurring in compound  $24^{4+}$ . The dashed arrow indicates excitation of the free-base porphyrin unit

a lifetime of 8.3 ns for the model porphyrin. The quenching does not occur in butyronitrile glass at 77 K, where the lifetime of the singlet is 11 ns, the same as that of the model. Deactivation can be assigned to an electron transfer from the singlet state localized on the free base  $^1\text{PH}_2 - \text{Ir} - \text{PAu}$  to the central Ir complex core to yield the charge separated state  $\text{PH}_2^+ - \text{Ir}^- - \text{PAu}$ , the electron being localized on a terpy ligand. On the other hand, excitation of the PAu part leads rapidly to the triplet state of the gold porphyrin  $\text{PH}_2 - \text{Ir} - ^3\text{PAu}$ , which decays with a lifetime of 1.4 ns as the model porphyrin, indicating that this state is not photoactive, as previously noticed. Deactivation of the primary CS state is faster in the triad (40 ps) than in the model  $\text{PH}_2 - \text{Ir}$  dyad (75 ps), indicating that a further deactivation step is open in the triad to  $\text{PH}_2^+ - \text{Ir}^- - \text{PAu}$ . With respect to the dyad, where deactivation of the corresponding charge separated state  $\text{PH}_2^+ - \text{Ir}^-$  can occur only by recombination to the ground state, deactivation in the triad can occur also via a further electron transfer step leading to the fully CS state  $\text{PH}_2^+ - \text{Ir}^- - \text{PAu}^-$ , with a rate of  $1.2 \times 10^{10} \text{ s}^{-1}$  [44, 45]. The fully CS state is, therefore, formed with an efficiency of 0.5. Due to the high driving force of the recombination reaction ( $\Delta G^0 = -1.55 \text{ eV}$ ), we were expecting a slow recombination reaction, in accord with the so-called Marcus inverted behavior [46], characterised by a slowing down of the reaction by increasing driving force. The lifetime was, on the contrary, rather short, 3.5 ns and was determined by a rapid recombination to the triplet excited state localized on the porphyrin,  $^3\text{PH}_2 - \text{Ir} - \text{PAu}$ . Fast spin flip from a singlet CS state to a triplet CS state, which is the rate determining step for recombina-

tion to a triplet, is again a peculiarity of the arrays containing heavy atoms as Ir(III) [45].

With this in mind, we tried to avoid the presence of triplet excited states at lower energy than the target CS state. To this aim, we selected zinc porphyrin as an electron donor and photosensitizer in the triad  $25^{4+}$  (Fig. 8) [45, 47]. Zinc porphyrin has a triplet excited state approximately 0.1 eV higher in energy than the free base and has a lower oxidation potential, by ca. 0.2 V (which places the CS states involving oxidized zinc porphyrin at energies lower by the same 0.2 eV amount). The experiments for triad  $25^{4+}$  were carried out both in moderately polar ( $\text{CH}_2\text{Cl}_2$ ) and in non-polar (toluene) solvents. The best results were obtained in toluene and the energy level diagram in this solvent is reported in Scheme 8. It can be immediately seen that in this case, compared to triad  $24^{4+}$ , the situation is more favorable in that the triplet excited state  $^3\text{PZn} - \text{Ir} - \text{PAu}$  is higher than the level of the CS state  $\text{PZn}^+ - \text{Ir} - \text{PAu}^-$ . Upon excitation of the zinc porphyrin unit, after a very fast quenching of the  $^1\text{PZn} - \text{Ir} - \text{PAu}$  luminescence ( $\tau < 20$  ps),  $\text{PZn}^+ - \text{Ir} - \text{PAu}^-$  formation is detected within the time resolution of the apparatus and decays with a lifetime of 450 ns. The results in dichloromethane were less satisfactory in that the fully CS state was not formed, due to the lack of driving force for the reaction leading from  $\text{PZn}^+ - \text{Ir}^- - \text{PAu}$  to  $\text{PZn}^+ - \text{Ir} - \text{PAu}^-$ . The difference in behavior of the triad in  $\text{CH}_2\text{Cl}_2$  and toluene is due to the different polarity of the solvents which stabilizes the states in a remarkably different way [45].

The parameters of charge separation for the examined porphyrin based triads are collected in Table 2.



**Scheme 8** Energy level diagram and reaction rates for the photoinduced processes occurring in triad  $25^{4+}$ . The dashed arrow indicates excitation of the Zn porphyrin unit

**Table 2** Properties of CS states formed in  $\text{Ru}(\text{terpy})_2^{2+}$  and  $\text{Ir}(\text{terpy})_2^{3+}$  complex-based triads containing porphyrins

Triad	Energy CS/eV	$\phi_{\text{CS}}^{\text{a}}$	$\tau_{\text{CS}}/\text{ns}$
$6^{3+}$	1.4	0.27	75
$7^{3+}$	1.23	0.60	33
$24^{4+}$	1.55	0.5	3.5
$25^{4+}$	1.34	1	450

<sup>a</sup> Efficiency of CS; for the solvent employed and the experimental conditions see [22, 45]

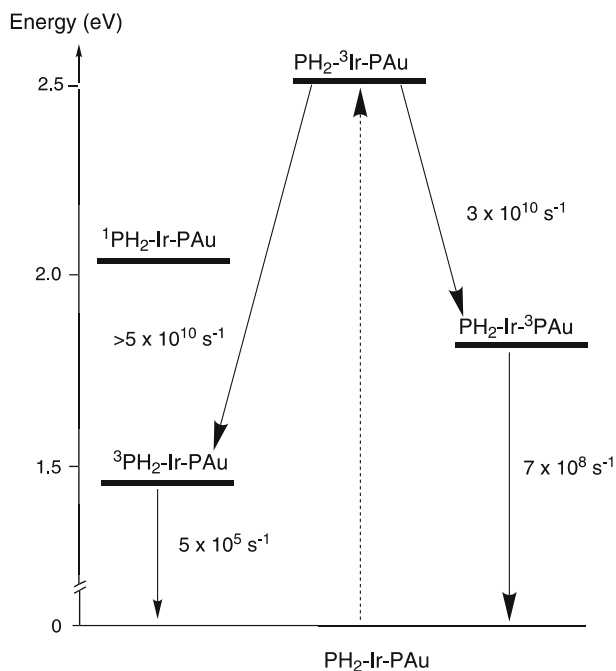
## 2.4

### Ir as Photoactive Centre

In the systems described above, a porphyrin is used as a photoactive centre, and the iridium complex acts only as a gathering metal and an electron relay. However the Ir(III) complex can also act as a photosensitizer if excited at a convenient wavelength. Indeed  $\text{Ir}(\text{terpy})_2^{3+}$  and derivatives (i) absorb moderately in the ultraviolet and high-energy visible region of the spectra, Table 1, (ii) the lowest excited state can store more energy than other photosensitizers, and (iii) have a remarkably long lifetime (see Sect. 2.2). For this reason we developed projects based on the use of iridium complex centres as photosensitizers.

The first experiments in this direction were carried out on the triads  $24^{4+}$  and  $25^{4+}$  (Fig. 8), by exciting preferentially the metal centre around 340–355 nm. Excitation at this wavelength region produces to a predominant extent the excited state localized on the iridium complex unit, the ligand centered triplets  $\text{PH}_2 - {}^3\text{Ir} - \text{PAu}$  or  $\text{PZn} - {}^3\text{Ir} - \text{PAu}$  [48]. Energy transfer to the porphyrin triplets dominates the deactivation of  $\text{PH}_2 - {}^3\text{Ir} - \text{PAu}$  in  $24^{4+}$ , with rate constants of  $2.9 \times 10^{10} \text{ s}^{-1}$  for the transfer to the gold porphyrin localized excited state and ca.  $10^{11} \text{ s}^{-1}$  to the free base porphyrin localized excited state, respectively (Scheme 9).

This is in contrast to the results obtained following selective excitation of the  $\text{PH}_2$  unit discussed above, and yielding a multi-step electron transfer leading to charge separation. The different outcome can be discussed on the basis of the overlap of the HOMO and LUMO orbitals involved in the electron transfer reaction for the Ir acceptor unit and the  $\text{PH}_2$  donor unit, with the aid of semi-empirical calculations [48]. Remarkably, the zinc porphyrin based array  $\text{PZn} - \text{Ir} - \text{PAu}$ ,  $25^{4+}$ , displays an efficient electron transfer with the formation of a CS state with unitary yield also upon excitation of the iridium complex. This happens because the selective excitation of the zinc porphyrin chromophore discussed above, and the deactivation of the excited state  $\text{PZn} - {}^3\text{Ir} - \text{PAu}$ , follow the same paths as those reported in Scheme 8.



**Scheme 9** Energy level diagram and reaction rates for the photoinduced processes occurring in compound  $24^{4+}$  following excitation of the Ir complex unit (*dashed arrow*)

A higher driving force for electron transfer in the case of  $25^{4+}$  compared to  $24^{4+}$  could explain the predominance of the electron transfer reaction with respect to energy transfer paths in the latter case.

A subsequent study dealt with system  $26^{4+}$ , a pseudo-rotaxane incorporating an Ir(III) terpy-type complex and a copper(I) centre with a pseudo tetrahedral coordination provided by a macrocycle and a monosubstituted phenanthroline (Fig. 9) [36]. Following selective excitation of the iridium complex at 390 nm in this dyad, the emission is almost completely quenched. In principle, this could be due both to electron and/or to energy transfer. As discussed previously, Ir(III) bis-terpy type complexes are, in fact, rather strong oxidants in their ground states,  $E_{1/2}$  ca.  $-0.75$  V vs SCE [49], whereas Cu(I)-phen-type complexes can easily oxidize to Cu(II), at a potential of ca.  $+0.6$  V vs SCE. The energy of the excited state stored on the Ir(III) complex could easily promote electron transfer from the iridium to the copper units, with a  $\Delta G^0$  of reaction of ca.  $-1$  eV. However energy transfer from the iridium to the copper unit (whose excited state lies at ca.  $1.7$  eV) is also thermodynamically feasible, with a  $\Delta G^0$  of ca.  $0.8$  eV. For the case of  $26^{3+}$ , it was difficult to evaluate the relative weight of the two contributions, given that both 2,9-unsubstituted and unsymmetrically substituted bis-phenanthroline derivatives are non-emissive [50]. A further step is the modification of the

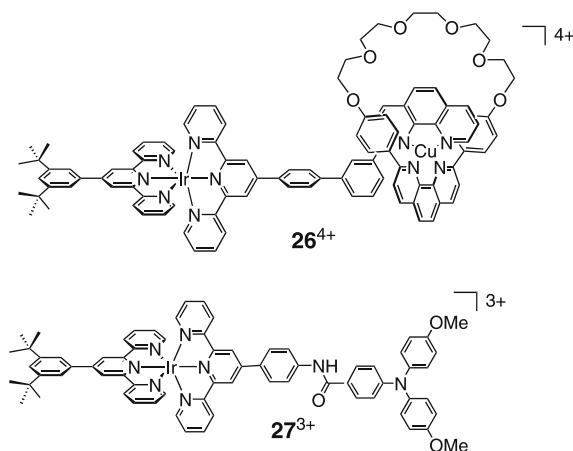


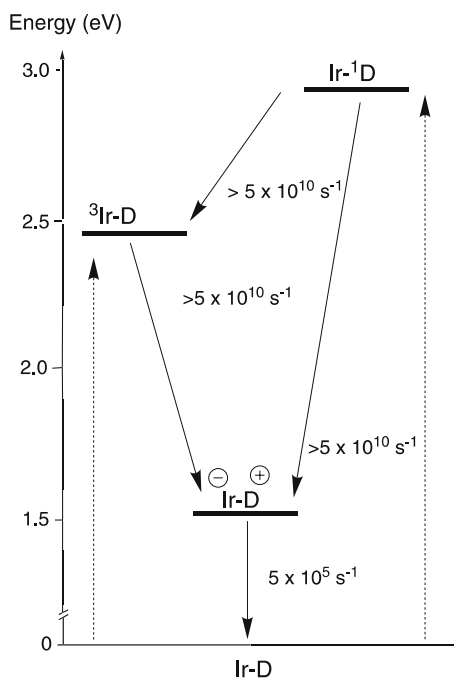
**Fig. 9** Chemical structures of compounds  $26^{4+}$  and  $27^{3+}$

copper ligand in order to prepare a luminescent Cu(I)-bis-phenanthroline derivative. This would allow, without changing the thermodynamic parameters of the system, an investigation of the sensitization of the luminescence of the copper unit, shedding light on the nature of the process.

In order to eliminate possible energy transfer processes depleting the Ir complex excited state, dyad  $27^{3+}$  (Fig. 9), made of a triarylamine electron donor D linked to the iridium bis-terpyridine complex by an amido-phenyl group was synthesized and examined [51]. D can be oxidized at 0.8 V vs. SCE, and has an excited state energy at ca. 3 eV, higher than the energy of the photosensitizer excited state, preventing an energy transfer process from the iridium complex unit (Scheme 10).

Selective excitation of metal complex unit in  $27^{3+}$  resulted in a complete quenching of its luminescence with the formation within 20 ps of the CS state  $\text{Ir}^- - \text{D}^+$ . The latter, identified from the absorption band peaking at 765 nm, decays with a life-time of 70 ps. Excitation of the D component around 330 nm also resulted in a complete quenching of the triphenylamine luminescence to yield the same CS state. The quenching mechanism can be described as a reductive quenching when the Ir complex is excited, i.e., an electron moves from the HOMO localized on the donor to the HOMO localized on the Ir complex. By contrast, when the donor is excited, an electron moves from the LUMO localized on the donor to the LUMO of the Ir complex acceptor, very likely localized on the bridging terpyridine. The localization of the extra electron on the bridging ligand, very close to the oxidized donor group, could be the reason for the relatively short lifetime of this CS state. On the other hand, the proximity allows for the formation of the CS state with a unity yield. We are presently working on the addition to the iridium complex centre of an ancillary electron acceptor group able to undergo a further





**Scheme 10** Energy level diagram and reaction rates for the photoinduced processes occurring in the dyad  $27^{3+}$ . The *dashed arrows* indicate excitation of both components

electron transfer step. This should increase the separation between the hole and the electron in the final charge separated state and hopefully slow down the recombination event.

## 2.5

### Related Systems Reported by Other Groups

In view of the development of chemical approaches to artificial photosynthesis, there are several possible ways towards multicomponent systems incorporating metal complex units [52, 53]. For instance, new types of metal centres can prove amenable to the preparation of assemblies suited for the study of CS and CR events. This is the case of the triadic systems built around an acetylide-Pt(II)-terpy centre,  $28^+$  and related systems (Fig. 10) [54]. For  $28^+$ , the energy content of the excited metal complex core is ca. 2.2 eV, and this energy can drive formation of a fully CS state, ending up with oxidation of the PTZ unit and reduction of the terpy-nitrostilbene ligand. The CS state lives 230 ns and is formed with an efficiency of 25–30%.

Finally, it is of worth recalling the continuing development of systems based on Ru(II)-tris-bidentate chromophores. Above, we have pointed out that this chromophore has limitations regarding both the stored energy con-

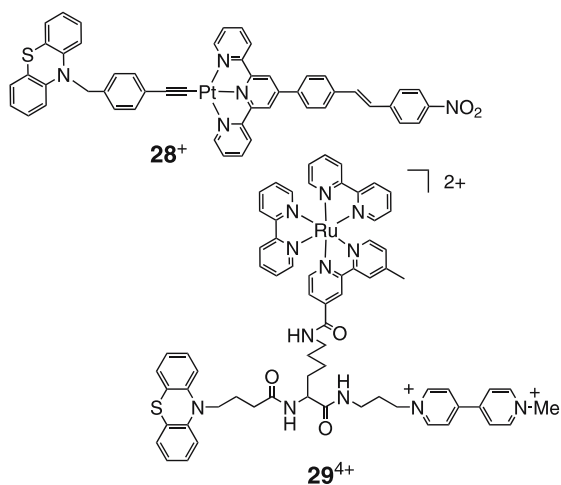


**Fig. 10** Chemical structures of compounds **28<sup>+</sup>** and **29<sup>2+</sup>**

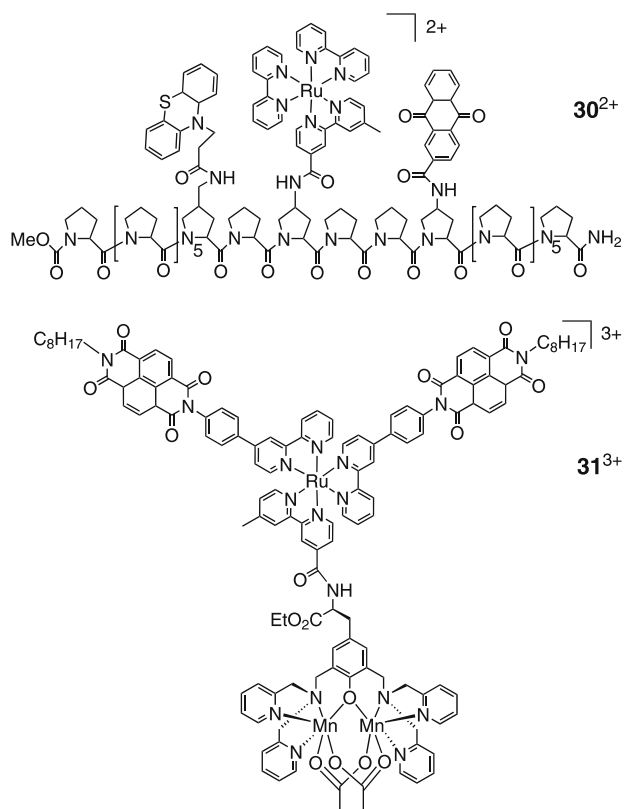


**Fig. 11** Chemical structures of compounds **30<sup>2+</sup>** and **31<sup>3+</sup>**

tent and the unfavourable geometric properties that do not allow a convenient spatial control of the products of the photoinduced events. However it is worth mentioning the work of Meyer and coworkers concerning the preparation of the lysine-based triadic system  $29^{4+}$ , Fig. 10 [55] and of large molecular assemblies similar to  $30^{2+}$  in Fig. 11 [28, 53]. For the donor-chromophore-acceptor system  $29^{4+}$ , excitation at metal-chromophore yields a  $PTZ^+ \cdot MV^+$  CS state with an efficiency of 0.34, which lives ca. 150 ns. Likewise, for the proline assembly  $30^{2+}$ , MLCT excitation leads to simultaneous appearance of transient absorption features due to the  $PTZ$  radical cation and the anthraquinone radical anion. This fully CS state is formed with a 53% efficiency, stores 1.65 eV, and lives 175 ns ( Fig. 11).

In addition, very recently it has been reported a  $\tau = 600 \mu\text{s}$  at room temperature (and 0.1–1 s at 140 K), for a CS state formed upon light absorption in the multicomponent system  $Mn_2(\text{II}, \text{II}) - Ru - \text{NDI } 31^{3+}$ , including a manganese dimer moiety ( $Mn_2(\text{II}, \text{II})$ ), and two naphthalenediimide (NDI) units, Fig. 11 [56]. The photoinduced events are driven by light absorption at the  $Ru(\text{bpy})_3^{2+}$  photosensitizing unit, resulting in oxidation of the manganese dimer,  $Mn_2(\text{II}, \text{III})$  and NDI reduction. This outstanding result was explained in terms of the Marcus theory [46], based on the unusually large reorganization energy (2 eV) for the CR step, due in turn to the large inner reorganization energy of the manganese dimer.

### 3

## Ruthenium-based Light-driven Molecular Machine Prototypes

### 3.1

#### Use of Dissociative Excited States

#### to Set Ru(II)-complexed Molecular Machines in Motion: Principle

Light irradiation has recently been reported to produce molecular motions, either alone or in conjunction with a redox chemical reaction [57–69]. Pure photonic stimuli are particularly promising as the system in motion is not altered by the addition of chemicals; however, only a few examples have been reported. Among the light-driven molecular machine prototypes which have been described in the course of the last few years, a very distinct family of dynamic molecular systems takes advantage of the dissociative character of ligand-field states in  $Ru(\text{diimine})_3^{2+}$  complexes [70–76]. In these compounds, one part of the system is set in motion by photochemically expelling a given chelate, the reverse motion being performed simply by heating the product of the photochemical reaction so as to regenerate the original state. In these systems, the light-driven motions are based on the formation of dissociative excited states. Complexes of the  $Ru(\text{diimine})_3^{2+}$  family are particularly well adapted to this approach. If distortion of the coordination octahedron is suffi-

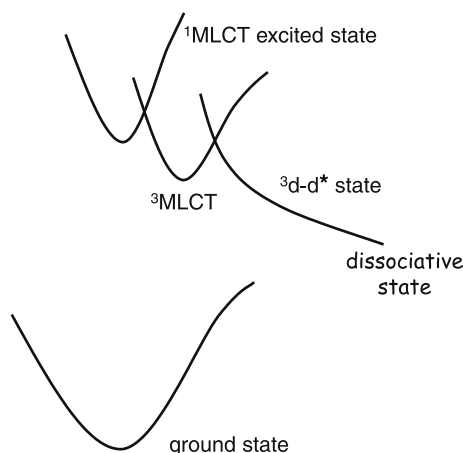


**Fig. 12** The ligand-field state  $^3d-d^*$  can be populated from the  $^3MLCT$  state, provided the energy difference between these two states is not too large: formation of this dissociative state leads to dissociation of a ligand

cient to significantly decrease the ligand field, which can be realized by using one or several sterically hindering ligands, the strongly dissociative ligand-field state ( $^3d-d^*$  state) can be efficiently populated from the metal-to-ligand charge transfer ( $^3MLCT$ ) state to result in expulsion of a given ligand. The principle of the whole process is represented in Fig. 12.

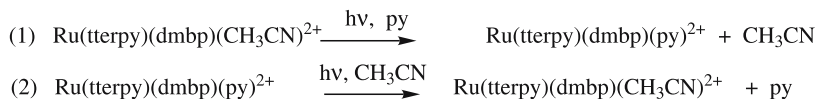
It is, thus, important that the ruthenium(II) complexes that are to be used as building blocks of the future machines contain sterically hindering chelates so as to force the coordination sphere of the metal to be distorted from the perfect octahedral geometry. We will discuss the photochemical reactivity of rotaxanes and catenanes of this family as well as non-interlocking systems like scorpionates since the lability of bulky monodentate ligands could also lead to useful photosubstitution reactions.

### 3.2

#### Photochemical and Thermal Ligand Exchange in a Ruthenium(II) Complex Based on a Scorpionate Terpyridine Ligand

Among the numerous ruthenium(II) complexes described in the literature, several lead to interesting photolabilisation reactions that are both efficient and selective [71–80]. For example,  $Ru(tterpy)(dmbp)(L)^{2+}$ , ( $L = \text{pyridine}$  or  $\text{CH}_3\text{CN}$ ) undergoes a reversible interchange of the sixth ligand  $L$  under visible light irradiation [81] (Scheme 11).

In order to investigate such systems further, we have prepared and characterised a series of ruthenium(II) complexes of the type  $Ru(terpy)(phen)(L)^{2+}$  in which  $L$  is a monodentate ligand such as pyridine, 2-isoquinoline,



**Scheme 11** Equations of the interchange of the sixth ligand L in the Ru(terpy)(dmbp)(L)<sup>2+</sup> type complexes

4-dimethylaminopyridine, 4-(4'-methyl-pyridinium)-pyridine, phenothiazine, DMSO, CH<sub>3</sub>CN, 4-methoxy-benzonitrile and H<sub>2</sub>O [82]. Our investigations of these complexes show that the nitrile ligand in Ru(terpy)(phen)(CH<sub>3</sub>CN)<sup>2+</sup> can be selectively photo-expelled and replaced by H<sub>2</sub>O under visible light irradiation in an acetone-water mixture (85 : 15, v/v). This process has been monitored by UV-visible and <sup>1</sup>H NMR spectroscopy. Both techniques demonstrate that the photochemical reaction is highly selective and quantitative. The reverse reaction, i.e., the thermal recoordination of an acetonitrile molecule, also takes place quantitatively at room temperature. We have also observed that a similar photochemical reaction occurs for the substitution of CH<sub>3</sub>CN by pyridine. We have proposed, therefore, a system that combines the general properties of scorpionate ligands with the ability of ruthenium(II) complexes to undergo ligand exchange under light irradiation [83]. The ruthenium complex **32**<sup>2+</sup> in which a benzonitrile group is tethered to the terpyridine subunit (Fig. 13) has been prepared.

In this complex, the benzonitrile coordinating group can be photoexpelled and thermally re-coordinated. The effect of tethering the benzonitrile group is to facilitate the recoordination of the nitrile functionality, since the effective concentration of the nitrile in the scorpionate complex is expected to be higher than if it were free in the bulk of the solution. The photolabilisation of the benzonitrile arm has initially been examined in pyridine solution. Both <sup>1</sup>H NMR and UV-visible measurements show that the reaction is clean and quantitative. Due to the strong coordination ability of pyridine it was not possible to restore the starting compound either thermally or photochemically. By contrast, a reversible system was obtained in acetone-H<sub>2</sub>O mixture. At a low concentration of **32**<sup>2+</sup> in acetone:water (85 : 15 v/v) the monitoring of the photochemical reaction by electronic absorption spectroscopy and TLC clearly indicates the complete disappearance of **32**<sup>2+</sup> (λ<sub>max</sub> = 454 nm) and the simultaneous appearance of the aqua-form (λ<sub>max</sub> = 490 nm). By <sup>1</sup>H NMR, in a more concentrated solution (10<sup>-3</sup> M), a stationary equilibrium is reached. The nature of the reaction product has also been unambiguously confirmed by ES-MS spectroscopy (peak at 939.2 for the aqua form; calculated for M-PF<sub>6</sub> = 939.0). The thermal recoordination of the nitrile arm takes place slowly at room temperature (82% of recovery in one day) or faster by heating the mixture at reflux for 1 h. At this concentration no by-product resulting from intermolecular complexation has been detected.

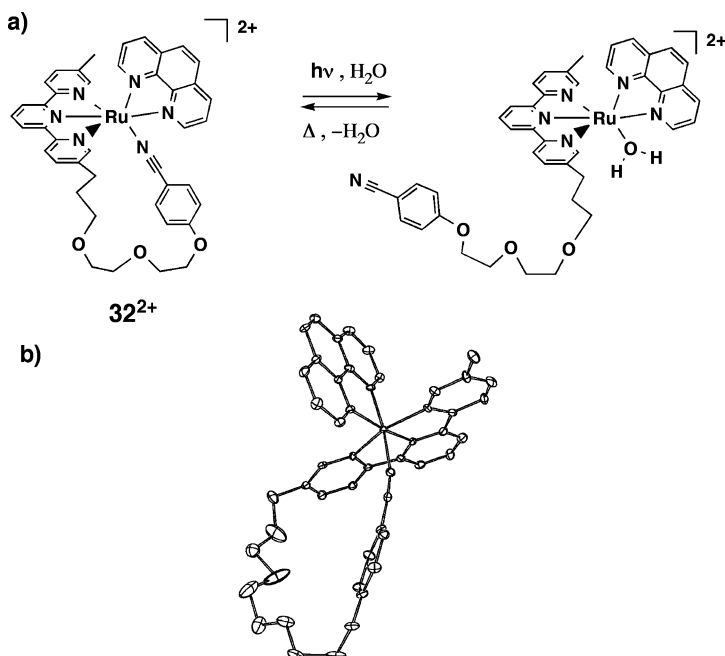


**Fig. 13** **a** Photolabilisation and thermal recoordination of complex  $32^{2+}$ . **b** ORTEP view of the ruthenium complex  $32^{2+}$ . Ellipsoids are scaled to enclose 30% of the electronic density

### 3.3

#### A Ru(terpy)(phen)-incorporating Ring and Its Light-induced Geometrical Changes

A particularly promising feature of the Ru(terpy)(phen)(L) $^{2+}$  series, in relation to future molecular machine and motors, is related to the pronounced effect of steric factors on the photochemical reactivity of the complexes [84]. When the bulkiness of the spectator phenanthroline moiety was increased, the steric congestion of the coordination sphere of the ruthenium complex also increased. This increased congestion was qualitatively correlated to the enhanced photoreactivities of these complexes (Fig. 14). More specifically, changing phen for dmp increased by one to two orders of magnitude the quantum yield of the photosubstitution reaction of L by pyridine with L = dimethylsulfide or 2,6-dimethoxybenzonitrile.

In the most congested case, (Ru(terpy\*)(dmp)(CH<sub>3</sub>SCH<sub>3</sub>) $^{2+}$ ), the photo-substitution quantum yield was shown to be  $\phi = 0.36$  at room temperature in pyridine, which is an extremely high value in ruthenium(II) photochemistry. The control of the bulkiness of the spectator chelates, leading to the control of the congestion of the complex and, hence, to the efficiency of ligand photoexpulsion, is a specific feature of the Ru(terpy)(phen)(L) $^{2+}$  core. This

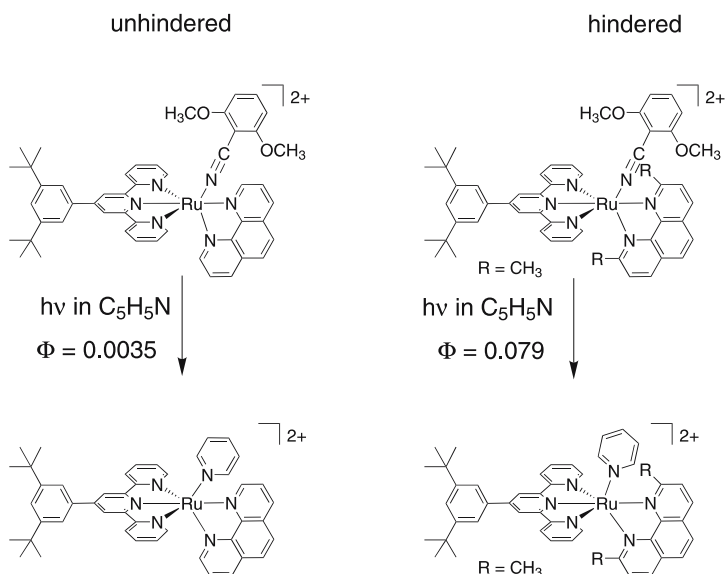


**Fig. 14** Photosubstitution quantum yield with the hindered dmp spectator chelate compared to its unhindered analog phen. Quantum yield values are given at room temperature in neat pyridine

new property, added to the potential variety of monodentate ligands *L* and to the expected mildness of thermal back-coordination conditions, makes the Ru(terpy)(phen)(*L*)<sup>2+</sup> family a highly promising photoactive core for elaborating future light-driven molecular machine.

Rings are essential components of molecular machine prototypes, especially within the catenane family [85]. A limited number of ruthenium(II)-incorporating macrorings have been made [86–89]. Since Ru(II) is substitutionally inert, the so-called self-assembly approach cannot be utilized [90]. Recently, we synthesized a novel Ru(II)-containing cycle, the ligand set consisting of a terpy derivative and a phen chelate. The sixth ligand can thermally or photochemically be substituted by another monodentate ligand [81, 91]. It consists of pyridine (py), acetonitrile or S-linked DMSO. In addition, a new photoisomerisation reaction of the ruthenium(II) complex leads to a dramatic change of the ring shape under the action of visible light, the reverse process regenerating the initial state by a thermal reaction. An example of the substitution-isomerisation in an acyclic complex is shown in Fig. 15.

The embedding of a Ru(terpy)(phen)<sup>2+</sup> moiety in a ring is certainly not trivial since the terpy fragment occupies three meridional sites of the metal octahedron and the phen chelate is almost opposite to the terpy in the metal coordination sphere. We thought that a convenient way to connect the phen and the terpy fragments was to interlink a lateral position of the phen (3 position) and the para position (4') of the central pyridinic nitrogen atom of

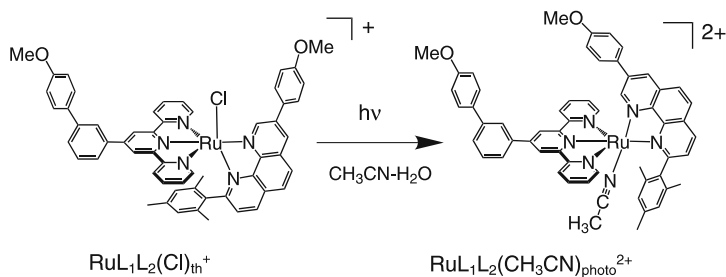


**Fig. 15** Photosubstitution-isomerisation processes in  $\text{Ru}(\text{L}_1)(\text{L}_2)(\text{Cl})^+$  complex

the terpy. This strategy should allow the formation of a large ruthenium(II)-containing ring.

A sequence of reactions, including the ring closing metathesis (RCM) reaction, leads to a 39-membered ring  $\mathbf{33}_{\text{photo}}^{2+}$  in the overall yield of 70% as depicted in Fig. 16. Although the photoisomers are very inert towards isomerisation for all the members of the family, a procedure was discovered which allowed for conversion of the photoisomer  $\mathbf{33}_{\text{photo}}^{2+}$  to the thermal isomer  $\mathbf{33}_{\text{th}}^{2+}$ . This procedure is quite general and can also be applied to acyclic complexes. The reaction is represented in a very schematic fashion in Fig. 16. It has been carried out with either pyridine or  $\text{CH}_3\text{CN}$  as the entering ligand from the intermediate DMSO complex.

The conversion of  $\mathbf{33}_{\text{photo}}^{2+}$  to  $\mathbf{33}_{\text{th}}^{2+}$  is performed in two steps: 1) substitution of py by DMSO and isomerisation, 2) substitution of DMSO by py. Its overall yield is above 80%. In order to perform a complete cycle, the photochemical reaction leading back to  $\mathbf{33}_{\text{photo}}^{2+}$  was carried out in the usual way (irradiation performed at room temperature with a 1000 W xenon arc-lamp filtered by a water filter) in pyridine. It turned out to be virtually quantitative.

This photochemical/thermal isomerisation of the ruthenium-containing ring is accompanied by a dramatic geometrical change of the compound. Molecular modelling studies [92] suggest that the distance between the two

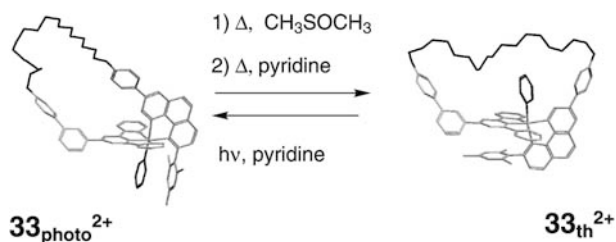


**Fig. 16** Thermal isomerisation of the photoisomer  $\mathbf{33}_{\text{photo}}^{2+}$  and the photochemical back reaction. The pyridine ligand moves from an external position to an intra-ring location while the  $-(\text{CH}_2)_{18}-$  fragment undergoes a folding/unfolding process



oxygen atoms borne by the phenyl rings of the terpy and phen ligands varies from 9.7 Å for the photochemical isomer  $33_{\text{photo}}^{2+}$  to 17.7 Å for  $33_{\text{th}}^{2+}$ . The  $-(\text{CH}_2)_{18}$  linker, which connects these two oxygen atoms, undergoes a folding/stretching process, as depicted in Fig. 16. In the past, the photochemical cis-trans isomerisation of an azo ( $-\text{N}=\text{N}-$ ) bond has been used to modify the shape of cyclic compounds [93]. Related geometrical changes have also been triggered by chemical means, in dinuclear copper(II) complexes [94].

### 3.4

#### Light-driven Unthreading Reaction in Rotaxane with a $[\text{Ru}(\text{diimine})_3]^{2+}$ Core

We have recently reported the synthesis of a [2]rotaxane constructed around a  $\text{Ru}(\text{diimine})_3^{2+}$  core [95]. The ring was a derivative of dmbp, and, in the course of the threading reaction, we noticed that both exo- and endo-coordination to the ruthenium(II) centre of the rod-like fragment take place, as schematically represented in Fig. 17.

In order to circumvent this synthetic difficulty, we replaced the dmbp motif by a 6,6'-diphenyl-2,2'-bipyridine chelate (dpbp), which provides the system with much better geometrical control. According to CPK models, exo coordination of a dpbp-incorporating ring is virtually impossible, except with very large rings. This approach turned out successful since the desired rotaxane and its non-stoppered analogue could be prepared in good yield, without formation of exo-coordinated species (Fig. 18). In addition, the photochemical behaviours of these compounds have shown that the ring is efficiently decoordinates from the ruthenium(II) centre under visible light irradiation. In a first step, we studied the photochemical behaviour of complex  $34^{2+}$ . By irradiating a solution of  $34^{2+} \cdot 2\text{PF}_6^-$  in 1,2-dichloroethane, using a band pass filter centered at around 470 nm and in the presence of a large excess of  $\text{Cl}^-$ , a clean photochemical reaction takes place. The photoinduced “unthreading” reaction was monitored by UV-vis spectroscopy. The series of visible spectra, characteristic of metal-to-ligand charge transfer (MLCT) bands, is given in Fig. 19.

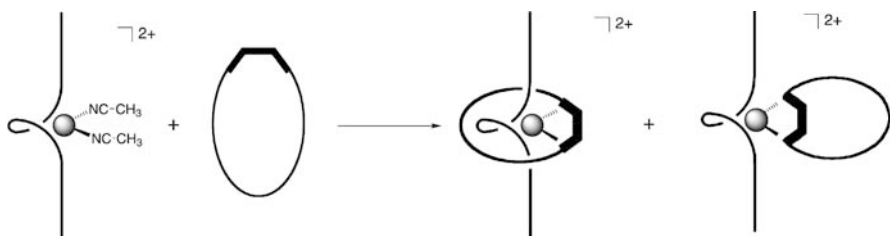


**Fig. 17** Synthesis of a pseudo-rotaxane and its *exo*-isomer

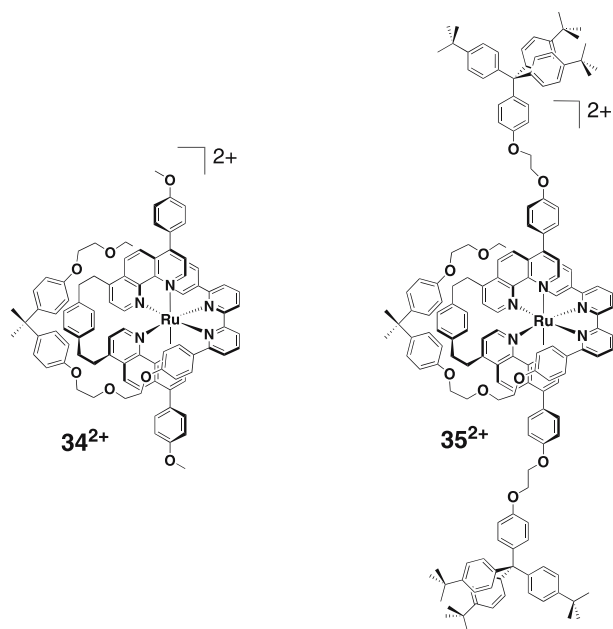


**Fig. 18** Formulae of the pseudo-rotaxane  $34^{2+}$  and of the rotaxane  $35^{2+}$

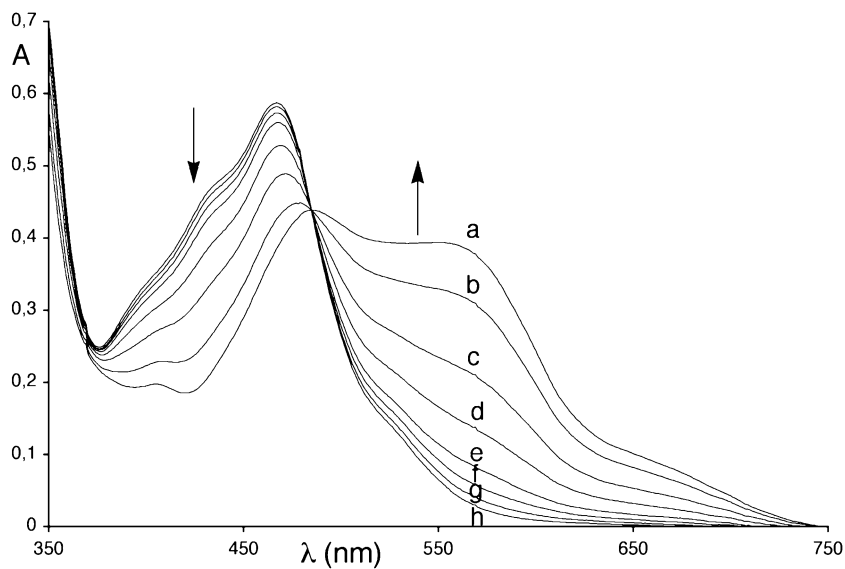


**Fig. 19** Absorption spectra (visible region) of a solution containing  $34^{2+}$  and  $\text{NET}_4^+\text{Cl}^-$  in  $\text{ClCH}_2\text{CH}_2\text{Cl}$  before, during, and after irradiation. Spectra were recorded at  $t = 0$  s a, 15 s b, 40 s c, 90 s d, 200 s e, 400 s f, 900 s g, 2400 s h

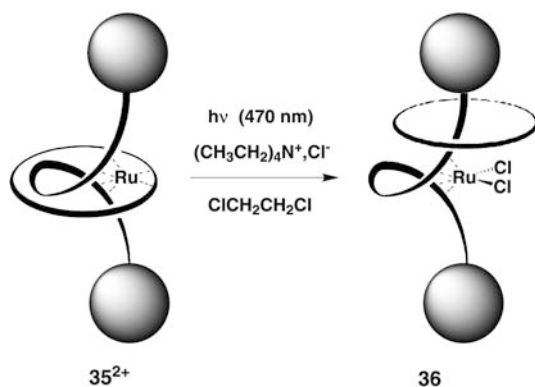


**Fig. 20** Schematic representation of the photochemical reaction leading to the disconnected rotaxane **36**

From a band centered at 465 nm, typical of a  $\text{Ru}(\text{diimine})_3^{2+}$  complex [96], a new spectrum is obtained by irradiation, which corresponds to a  $\text{RuCl}_2(\text{diimine})_2$  complex ( $\lambda_{\text{max}} = 562$  nm). As expected, the MLCT band for the photochemical product is strongly bathochromically shifted from that of the tris-diimine complex. The presence of a clean isosbestic point at 485 nm indicates that the photochemical reaction is selective and quantitative. This has been confirmed by  $^1\text{H}$  NMR spectroscopy and by thin-layer chromatography. Only one photochemical product was detected and the starting complex  $34^{2+}$  has completely disappeared. Similar experiments have been performed with the rotaxane  $35^{2+}$ . The reaction is represented in a schematic fashion in Fig. 20.

The photochemical decooordination of the ring in  $35^{2+}$  is also selective and clean. Here again, in an analogous way as with  $34^{2+}$ , an isosbestic point is observed at 486 nm. Thin-layer chromatography turned out to be particularly useful to monitor the reaction. It showed that  $35^{2+} \cdot 2\text{PF}_6^-$  is gradually converted to a single purple complex, **36**, under irradiation (470 nm). Importantly, traces of the free ring could not be detected, demonstrating that both forms of the rotaxane,  $35^{2+}$  and **36**, do not undergo unthreading, even to a minor extent. Unfortunately, the thermal recoordination reaction of the ring to lead back to  $35^{2+}$  is not as clean and selective as the presently described threading reaction used to prepared  $34^{2+}$  nor as in the case of a related catenane (see next paragraph).

### 3.5

#### Photoinduced Decoordination and Thermal Recoordination of a Ring in a Ruthenium(II)-Containing [2]Catenane

For this latter system, the synthetic approach is based on the template effect of an octahedral ruthenium(II) centre [97–100]. Two 1,10-phenanthroline ligands are incorporated in a ring, affording the precursor to the catenane. The

main point of the design is the observation that it should be possible to incorporate two bidentate chelates of the octahedron in a ring and subsequently to thread a fragment containing the third chelate through the ring. This second process would of course be driven by coordination to the central metal. The synthetic procedure starts with the preparation of a large ring incorporating two phen units [99, 100]. The choice of the ring was dictated by CPK models and by synthesis considerations. The [2]catenanes  $37^{2+}$  and  $38^{2+}$ , which differ essentially by the size of the ring incorporating the ruthenium core, are represented in Fig. 21. Compound  $37^{2+}$  consists of a 50-membered ring which incorporates two phen units and a 42-membered ring which contains the bpy chelate. Compound  $38^{2+}$  contains the same bpy-incorporating ring as  $37^{2+}$ , but the other ring is a 63-membered ring. Clearly, from CPK model considerations,  $38^{2+}$  is more adapted than  $37^{2+}$  to molecular motions in which both constitutive rings would move with respect to one another since the situation is relatively tight for the latter catenane. The light-induced motion and the thermal back reaction carried out with  $37^{2+}$  or  $38^{2+}$  are represented in Fig. 21. They are both quantitative, as shown by UV/Vis measurements and by  $^1\text{H}$  NMR spectroscopy.

The photoproducts, [2]catenanes  $37'$  and  $38'$ , contain two disconnected rings since the photochemical reaction leads to decomplexation of the bpy chelate from the ruthenium(II) centre. In a typical reaction, a degassed  $\text{CH}_2\text{Cl}_2$  solution of  $38^{2+}$  and  $\text{NEt}_4^+\cdot\text{Cl}^-$  was irradiated with visible light, at

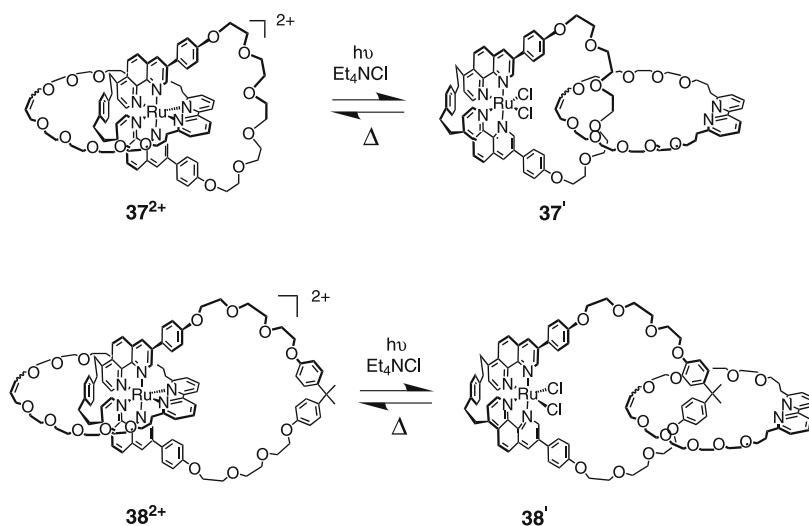


**Fig. 21** Catenanes  $37^{2+}$  or  $38^{2+}$  undergo a complete rearrangement by visible light irradiation: the bpy-containing ring is efficiently decomplexed in the presence of  $\text{Cl}^-$ . By heating the photo-products  $37'$  or  $38'$ , the starting complexes  $37^{2+}$  or  $38^{2+}$  are quantitatively regenerated

room temperature. The colour of the solution rapidly changed from red ( $38^{2+}$ :  $\lambda_{\max} = 458$  nm) to purple ( $38'$ :  $\lambda_{\max} = 561$  nm) and after a few minutes the reaction was complete. The recoordination reaction  $38' \rightarrow 38^{2+}$  was carried out by heating a solution of  $38'$ . The quantum yield for the photochemical reaction  $38^{2+} \rightarrow 38'$  at 25 °C and  $\lambda = 470$  nm ( $\pm 50$  nm) can be very roughly estimated as  $0.014 \pm 0.005$ . One of the weak points of the present system is certainly the limited control over the shape of the photoproduct since the decoordinated ring can occupy several positions. It is hoped that, in the future, an additional tuneable interaction between the two rings of the present catenanes,  $37'$  or  $38'$  will allow better control over the geometry of the whole system. In parallel, two-colour machines will be elaborated, for which both motions will be driven by photonic signals operating at different wavelengths.

## 4

### Conclusion

The modern tools available in synthetic chemistry, either from the organic viewpoint or concerning the preparation of transition metal complexes, allow one to prepare more and more sophisticated molecular systems. In parallel, time-resolved photochemistry and photophysics are nowadays particularly efficient to disentangle complex photochemical processes taking place on multicomponent molecules. In the present chapter, we have shown that the combination of the two types of expertise, namely synthesis and photochemistry, permits to tackle ambitious problems related to artificial photosynthesis or controlled dynamic systems. Although the two families of compounds made and studied lead to completely different properties and, potentially, to applications in very remote directions, the structural analogy of the complexes used is striking.

In the course of the last three decades, the archetype  $\text{Ru}(\text{bpy})_3^{2+}$  has been at the origin of an extremely active field of research aimed at converting light energy into chemical energy. It has also been used more recently by a few groups to fabricate light-driven molecular machines.

1.  $\text{Ir}(\text{terpy})_2^{3+}$  is reminiscent of  $\text{Ru}(\text{bpy})_3^{2+}$  by some of its photochemical properties but, it is at the same time very different as far as its geometrical properties are concerned and for its electronic and photochemical characteristics. This complex has been used both as a chromophore and as an electron relay, in relation to charge separation. It is expected that, in the future, long-lived charge-separated states will be obtained by constructing carefully designed molecular triads with an  $\text{Ir}(\text{terpy})_2^{3+}$  central core.
2.  $[\text{RuL}^1\text{L}^2\text{L}^3]^{2+}$  leads to photochemically labile complexes, able to undergo controlled ligand substitution under light irradiation, provided the three diimine chelates  $\text{L}^n$  have been selected in the proper way. Such systems,

once incorporated in rotaxanes or catenanes, represent promising light-driven molecular machine prototypes.

**Acknowledgements** We would like to thank all the very talented and enthusiastic researchers who participated in the work discussed in the present review article. Their names appear in the references. We thank CNR of Italy (PM-P04-ISTM-C1/ISOF-M5), CNRS (France), Ministero dell'Istruzione, dell'Università e della Ricerca of Italy (FIRB, RBNE019H9K) and COST D31 for financial support. SB acknowledges the Région Alsace for financial support.

## References

1. Balzani V, Carassiti V (1970) *Photochemistry of Coordination Compounds*. Academic Press, London
2. Balzani V, Moggi L (1990) *Coord Chem Rev* 97:313
3. Gafney HD, Adamson AW (1972) *J Am Chem Soc* 94:8238
4. Juris A, Balzani V, Barigelletti F, Campagna S, Belser P, von Zelewsky A (1988) *Coord Chem Rev* 84:85
5. Danielson E, Elliott CM, Merkert JW, Meyer TJ (1987) *J Am Chem Soc* 109:2519
6. Di Marco G, Lanza M, Mamo A, Stefio I, Di Pietro C, Romeo G, Campagna S (1998) *Anal Chem* 70:5019
7. Gao RM, Ho DG, Hernandez B, Selke M, Murphy D, Djurovich PI, Thompson ME (2002) *J Am Chem Soc* 124:14828
8. Lo KKW, Chung CK, Lee TKM, Lui LH, Tsang KHK, Zhu NY (2003) *Inorg Chem* 42:6886
9. Adachi C, Baldo MA, Forrest SR, Thompson ME (2000) *Appl Phys Lett* 77:904
10. Lamansky S, Djurovich P, Murphy D, Abdel-Razzaq F, Lee HE, Adachi C, Burrows PE, Forrest SR, Thompson ME (2001) *J Am Chem Soc* 123:4304
11. Tsuboyama A, Iwawaki H, Furugori M, Mukaide T, Kamatani J, Igawa S, Moriyama T, Miura S, Takiguchi T, Okada S, Hoshino M, Ueno K (2003) *J Am Chem Soc* 125:12971
12. Gong X, Ostrowski JC, Moses D, Bazan GC, Heeger AJ (2003) *Adv Funct Mat* 13:439
13. Nazeeruddin MK, Humphry-Baker R, Berner D, Rivier S, Zuppiroli L, Graetzel M (2003) *J Am Chem Soc* 125:8790
14. Beeby A, Bettington S, Samuel IDW, Wang ZJ (2003) *J Mater Chem* 13:80
15. Holder E, Langeveld BMW, Schubert US (2005) *Adv Mater* 17:1109
16. Holder E, Marin V, Kozodaev D, Meier MAR, Lohmeijer BGG, Schubert US (2005) *Macromol Chem Phys* 206:989
17. Leslie W, Poole RA, Murray PR, Yellowlees LJ, Beeby A, Williams JAG (2004) *Polyhedron* 23:2769
18. Sajoto T, Djurovich PI, Tamayo A, Yousufuddin M, Bau R, Thompson ME, Holmes RJ, Forrest SR (2005) *Inorg Chem* 44:7992
19. Yang CH, Li SW, Chi Y, Cheng YM, Yeh YS, Chou PT, Lee GH, Wang CH, Shu CF (2005) *Inorg Chem* 44:7770
20. Collin JP, Guillerez S, Sauvage JP, Barigelletti F, De Cola L, Flamigni L, Balzani V (1991) *Inorg Chem* 30:4230
21. Collin JP, Guillerez S, Sauvage JP, Barigelletti F, De Cola L, Flamigni L, Balzani V (1992) *Inorg Chem* 31:4112
22. Harriman A, Odobel F, Sauvage JP (1995) *J Am Chem Soc* 117:9461

23. Andreasson J, Kodis G, Lin S, Moore AL, Moore TA, Gust D, Martensson J, Albinsson B (2002) *Photochem Photobiol* 76:47
24. Flamigni L, Barigelletti F, Armaroli N, Collin JP, Sauvage JP, Williams JAG (1998) *Chem Eur J* 4:1744
25. Flamigni L, Armaroli N, Barigelletti F, Balzani V, Collin JP, Dalbavie JO, Heitz V, Sauvage JP (1997) *J Phys Chem B* 101:5936
26. Sauvage JP, Collin JP, Chambron JC, Guillerez S, Coudret C, Balzani V, Barigelletti F, De Cola L, Flamigni L (1994) *Chem Rev* 94:993
27. Flamigni L, Barigelletti F, Armaroli N, Ventura B, Collin JP, Sauvage JP, Williams JAG (1999) *Inorg Chem* 38:661
28. Huynh MHV, Dattelbaum DM, Meyer TJ (2005) *Coord Chem Rev* 249:457
29. Kober EM, Caspar JV, Lumpkin RS, Meyer TJ (1986) *J Phys Chem* 90:3722
30. Treadway JA, Chen PY, Rutherford TJ, Keene FR, Meyer TJ (1997) *J Phys Chem A* 101:6824
31. Goze C, Chambron JC, Heitz V, Pomeranc D, Salom-Roig XJ, Sauvage JP, Morales AF, Barigelletti F (2003) *Eur J Inorg Chem*, p 3752
32. Flynn CM Jr, Demas JN (1974) *J Am Chem Soc* 96:1959
33. Demas JN, Harris EW, Flynn CM, Diemente D (1975) *J Am Chem Soc* 97:3838
34. Collin JP, Dixon IM, Sauvage JP, Williams JAG, Barigelletti F, Flamigni L (1999) *J Am Chem Soc* 121:5009
35. Flamigni L, Ventura B, Barigelletti F, Baranoff E, Collin JP, Sauvage JP (2005) *Eur J Inorg Chem*, p 1312
36. Baranoff E, Griffiths K, Collin JP, Sauvage JP, Ventura B, Flamigni L (2004) *New J Chem* 28:1091
37. De Cola L, Balzani V, Barigelletti F, Flamigni L, Belser P, Vonzelewsky A, Frank M, Vogtle F (1993) *Inorg Chem* 32:5228
38. Guardigli M, Flamigni L, Barigelletti F, Richards CSW, Ward MD (1996) *J Phys Chem* 100:10620
39. Stone ML, Crosby GA (1981) *Chem Phys Lett* 79:169
40. Passalacqua R, Loiseau F, Campagna S, Fang YQ, Hanan GS (2003) *Angew Chem Int Ed* 42:1608
41. Wang JH, Hanan GS, Loiseau F, Campagna S (2004) *Chem Commun*, p 2068
42. Medlycott EA, Hanan GS (2005) *Chem Soc Rev* 34:133
43. Abrahamsson M, Wolpher H, Johansson O, Larsson J, Kritikos M, Eriksson L, Norrby PO, Bergquist J, Sun LC, Akermark B, Hammarström L (2005) *Inorg Chem* 44:3215
44. Dixon IM, Collin JP, Sauvage JP, Barigelletti F, Flamigni L (2000) *Angew Chem Int Edit* 39:1292
45. Dixon IM, Collin JP, Sauvage JP, Flamigni L (2001) *Inorg Chem* 40:5507
46. Marcus RA (1993) *Angew Chem Int Ed* 32:1111
47. Flamigni L, Dixon IM, Collin JP, Sauvage JP (2000) *Chem Commun*, p 2479
48. Flamigni L, Marconi G, Dixon IM, Collin JP, Sauvage JP (2002) *J Phys Chem B* 106:6663
49. Dixon IM, Collin JP, Sauvage JP, Flamigni L, Encinas S, Barigelletti F (2000) *Chem Soc Rev* 29:385
50. Dietrich-Buchecker CO, Nierengarten JF, Sauvage JP, Armaroli N, Balzani V, De Cola L (1993) *J Am Chem Soc* 115:11237
51. Baranoff E, Dixon IM, Collin JP, Sauvage JP, Ventura B, Flamigni L (2004) *Inorg Chem* 43:3057
52. Eisenberg R, Nocera DG (2005) *Inorg Chem* 44:6799

53. Alstrum-Acevedo JH, Brennaman MK, Meyer TJ (2005) *Inorg Chem* 44:6802
54. Chakraborty S, Wadas TJ, Hester H, Schmehl R, Eisenberg R (2005) *Inorg Chem* 44:6865
55. Mecklenburg SL, Peek BM, Erickson BW, Meyer TJ (1991) *J Am Chem Soc* 113:8540
56. Borgström M, Shaikh N, Johansson O, Anderlund MF, Styring S, Akermark B, Magnuson A, Hammarström L (2005) *J Am Chem Soc* 127:17504
57. Livoreil A, Sauvage J-P, Armaroli N, Balzani V, Flamigni L, Ventura B (1997) *J Am Chem Soc* 119:12114
58. Armaroli N, Balzani V, Collin J-P, Gaviña P, Sauvage J-P, Ventura B (1999) *J Am Chem Soc* 121:4397
59. Mobian P, Kern J-M, Sauvage J-P (2004) *Angew Chem Int Ed* 43:2392
60. Koumura N, Geertsema EM, v Gelder MB, Meetsma A, Feringa BL (2002) *J Am Chem Soc* 124:5037
61. Koumura N, Zijistra RWJ, van Delden RA, Harada N, Feringa BL (1999) *Nature* 401:152
62. ter Wiel MKJ, van Delden RA, Meetsma A, Feringa BL (2003) *J Am Chem Soc* 125:15076
63. Norikane Y, Tamaoki N (2004) *Organic Lett* 6:2595
64. Muraoka T, Kinbara K, Kabayashi Y, Aida T (2003) *J Am Chem Soc* 125:5612
65. Kojima T, Sakamoto T, Matsuda Y (2004) *Inorg Chem* 43:2243
66. Jouvenot D, Koizumi M, Collin J-P, Sauvage J-P (2005) *Eur J Inorg Chem*, p 1850
67. Ballardini R, Balzani V, Gandolfi MT, Prodi L, Venturi M, Philp D, Ricketts HG, Stoddart JF (1993) *Angew Chem Int Ed Eng* 32:1301
68. Ashton PR, Ballardini R, Balzani V, Credi A, Dress KR, Ishow E, Kleverlaan CJ, Kocian O, Preece JA, Spencer N, Stoddart JF, Venturi M, Wenger S (2000) *Chem Eur J* 6:3558
69. Murakami H, Kawabuchi A, Kotoo K, Kunitake M, Nakashima N (1997) *J Am Chem Soc* 119:7605
70. Adelt M, Devenney M, Meyer TJ, Thompson DW, Treadway JA (1998) *Inorg Chem* 37:2616
71. Van Houten J, Watts J (1978) *Inorg Chem* 17:3381
72. Suen HF, Wilson SW, Pomerantz M, Walsch JL (1989) *Inorg Chem* 28:786
73. Pinnick DV, Durham B (1984) *Inorg Chem* 23:1440
74. Durham B, Caspar JV, Nagle JK, Meyer TJ (1982) *J Am Chem Soc* 104:4803
75. Tachiyashiki S, Mizumachi K (1994) *Coord Chem Rev* 132:113
76. von Zelewsky A, Gremaud G (1988) *Helv Chim Acta* 71:1108
77. Hichida H, Tachiyashiki S, Sasaki Y (1989) *Chem Lett* 1579
78. Collin J-P, Laemmel A-C, Sauvage J-P (2001) *New J Chem* 25:22
79. Baranoff E, Collin J-P, Furusho J, Furusho Y, Laemmel A-C, Sauvage J-P (2002) *Inorg Chem* 41:1215
80. Laemmel A-C, Collin J-P, Sauvage J-P, Accorsi G, Armaroli N (2003) *Eur J Inorg Chem*, p 467
81. Laemmel A-C, Collin J-P, Sauvage J-P (2000) *CR Acad Sci* 3:43
82. Bonnet S, Collin J-P, Gruber N, Sauvage J-P, Schofield ER (2003) *Dalton Trans*
83. Schofield ER, Collin J-P, Gruber N, Sauvage J-P (2003) *Chem Commun*, p 188
84. Bonnet S, Schofield ER, Collin J-P, Sauvage J-P (2004) *Inorg Chem* 43:8346
85. Sauvage J-P, Dietrich-Buchecker CO (eds) (1999) *Molecular Catenanes, Rotaxanes and Knots*. Wiley, Weinheim
86. Baranoff E, Collin J-P, Furusho Y, Laemmel A-C, Sauvage J-P (2000) *Chem Commun*, p 1935



87. Leising RA, Grzybowski J-J, Takeuchi KJ (1988) *Inorg Chem* 27:
88. Perez WJ, Lake CH, See RF, Toomey LM, Churchill MR, Takeuchi KJ, Radano CP, Boyko WJ, Bessel CA (1999) *J Chem Soc Dalton Trans*, p 2281
89. Cardenas DJ, Gavina P, Sauvage J-P (1997) *J Am Chem Soc* 119:2656
90. Fujita M (1999) *Acc Chem Res* 32:53
91. Hecker CR, Fanwick PE, McMillin DR (1991) *Inorg Chem* 30:659
92. Dudek MJ, Ponder JW (1995) *J Comput Chem* 16:791
93. Shinkai S, Nakaji T, Nishida Y, Ogawa T, Manabe O (1980) *J Am Chem Soc* 102:5860
94. Fabbrizzi L, Foti F, Patroni S, Pallavicini P, Taglietti A (2004) *Angew Chem Int Ed Eng* 43:5073
95. Pomeranc D, Jouvenot D, Chambron J-C, Collin J-P, Heitz V, Sauvage J-P (2003) *Chem Eur J* 9:4247
96. Balzani V, Credi A, Venturi M (1998) *Coord Chem Rev* 171:3
97. Hayoz P, von Zelewsky A, Stoeckli-Evans H (1993) *J Am Chem Soc* 115:51111
98. Arico F, Mobian P, Kern J-M, Sauvage J-P (2003) *Organic Lett* 5:1887
99. Mobian P, Kern J-M, Sauvage J-P (2003) *J Am Chem Soc* 125:2016
100. Mobian P, Kern J-M, Sauvage J-P (2003) *Helv Chim Acta* 86:4195

# Metal-based Photoswitches Derived from Photoisomerization

Shoko Kume · Hiroshi Nishihara (✉)

Graduate School of Science, The University of Tokyo, 7-3-1, Hongo, Bunkyo-ku,  
113-0033 Tokyo, Japan  
*nishihara@chem.e.u-tokyo.ac.jp*

1	Introduction . . . . .	80
2	Spiropyran-, Spirooxazine-, and Chromene-Attached Complexes . . . . .	81
3	Diarylethene-Attached Complexes . . . . .	87
4	Stilbene- and Azobenzene-Attached Complexes . . . . .	92
5	Other Systems Using Organic Photochromic Molecules . . . . .	107
6	Concluding Remarks . . . . .	109
	References . . . . .	110

**Abstract** A combination of photochromism and other molecular functionalities is an efficient way to construct novel multi-mode photofunctional molecules. From this perspective, a considerable number of photochromic metal complexes involving photochromic moieties and coordination compounds with unique electronic, magnetic and optical properties have been investigated. One research point of interest in the photochromic complexes focuses on how metal coordination affects the isomerization behavior of the photochromic moiety. Proper molecular structural design can more strongly stabilize a metastable state in support of feasible metal–ligand interactions, improving the thermal durability of the molecular photomemory. Moreover, isomerization can be caused not only by the excitation at the photochromic moiety, but also by the stimulation (light or electron) at the metal complex moiety. The multi-moiety combined response may be able to construct an integrated memory or a logic gate in a single molecule. Another research point of interest focuses on how structural conversion at the photochromic moiety affects electromagnetic properties at the complex moiety. Several studies have shown how photon information/energy is converted to luminescence, an electronic signal, or a magnetic response at the complex moiety. Interactions between multiple complex moieties can also be reversibly tuned with light when the photochromic moiety is used as a spacer between them. Here we review recent studies on the combination of photochromic moieties with coordination compounds, categorizing the research findings according to the structure of the photochromic moieties.

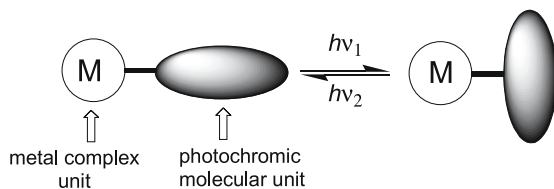
**Keywords** Metal complex · Multi-mode function · Photochromism

## 1 Introduction

Photochromic molecules for which the structure – more specifically, the electronic structure and color – changes reversibly in response to photo-irradiation have attracted much recent attention because of their possible applications in the area of photon-mode high-density information storage and photo-switching devices. Thus far, many photochromic molecules have been found, including spiropyran, spiroxazine, chromene, fulgide, diarylethene, stilbene, azobenzene, and so on [1]. In the research regarding such compounds, the tuning of their photochromic and other properties by introducing appropriate substituents has been explored, and the development of hybrid materials with polymers and liquid crystals to achieve conversion of photo-signals into other signals has been extensively investigated.

In addition, molecules that can act as devices by themselves have attracted much recent attention in the field of molecular-scale electronics [2]. Such molecules are required to show bi-stable or multi-stable states that can be reversibly interconverted by applying external stimuli such as photons, electrons, protons, and so on. Metal complexes are excellent candidates that have been known to exhibit unique physical properties that can respond to various stimuli from an external field. It is thus an effective approach to make device-performing single molecules from a combination of metal complex units with photochromic molecular units in a single molecule. There are two interesting questions with regard to the photochromic molecule-containing metal complexes (Fig. 1). First, what are the effects of metal complex units on the photo-transformation of the ligand? And second, what are the changes in the physical properties of metal complex units caused by the ligand transformation?

In the present article, we provide an overview of the studies dealing with metal complexes with photochromic ligands. It should be noted that there are certain photochromic metal complexes that show their photochromism



**Interest in metal complexes with photochromic ligand(s) is twofold.**

- 1) Effects of complex units on the isomerization of azo units.
- 2) Changes in physical properties of the complex by isomerization of the azo units.

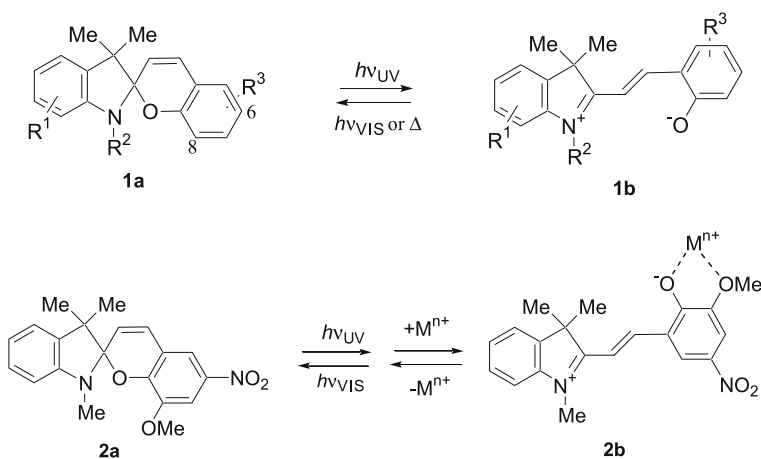
**Fig. 1** Concept of photochromic molecule-bound metal complexes

by a change in the coordination structure or intermolecular interactions, but they will not be included in this review.

## 2 Spiropyran-, Spirooxazine-, and Chromene-Attached Complexes

The thermodynamically stable form of spiropyran (**1a**) is almost colorless and has a closed structure of two doubly fused rings. UV light irradiation to this closed form cleaves the C–O bond to give a colored open form, *trans*-merocyanine (**1b**), with extended  $\pi$ -conjugation (*cis*-merocyanine is formed as a short-lived reaction intermediate). Merocyanine **1b** returns to **1a** by visible-light irradiation or by heating. Spirooxazine and chromene undergo similar photochromic reactions between closed and open forms. The thermodynamic stability balance between spiropyran and merocyanine forms is considerably altered by the electronic effects of substituents on the backbone. Among the spiropyran family, spiropyrans with a nitro group at the six-position have been widely employed for the study of photochemistry. It has been found that when a heteroatom (O, N, etc.) is attached to the eight-position, steric hindrance makes it difficult for the closed spiropyran form to bind to a metal ion, but the open form can act as a good chelating ligand [3]. As a result of this finding, numerous studies investigating the relationship between the complexation of *d*- and *f*-transition metal ions and photochromic properties have been carried out.

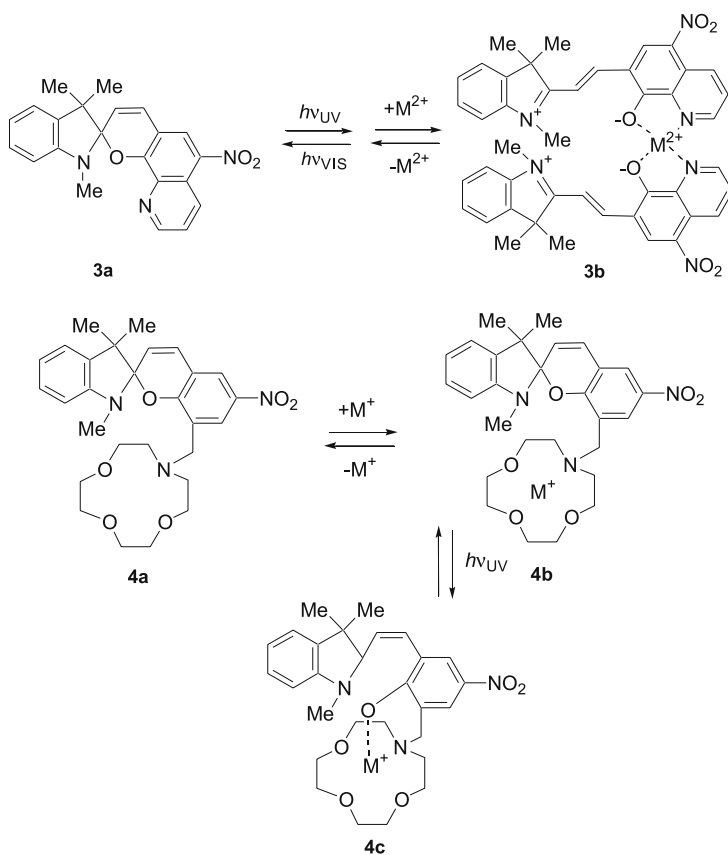
A spiropyran with a methoxy group at the eight-position, **2a** and its derivatives show a blue shift of the absorption peak when a metal ion is attached to form a chelate complex, **2b** [4, 5]. The type of metal ion has little effect on the wavelength of the absorption maximum,  $\lambda_{\text{max}}$ , but it has a strong influence



on the stability of the photo-excited state. The photo-reaction mechanism and kinetics upon the complexation of the merocyanine form with metal ions have been analyzed [6, 7].

The coordination ability of the merocyanine form has been utilized for the sensing of heavy metal ions. For example, the  $\lambda_{\max}$  of *trans*-merocyanine form of nitroquinospiropyranindoline (3a) is 580 nm, which shifts to 518–538 nm by coordinating the N and O atoms to  $\text{Zn}^{2+}$ ,  $\text{Co}^{2+}$ ,  $\text{Hg}^{2+}$ ,  $\text{Cu}^{2+}$ ,  $\text{Cd}^{2+}$ , or  $\text{Ni}^{2+}$  ions; the degree of the shift depends on the type of metal ion [8, 9], and this phenomenon has been utilized for application in the selective sensing of metal ions.

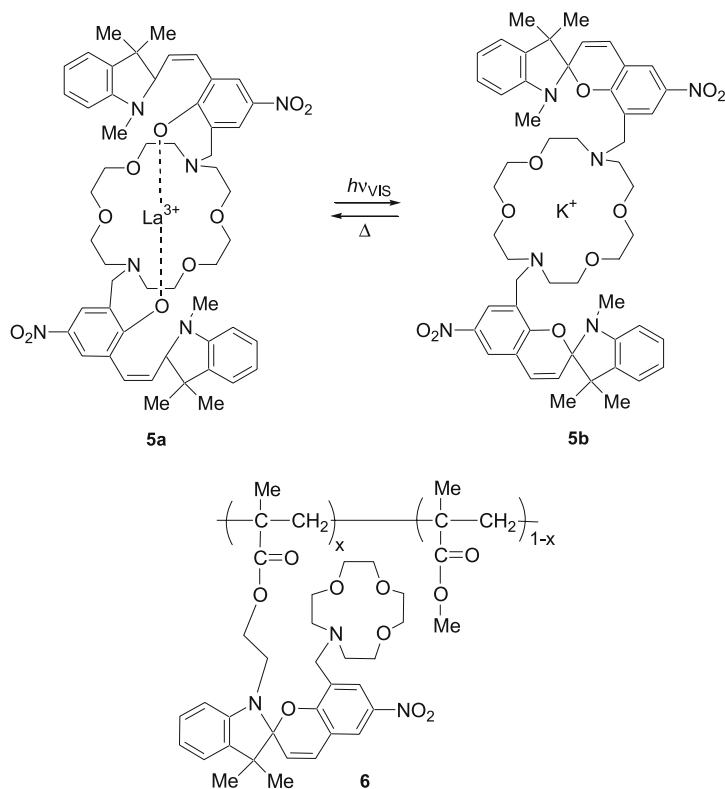
The ability to tune the photochromic behavior of crown ether-bound spiropyrans, 4a and 5a, by connecting them to metal ions, was investigated by Kimura and his coworkers [10, 11]. This complexation of the crown ether moiety with a metal ion accelerates the transformation from spiropyran, 4b to merocyanine, 4c, by light or heat. When this complexation effect is weak, thermodynamic equilibrium favors the spiropyran form, and

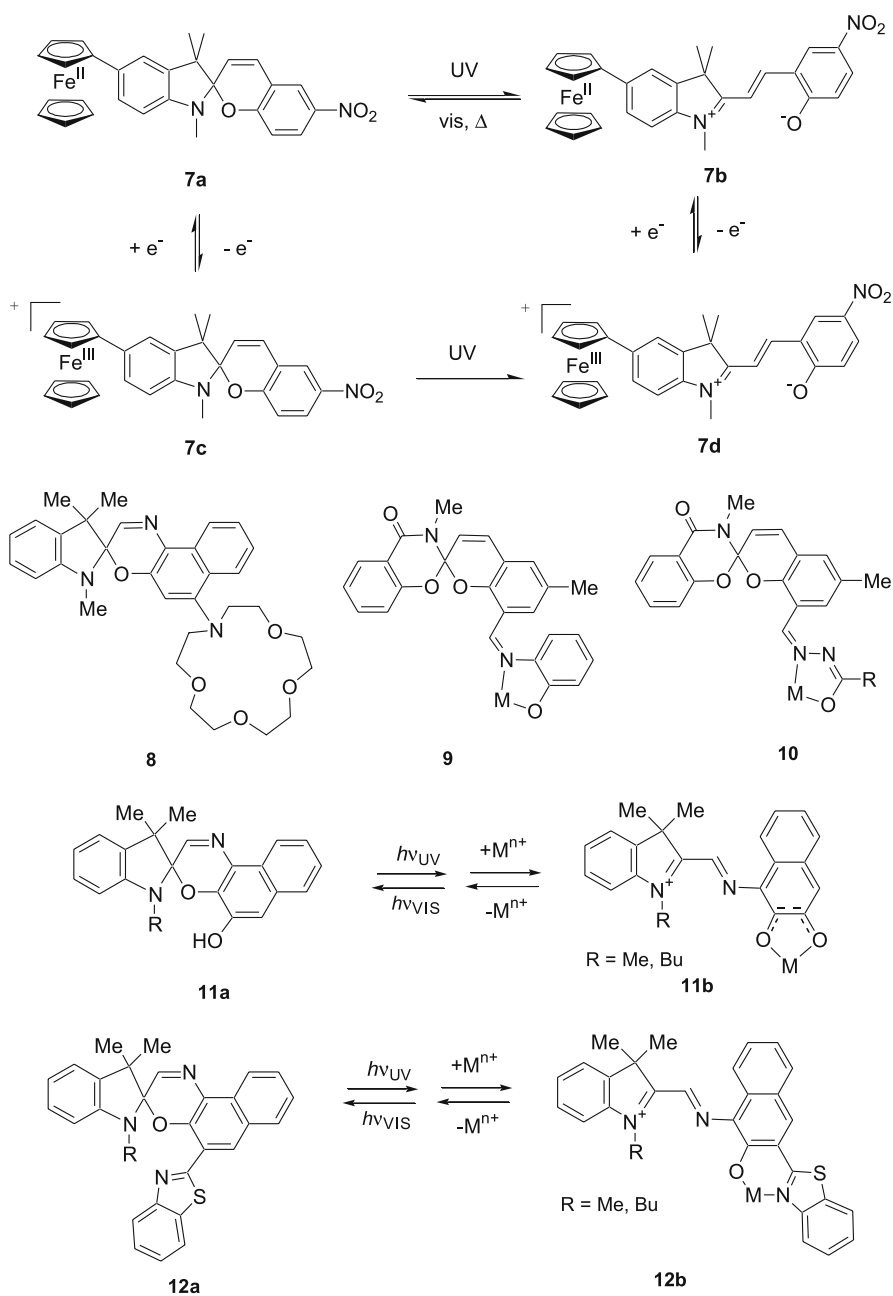


transformation to the merocyanine occurs upon UV light irradiation. On the other hand, when the complexation ability is strong, thermodynamic equilibrium lies further to the merocyanine form and UV light irradiation results in transformation to the spiroopyran form. This result implies that the direction of the photoisomerization can be switched by metal coordination. Crowned bis(spiropyran) **5a** causes the coordination metal to change from  $\text{La}^{3+}$  to  $\text{K}^+$  by visible light irradiation leading to merocyanine-to-spiropyran isomerization [11]. Crowned spiroopyran vinyl polymers, **6**, also have a photochromic ability to show photoresponsive ion-conducting behavior [12].

5-Ferrocenylspiroopyran, **7**, can control the stability of the merocyanine form by changing the oxidation state of the ferrocene moiety [13]. This system works not only in liquid solution but also in a polymer electrolyte.

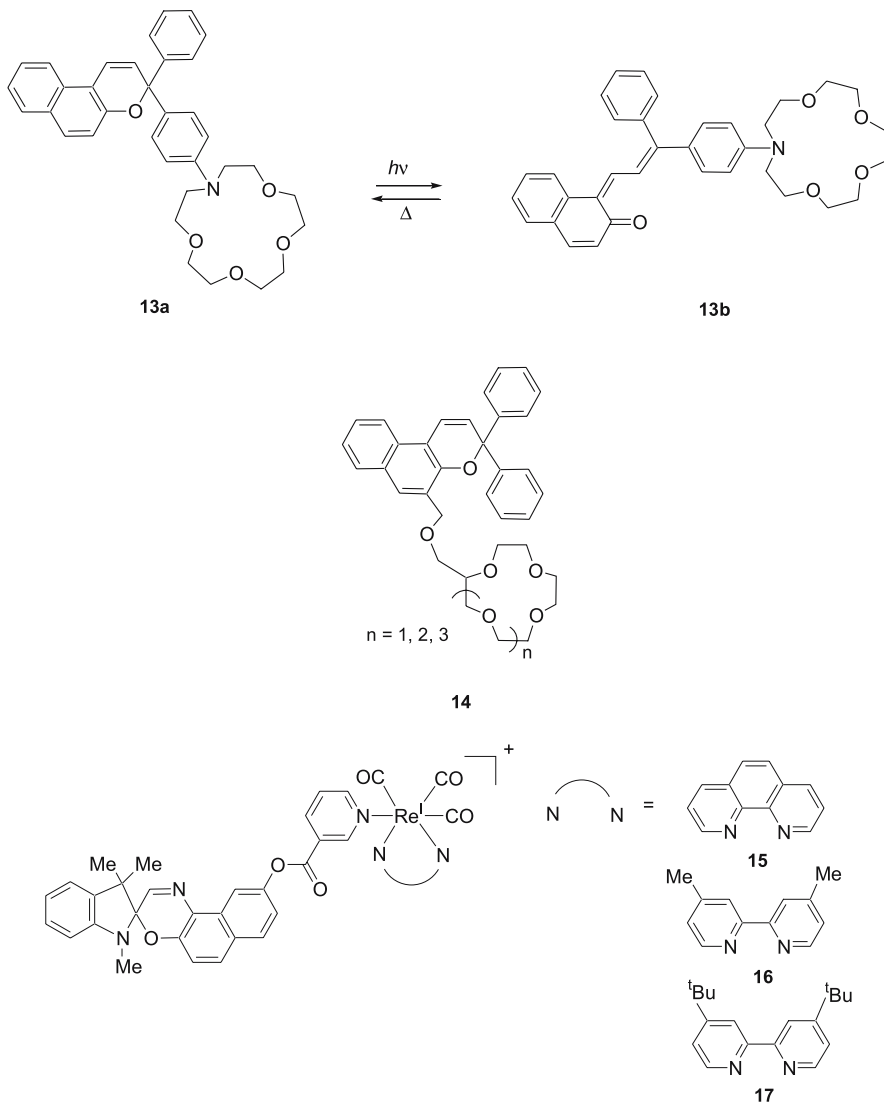
Spiroanthoxazine with a crown ether, **8**, also shows photochromic behavior that is sensitive to the type of alkali and alkaline earth metal ions [14]. Other derivatives of spiroopyran and spirooxazine, **9–12**, which can chelate metal ions were synthesized, and the effects of complexation on their photochromic behavior have been investigated [15–17].





The effects of the reversible photochromic reaction of an azacrown-containing benzochromene **13** on complex formation with  $\text{Ca}^{2+}$  in acetonitrile were studied by Ushakov et al. [18]. It was found that both the initial

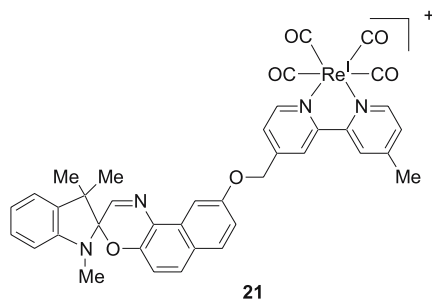
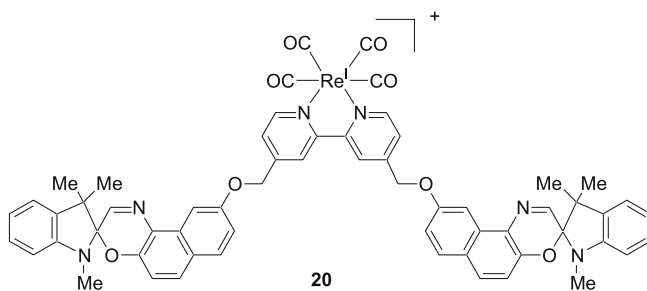
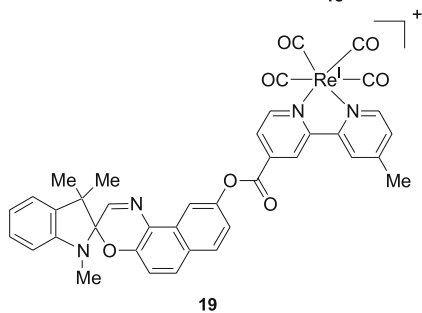
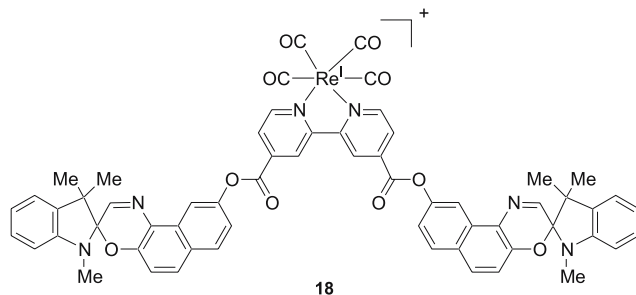
chromene **13a** and its photoinduced merocyanine isomer **13b** are able to form 1 : 1 complexes with  $\text{Ca}^{2+}$ , and the complexation causes strong spectroscopic shifts, leading to an increase in the dark lifetime of **13b**. The equilibrium constant for the 1 : 1 complexation decreases upon photoinduced ring-opening reaction. Another series of chromene derivatives with crown ethers, **14**, not only show photochromism but also induce aggregation to form the 1 : 2 complex, resulting in the switching of the complex stoichiometry by UV irradiation [19]. Compound **14** also exhibits ion-responsive

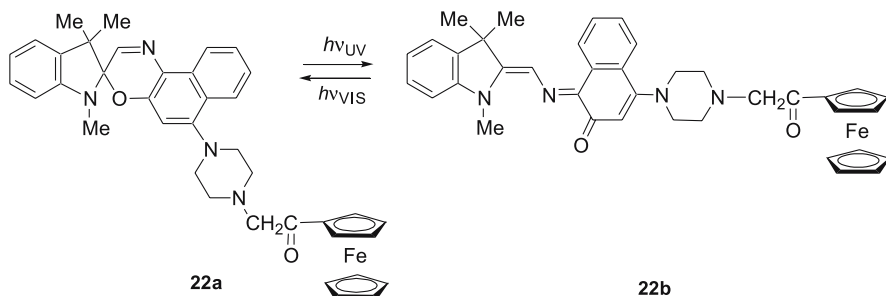




photochromism depending on the metal ion-binding ability of their crown ether moieties.

A series of spironaphthoxazine-containing  $\text{Re}^{\text{I}}$  tricarbonyl diimine complexes, 15–21, were prepared by Yam and her coworkers [20,21]. All the





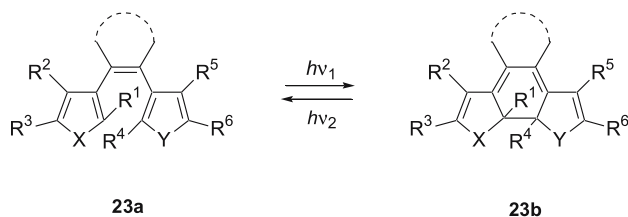
complexes undergo a photochromic reaction upon irradiation at 365 nm, exciting the  $\pi - \pi^*$  transitions, and 15–17 also react upon irradiation at 420 nm, exciting the MLCT ( $d\pi \rightarrow \pi^*$  (diimine)) transition [20]. The complexes 18 and 19 exhibit strong  $^3\text{MLCT}$  phosphorescence at 642 and 600 nm, respectively, in EtOH/MeOH/CH<sub>2</sub>Cl<sub>2</sub> glass at 77 K, and this emission band would be switched to LC phosphorescence of the photomerocyanine moiety at 705–710 nm upon conversion to the open form [21].

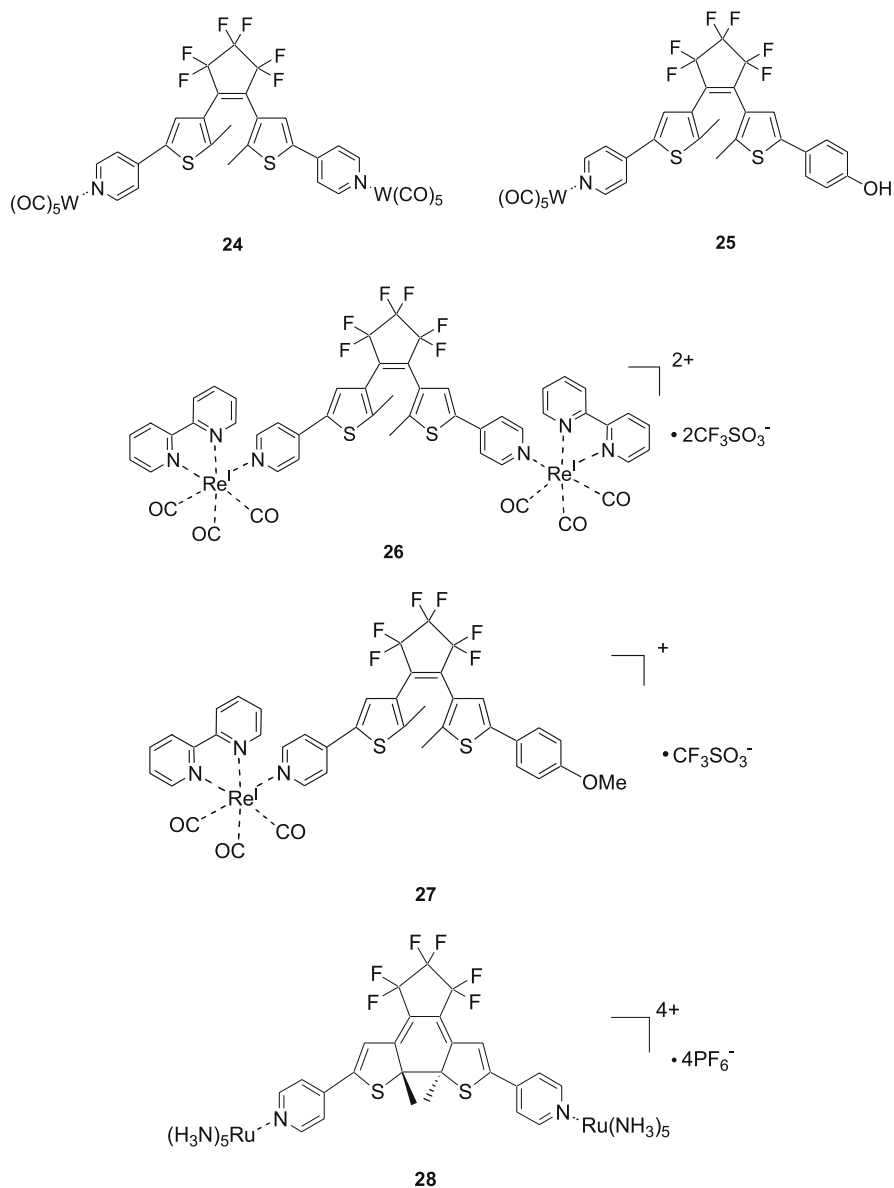
A ferrocene moiety-attached spironaphthoxazine derivative, 22a, which isomerizes into a thermally stable merocyanine form, 22b, and its application in rewritable high density optical data storage have been reported by Song et al. [22].

### 3

#### Diarylethene-Attached Complexes

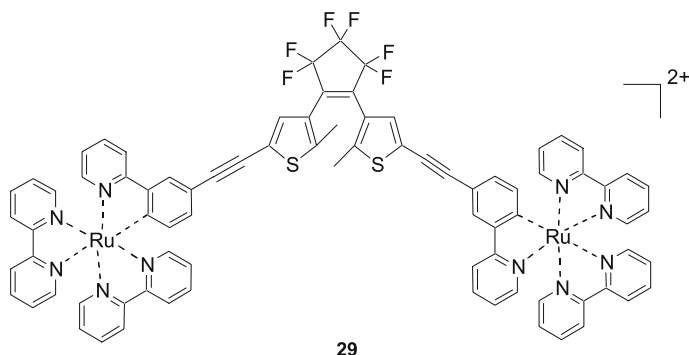
Diarylethene, 23a, found by Irie and Mohri [23], exhibits phototransformation into a closed form, 23b, and has various advantages, such as high stability, high reversibility, high reproducibility, high quantum yield, and a large difference in  $\lambda_{\text{max}}$  between the two forms [24]. Fernández-Acebes and Lehn synthesized W, Re and Ru complexes of pyridyldithienylethenes, 24–28, and showed their pronounced photochromic properties [25, 26]. Irradiation of the open forms of 24–27 with UV light was found to result in essentially quantitative photocyclization to the closed forms, and the back reaction occurred





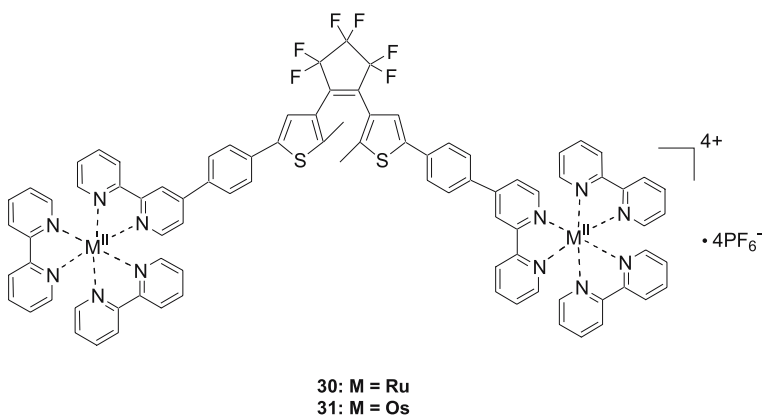
by irradiation with visible light of  $\lambda > 600$  nm. The complexes display a fluorescence discrimination between their open and closed forms. In contrast, the closed form of a Ru complex, **28**, is photochemically stable.

Frayse et al. have synthesized a derivative with two ruthenium centers, **29**, and have investigated its photochromic and redox properties [27]. The closed form of this complex is obtained with 254-nm light irradiation in 75%



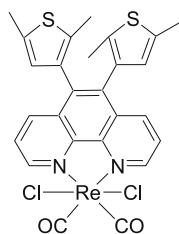
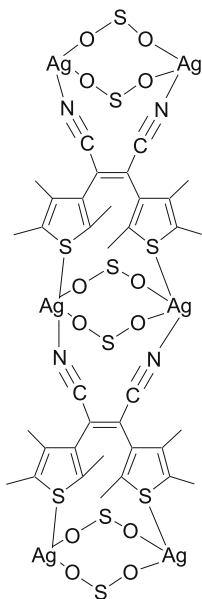
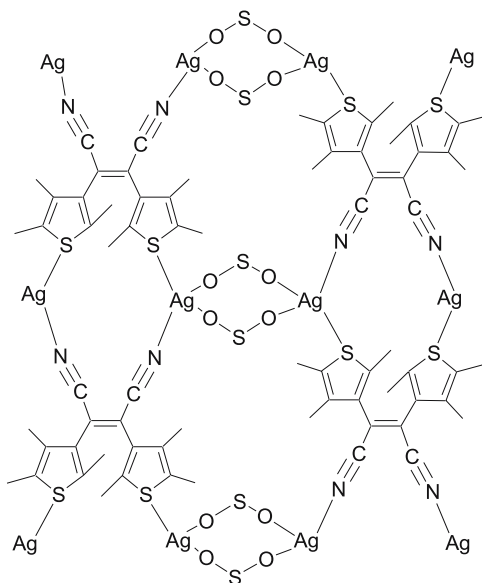
yield. The redox potentials of the  $\text{Ru}^{\text{III}}/\text{Ru}^{\text{II}}$  couple are almost the same in both open and closed forms (0.53 and 0.52 V vs. SCE, respectively). In the oxidized form of this complex, the open form shows no absorption band in the near-infrared region, whereas the closed form exhibits an intervalence charge transfer (IVCT) band at wavelengths longer than 1000 nm due to the formation of a stable mixed-valence state. This result implies that the electron communication between two metal sites is controlled by the photochemical transformation of the bridging diarylethene moiety. A gradual ring-opening process in the oxidized state of the closed form has also been found.

De Cola et al. have found efficient photocyclization from a low-lying triplet state for a diethynylperfluorocyclopentene with  $\text{Ru}(\text{bpy})_2$  units attached via a phenylene linker to the thiophene rings, **30** [28]. The ring-closure reaction in the nanosecond domain is sensitized by the metal complexes. Upon photoexcitation into the lowest Ru-to-bpy  $^1\text{MLCT}$  state followed by intersystem crossing to emitting  $^3\text{MCLT}$  states, photoreactive  $^3\text{IL}$  states are populated by an efficient energy-transfer process. In contrast, replacement of both  $\text{Ru}^{\text{II}}$  centers by  $\text{Os}^{\text{II}}$  (**31**) completely prevents the photocyclization reaction upon excitation into the low-lying Os-to-bpy  $^1\text{MLCT}$  state.

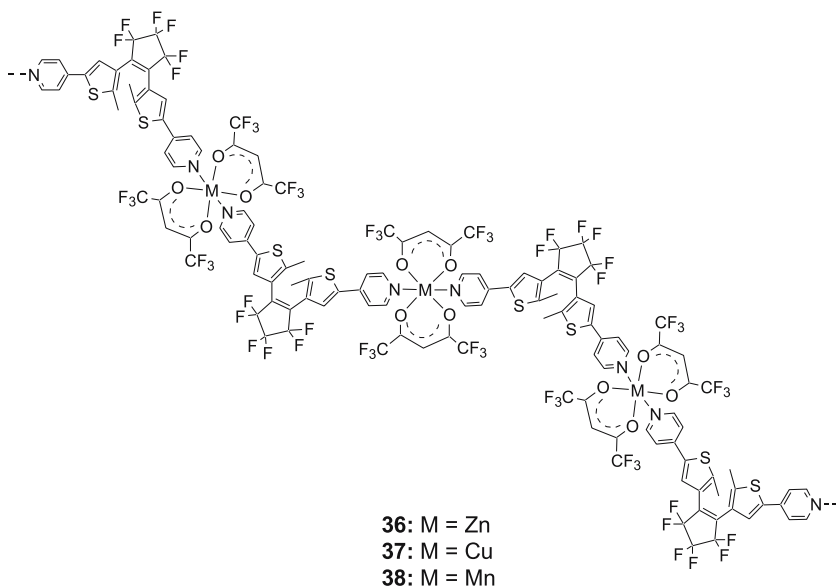
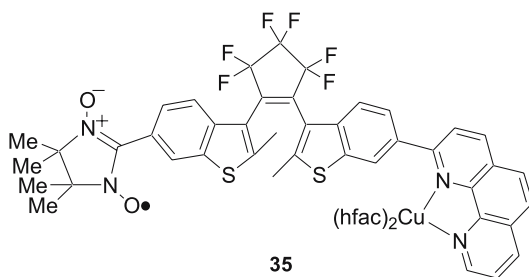


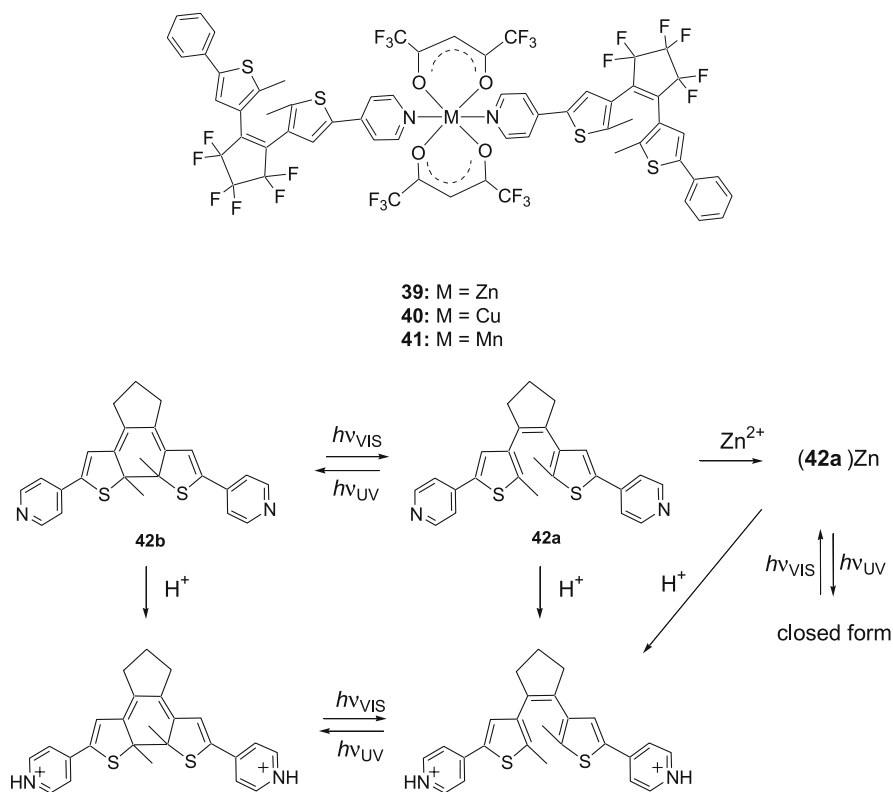
Yam and her coworkers have synthesized a  $\text{Re}^{\text{I}}$  tricarbonyl complex of a photochromic ligand, bis(2,5-dimethyl-3-thienyl)-1,10-phenanthroline, **32**, which shows an expansion of the excitation wavelength region to ca. 480 nm in the visible region, corresponding to the MLCT excitation [29]. The photosensitization mechanism involves an intramolecular energy-transfer process from the  $^3\text{MLCT}$  to the  $^3\text{IL}$  state that initiates the ring-closure reaction [30]. Reversible switching of the emissive state by the photochromic reaction has also been demonstrated [29].

Novel  $\text{Ag}^{\text{I}}$  coordination polymers with a diarylethene derivative, *cis*-dbe, have been synthesized by Munakata et al. [31]. Polymers with a one-dimensional infinite chain structure, **33**, and another with a two-dimensional sheet structure, **34**, were synthesized and their reversible photoreactions with 450 nm and 560 nm light in the solid state were revealed.

**32****33****34**

Irie, Matsuda and coworkers have presented photoswitching of an intramolecular spin-exchange interaction between a  $\text{Cu}^{\text{II}}$  ion and a nitroxyl radical by using a metal complex of diarylethene-1,10-phenanthroline ligand, **35** [32]. EPR measurement has shown that a large exchange interaction appears between spins of the nitroxyl radical and  $\text{Cu}^{\text{II}}$  by irradiation with 366 nm light, causing an isomerization from the open to the closed form and creating the largest magnetic photoswitching phenomenon recorded in diarylethene systems.  $\text{Zn}^{\text{II}}$ ,  $\text{Mn}^{\text{II}}$ , and  $\text{Cu}^{\text{II}}$  complexes of bidentate and monodentate diarylethene ligands, **36–41**, having polymeric and discrete 1 : 2 complexes, respectively, were synthesized and their photoinduced coordination structural changes were also studied [33]. The reversible change in the EPR spectra of the copper complexes of the bidentate ligand by photoirradiation indicates the photoisomerization-induced change of the coordination structure. The complex composed of  $\text{ZnCl}_2$  and the monodentate ligand undergoes a photochromic reaction in the crystalline state by alternate irradi-





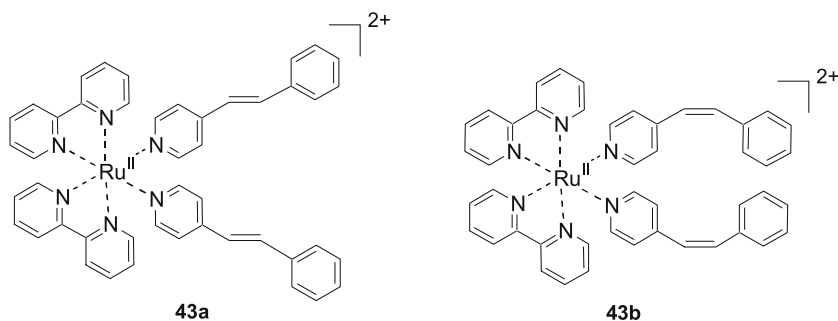
ation with UV and visible light, while crystals of the complex of the bidentate ligand with  $ZnCl_2$  show no photoreactivity [34].

Tian et al. have reported that bis(5-pyridyl-2-methylthien-3-yl)cyclopentene ligand **42** shows enhancement of photochromism by complexation with a  $Zn^{2+}$  ion [35]. They also found that the fluorescent properties, including the intensity and emission peak wavelengths of the compound, can be reversibly regulated by UV-vis light,  $Zn^{2+}$ , and protons [36].

## 4

### Stilbene- and Azobenzene-Attached Complexes

Stilbene and azobenzene cause photoisomerization between *trans* and *cis* forms, and their structures are simple enough to provide many derivatives; thus various combinations with transition metals have been reported.  $Ru^{II}$  complexes with both *trans* and *cis* forms of 4-stilbazole (stpy),  $Ru(bpy)_2(\textit{trans}\text{-stpy})$  (**43a**) and  $Ru(bpy)_2(\textit{cis}\text{-stpy})$  (**43b**) have been synthesized by Whitten et al., and the *trans/cis* ratio ( $D_{ct}$ ) of each in the photo-

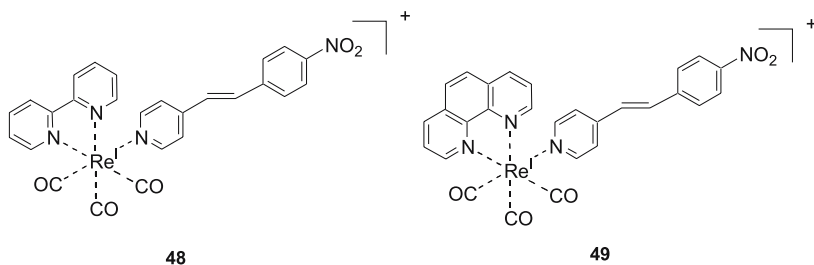
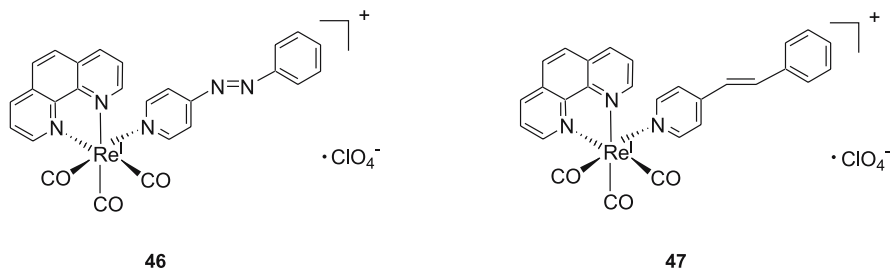
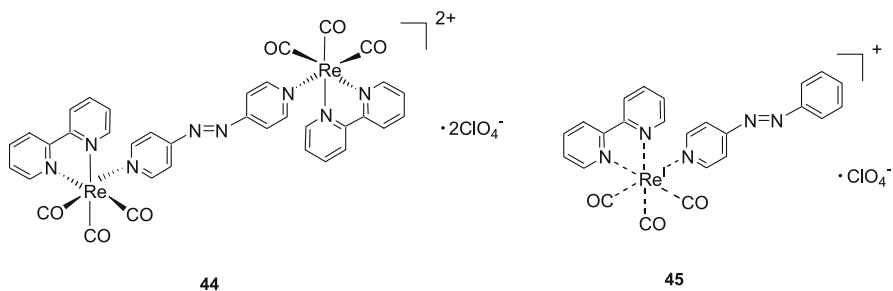


stationary state (PSS) has been examined [37, 38]. A characteristic of these complexes is that they have a metal-to-ligand charge-transfer (MLCT) ( $d-\pi^*$ ) transition in the low-energy region around 340–500 nm. The  $D_{c/t}$  value is 0.96 on photoirradiation at 313 nm, which is not significantly different from the value of 1.36 for free styrylpyridine, because isomerization results from activation of the  $\pi-\pi^*$  band. In the complex, trans-to-cis isomerization with  $D_{c/t}$  equaling 0.04 is observed in response to photoirradiation at 546 nm, where the free ligand has no absorption. This photoreaction is caused by the MLCT transition.

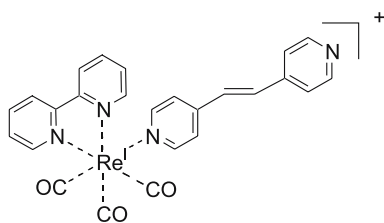
Light-induced excited spin state trapping (LIESST), in which the spin state of the molecule changes between low and high spin states, is an interesting phenomenon for application to photomagnetic memories. Originally, the subject of photo-activation was the ligand-field ( $d-d$ ) transition, but recently a ligand-driven light-induced spin change (LD-LISC) has been discovered. In this phenomenon, photo-activation of a transition of a ligand molecule causes a similar spin transition. A complex with a *trans*-stilbene-containing ligand,  $\text{Fe}^{\text{II}}(4\text{-trans-stpy})_4(\text{NCBPh}_3)_2$  undergoes a thermal low-spin/high-spin transition at 190 K; in contrast, the complex containing the *cis*-ligand retains a high-spin state at any temperature [39]. Light irradiation to this complex at 140 K at 322 nm causes a trans-to-cis isomerization, and this is reversed by 260-nm irradiation.

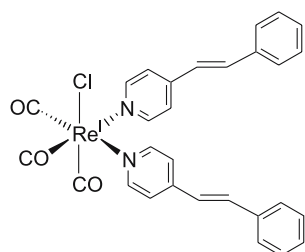
Yam et al. have synthesized compounds, 44–49, in which a luminescent tricarbonyldiiminerhenium(I) unit is bound to a pyridylazo or pyridylvinyl ligand, and they have examined the photochemical and electrochemical properties of these compounds [40–42]. All the complexes except 47 show trans-to-cis isomerization by light irradiation at wavelengths longer than 350 nm. In particular, the quantum yields of the photoreaction are 0.66 and 0.47, respectively, and the cis ratios in PSS are both 74% for 4-(4-nitrostyryl)pyridine (NSP) complexes, 48 and 49. These values are similar to those of free NSP, which has a quantum yield of 0.81 and a cis ratio of ca. 80%. It is also interesting that the quantum efficiency of photoluminescence in the trans form of a phenylazopyridine complex, 46, is  $7.2 \times 10^{-4}$ , whereas it increases to 0.027 in the cis form [40, 41]. This result indicates that isomerization



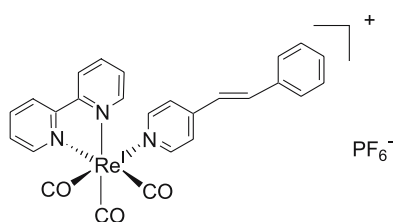


switches the photoluminescence property. Gray and his coworkers have also reported photoswitchable luminescence of different tricarbonyldiiminerhenium(I) complexes, **50** [43]. Vlček et al. have analyzed ultrafast excited-state dynamics preceding a ligand trans-cis isomerization of **51** and **52**, concluding that coordination of the styrylpyridine ligand to the  $\text{Re}^{\text{I}}$  center switches the ligand trans-cis isomerization mechanism from singlet to triplet (intramolec-





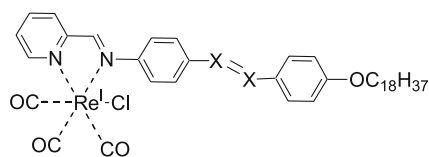
51



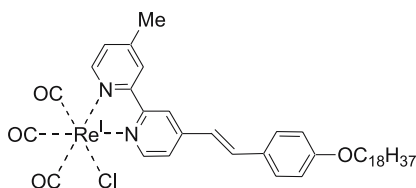
52

ular sensitization) [44]. In the case of **52**, a  $^1\text{MLCT} \rightarrow ^3\text{MLCT}$  intersystem crossing takes place first with a time constant of 0.23 ps, followed by an intramolecular energy transfer from the  $\text{Re}^{\text{I}}(\text{CO})_3\text{-(bpy)}$  chromophore to a ligand  $^3\text{IL}$  state with a 3.5 ps time constant. Photoisomerization phenomena of  $\text{Re}^{\text{I}}$  complexes with long alkyl chains have been investigated by Yam et al. [45]. The isomerization of complex **53** with an azo group is reversed by alternate photoirradiation at 365 and 450 nm light, and that of complex **54** with a stilbene group reverses with alternate photoirradiation at 365 and 254 nm light. Further, it is interesting that complex **55** exhibits isomerization by excitation of the MLCT band at 480 nm. It has been reported that the Langmuir-Blodgett films of these complexes do not show photoisomerization behavior. This inhibition of isomerization is attributed to insufficient free space for the structural change between trans and cis forms to occur.

Tsuchiya has succeeded in controlling intramolecular electron transfer through photoisomerization by employing a molecule in which two tetraphenylporphyrin units (free-base and/or Zn complex) are connected at



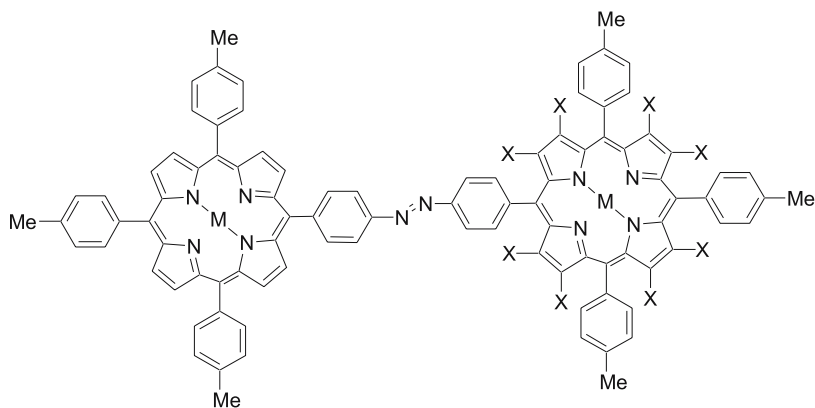
53: X = N, 54: X = CH



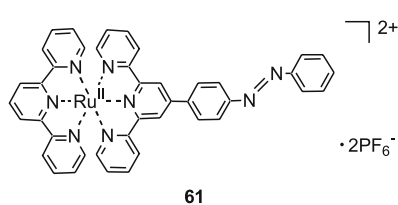
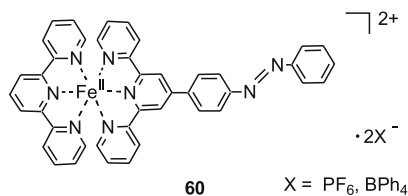
55

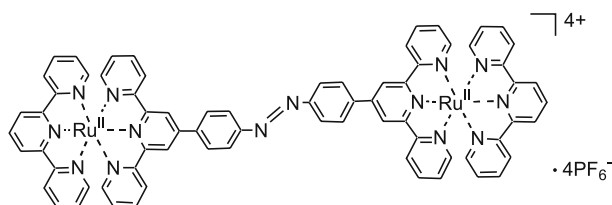
the meso-positions [46]. He prepared two types of diporphyrin compounds, one involving an electron-withdrawing F-substituted porphyrin ring, **56** and **57**, and the other involving two regular porphyrin rings, **58** and **59**. By comparing the physical properties of the two types of compounds, he was able to evaluate the electron transfer between donor and acceptor moieties. He has found that both azo-bridged diporphyrins cause trans-to-cis isomerization at wavelengths shorter than 440 nm, and that the reverse cis-to-trans isomerization occurs thermally. Interestingly, the photoluminescence intensity of the donor-acceptor-type diporphyrins, **56** and **57**, decreases with the transformation into the cis form. Since no similar change was observed in **58** or **59**, this phenomenon can be ascribed to intramolecular electron transfer.

Multi-mode molecular switching properties and functions of azo-conjugated terpyridine complexes of transition metals have been studied [47–49]. The dependences of the photoisomerization behavior on the metal center and its oxidation state were investigated using azobenzene-attached terpyridine complexes of four metals: Fe, Co, Ru, and Rh. As for the Fe<sup>II</sup> and Ru<sup>II</sup> complexes, **60–62**, photoisomerization is totally inhibited when UV light irradiation excites the  $\pi - \pi^*$  band of the azobenzene moiety in the trans form due to the occurrence of energy transfer from the azobenzene unit to the complex unit [50–53].



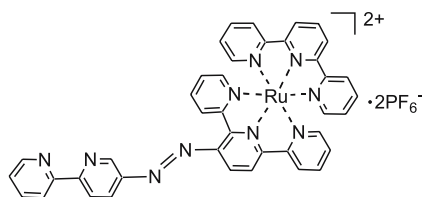
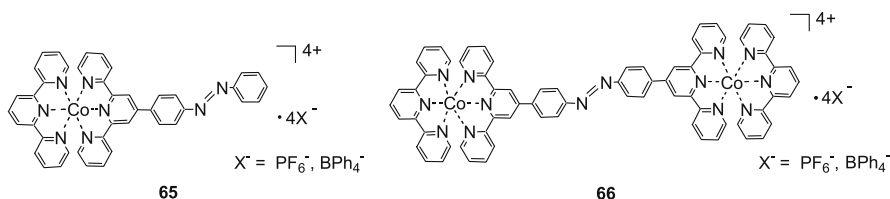
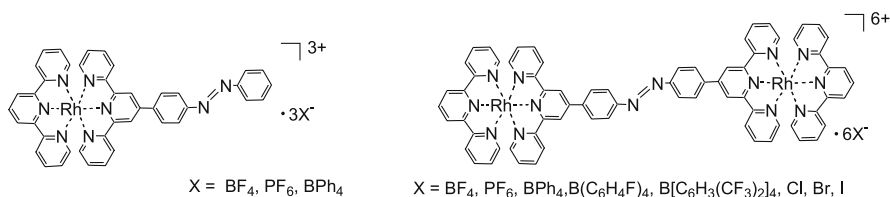
**56:** M = Zn, X = F, **57:** M = H<sub>2</sub>, X = F, **58:** M = Zn, X = H, **59:** M = H<sub>2</sub>, X = H,





In contrast to the group 8 metal (Fe, Ru) complexes, the group 9 metal (Co, Rh) complexes, **63–66**, undergo significant trans-to-cis photoisomerization [50–52], whereas the cis-to-trans photoisomerization, upon excitation of the azo  $n-\pi^*$  transition by 430-nm light irradiation, does not occur for any of the mononuclear and dinuclear Rh complexes, **63** and **64**, and their thermal cis-to-trans isomerization proceeds at a much slower rate than that of the free ligands. The quantum yield of the trans-to-cis photoisomerization for **63** and **64** is much smaller than that of organic azobenzenes, and depends strongly on the counterions and solvents.

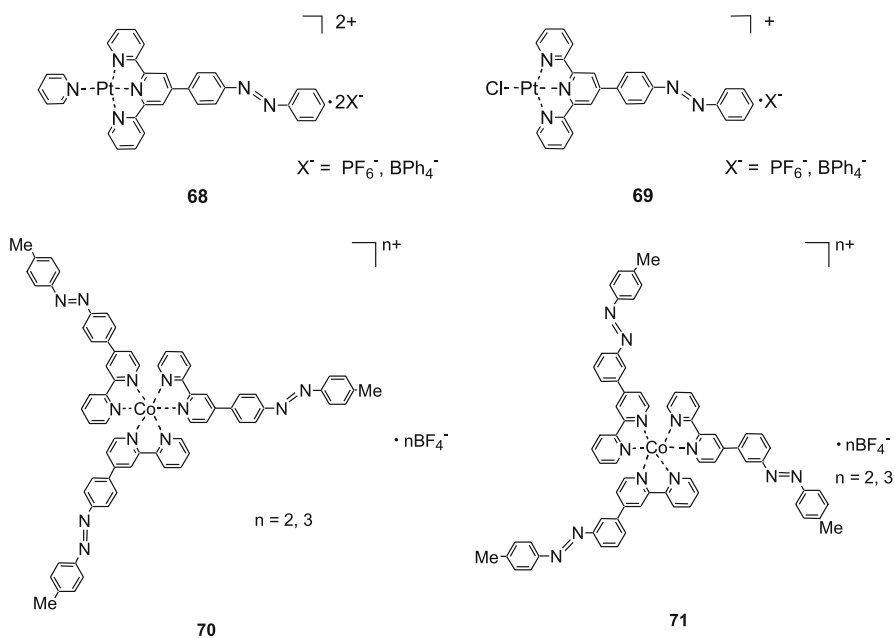
Otsuki et al. have studied electrochemical and optical properties of Ru<sup>II</sup> complexes with azobis(2,2'-bipyridine)s [54]. They have found that not only

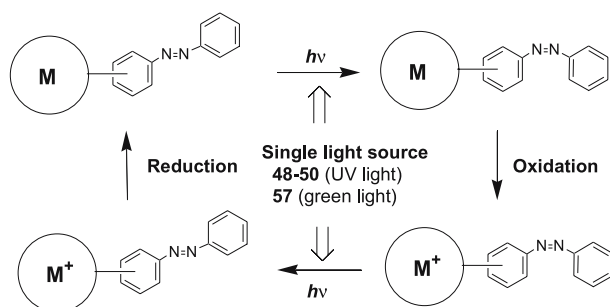


the ligands, but also the mononuclear Ru<sup>II</sup> complex, **67**, isomerize reversibly upon light irradiation, and that the low-energy MLCT state sensitizes the isomerization of the azo moiety in this complex.

Azobenzene-containing Pt<sup>II</sup> complexes, **68** and **69**, for which the emission properties can be switched by delivering photons, were synthesized. Square-planar Pt<sup>II</sup> terpyridine complexes are strongly luminescent in the visible region, with several emission modes due to the intra-ligand  $\pi - \pi^*$  state, the MLCT state, and states originating from intermolecular  $\pi - \pi$  or Pt - Pt interactions in the solid state or in fluid solution [55]. UV-vis spectra of **68** and **69** in DMF exhibit an intense azo  $\pi - \pi^*$  band of the ligand at 350 nm that overlaps with the less intense MLCT bands of the complex unit, and their photoirradiation using 366-nm light causes *trans*-to-*cis* photoisomerization; *cis*-to-*trans* isomerization occurs by either photoirradiation with visible light (wavelength > 430 nm) or by heat. The emission at 600 nm was switched on upon *trans*-to-*cis* photoisomerization of **68** and **69**. The emission lifetime was measured as 40  $\mu$ s, indicating that the emission is assignable to <sup>3</sup>MLCT origin.

The first example of facile reversible *trans*-to-*cis* isomerization of the azo group through a combination of photoirradiation and a redox cycle has been achieved in an azobenzene-attached tris(bipyridine)cobalt system [56–58]. This combination makes possible both forward and backward isomerization in response to irradiation from a single light source (Scheme 1). The Co<sup>II</sup> complex, **70**·2BF<sub>4</sub><sup>-</sup>, with *trans*-azobenzene moieties affords the *cis* form in

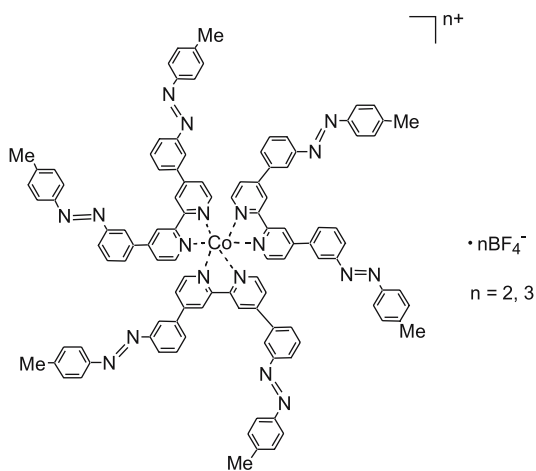




**Scheme 1** Reversible isomerization using a single light source and redox reaction

yield of 40% in PSS upon irradiation with 365-nm light in dichloromethane, and the irradiation with 438-nm light causes *cis*-to-*trans* isomerization. In contrast, the yield of the *cis* form in PSS with 365-nm light irradiation for the  $\text{Co}^{\text{III}}$  complex, **70**· $3\text{BF}_4^-$ , is only 6% [56].

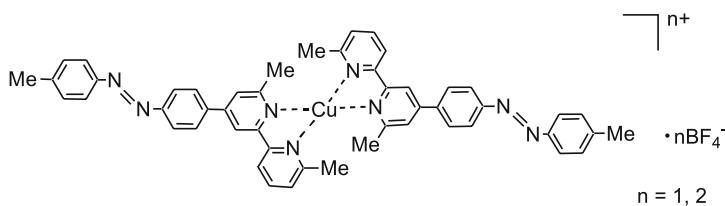
The redox-coupled photoisomerization cycle shown in Scheme 1 was confirmed by the results of a sequence of experiments involving photoirradiation of  $\text{Co}^{\text{II}}$  species with 365-nm light, chemical oxidation from  $\text{Co}^{\text{II}}$  to  $\text{Co}^{\text{III}}$ , photoirradiation with 365-nm light, and chemical reduction, enabling continuous control of total conversion to the *cis* form of azobenzene moieties in PSS within a range of 6–40%. The *trans*-to-*cis* conversion is extended to 9–57% by using the redox reaction in the *meta*-substituted cobalt complex, **71**; an efficient reaction was induced by altering the substitution position between the bipyridine and azo moieties, thereby weakening their electronic interaction [57]. A tris(bipyridine)cobalt complex containing six azobenzene moieties, **72**, also shows redox-conjugated reversible photoisomerization.

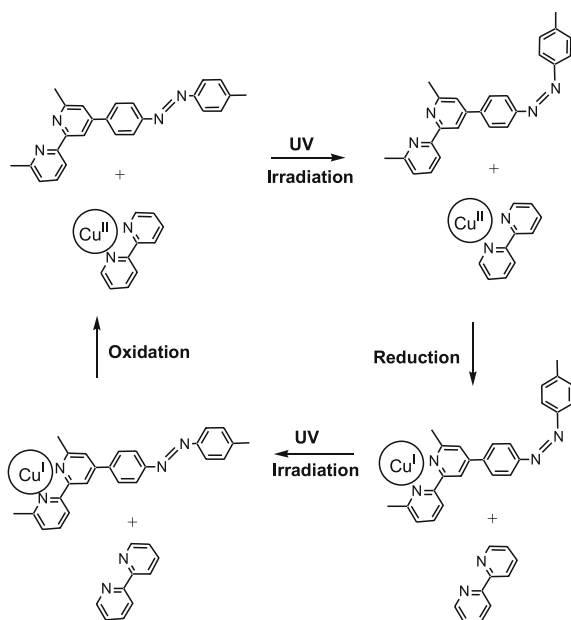


merization using UV light with conversion in the range of 9–54%. There is little cooperation among the photochemical structural changes of six azobenzene moieties in **72**, as investigated with  $^1\text{H}$  NMR spectroscopy, and each azobenzene moiety is isomerized to a cis-isomer with a random probability of 50% [58]. The femtosecond transient absorption spectra of the ligands and the complexes, **71** and **72**, have suggested that the photo-excited states of the azobenzene moieties in the  $\text{Co}^{\text{III}}$  complexes are strongly deactivated by electron-transfer from the azobenzene moiety to the cobalt center to form an azobenzene radical cation and a  $\text{Co}^{\text{II}}$  center [58].

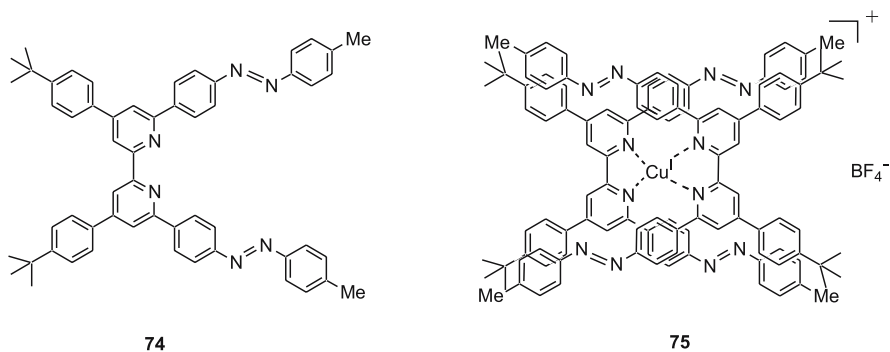
In contrast to Co, which favors the formation of a hexa-coordinate tris(bipyridine) complex, as noted above, Cu gives a tetra-coordinate bis(bipyridine) complex. The redox reaction of this complex is accompanied by a unique structural conversion of the favored geometry from a tetra-coordinate square planar or a penta- or hexa-coordinate structure of  $\text{Cu}^{\text{II}}$  to a tetra-coordinate tetrahedral structure of  $\text{Cu}^{\text{I}}$ . Based on this property of Cu, a molecularly synchronized system, in which the trans-to-cis and cis-to-trans isomerization of azobenzene-attached bipyridine is controlled by its binding/release reaction to copper driven by a  $\text{Cu}^{\text{II}}/\text{Cu}^{\text{I}}$  redox change, was constructed with a 6,6'-dimethyl-substituted, azobenzene-attached bipyridine ligand and its Cu complex, **73** [59]. A mixture of a  $\text{Cu}^{\text{I}}$  complex,  $73 \cdot \text{BF}_4^-$  and 2 equiv of bpy in dichloromethane formed 32% cis isomer by irradiation with 365-nm light, while the cis yield in the UV-light irradiation of the mixture after oxidation to the  $\text{Cu}^{\text{II}}$  state was 70%. These results demonstrate that the isomerization behavior is controllable with a single UV light source and that the ligand's binding/release reaction is reversibly brought about by the  $\text{Cu}^{\text{II}}/\text{Cu}^{\text{I}}$  redox change (Scheme 2).

Another system constructed based on the unique coordination property of Cu is a "molecular photo-electro transducer", which works in a cyclic manner totally powered by light irradiation [60]. The UV/blue light controlled repetitive motion of azobenzene moieties in 6,6'-bis(4''-tolylazo)-4,4'-bis(4-*tert*-butylphenyl)-2,2'-bipyridine, **74**, causes reciprocal  $\text{Cu}^{\text{I}}$  translocation between two coordination environments in complex **75**, resulting in pumping of the redox potential of  $\text{Cu}^{\text{I}}$  (Scheme 3). Therefore, UV/blue light information can be successfully transformed into an electrode potential change and





**Scheme 2** Reversible isomerization using a single UV light source synchronized with redox and ligand-exchange reactions

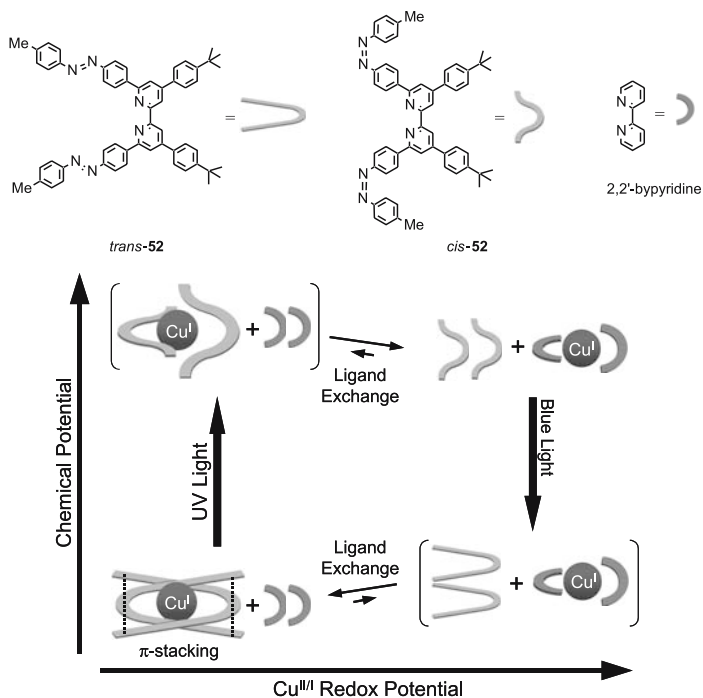


positive/negative current response, which is closely related to natural visual transduction both functionally and mechanically.

Unique photoisomerization behavior of ferrocene-bound stilbene, **76**, has been reported by Kunkely and Vogler [61]. Complex **76** shows two long-wavelength absorptions near 570 and 370 nm, which are assigned to metal-to-ligand charge transfer (MLCT) and intra-ligand charge transfer (ILCT) transitions, respectively. MLCT as well as ILCT excitation leads to a *trans/cis* isomerization at the olefinic double bond.

Azoferrocene, **77**, is a  $\pi$ -conjugated ferrocene dimer and one of the simplest analogues of azobenzene, having two redox-active metal complex units.

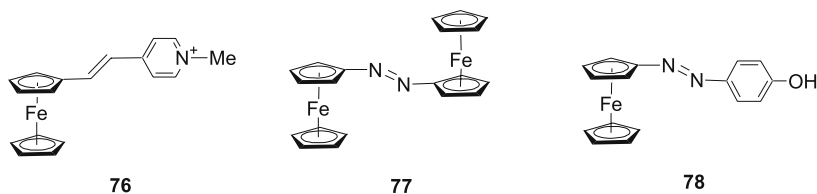




**Scheme 3** A molecular photo-electro transducer

Photoirradiation of **77** in the trans form, *trans-77*, in acetonitrile with 365-nm UV light exciting the  $\pi - \pi^*$  transition, and also with 546 nm green light exciting the metal-to-ligand charge-transfer (MLCT) transition causes a decrease in the intensity of the  $\pi - \pi^*$  band and growth of a new band at 368 nm that shows isosbestic points [62]. It has recently been reported that the presence of trace protons in the photoreaction medium causes an irreversible photoreaction of azoferrocenes [63, 64]. For example, the photoreaction of 4-ferrocenylazophenol (**78**) in ethanol or acetonitrile with a trace amount of water affords a phenylhydrazonocyclopentadiene derivative, indicating that hydrolysis of the photoexcited species has occurred.

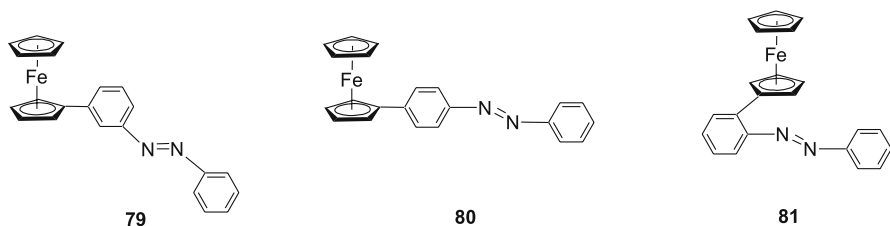
3-Ferrocenylazobenzene, **79**, has been found to be a more stable photoisomerization molecular system sensitive to green light. This compound



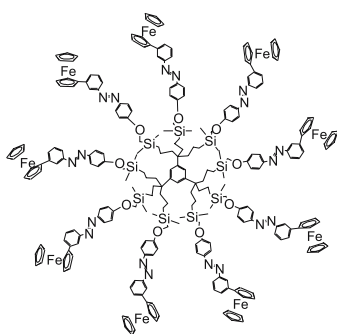
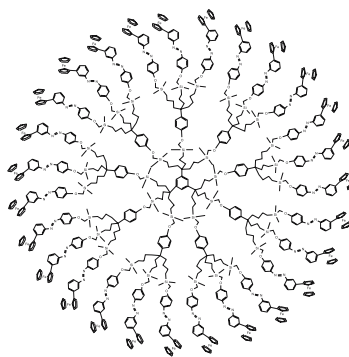
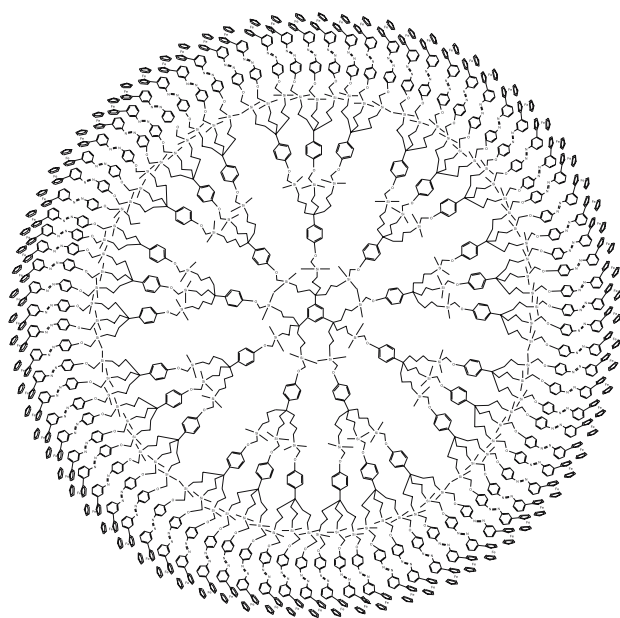
achieves reversible isomerization using a single green light source by combining it with the reversible redox reaction between  $\text{Fe}^{\text{II}}$  and  $\text{Fe}^{\text{III}}$  (Scheme 1) [65].

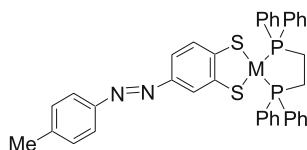
*Trans*-**79** ( $\text{Fe}^{\text{II}}$ ) shows an azo  $\pi - \pi^*$  band at  $\lambda_{\text{max}} = 318 \text{ nm}$  and a less intense visible band at  $444 \text{ nm}$ . The *trans*-to-*cis* isomerization proceeds through both green ( $546 \text{ nm}$ ) and UV ( $320 \text{ nm}$ ) light irradiation, whose wavelengths correspond to an edge of the visible band and the maximum in the azo  $\pi - \pi^*$  band, respectively. The *cis* molar ratio reached 35% and 61% in the PSS upon the green-light and the UV-light irradiation, respectively. The quantum yield for the *trans*-to-*cis* isomerization,  $\Phi_{t \rightarrow c}$ , was estimated to be 0.51 for the green light ( $546 \text{ nm}$ ), which is much higher than that (0.021) for the UV light ( $320 \text{ nm}$ ) and which exceeds that of azobenzene ( $\Phi_{t \rightarrow c} = 0.12$  (313-nm excitation)). The MLCT band diminishes in the UV-vis spectrum of *trans*-**79**<sup>+</sup> ( $\text{Fe}^{\text{III}}$ ), so that its photoisomerization occurs with UV-light irradiation but not the green light irradiation. When an acetonitrile solution of *trans*-**79** ( $\text{Fe}^{\text{II}}$ ) was irradiated with the green light to reach the PSS (35% *cis* molar ratio), followed by a chemical oxidation to the  $\text{Fe}^{\text{III}}$  state, thermal isomerization to the *trans* form proceeded very slowly ( $k = 8.7 \times 10^{-4} \text{ s}^{-1}$  at  $70 \text{ }^\circ\text{C}$ ), while the green light irradiation into the mixture of *trans*- and *cis*-**79**<sup>+</sup> ( $\text{Fe}^{\text{III}}$ ) promoted a change to reach the all-*trans* PSS, suggesting that *cis*-**79**<sup>+</sup> is isomerized to the *trans* form by excitation of the  $n-\pi^*$  band with the green light.

The photoisomerization behavior and the thermal isomerization behavior of ferrocenylazobenzenes are strongly influenced by the substituents on the benzene rings and by the substitution position of the ferrocenyl moiety on the benzene ring [65, 66]. Among the derivatives of **79**, 2-chloro-5-ferrocenylazobenzene exhibits the highest *cis* molar ratio (47%) in the PSS of green light irradiation. 4- and 2-Ferrocenylazobenzenes, **80** and **81**, also respond to green light in addition to UV light exciting the  $\pi-\pi^*$  transition but the *cis* molar ratio in the PSS is lower than that of **79**. The response to green light in **80** and **81** is caused by the MLCT (from  $\text{Fe } d$  orbital to azo  $\pi^*$  orbital) band excitation, while the character of the MLCT band, as estimated by a TD-DFT calculation, differs for **79** and **80**. The oxidized form of **80** undergoes facile *cis*-to-*trans* thermal isomerization. In addition, both **79** and **80** undergo facile protonation and show proton-catalyzed *cis*-to-*trans* isomerization.



A family of 3-ferrocenylazobenzene-attached dendrimers, 9mer (**82**), 27mer (**83**) and 81mer (**84**), which is the first series of redox-active photochromic dendrimers, exhibit photochromism responding to three different light sources, i.e., 365, 436, and 546 nm lights [67]. Decreases in the size of the dendrimers induced by *trans*-to-*cis* photoisomerization appear and become more significant with increases in the size of the dendrimers up to

**82** (9mer)**83** (27mer)**84** (81mer)



**85:** M = Ni

**86:** M = Pd

**87:** M = Pt

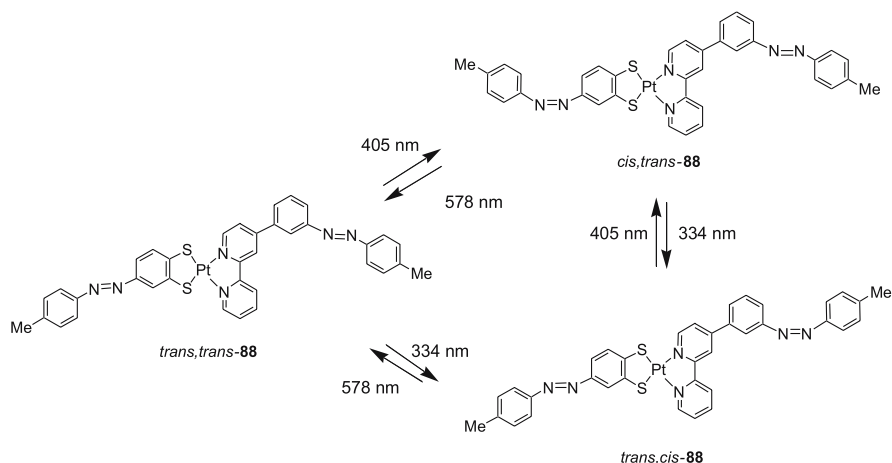
81mer. Electrochemical treatment of the 81mer provides a photo-sensitive and redox-active dendrimer film-coated electrode.

Late transition metal dithiolato complexes possess an aromatic nature, showing reversible redox activity and deep color. The combination of dithiolene complexes of Ni, Pd, and Pt with the azo group, **85–87**, shows reversible photoisomerization and protonation behavior in addition to the protonation-catalyzed *cis*-to-*trans* isomerization of the complexes [68, 69]. The *trans*-to-*cis* isomerization of **85–87** in acetonitrile occurs by irradiation of the transition from metalladithiolene  $\pi$  to azobenzene  $\pi^*$  orbital at  $\lambda_{\max} = 405$  nm ( $\epsilon_{\max} = \text{ca. } 2 \times 10^4 \text{ mol}^{-1} \text{ dm}^3 \text{ cm}^{-1}$ ), whereas the *cis*-to-*trans* isomerization proceeds by photoirradiation at 360 nm in **85**, and at 310 nm in both **86** and **87**. Immediate *cis*-to-*trans* transformations occur when a slight amount of acid is added to a solution containing *cis*-**85–87**.

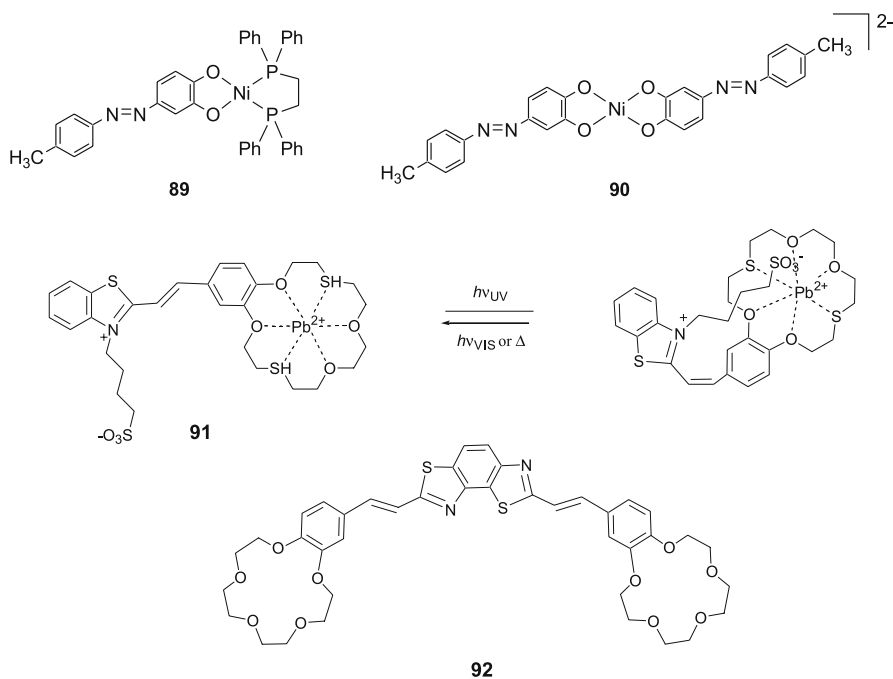
A platinum complex with both an *azo*-bound dithiolato ligand and an azobenzene-bound bipyridine ligand, **88**, was synthesized [70]. This complex exhibits tri-stability which is reversibly controllable using different energy lights. The *trans,trans*-**88** is converted to *trans,cis*-**88** by 334 nm-light irradiation to excite into the  $\pi - \pi^*$  transition of the azobenzene moiety on the bipyridine ligand, and to *cis,trans*-**88** by 405 nm-light irradiation to excite into the  $\pi(\text{dithiolene})-\pi^*(\text{azobenzene})$  transition of the dithiolato ligand. Both *trans,cis*- and *cis,trans*-forms return to *trans,trans*-**88** by irradiation of the MLCT band with 578 nm light (Scheme 4).

An *azo*-conjugated catecholato ligand and its nickel complexes, **89** and **90**, were synthesized, and their physical and chemical properties were investigated [71]. The complex with one *azo*-catecholato ligand, **89**, shows no obvious photo-response, whereas the compound with two *azo*-catecholato ligands, **90**, causes some photoisomerization. Both complexes show remarkable proton responses.

Crown ether-bound styryl dyes have been studied by Fedorova and her coworkers. The photochromic properties of the dyes, **91**, are based on reversible *trans*-*cis* isomerization and [2 + 2]-photocycloaddition. They exhibit a strong preference for formation of complexes with heavy metal ions [72]. Due to its specific structure, the betaine-type dye is able to form an “anion-capped” *trans*-isomer. Intramolecular coordination in the “anion-capped” isomer enhances its stability and causes a sharp deceleration of its dark *trans*-



**Scheme 4** Tri-stable photochromism with three-color light



*cis* isomerization [73]. A large ionochromic effect and fluorescence quenching on complex formation with alkaline-earth metal cations have been found for 2-styrylbenzothiazole containing a phenylazacrown ether moiety. However, considerable distinctions in the spectral properties of the photoisomers and their ability to form a complex were not found [74]. A benzo[1,2-*d*:3,4-*d'*]bisthiazole derivative with two crown ethers, **92**, forms relatively strong

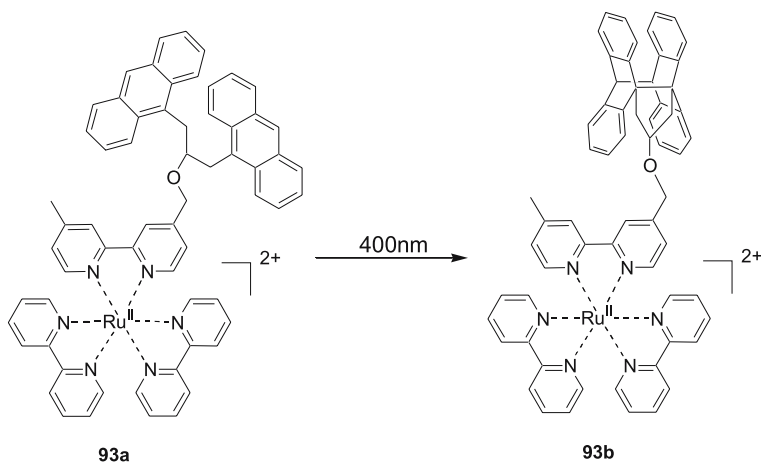
2 : 2 stoichiometric complexes with  $K^+$ , among the alkali metal cations, and  $Ba^{2+}$ , among the alkaline earth metal cations [75].

Einaga and his coworkers have presented photo-controllable molecular systems, salts of  $[M(en)_2][Pt(en)_2Cl_2]^{4+}$  ( $M^{2+} = Pt^{II}, Pd^{II}$  and en = ethylenediamine) and 4-[4-(*N*-methyl-*N*-*n*-dodecylamino)phenylazo]benzene sulfonate ions, which have been designed by the self-assembly of chloride-bridged platinum/palladium complexes [76]. Reversible structural changes caused by *cis*-*trans* photoisomerization of azo groups in the compounds occur by alternating irradiation of UV and visible light. Visible light irradiation causes a *trans*-to-*cis* isomerization of the azo group, leading to the formation of plate-like structures, whereas UV light irradiation causing *cis*-to-*trans* isomerization does fragmentation of the assembling structures. This fragmentation brings about reversible changes in the electronic states of the chloride-bridged platinum/palladium complexes; the plate-like structures exhibit CT absorption of chloride-bridged platinum complexes and delocalized  $Pt^{II}/Pt^{IV}$  states, while the fragments of the separated complexes exhibit no CT bands.

## 5

### Other Systems Using Organic Photochromic Molecules

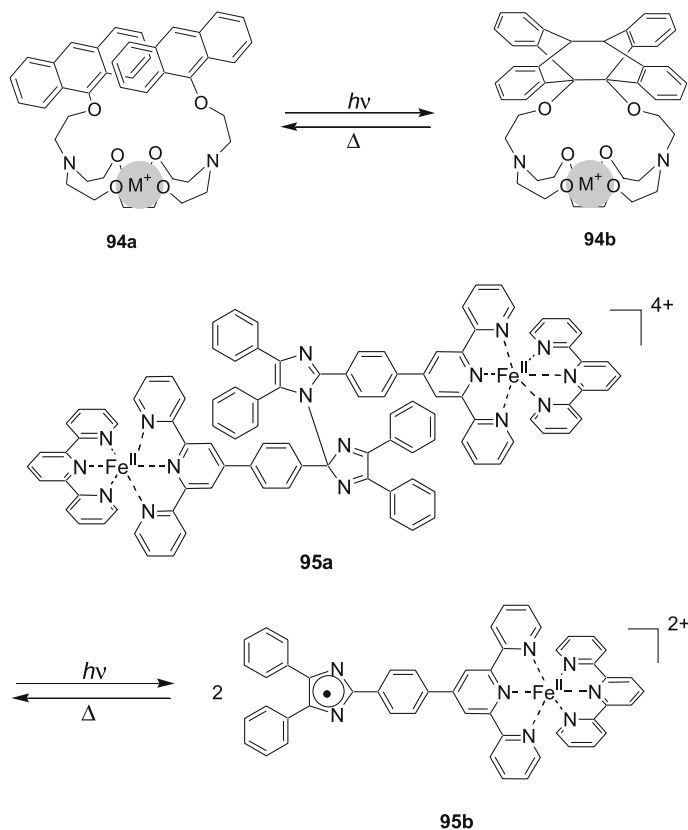
Several kinds of organic molecules are known to undergo dimerization or its reverse reaction by photoirradiation. Castellano et al. have shown that the coupling of the irreversible dianthryl photo-dimerization to the  $Ru^{II}$  complex emission using **93** permits nondestructive photoluminescence read-out of binary information photochemically recorded at the molecular level in a polystyrene matrix [77, 78]. McSkimming et al. have reported an aza-

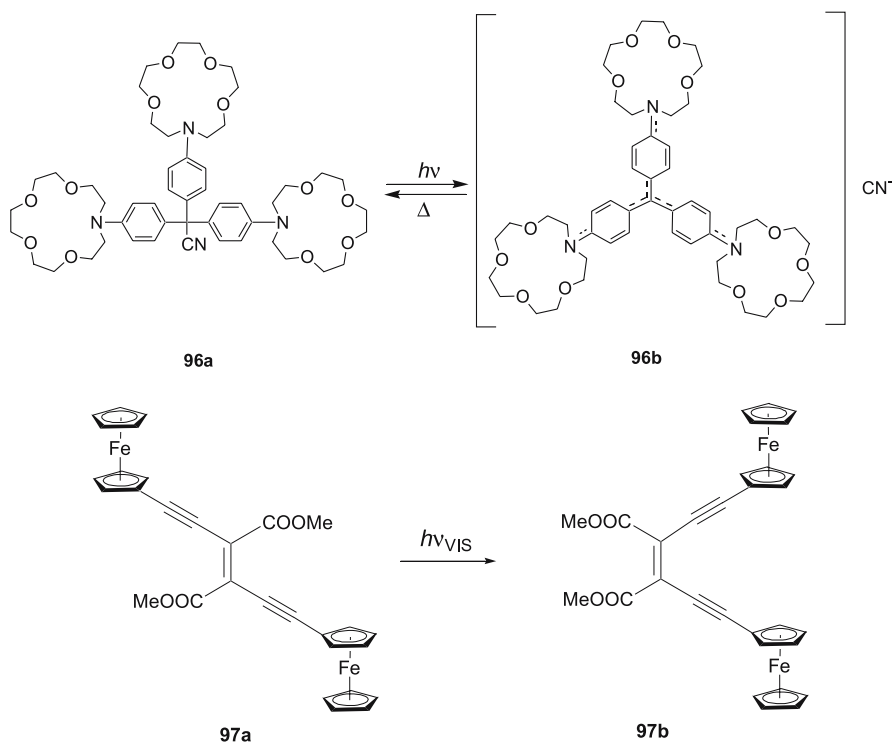


crown ether with anthracene-containing pendant arms, **94**, which shows a reversible intramolecular  $[4\pi + 4\pi]$  cycloaddition reaction upon irradiation at  $\lambda > 300$  nm [79]. This crown ether forms complexes of 1 : 1 stoichiometry with cations, and the above photochromic process is cation-dependent; in particular, the rate of the thermal reverse reaction is decreased by smaller cations and increased by larger cations, especially  $\text{Rb}^+$ .

A  $\text{Fe}^{\text{II}}$  complex of a photochromic ligand, bis(terpyridyl)hexaarylbiimidazole (bistpy-HABI) **95**, was synthesized, and its photochromic cleavage into a pair of terpyridyltriphenylimidazolyl radicals on irradiation with UV light was studied by Abe and his coworkers [80]. The triplet state of the light-induced radical pair from **95**, as well as that from the free ligand, was confirmed to be a ground state or nearly degenerated with a singlet state. The first observation of a decrease in activation energy of the radical recombination reaction by the formation of a metal-coordinated radical complex was reported.

Kimura et al. have reported a dramatic conformational change of a Crystal Violet derivative with three crown ether moieties, **96**, on its cesium-ion





complexation, which decelerates the photochemical reaction of the crystal violet [81].

It has been recently reported that the *E*-form of bis(ferrocenylethynyl)ethane, **97a**, can undergo photoisomerization to the *Z*-form, **97b**, by excitation of a charge transfer band with visible light [82]. This structural change affords a decrease in the “through bond” mixed-valence interaction between two ferrocenes.

## 6 Concluding Remarks

We have described herein different single-molecule systems combining photochromic molecular units and metal complex units. These systems show unique behaviors that have not been seen in common organic photochromic compounds. Table 1 summarizes such behaviors and phenomena. The findings regarding photochromic metal complexes denote the creation of new types of photo-responsive materials having multi-mode functions via properly designed communication between photochromic molecules and metal complexes. These materials will be useful for the development of chemosen-



**Table 1** New functions developed in photochromic metal complexes

Metal complex properties	Developed functions	Refs.
<i>Control of isomerization with a metal complex moiety</i>		
Complexation	Durable memory	[4, 5, 13, 15, 22]
	Positive/negative photochromism	[10]
Ligand exchange	Single-light isomerization	[59]
Redox reaction	Single-light isomerization	[56–59, 65]
CT excitation	Isomerization with low photon energy	[20, 21, 28–30, 37]
	Site-selective isomerization	[38, 54, 61, 65]
Electron donation	Proton-catalyzed isomerization	[70]
Bulkiness	Irreversible isomerization	[68, 69]
<i>Tuning of metal complex properties with photoisomerization</i>		
Photoluminescence	Luminescence on/off	[25, 26, 29, 40, 42, 43, 55]
Redox reaction	Photo-electron transfer	[60]
Ligand exchange	Photo-transduction	[60]
Magnetic properties	Spin–spin interaction tuning	[32]
	LD-LISC	[39]
Complexation	Ion sensing	[8, 11, 18, 19, 79]
Mixed valence state	Electron mobility tuning	[27, 82]
	Photo-controlled 1D-chain structure	[76]
Photo-induced electron transfer	Electron mobility tuning	[46, 76]

sors, and also multi-mode switching and information storage systems at the molecular level.

## References

- Irie M (ed) (2000) Chem Rev 100:1683
- Joachim C, Gimzewski JK, Aviram A (2000) Nature 408:541
- Phillips JP, Mueller A, Przystal F (1965) J Am Chem Soc 87:4020
- Wojtyk JTC, Kazmaier PM, Buncel E (2001) Chem Mater 13:2547
- Wojtyk JTC, Kazmaier PM, Buncel E (1998) Chem Commun, p 1703
- Chibisov AK, Görner H (1998) Chem Phys 237:435
- Atabekyan LS (2002) High Energy Chemistry 36:397
- Collins GE, Choi L-S, Ewing KJ, Michelet V, Bowen CM, Winkler JD (1999) Chem Commun 321
- Evans L, Collins GE, Shaffer RE, Michelet V, Winkler JD (1999) Anal Chem 71:5322

10. Tanaka M, Nakamura M, Salhin MAA, Ikeda T, Kamada K, Ando H, Shibutani Y, Kimura K (2001) *J Org Chem* 66:1533
11. Keiichi K, Sakamoto H, Kado S, Arakawa R, Yokoyama M (2000) *Analyst* 125:1091
12. Kimura K, Sakamoto H, Uda RM (2004) *Macromolecules* 37:1871
13. Nagashima S, Murata M, Nishihara H (2006) *Angew Chem Int Ed* 45:4298
14. Strokach YP, Fedorova OA, Gromov SP, Koshkin AV, Valova TM, Barachevsky VA, Alfimov MV, Lokshin VA, Samat A, Guglielmetti R (2002) *Russ Chem Bull* 51:58
15. Jeliaskova BG, Minkovska S, Deligeorgiev T (2005) *J Photochem Photobiol A: Chem* 171:153
16. Minkovska S, Fedieva M, Jeliaskova B, Deligeorgiev T (2004) *Polyhedron* 23:3147
17. Bulanov AO, Luk'yanov BS, Kogan VA, Stankevich NV, Lukov VV (2002) *Russ J Coord Chem* 28:46
18. Ushakov EN, Nazarov VB, Fedorova OA, Gromov SP, Chebun'kova AV, Alfimov MV, Barigelletti F (2003) *J Phys Org Chem* 16:306
19. Ahmed SA, Tanaka M, Ando H, Iwamoto H, Kimura K (2004) *Tetrahedron* 60:3211
20. Yam VW-W, Ko C-C, Wu L-X, Wong KM-C, Cheung K-K (2000) *Organometallics* 19:1820
21. Ko C-C, Wu L-X, Wong KM-C, Zhu N, Yam VW-W (2004) *Chem Eur J* 10:766
22. Yuan W, Sun L, Tang H, Wen Y, Jiang G, Huang W, Jiang L, Song Y, Zhu D (2005) *Adv Mater* 17:156
23. Irie M, Mohri M (1988) *J Org Chem* 53:803
24. Irie M (2000) *Chem Rev* 100:1685
25. Fernández-Acebes A, Lehn J-M (1998) *Adv Mater* 10:1519
26. Fernández-Acebes A, Lehn J-M (1999) *Chem Eur J* 5:3285
27. Frayse S, Coudret C, Launay J-P (2000) *Eur J Inorg Chem* 1581
28. Jukes RTF, Adamo V, Hartl F, Belsler P, De Cola L (2004) *Inorg Chem* 43:2779
29. Yam VW-W, Ko C-C, Zhu N (2004) *J Am Chem Soc* 126:12734
30. Ko C-C, Kwok W-M, Yam VW-W, Phillips DL (2006) *Chem Eur J* 12:5840
31. Konaka H, Wu LP, Munakata M, Kuroda-Sowa T, Maekawa M, Suenaga Y (2003) *Inorg Chem* 42:1928
32. Takayama K, Matsuda K, Irie M (2003) *Chem A Eur J* 9:5605
33. Matsuda K, Takayama K, Irie M (2004) *Inorg Chem* 43:482
34. Matsuda K, Shinkai Y, Irie M (2004) *Inorg Chem* 43:3774
35. Qin B, Yao R, Zhao X, Tian H (2003) *Org Biomol Chem* 1:2187
36. Tian H, Qin B, Yao R, Zhao X, Yang S (2003) *Adv Mater* 15:2104
37. Zarnegar PP, Whitten DG (1971) *J Am Chem Soc* 93:3776
38. Zarnegar PP, Bock CR, Whitten DG (1973) *J Am Chem Soc* 95:4367
39. Boillot M-L, Roux C, Audière J-P, Dausse A, Zarembowitch J (1996) *Inorg Chem* 35:3975
40. Yam VW-W, Lau VC-Y, Cheung K-K (1995) *J Chem Soc Chem Commun*, p 259
41. Yam VW-W, Lau VC-Y, Cheung K-K (1995) *J Chem Soc Chem Commun*, p 1195
42. Yam VW-W, Lau V C-Y, Wu L-X (1998) *Dalton Trans* 1461
43. Wenger OS, Henling LM, Day MW, Winkler JR, Gray HB (2004) *Inorg Chem* 43:2043
44. Busby M, Matousek P, Towrie M, Vlček A Jr (2005) *J Phys Chem A* 109:3000
45. Yam VW-W, Yang Y, Zhang J, Chu BW-K, Zhu N (2001) *Organometallics* 20:4911
46. Tsuchiya S (1999) *J Am Chem Soc* 121:48
47. Kurihara M, Nishihara H (2002) *Coord Chem Rev* 226:125
48. Nishihara H (2004) *Bull Chem Soc Jpn* 77:407
49. Nishihara H (2005) *Coord Chem Rev* 249:1468
50. Yutaka T, Kurihara M, Nishihara H (2000) *Mol Cryst Liq Cryst* 343:193

51. Yutaka T, Kurihara M, Kubo K, Nishihara H (2000) *Inorg Chem* 39:3438
52. Yutaka T, Mori I, Kurihara M, Mizutani J, Kubo K, Furusho S, Matsumura K, Tamai N, Nishihara H (2001) *Inorg Chem* 40:4986
53. Yutaka T, Mori I, Kurihara M, Tamai N, Nishihara N (2003) *Inorg Chem* 42:6306
54. Otsuki J, Omokawa N, Yoshiba K, Yoshikawa I, Akasaka T, Suenobu T, Takido T, Araki K, Fukuzumi S (2003) *Inorg Chem* 42:3057
55. Yutaka T, Mori I, Kurihara M, Mizutani J, Tamai N, Kawai T, Irie M, Nishihara H (2002) *Inorg Chem* 41:7143
56. Kume S, Kurihara M, Nishihara H (2001) *Chem Commun* 1656
57. Kume S, Kurihara M, Nishihara H (2002) *J Korean Electrochem Soc* 5:189
58. Yamaguchi K, Kume S, Namiki K, Murata M, Tamai N, Nishihara H (2005) *Inorg Chem* 44:9056
59. Kume S, Kurihara M, Nishihara H (2003) *Inorg Chem* 42:2194
60. Kume S, Murata M, Ozeki T, Nishihara H (2005) *J Am Chem Soc* 127:490
61. Kunkely H, Vogler A (2001) *J Organomet Chem* 637–639:777
62. Kurihara M, Matsuda M, Hirooka A, Yutaka T, Nishihara H (2000) *J Am Chem Soc* 122:12373
63. Kurihara M, Matsuda T, Hirooka A, Yutaka T, Nishihara H (2004) *J Am Chem Soc* 126:4740
64. Men Y, Korupoju SR, Kurihara M, Mizutani J, Nishihara H (2005) *Chem Eur J* 11:7322
65. Kurihara M, Hirooka A, Kume S, Sugimoto M, Nishihara H (2002) *J Am Chem Soc* 124:8800
66. Sakamoto A, Hirooka A, Namiki K, Kurihara M, Murata M, Sugimoto M, Nishihara H (2005) *Inorg Chem* 44:7547
67. Daniel M-C, Sakamoto A, Ruiz J, Astruc D, Nishihara H (2006) *Chem Lett* 35:38
68. Nihei M, Kurihara M, Mizutani J, Nishihara H (2001) *Chem Lett* 852
69. Nihei M, Kurihara M, Mizutani J, Nishihara H (2003) *J Am Chem Soc* 125:2964
70. Sakamoto R, Murata M, Kume S, Sampei H, Sugimoto M, Nishihara H (2005) *Chem Commun*, p 1215
71. Nagashima S, Nihei M, Yamada T, Murata M, Kurihara M, Nishihara H (2003) *Macromol Symp* 204:93
72. Fedorova OA, Fedorov YV, Vedernikov AI, Gromov SP, Yescheulova OV, Alfimov MV, Woerner M, Bossmann S, Braun A, Saltiel J (2002) *J Phys Chem A* 106:6213
73. Fedorova OA, Fedorov YV, Vedernikov AI, Yescheulova OV, Gromov SP, Alfimov MV, Kuz'mina LG, Churakov AV, Howard JAK, Zaitsev SY, Sergeeva TI, Moebius D (2002) *New J Chem* 26:543
74. Fedorov YV, Fedorova OA, Gromov SP, Bobrovskii MB, Andryukhina EN, Alfimov MV (2002) *Russ Chem Bull* 51:789
75. Fedorov YV, Fedorova O, Schepel N, Alfimov M, Turek AM, Saltiel J (2005) *J Phys Chem A* 109:8653
76. Einaga Y, Mikami R, Akitsu T, Li G (2005) *Thin Solid Films* 493:230
77. Tyson DS, Bignozzi CA, Castellano FN (2002) *J Am Chem Soc* 124:4562
78. Ferri V, Scoptoni M, Bignozzi CA, Tyson DS, Castellano FN, Doyle H, Redmond G (2004) *Nano Lett* 4:835
79. McSkimming G, Tucker JHR, Bouas-Laurent H, Desvergne J-P, Coles SJ, Hursthouse MB, Light ME (2002) *Chem A Eur J* 8:3331
80. Miyamoto Y, Kikuchi A, Iwahori F, Abe J (2005) *J Phys Chem A* 109:10183
81. Uda RM, Oue M, Kimura K (2002) *J Supramol Chem* 2:311
82. Sakamoto R, Murata M, Nishihara H (2006) *Angew Chem Int Ed* 45:4793

# Transition Metal Complexes for Photovoltaic and Light Emitting Applications

M. K. Nazeeruddin (✉) · M. Grätzel

Laboratory for Photonics and Interfaces,  
Institute of Molecular and Biological Chemistry, School of Basic Sciences,  
Swiss Federal Institute of Technology, 1015 Lausanne, Switzerland  
*MdKhaja.Nazeeruddin@epfl.ch*

<b>1</b>	<b>Dye-Sensitized Solar Cells</b> . . . . .	114
1.1	History of Dye Sensitization . . . . .	114
1.2	Operating Principles of the Dye-Sensitized Solar Cell . . . . .	116
1.3	Device Fabrication . . . . .	117
1.4	Incident Photon to Current Efficiency and Open Circuit Photovoltage . . . . .	119
1.5	Molecular Sensitizers . . . . .	120
1.5.1	Modulation of Sensitizer's Spectral Response . . . . .	122
1.6	Surface Chelation of Polypyridyl Complexes onto the TiO <sub>2</sub> Oxide Surface . . . . .	136
1.6.1	Acid–Base Equilibria of <i>cis</i> -Dithiocyanato Bis(2,2'-bipyridine-4,4'-dicarboxylate)Ru(II) Complex(2) . . . . .	138
1.7	Photovoltaic Properties . . . . .	139
1.7.1	Effect of Protons Carried by the Sensitizer on the Performance . . . . .	139
1.7.2	Comparison of IPCE Obtained with Various Sensitizers . . . . .	141
1.7.3	Solid State Dye-Sensitized Solar Cells . . . . .	142
1.8	Stability . . . . .	144
1.9	Pilot Production of Modules, Outdoor Field Tests and Commercial DSC Development . . . . .	146
1.9.1	Outlook . . . . .	149
<b>2</b>	<b>Iridium Complexes as Triplet Emitters in Organic Light-Emitting Diodes</b> . . . . .	149
2.1	Introduction . . . . .	149
2.2	Photophysical Properties . . . . .	150
2.3	Tuning of Phosphorescence Colors in Neutral Iridium Complexes . . . . .	151
2.4	Tuning of Phosphorescence Colors in Cationic Iridium Complexes . . . . .	154
2.5	Tuning of Phosphorescence Colors in Anionic Iridium Complexes . . . . .	158
2.5.1	Phosphorescent Color Shift in Anionic Iridium Complexes by Tuning of HOMO Levels . . . . .	161
2.6	Controlling Quantum Yields in Iridium Complexes . . . . .	163
2.7	Application of Iridium Complexes in Organic Light Emitting Devices . . . . .	164
2.7.1	Standard OLED Device Architecture . . . . .	165
2.8	Light-Emitting Electrochemical Cell Device Architecture . . . . .	170
	<b>References</b> . . . . .	171

**Abstract** The aim of this chapter is to give an in-depth analysis of transition metal complexes that are useful in conversion of solar energy into electricity, and in organic light emitting diodes. In the first part we discuss the historical background of sensitization

phenomenon, operating principles of dye-sensitized solar cells, tuning of photophysical and electrochemical properties of sensitizers, evolution of photovoltaic performance, present status and future prospects for dye-sensitized solar cells. In the second part, we elucidate the modulation of phosphorescent color and quantum yields in neutral, cationic, and anionic iridium complexes and their application in light emitting devices.

**Keywords** Dye-sensitized solar cells · Iridium triplet emitters · Light emitting electrochemical cells · OLED · Photovoltaic · Ruthenium sensitizers

### Abbreviations

CIGS	Copper indium gallium selenide
dcbiq	4,4'-Dicarboxy-2,2'-biquinoline
dcbpy	4,4'-Dicarboxy-2,2'-bipyridine
DSC	Dye-sensitized solar cell
Fc <sup>+ / 0</sup> )	Ferrocenium/ferrocene
FF	Fill factor
HOMO	Highest occupied molecular orbitals
IPCE	Incident monochromatic photon-to-current conversion efficiency
LUMO	Lowest unoccupied molecular orbitals
MLCT	Metal-to-ligand charge transfer
OLED	Organic light emitting diode
ppy	2-Phenylpyridine
SCE	Saturated calomel electrode
UV-Vis	Ultraviolet-visible
$J_{sc}$	Short circuit current
$V_{oc}$	Open-circuit potential

## 1

### Dye-Sensitized Solar Cells

#### 1.1

##### History of Dye Sensitization

The history of the sensitization of semiconductors to light of wavelength longer than that corresponding to the band gap is an interesting convergence of photography and photoelectrochemistry, both of which rely on photoinduced charge separation at a liquid–solid interface [1]. The silver halides used in photography have band gaps of the order of 2.7–3.2 eV and are therefore insensitive towards much of the visible spectrum, as are the metal oxide films now used in dye-sensitized solar cells.

The first panchromatic film, able to render the image of a scene realistically into black and white, followed on the work of Vogel in Berlin after 1873, [2] in which he associated dyes with the halide semiconductor grains. The first sensitization of a photoelectrode was reported shortly thereafter, using a similar chemistry [3]. However, the clear recognition of the parallels between the

two procedures – a realization that the same dyes in principle can function in both systems [4] and a verification that their operating mechanism is by injection of electrons from photoexcited dye molecules into the conduction band of the n-type semiconductor substrates – date to the 1960s [5]. In subsequent years the idea developed that the dye could function most efficiently if chemisorbed on the surface of the semiconductor [6, 7]. The concept of using dispersed particles to provide a sufficient interface area emerged [8], and was subsequently employed for photoelectrodes [9].

Titanium dioxide became the semiconductor of choice for the photoelectrode. The material has many advantages for sensitized photochemistry and photoelectrochemistry: it is a low cost, widely available, nontoxic and biocompatible material, and as such is even used in health care products as well as in domestic applications such as paint pigmentation. Initial studies employed  $[\text{Ru}(4,4'\text{-dicarboxylic acid } 2,2'\text{-bipyridine ligand})_3]$  (1) as the sensitizer for photochemical studies. Progress thereafter, until the announcement in 1991 [10] of a sensitized electrochemical photovoltaic device with a conversion efficiency of 7.1% under solar illumination, was incremental, through the combining of a synergy of structure, substrate roughness and morphology, dye photophysics, and electrolyte redox chemistry. That evolution has continued progressively since then, with certified efficiencies now over 11% [11].

The dye-sensitized solar cell technology developed at the EPFL contains broadly five components:

1. Conductive mechanical support
2. Semiconductor film
3. Sensitizer
4. Electrolyte containing  $\text{I}^-/\text{I}_3^-$  redox couple
5. Counter electrode with a triiodide reduction catalyst

A cross-section of the dye-sensitized solar cell is shown in Fig. 1. The total efficiency of the dye-sensitized solar cell depends on the optimization and compatibility of each of these constituents [12]. To a large extent, the nanocryst-

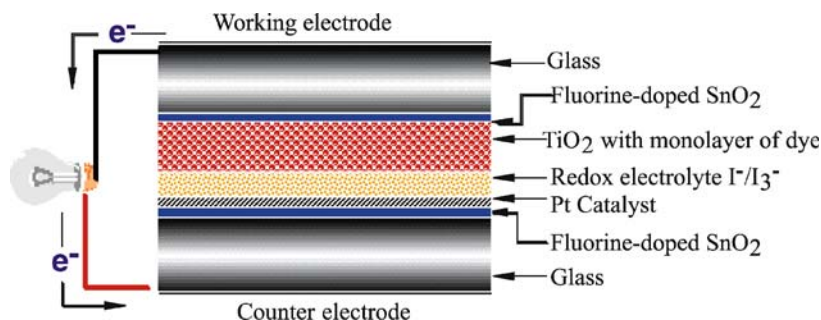


**Fig. 1** Schematic representation of the cross-section of a dye-sensitized solar cell

talline semiconductor film technology along with the dye spectral responses is mainly responsible for the high efficiency [12]. A way to successfully trap solar radiation is by a sensitizer molecule anchored to a rough titania surface, analogous to the light-absorbing chlorophyll molecule found in the nature. The high surface area and the thickness of the semiconductor film yield increased dye optical density resulting in efficient light harvesting [13].

## 1.2

### Operating Principles of the Dye-Sensitized Solar Cell

The details of the operating principles of the dye-sensitized solar cell are given in Fig. 2. The photoexcitation of the metal-to-ligand charge transfer (MLCT) of the adsorbed sensitizer (Eq. 1) leads to injection of electrons into the conduction band of the oxide (Eq. 2). The oxidized dye is subsequently reduced by electron donation from an electrolyte containing the iodide/triiodide redox system (Eq. 3). The injected electron flows through the semiconductor network to arrive at the back contact and then through the external load to the counter

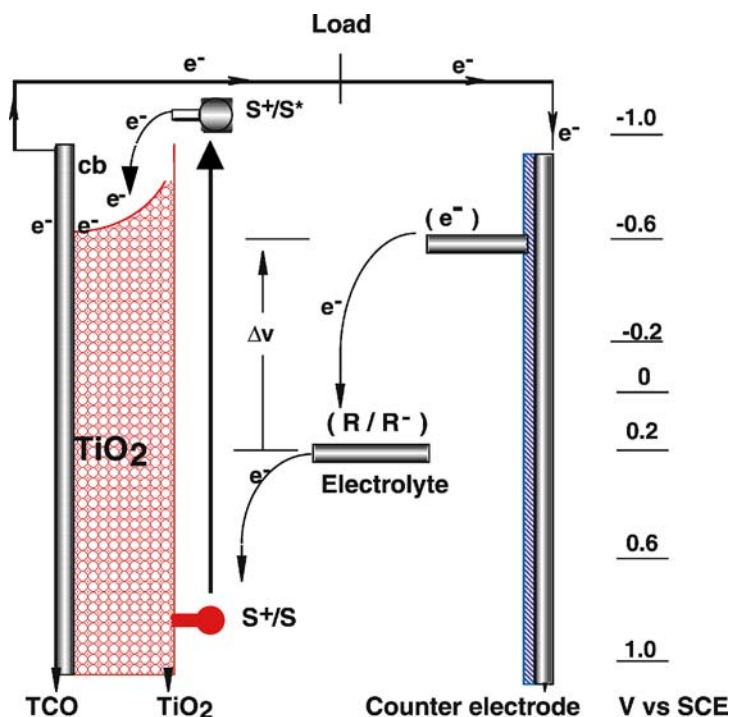
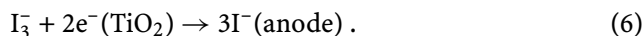
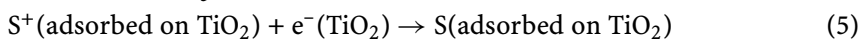
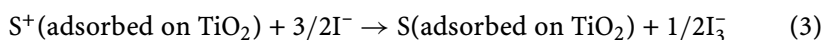
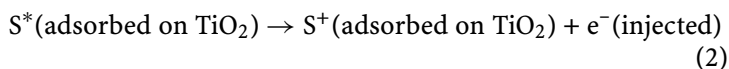
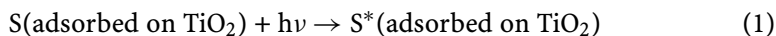


**Fig. 2** Operating principles and energy level diagram of dye-sensitized solar cell. S/S<sup>+</sup>/S\* represent the sensitizer in the ground, oxidized, and excited state, respectively. R/R<sup>-</sup> represent the redox mediator (I<sup>-</sup>/I<sub>3</sub><sup>-</sup>)

electrode. At the counter electrode, reduction of triiodide in turn regenerates iodide (Eq. 4), which completes the circuit. With a closed external circuit and under illumination, the device then constitutes a photovoltaic energy conversion system, which is regenerative and stable. However, there are undesirable reactions, which are that the injected electrons may recombine either with oxidized sensitizer (Eq. 5) or with the oxidized redox couple at the TiO<sub>2</sub> surface (Eq. 6), resulting in losses in the cell efficiency.



At the heart of the system is a mesoporous oxide layer composed of nanometer-sized particles, which have been sintered together to allow electronic conduction to take place. The material of choice has been TiO<sub>2</sub> (anatase) although alternative wide band gap oxides such as ZnO, SnO<sub>2</sub> and Nb<sub>2</sub>O<sub>5</sub> have also been investigated. Attached to the surface of the nanocrystalline film is a monolayer of a sensitizer. The high surface area of the mesoporous metal oxide film is critical to efficient device performance as it allows strong absorption of solar irradiation to be achieved by only a monolayer of adsorbed sensitizer. The use of a dye monolayer avoids any requirement for excited state (or “exciton”) diffusion to the dye/metal oxide interface. It also avoids the acceleration in non-radiative excited state decay to ground state that is often associated with thicker molecular films. The use of a mesoporous film results in a dramatic enhancement of the interfacial surface area by more than 1000-fold for a 10 nm thick film. This leads to high visible light absorbance from the monolayer of adsorbed dye (a dye monolayer adsorbed to a flat interface exhibits only negligible light absorption as the optical absorption cross-sectional area for molecular dyes are typically two to three orders of magnitude smaller than their physical cross-sections). The high surface area of such mesoporous films does however have a significant downside, as it also enhances interfacial charge recombination losses, a topic we return to in more detail in Sect. 1.5.1.4.

### 1.3

#### Device Fabrication

Dye-sensitized solar cells are typically fabricated upon transparent conducting glass substrates, enabling light irradiance through this substrate under



photovoltaic operation. The conductive coating typically used is fluorine-doped SnO<sub>2</sub> (fluorine tin oxide, FTO), preferred over its indium-doped analogue (ITO) for reasons of lower cost and enhanced stability. Prior to deposition of the mesoporous TiO<sub>2</sub> film, a dense TiO<sub>2</sub> film may be deposited to act as a hole-blocking layer, preventing recombination (shunt resistance) losses between electrons in the FTO and oxidized redox couple.

The TiO<sub>2</sub> nanoparticles are typically fabricated by the aqueous hydrolysis of titanium alkoxide precursors, followed by autoclaving at temperatures of up to 240 °C to achieve the desired nanoparticle dimensions and crystallinity (anatase) [14]. The nanoparticles are deposited as a colloidal suspension by screen printing or doctor blading, followed by sintering at ~ 450 °C to ensure good interparticle connectivity. The porosity of the film is controlled by the addition of an organic filler (e.g., carbowax) to the suspension prior to deposition; this filler is subsequently burnt off during the sintering step. Figure 3 shows a scanning electron microscope image of a typical mesoporous TiO<sub>2</sub> film. Typical film thicknesses are 5–20 μm, with TiO<sub>2</sub> mass of about 1–4 mg cm<sup>-2</sup>, film porosity 50–65%, average pore size 15 nm, and particle diameters 15–20 nm.

The classic sensitizer dye employed in DSC is a Ru(II) bipyridyl dye, *cis*-bis(isothiocyanato)-bis(2,2'-bipyridyl-4,4'-dicarboxylato)-Ru(II), often referred to as "N3", or in its partially deprotonated form (a di-tetrabutylammonium salt) as N719. The structure of these dyes are shown in 2 and 26. The incorporation of carboxylate groups allows immobilization of sensitizer to the film surface via the formation of bidentate coordination and ester linkages, whilst the (–NCS) groups enhance the visible light absorption. Adsorption of the dye to the mesoporous film is achieved by simple immersion of the film in a solution of dye, which results in the adsorption of a dye monolayer to the film surface. The counter electrode is fabricated from FTO-coated glass, with the addition of a Pt catalyst to catalyze the reduc-

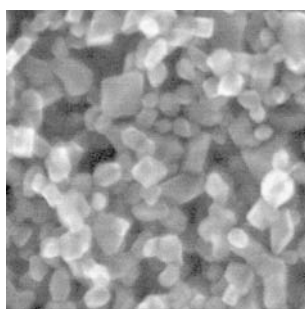


**Fig. 3** Scanning electron microscope image of a typical mesoporous TiO<sub>2</sub> film employed in DSC. Note the bipyramidal shape of the particles having (101) oriented facets exposed. The average particle size is 20 nm

tion of the triiodide at this electrode. Electrical contact between working and counter electrode is achieved by the redox electrolyte, with capillary forces being sufficient to ensure that the electrolyte efficiently penetrates the film pores.

## 1.4

### Incident Photon to Current Efficiency and Open Circuit Photovoltage

The incident monochromatic photon-to-current conversion efficiency (IPCE), defined as the number of electrons generated by light in the external circuit divided by the number of incident photons as a function of excitation wavelength, is expressed in Eq. 7 [15]. The open-circuit photovoltage is determined by the energy difference between the Fermi level of the solid under illumination and the Nernst potential of the redox couple in the electrolyte (Fig. 2). However, the experimentally observed open-circuit potential for various sensitizers is smaller than the difference between the conduction band edge and the redox couple, probably due to the competition between electron transfer and charge recombination pathways. Knowledge of the rates and mechanisms of these competing reactions are vital for the design of efficient sensitizers and, thereby, improvement of the solar devices [16–18].

$$\text{IPCE} = \frac{[(1.25 \times 10^3) \times \text{photocurrent density [mA cm}^{-2}\text{]}]}{[\text{wavelength [nm]} \times \text{photon flux [W m}^{-2}\text{]}]}. \quad (7)$$

Power output from the DSC requires not only efficient charge collection by the electrodes, but the generation of a photovoltage corresponding to a free energy difference between the working and counter electrodes. In the dark at equilibrium, the Fermi energy of the  $\text{TiO}_2$  electrode (corresponding to the free energy of electrons in this film after thermalization) equilibrates with the midpoint potential of the redox couple, resulting in zero output voltage. Under these conditions, the  $\text{TiO}_2$  Fermi level lies deep within the band gap of the semiconductor, and the film is effectively insulating, with a negligible electron density in the  $\text{TiO}_2$  conduction band. Photoexcitation results in electron injection into the  $\text{TiO}_2$  conduction band and the concomitant hole injection into (oxidation of) the redox electrolyte. The high concentrations of oxidized and reduced redox couple present in the electrolyte in the dark mean that this photooxidation process does not result in a significant change in chemical potential of the electrolyte, which remains effectively fixed at its dark, resting value. In contrast, electron injection into the  $\text{TiO}_2$  conduction band results in a dramatic increase in electron density (from the order of  $10^{13} \text{ cm}^{-3}$  to  $10^{18} \text{ cm}^{-3}$ ), raising the  $\text{TiO}_2$  Fermi level (technically the electron quasi-Fermi level) towards the conduction band edge, and allowing the film to become conducting. This shift of the  $\text{TiO}_2$  Fermi level under irradiation increases the free energy of injected electrons and is responsible for the generation of the photovoltage in the external circuit.

The midpoint potential of the redox couple is given by the Nernst equation, and is therefore dependent upon the relative concentrations of iodide and iodine. The concentrations of these species required for efficient device function are in turn constrained by kinetic requirements of dye regeneration at the working electrode, and iodide regeneration at the counter electrode, as discussed below. Typical concentrations of these species are in the range 0.5–1.2 M iodide and 10–200 mM iodine, constraining the midpoint potential of this electrolyte to  $\sim 0.4$  V vs NHE. It should furthermore be noted that in the presence of excess iodide, the iodine is primarily present in the form  $I_3^-$ , resulting in this electrolyte often being referred to as an iodide/triiodide redox couple.

The overall conversion efficiency ( $\eta$ ) of the dye-sensitized solar cell is determined by the photocurrent density ( $j_{\text{ph}}$ ), the open circuit potential ( $V_{\text{oc}}$ ), the fill factor (FF) of the cell and the intensity of the incident light ( $I_s$ ), (Eq. 8) [19].

$$\eta_{\text{global}} = j_{\text{ph}} V_{\text{oc}} \text{FF} / I_s \quad (8)$$

## 1.5

### Molecular Sensitizers

The photophysical and photochemical properties of 4d and 5d metal complexes containing polypyridyl ligands have been thoroughly investigated over the last three decades. The main thrust behind these studies was to understand the energy and electron transfer processes in the excited states and to apply this knowledge to potential practical applications such as dye-sensitized solar cells, organic light-emitting diodes, and light-emitting electrochemical cells. Particularly, there is currently considerable interest in Ru(II) polypyridyl complexes because of their applications in nanocrystalline  $\text{TiO}_2$ -based solar cells [20–23]. The choice of Ru metal is of interest for a number of reasons:

- Because of its octahedral geometry specific ligands can be introduced in a controlled manner
- The photophysical and electrochemical properties of Ru complexes can be tuned in a predictable way
- The Ru metal center possess stable and accessible oxidation states from I to III

The ground and the excited state electrochemical and photophysical properties of these complexes play an important role in the charge transfer dynamics at the interfaces.

The optimal sensitizer for the dye-sensitized solar cell should be panchromatic, i.e., absorb visible light of all colors. Ideally, all photons below a threshold wavelength of about 920 nm should be harvested and converted to electric current. This limit is derived from thermodynamic considerations, showing

that the conversion efficiency of any single-junction photovoltaic solar converter peaks at approximately 33% near a threshold energy of 1.4 eV [24, 25]. Also, the sensitizer should have suitable ground and excited state redox properties, and interlocking groups for grafting the dye on the semiconductor surface. These ascertain intimate electronic coupling between its excited state wave function and the conduction band manifold of the semiconductor [26, 27].

Molecular engineering of Ru complexes that can act as panchromatic charge transfer sensitizers for TiO<sub>2</sub>-based solar cells presents a challenging task as several requirements have to be fulfilled by the dye that are very difficult to be met simultaneously. The lowest unoccupied molecular orbitals (LUMO) and the highest occupied molecular orbitals (HOMO) have to be maintained at levels where photoinduced electron transfer in the TiO<sub>2</sub> conduction band and regeneration of the dye by iodide can take place at practically 100% yield. This greatly restricts the options available to accomplish the desired red shift of the MLCT transitions to about 900 nm.

The spectral and redox properties of Ru polypyridyl complexes can be tuned in two ways. Firstly, by introducing a ligand with a low-lying  $\pi^*$  molecular orbital and secondly by destabilization of the metal  $t_{2g}$  orbital through the introduction of a strong donor ligand. Meyer et al. have used these strategies to considerably tune the MLCT transitions in Ru complexes [28]. Heteroleptic complexes containing bidentate ligands with low-lying  $\pi^*$  orbitals, together with others having strong  $\sigma$  donating properties, indeed show impressive panchromatic absorption properties. However, the extension of the spectral response into the near IR was gained at the expense of shifting the LUMO to lower levels, from where charge injection into the TiO<sub>2</sub> conduction band can no longer occur [29].

Near-infrared response can also be gained by upward shifting of the Ru  $t_{2g}$  (HOMO) levels. However, it turns out that the mere introduction of strong  $\sigma$  donor ligands into the complex often does not lead to the desired spectral result as both the HOMO and LUMO are displaced in the same direction. Furthermore, the HOMO position cannot be varied freely as the redox potential of the dye must be maintained sufficiently positive to ascertain rapid regeneration of the dye by electron donation from iodide following charge injection into the TiO<sub>2</sub>. Therefore, the optimum Ru polypyridyl complexes should exhibit excited state oxidation potential of at least  $-0.9$  V vs. SCE, in order to inject electrons efficiently into the TiO<sub>2</sub> conduction band [30]. The ground state oxidation potential should be about  $0.5$  V vs. SCE in order to be regenerated rapidly via electron donation from the electrolyte (iodide/triiodide redox system or a hole conductor). A significant decrease in electron injection efficiencies will occur if the excited and ground state redox potentials are lower than these values. To trap solar radiation efficiently in the visible and the near-infrared region of the solar spectrum requires engineering of sensitizers at a molecular level [30].

### 1.5.1 Modulation of Sensitizer's Spectral Response

Ruthenium complexes show strong visible bands due to charge transfer transition from metal  $t_{2g}$  (HOMO) orbitals to  $\pi^*$  (LUMO) orbitals of the ligand. From spectroscopic and electrochemical studies of polypyridyl complexes of Ru, it has been concluded that the oxidation and reduction potentials are the best indicators of the energy levels of the HOMO and LUMO [31]. The energy gap between the metal  $t_{2g}$  orbitals and  $\pi^*$  orbitals can be reduced either by raising the energy of the  $t_{2g}$  or by decreasing the energy of the  $\pi^*$  orbitals with donor acceptor ligands, respectively (Fig. 4). In the following sections we will discuss the ways to tune HOMO and LUMO energy levels by introducing various ligands.

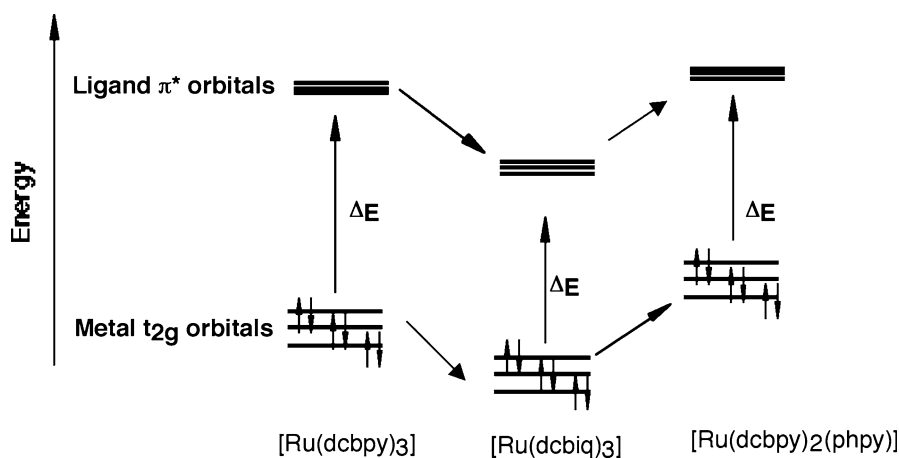
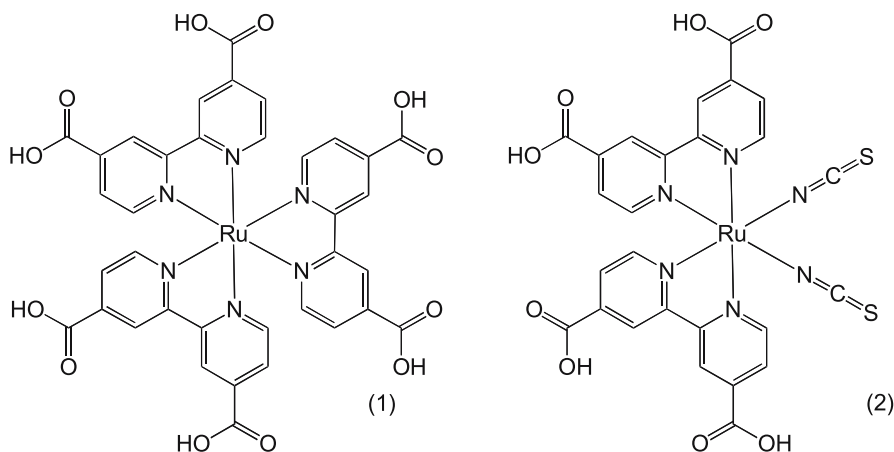


**Fig. 4** Schematic representation of tuning the HOMO ( $t_{2g}$ ) and LUMO ( $\pi^*$ ) orbital energies

#### 1.5.1.1 Spectral Tuning in "Push–Pull" Type of Complexes

The lowest energy MLCT transition of Ru polypyridyl complexes of the type tris-[Ru(4,4'-dicarboxy-2,2'-bipyridine)<sub>3</sub>] (1), can be lowered so that it absorbs more in the red region of the visible spectrum by replacing one 4,4'-dicarboxy-2,2'-bipyridine (dcbpy) with two thiocyanate donor ligands [Ru(dcbpy)<sub>2</sub>(NCS)<sub>2</sub>] (2). In complex 2, the two 4,4'-dicarboxylic acid 2,2'-bipyridine ligands pull while the two thiocyanate donor ligands push electrons. The oxidation potential of the complex 2 is 0.85 V vs. SCE, which is cathodically shifted significantly (0.65 V vs. SCE) compared to the homoleptic type of complex 1, which shows Ru(III/II) couple at 1.5 V vs. SCE. Thus, the



energy of the HOMO is varied 0.65 V, by replacing one 4,4'-dicarboxylic acid 2,2'-bipyridine with two thiocyanate ligands.

Figure 5 shows the absorption spectra of complexes 1 and 2, which exhibit maxima at 465 nm, and 535 nm, respectively. It is interesting to note the magnitude of the spectral shift for the lowest energy charge transfer transition, i.e.,  $\approx 0.35$  eV, and the shift in the oxidation potential,  $\approx 0.65$  eV. This clearly shows that the HOMO tuning is not all translated into the spectral shift of the complex. The apparent 0.3 eV difference is involved in raising the energy of the  $\pi^*$  orbitals of the pulling ligands caused by the pushing ligands [32]. In complex 2, the purpose of incorporating carboxylic acid groups in the 4,4'-position of 2,2'-bipyridine ligand is twofold: to graft the dye on

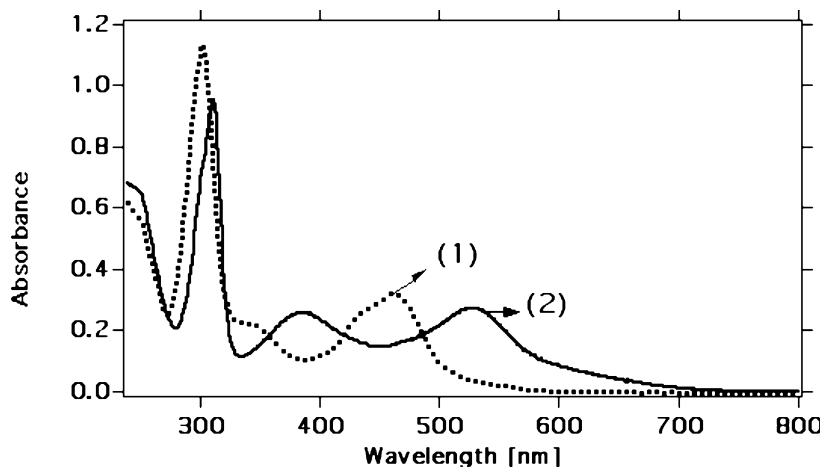
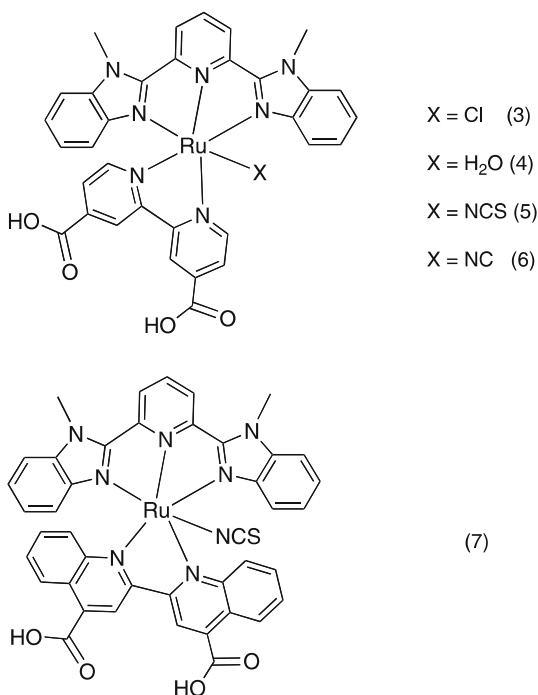


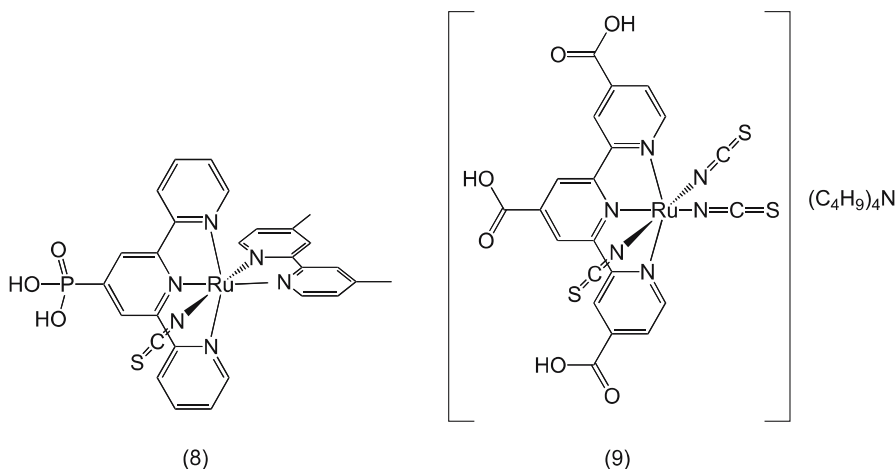
**Fig. 5** Comparison of absorption spectra of complexes 1 and 2

the semiconductor surface, and to provide intimate electronic coupling between its excited state wave-function and the conduction band manifold of the semiconductor. The role of the thiocyanato ligands is to tune the metal  $t_{2g}$  orbitals of Ru(II) and possibly to stabilize the hole that is being generated on the metal, after having injected an electron into the conduction band.

The other interesting class of compounds, which contains donor and acceptor groups in the same hybrid ligand such as 2,6-bis(1-methylbenzimidazol-2'-yl)-pyridine (3–7). The hybrid ligand in these complexes contains donor (benzimidazol-2'-yl) and acceptor groups and was further tuned by introducing different substituents on the benzimidazol-2'-yl group. The complexes containing these ligands show intense UV absorption bands at 362 and 346 nm due to intraligand  $\pi-\pi^*$  transition of 2,6-bis(1-methylbenzimidazol-2'-yl)-pyridine, which acts as a UV filter in dye-sensitized solar cells [33].



The MLCT bands of these complexes are broad and red-shifted by 140 nm, compared to the complex 1. The lowest-energy MLCT transitions within this series were shifted from 486 to 608 nm, and the HOMO level varied over an extent of 0.45 V vs SCE. The energy of the MLCT transition in these complexes decreases with the decrease in the  $\pi$ -acceptor strength of the ancillary ligand, i.e., CN<sup>-</sup>, NCS<sup>-</sup>, H<sub>2</sub>O, or Cl<sup>-</sup>. The red shift of the absorption maxima in complexes containing 4,4'-dicarboxy-2,2-biquinoline (dcbiq) (7) as



opposed to complex **5** (which contains dcbpy) is due to the low-lying  $\pi^*$  orbitals of dcbpy. The resonance Raman spectra of these complexes for excitation at 568 nm show predominantly bands associated with the dcbpy and dcbiq ligands, indicating that the lowest excited state is a metal-to-dcbpy or dcbiq ligand charge transfer state [34].

### 1.5.1.2

#### Influence of Nonchromophoric Ligands on MLCT Transitions

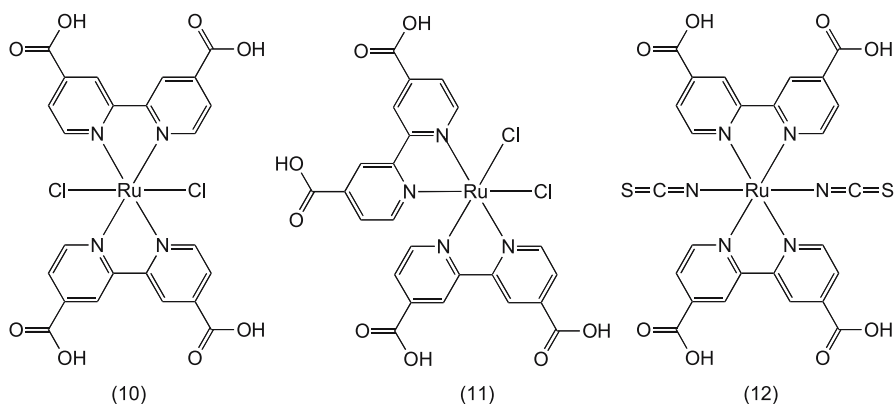
In this section we will compare the spectral response of the two complexes of the type  $[\text{Ru}(\text{P-terpy})(\text{Me}_2\text{bpy})(\text{NCS})]$  (**8**), and  $((\text{C}_4\text{H}_9)_4\text{N})_2[\text{RuL}(\text{NCS})_3]$  (**9**) (P-terpy = 4-phosphonato-2,2':6',2''-terpyridine,  $\text{Me}_2\text{bpy}$  = 4,4'-dimethyl-2,2'-bipyridine,  $\text{L}' = 4,4',4''$ -tricarboxy-2,2':6',2''-terpyridine), where the number of nonchromophoric ligands such as  $\text{NCS}^-$  changed from one to three. The MLCT transition maxima of complexes **8** and **9** are at 500 and 620 nm, respectively. The 120-nm red shift of complex **9** compared to complex **8** is due to an increase in the energy of the metal  $t_{2g}$  orbitals caused by introducing nonchromophoric ligands. The electrochemical data are consistent with the above assignments [35, 36].

### 1.5.1.3

#### Geometrical Isomers

Isomerization is another approach for tuning the spectral properties of metal complexes [37–39]. The UV-Vis absorption spectrum of the *trans*-dichloro complex (**10**) in dimethylformamide (DMF) solution shows at least three MLCT absorption bands in the visible region at 690, 592, and 440 nm. On the other hand, the *cis*-dichloro complex (**11**) in DMF solution shows only





two distinct broad bands in the visible region at 590 and 434 nm, which were assigned to MLCT transitions. The lowest energy MLCT band in *trans*-dithiocyanate complex (12) is significantly red-shifted compared to the corresponding *cis*-complex (2) (Fig. 6). This red shift is due to stabilization of the LUMO of the dcby ligand in the *trans* species relative to the *cis* species. The red shift (108 nm) of the lowest energy MLCT absorption in the spectrum of the *trans*-dichloro complex compared to the spectrum of the *trans*-

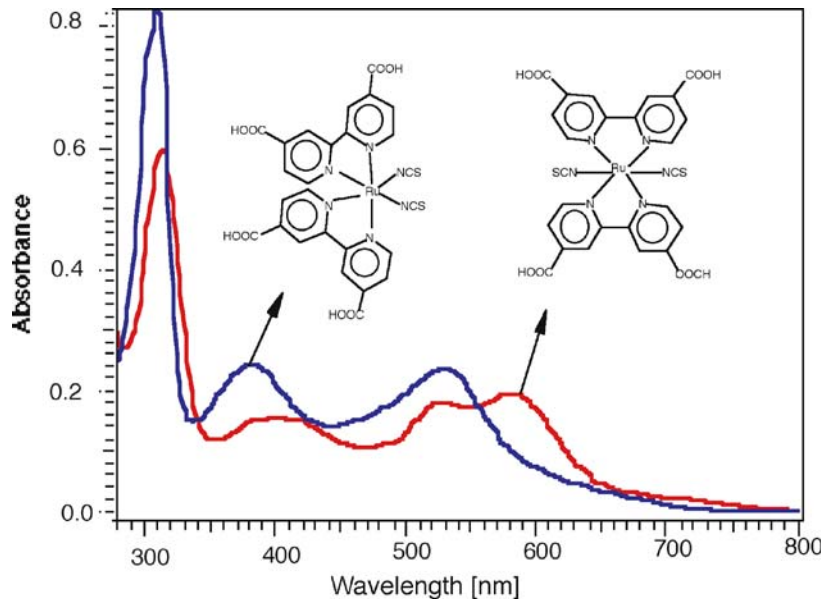


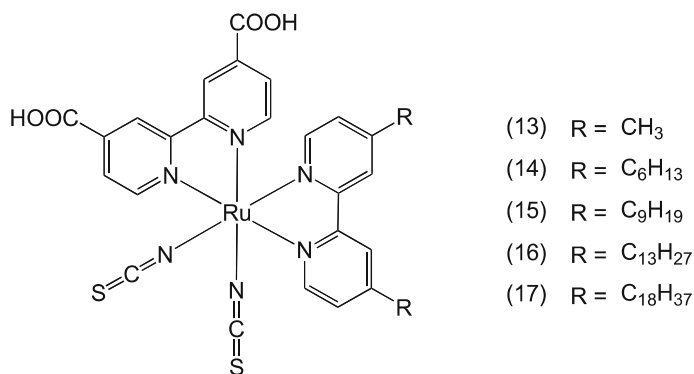
**Fig. 6** UV-Vis absorption spectra of *cis*-, and *trans*-bis(4,4'-dicarboxy-2,2'-bipyridine) Ru(II)(NCS)<sub>2</sub> complexes

dithiocyanato is due to the strong  $\sigma$  donor property of the  $\text{Cl}^-$  compared to the  $\text{NCS}^-$  ligand. The chloride ligands cause destabilization of the metal  $t_{2g}$  orbitals, and raise them in energy relatively closer to the ligand  $\pi^*$  orbitals, resulting in a lower energy MLCT transition.

#### 1.5.1.4

##### Hydrophobic Sensitizers

The other important aspect in dye-sensitized solar cells is water-induced desorption of the sensitizer from the  $\text{TiO}_2$  surface. Extensive efforts have been made in our laboratory to overcome this problem by introducing hydrophobic properties in the ligands 13–17. The absorption spectra of these complexes show broad features in the visible region and display maxima around 530 nm. The performance of these hydrophobic complexes as charge transfer photosensitizers in nanocrystalline  $\text{TiO}_2$ -based solar cells shows excellent stability towards water-induced desorption [36].



The rate of electron transport in dye-sensitized solar cells is a major element of the overall efficiency of the cells. The injected electrons into the conduction band, from optically excited dye, can traverse the  $\text{TiO}_2$  network and can be collected at the transparent conducting glass or can react either with oxidized dye molecule or with the oxidized redox couple (recombination). The reaction of injected electrons into the conduction band with the oxidized redox mediator gives undesirable dark currents, reducing significantly the charge-collection efficiency, and thereby decreasing the total efficiency of the cell (Fig. 7).

Several groups have tried to reduce the recombination reaction by using sophisticated device architecture such as composite metal oxides as the semiconductor with different band gaps [40, 41]. Gregg et al. have examined surface passivation by deposition of insulating polymers [42]. We have studied the influence of spacer units between the dye and the  $\text{TiO}_2$  surface with little

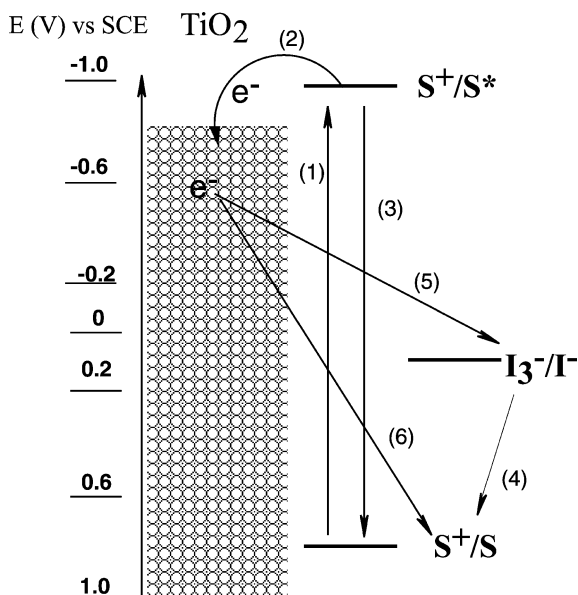


**Fig. 7** Illustration of the interfacial charge transfer processes in nanocrystalline dye-sensitized solar cell.  $S/S^+/S^*$  represents the sensitizer in the ground, oxidized and excited state, respectively. Visible light absorption by the sensitizer (1) leads to an excited state, followed by electron injection (2) into the conduction band of  $TiO_2$ . The oxidized sensitizer (3) gets reduced by  $I^-/I_3^-$  redox couple (4). The injected electrons into the conduction band may react either with the oxidized redox couple (5) or with oxidized dye molecule (6)

success [30]. Nevertheless, by using  $TiO_2$  films containing hydrophobic sensitizers that contain long aliphatic chains (13–17) the recombination reaction was suppressed considerably [43, 44]. The most likely explanation for the reduced dark current is that the long chains of the sensitizer interact laterally to form an aliphatic network, as shown in Fig. 8, thereby preventing triiodide from reaching the  $TiO_2$  surface.

### 1.5.1.5

#### High Molar Extinction Coefficient Sensitizers

Complex 2 has become a paradigm in the area of dye-sensitized nanocrystalline  $TiO_2$  films [45]. In spite of this, the main drawback of this sensitizer is the lack of absorption in the red region of the visible spectrum and also a relatively low molar extinction coefficient. Therefore, a new series of high molar extinction coefficient sensitizers (18–20) featuring alkyoxy groups has been synthesized and utilized in dye-sensitized solar cells. The purpose of the 4,4'-di-(2-(3,6-dimethoxyphenyl)ethenyl)-2,2'-bipyridine ligand, which contains extended  $\pi$ -conjugation with substituted methoxy groups, is to enhance

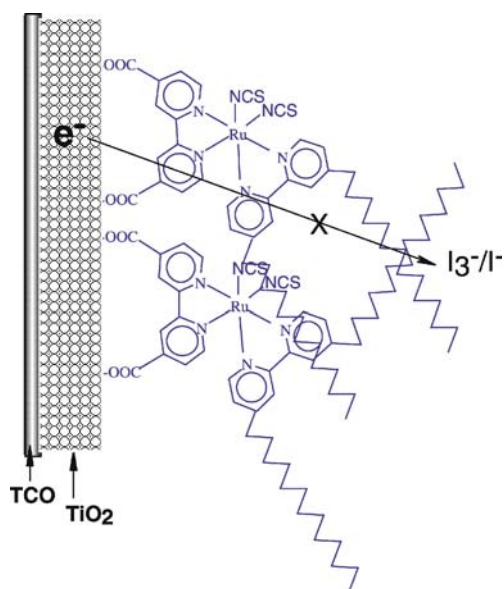
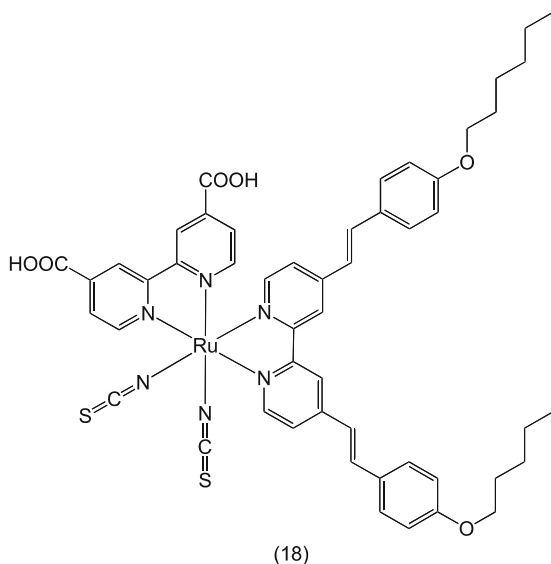
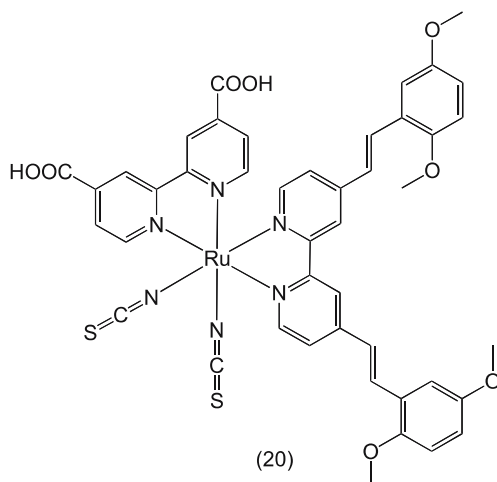
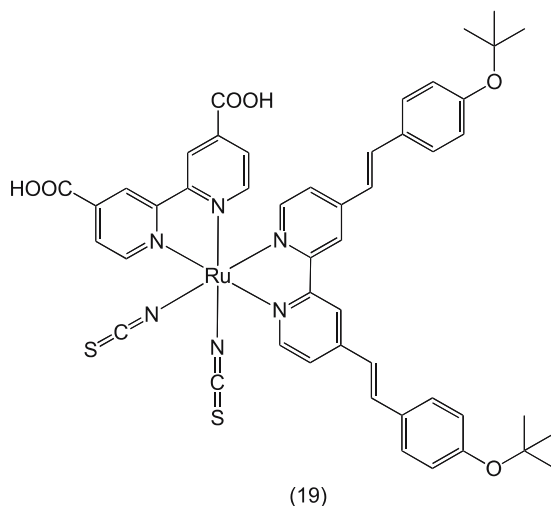


**Fig. 8** Pictorial representation of the blocking of the oxidized redox couple  $I_3^-$  from reaching the surface of  $TiO_2$  for conduction band electrons using hydrophobic sensitizers, which form an aliphatic network



the molar extinction coefficient of the sensitizers, and furthermore to provide directionality in the excited state by fine tuning the LUMO level of the ligand with the electron-donating alkoxy groups.



The absorption spectra of complexes **18–20** are dominated by the MLCT transitions in the visible region, and the lowest allowed MLCT bands appearing at 400 and 545 nm. The molar extinction coefficients of these bands are close to 35 000 and 19 000  $\text{M}^{-1}\text{cm}^{-1}$ , respectively, which are significantly higher than those of the standard sensitizer *cis*-dithiocyanatobis(4,4'-dicarboxy-2,2'-bipyridine)Ru(II), (**2**) (Fig. 9).

Figure 10 shows an INDO/S and DFT (density functional theory) study of the electronic and optical properties of complexes **18–20**. The theoretical data point to the top three frontier-filled orbitals having essentially Ru 4d ( $t_{2g}$  in octahedral group) character with sizable contribution coming from the NCS ligand orbitals [46]. Most critically, the calculations reveal that for

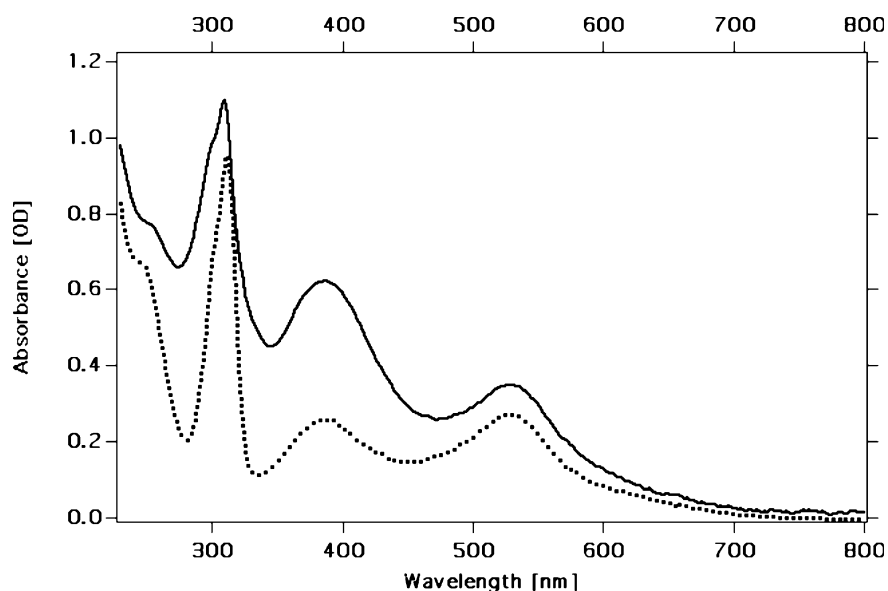


**Fig. 9** Comparison of absorption spectra of complexes 2 and 20 in ethanol

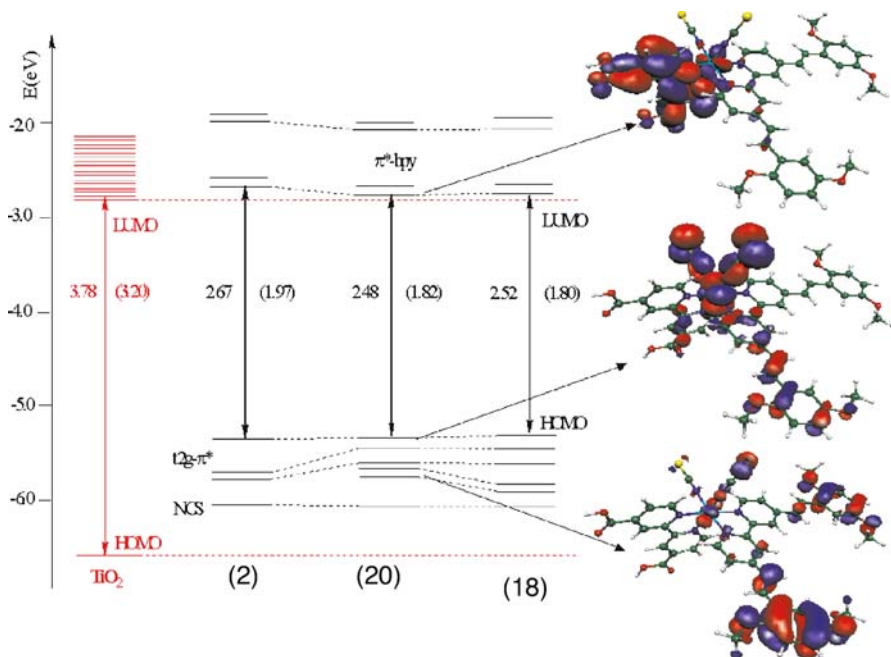


**Fig. 10** Molecular orbital energy diagram of complexes 2, 18, and 20 compared to that of a TiO<sub>2</sub> nanoparticle model. HOMO-LUMO gaps (eV) and lowest TDDFT excitation energies (eV, data in parenthesis) are reported together with isodensity plots of the HOMO-3, HOMO, and LUMO of complex 20

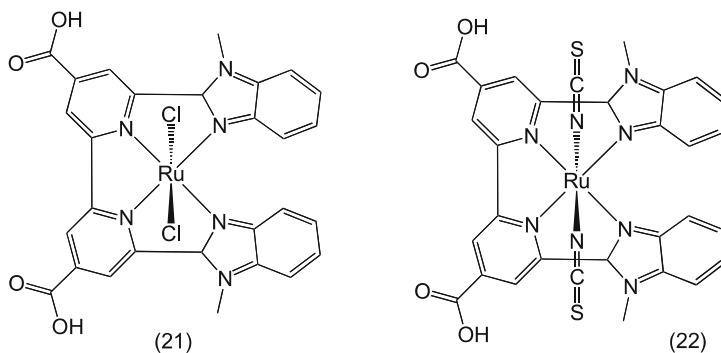
the TiO<sub>2</sub>-bound sensitizers 18–20, excitation directs charge into the carboxyl-bipyridine ligand bound to the TiO<sub>2</sub> surface. The photovoltaic data of these sensitizers using an electrolyte containing 0.60 M butylmethylimidazolium iodide (BMII), 0.03 M I<sub>2</sub>, 0.10 M guanidinium thiocyanate and 0.50 M *tert*-butylpyridine in a mixture of acetonitrile and valeronitrile (volume ratio: 85 : 15), exhibited a short circuit photocurrent density of  $16.50 \pm 0.2 \text{ mA cm}^{-2}$ , with an open circuit voltage of  $790 \pm 30 \text{ mV}$  and a fill factor of  $0.72 \pm 0.03$ . This corresponds to an overall conversion efficiency of 9.6% under standard AM 1.5 sunlight and demonstrates stable performance under light and heat soaking at 80 °C [47].

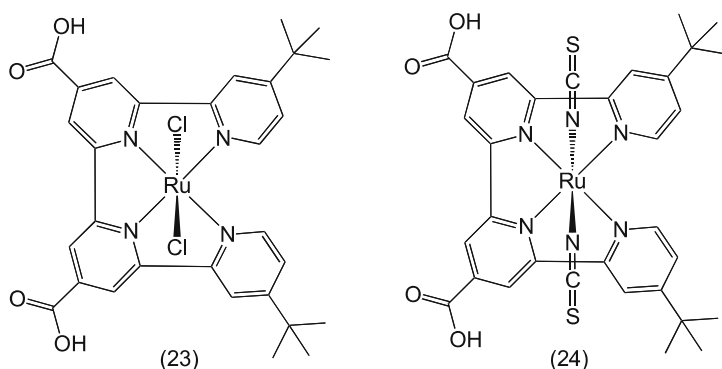
### 1.5.1.6

#### Sensitizers Containing Functionalized Hybrid Tetradentate Ligands

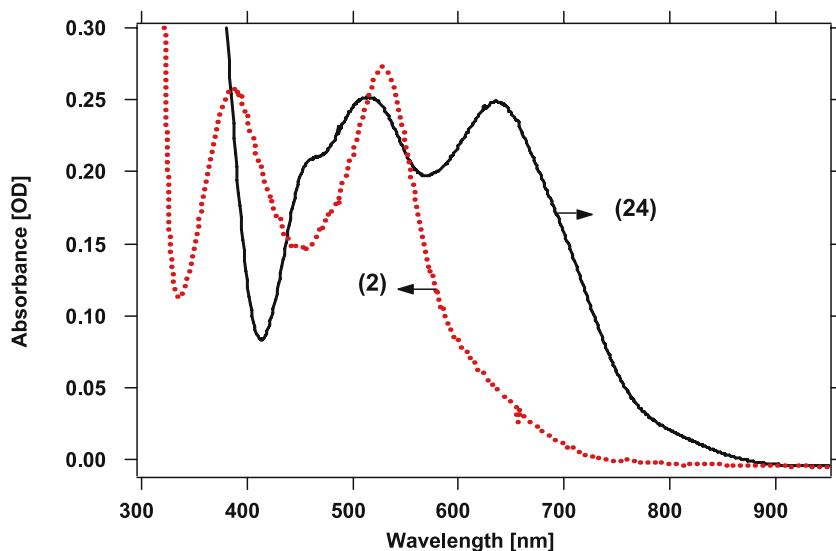
The main advantage of *trans* complexes 10 and 12 discussed above is their panchromatic response, but the drawback is thermal and photoinduced isomerization back to the *cis* configuration. In an effort to stabilize the *trans* configuration of an octahedral Ru complex and integrate the concepts of donor and acceptor in a single complex, Renouard et al. and Barolo et al. have developed functionalized hybrid tetradentate ligands and their Ru complexes (21–24) [48, 49]. In these complexes the donor units of the tetradentate ligand (benzimidazole in 21–22 and *tert*-butylpyridine in 23–24) tune the metal *t*<sub>2g</sub> orbital energies, and the acceptor units (methoxycarbonyl) tune the  $\pi^*$  molecular orbitals. The application of a tetradentate ligand will inhibit the *trans* to *cis* isomerization process. The axial coordination sites are used to further fine-tune the spectral and redox properties and to stabilize the hole that is being generated on the metal during electron injection into the conduction band.

The *trans*-dichloro and dithiocyanate complexes 21–24 show MLCT transitions in the entire visible and near IR region. The lowest energy MLCT transition band of the *trans*-dichloro complexes 21 is around 700 nm in DMF





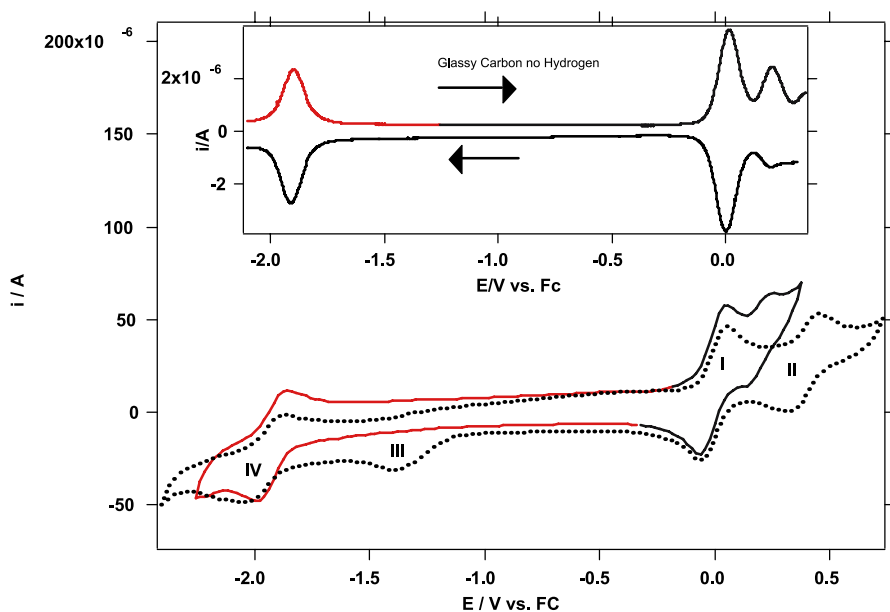
solution and they show weak and broad emission signals with onset above 950 nm [48]. The absorption spectra of the *trans*-dithiocyanate complex **24** are blue-shifted with respect to its *trans*-dichloro analogues due to the weak  $\sigma$  donor property of the  $\text{NCS}^-$  compared to the  $\text{Cl}^-$ , which is consistent with the electrochemical data of these complexes. A comparison of absorption spectra of complex **24** and complex **2** is shown in Fig. 11. The spectra are dominated by features in the entire visible region at 382(sh), 465, 515, and 637 nm, which are assigned as MLCT. The lowest energy MLCT band in complex **24** is red-shifted by 107 nm when compared to the standard sensitizer **2** (see Fig. 11).



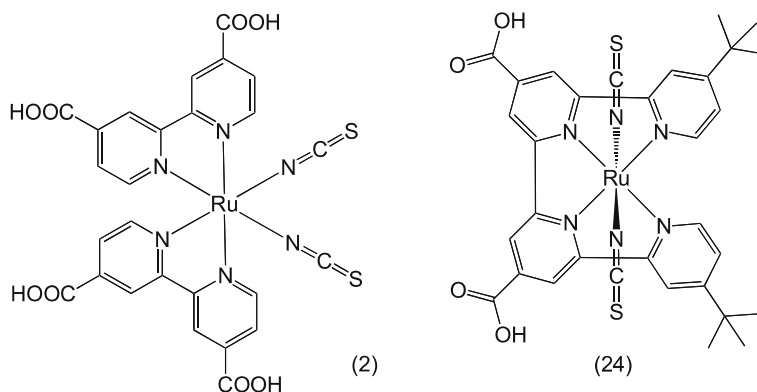
**Fig. 11** UV-Vis absorption spectra of complexes **24** and **2** (concentration  $3.5 \times 10^{-5}$  M) and N719 (concentration  $2.0 \times 10^{-5}$  M) measured in ethanol solution and their chemical structures



Figure 12 shows the cyclic voltammogram of complex 24. The Ru(III/II) redox potentials of the thiocyanate complexes were more positive (by  $\approx 350$  mV) than their corresponding dichloro complexes and show quasi-reversible behavior [49]. This is in good agreement with the ligand electrochemical parameter scale, according to which the thiocyanate Ru(III/II) wave should be  $\sim 340$  mV more positive than that of the dichloro species [50]. The  $i_{\text{ox}}/i_{\text{red}}$  peak current is substantially greater than unity due to the oxidation of the thiocyanate ligand subsequent to the oxidation of the Ru(II) center. At negative potentials an irreversible reduction wave (labeled as III in Fig. 12) appeared at  $-1.39$  V, which is due to reduction of protons on the carboxylic acid of 4,4''-di-(*tert*-butyl)-2,2':6,2'':6'',2'''-quaterpyridine-4',4''-dicarboxylic acid [51]. The quasi-reversible wave at  $E_{1/2} = -1.93$  V vs. Fc is assigned to the reduction of the 4,4''-di-(*tert*-butyl)-2,2':6,2'':6'',2'''-quaterpyridine-4',4''-



**Fig. 12** Cyclic voltammogram of complex 24 in protonated (*black line*) and deprotonated state (*red line*) measured in DMF solution containing 0.1 M TBA(PF<sub>6</sub>) using a glassy carbon electrode with scan rate of 500 mV s<sup>-1</sup>. The redox couple labeled I is due to ferrocenium/ferrocene, which is used as an internal standard; II is Ru(III/II); III is proton reduction and IV is due to ligand reduction. *Insert* shows differential pulse voltammogram of complex 24 in the deprotonated state, measured in DMF solution containing 0.1 M TBA(PF<sub>6</sub>) using a glassy carbon electrode with ferrocene as an internal reference. The direction of the change in electrode polarization is shown with *arrows* (from negative to positive (*red curve*) and positive to negative potentials (*black curve*)), with a step potential of 10 mV, modulation amplitude 25 mV, modulation time 0.05 s, and interval time 0.5 s



dicarboxylic acid ligand (wave IV). Upon deprotonation of the complex by treating with tetrabutylammonium hydroxide or by electrochemical reduction of protons to hydrogen the irreversible couple (wave III) disappeared, accompanied by a quasi-reversible wave IV. The ligand-based reduction couple in the deprotonated form compares well with that of the protonated form. Therefore, the origin of the irreversible peak is explicitly attributed to reduction of protons to hydrogen.

The electronic spectra of **24** were calculated by DFT/TDDFT and compared with the experimental data. Geometry optimization of **24** produced a structure with  $C_2$  point group symmetry [49]. The schematic isodensity plots of the frontier orbitals of **24** are shown in Fig. 13. The seven HOMOs of **24** show contributions from both the Ru center and the SCN ligands in variable percentages. In particular, the first two almost degenerate HOMOs, lying within 0.04 eV, are antibonding combinations of the Ru  $d_{xz}$  and  $d_{yz}$  orbitals with the SCN  $\pi$  orbitals, while HOMO-2 and HOMO-4, lying 0.51 and 0.93 eV below the HOMO, respectively, are non-bonding  $d_{xy}$ -SCN  $\pi$  combinations. HOMO-3, lying 0.80 eV below the HOMO, is a pure SCN  $\pi$  orbital, while the almost degenerate HOMO-5/HOMO-6 represent the bonding counterpart of the  $d_{xz}/d_{yz}(\text{Ru})-\pi(\text{SCN})$  orbitals and lie 1.32 eV below the HOMO. It is interesting to compare the electronic structure of complex **2** with that of complex **24**. Both complexes show seven highest HOMOs of mixed Ru-SCN character.

The seven LUMOs of complex **24** are  $\pi^*$  combinations localized on the quaterpyridine ligand, while the LUMO+7 and LUMO+8 have  $d_{z^2}(\text{Ru})$  and  $d_{x^2-y^2}(\text{Ru})$  character, respectively, and lie ca. 0.8 eV above LUMO+6. The LUMO/LUMO+2 are mainly localized on the portion of the ligand bearing the COOH groups. In particular, the LUMO is localized on the pyridines bearing the carboxylic groups and on the carbon-carbon bond connecting them. The LUMO+1/LUMO+2, lying 0.55 eV above the LUMO, also have amplitudes on the carbon-carbon bonds connecting the pyridines. The LUMO+3 and LUMO+6, lying 1.27 and 2.06 eV above the LUMO, are completely delocal-

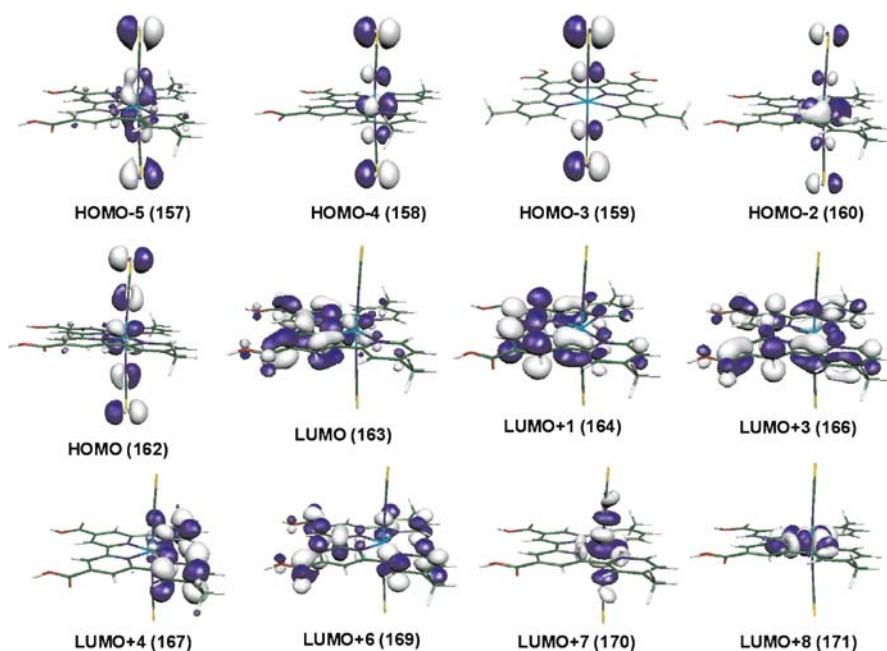


**Fig. 13** Isodensity plots of the frontier orbitals of complex 24

ized over the tetradentate ligand; the LUMO+4/LUMO+5, found 1.62 eV above the LUMO, are localized on the two pyridine bearing the alkyl-substituted groups. LUMO, LUMO+3, and LUMO+6 show contributions from the COOH groups.

## 1.6

### Surface Chelation of Polypyridyl Complexes onto the TiO<sub>2</sub> Oxide Surface

The functional groups serve to anchor the dye onto the TiO<sub>2</sub> films. The grafting of polypyridyl complexes onto the oxide surface, which allows for electronic communication between the complex and the substrate, is an important feature in dye-sensitized solar cells. Several Ru complexes containing substituted groups such as carboxylic acid, hydroxamic acid dihydroxy, and phosphonic acid on pyridine ligands are described [52–61]. These functional moieties serve as an anchoring group to immobilize the complex on the nanocrystalline TiO<sub>2</sub> films. The immobilized sensitizer absorbs a photon to produce an excited state, which transfers an electron onto the TiO<sub>2</sub> conduction band. To achieve high quantum yields for electron injection, the dye needs to be in intimate contact with the semiconductor surface to produce close overlap of the ligand  $\pi^*$  orbitals with the titanium 3d orbitals. The values reached with Ru complexes that have carboxylic acid and phospho-

nic acid groups are close to 100%. A quantum yield near unity implies that the electron injection is at least a hundred times more rapid than the natural decay time of the sensitizer, which is in the nanosecond range.

The interaction between the adsorbed sensitizer and the semiconductor surface has been addressed using resonance Raman and FT-IR spectroscopy. The carboxylic acid functional group could adsorb on the surface in a unidentate, bidentate, or bridging fashion. Yanagida et al. concluded that the sensitizer *cis*-dithiocyanato bis(2,2'-bipyridine-4,4'-dicarboxylate)Ru(II) (2) binds to the surface using ester-like chelating linkages [62]. Finnie et al. have reported that the sensitizer 2 anchors on the surface of TiO<sub>2</sub> as a bidentate or bridging mode using two carboxylate groups per dye [63]. However, Fillingner

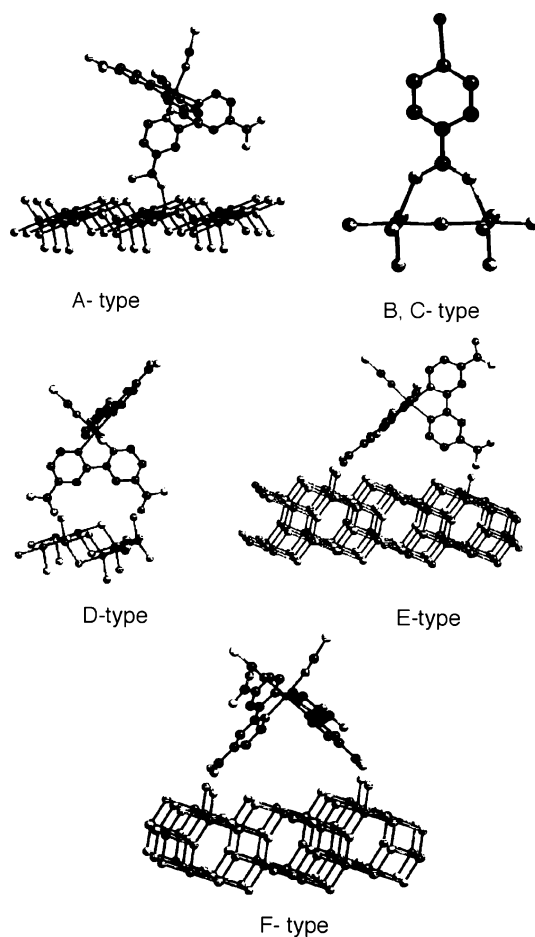


**Fig. 14** Possible anchoring modes for sensitizer 2 using carboxylate functional group on TiO<sub>2</sub> surface

and Parkinson studied the adsorption behavior of the sensitizer **2** and found that the initial binding involves one carboxylate, with subsequent additional binding of two or more carboxylate groups on the surface [64].

Shklover et al. have reported the crystal structure and molecular dynamics modeling of the sensitizer **2** with different anchoring types to the TiO<sub>2</sub> anatase surface [65]. In their modeling the initial attachment of the dye is a single bond A-type (Fig. 14). The main feature of this type of anchoring is the great rotational freedom of the molecule, which leads to immediate capture of another carboxylic group by a neighboring Ti atom, resulting in anchoring B- and C-type (Fig. 14). When the sensitizer **2** anchors onto the TiO<sub>2</sub> surface, using both carboxylic groups of the same bipyridyl ligand, this results in a two-bond anchoring of the D-type (Fig. 14). In E- and F-type configuration, attachment occurs via two of its four carboxylic groups. The carboxylic group either bridges two adjacent rows of titanium ions through bidentate coordination or interact with surface hydroxyl groups through hydrogen bonds. The two remaining carboxylic groups remain in the protonated state. Thermodynamically the bonding geometry of the E- and F-type are most favorable. The ATR-FTIR data of the sensitizer **2** and its different protonated forms adsorbed on TiO<sub>2</sub> are consistent with the anchoring of F-type where the sensitizer adsorbs on the surface using two carboxylic groups as a bridging bidentate fashion, which are *trans* to the NCS ligands [66].

### 1.6.1

#### **Acid–Base Equilibria of *cis*-Dithiocyanato Bis(2,2'-bipyridine-4,4'-dicarboxylate)Ru(II) Complex(2)**

Understanding of the binding nature of sensitizers onto the TiO<sub>2</sub> surface requires detailed knowledge of the pK<sub>a</sub>'s of the sensitizer. Here we discuss pK<sub>a</sub>'s of the sensitizer **2** and its implications for the adsorption studies. The ground state pK<sub>a</sub> values of **2** were determined from the relationship between the change in the optical density or the peak maximum with the pH for a given wavelength [26]. The plot of λ<sub>max</sub> change vs. pH for **2** shows the expected sigmoidal shape, with the pH at the inflection point giving two ground state pK<sub>a</sub> values at 3 and 1.5 ± 0.1. In complex **2** there are two 4,4'-dicarboxy-2,2'-bipyridine ligands that could give four separate acid–base equilibria, if the dissociation is stepwise. On the other hand, if the dissociations were simultaneous one would expect one equilibrium constant. The two separate equilibria in complex **2**, suggests that the pyridyl subunits are not equivalent [66]. The stronger Lewis basicity of the thiocyanato compared to the bipyridine ligand increases the pK<sub>a</sub> value of the pyridine carboxylic acid, which is opposite to its own position in the octahedral complex, shifting its pK<sub>a</sub> to a higher value than that of the second pyridine carboxylic acid, to which it is connected.

## 1.7

### Photovoltaic Properties

The best photovoltaic performance, both in terms of conversion yield and long term stability, has so far been achieved with polypyridyl complexes of Ru in which two 2,2'-bipyridyl-4,4'-dicarboxylic acid and thiocyanate ligands have been used. Thus, the Ru complex *cis*-RuL<sub>2</sub>(NCS)<sub>2</sub> (**1**), known as N3 dye, has become the paradigm of heterogeneous charge transfer sensitizer for mesoporous solar cells [19]. The fully protonated N3 has absorption maxima at 535 and 400 nm, the extinction coefficients being 1.45 and  $1.41 \times 10^4 \text{ M}^{-1} \text{ cm}^{-1}$ , respectively. The complex emits at 750 nm with a lifetime of 60 ns. The optical transition has MLCT character: excitation of the dye involves transfer of an electron from the metal to the  $\pi^*$  orbital of the surface anchoring carboxylated bipyridyl ligand. From here it is released within femto- to picoseconds into the conduction band of TiO<sub>2</sub>, generating electric charges with near-unit quantum yield.

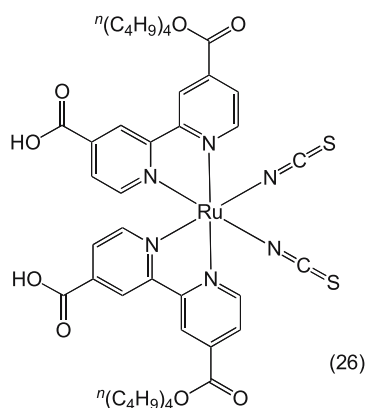
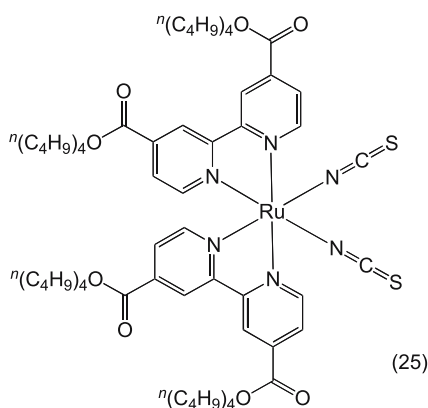
#### 1.7.1

##### Effect of Protons Carried by the Sensitizer on the Performance

In order to obtain high overall light to electric power conversion efficiencies, optimization of the short circuit photocurrent ( $i_{sc}$ ) and open circuit potential ( $V_{oc}$ ) of the solar cell is essential. The conduction band of the TiO<sub>2</sub> is known to have a Nernstian dependence on pH [55,67]. The fully protonated sensitizer **2**, upon adsorption transfers most of its protons to the TiO<sub>2</sub> surface, charging it positively. The electric field associated with the surface dipole generated in this fashion enhances the adsorption of the anionic Ru complex and assists electron injection from the excited state of the sensitizer into the titania conduction band, favoring high photocurrents (18–19 mA cm<sup>-2</sup>). However, the open-circuit potential (0.65 V) is lower due to the positive shift of the conduction band edge induced by the surface protonation.

On the other hand, the sensitizer **25**, which carries no protons, shows high open-circuit potential compared to complex **2**, due to the relative negative shift of the conduction band edge induced by the adsorption of the anionic complex. However, as a consequence the short circuit photocurrent is lower. Thus, there should be an optimal degree of protonation of the sensitizer in order to maximize the product of short circuit photocurrent and open circuit potential, which along with the fill factor determines the power conversion efficiency of the cell.

The performance of the three sensitizers **2**, **25** and **26**, which contain different degrees of protonation, were studied on nanocrystalline TiO<sub>2</sub> electrodes [26]. Figure 16 shows the photocurrent action spectra obtained with a monolayer of these complexes coated on TiO<sub>2</sub> films.



The incident monochromatic photon-to-current conversion efficiency (IPCE) is plotted as a function of excitation wavelength. The IPCE value in the plateau region is 80% for complex **2**, while for complex **25** it is only about 66%. In the red region, the difference is even more pronounced. Thus, at 700 nm the IPCE value is twice as high for the fully protonated complex **2** as compared to the deprotonated complex **25**. As a consequence, the short circuit photocurrent is 18–19 mA cm<sup>-2</sup> for complex **2**, while it is only about 12–13 mA cm<sup>-2</sup> for complex **25**. However, there is a trade-off in photovoltage, which is 0.9 V for complex **25**, as compared to 0.65 V for complex **2**. Nevertheless, this is insufficient to compensate for the current loss. Hence, the

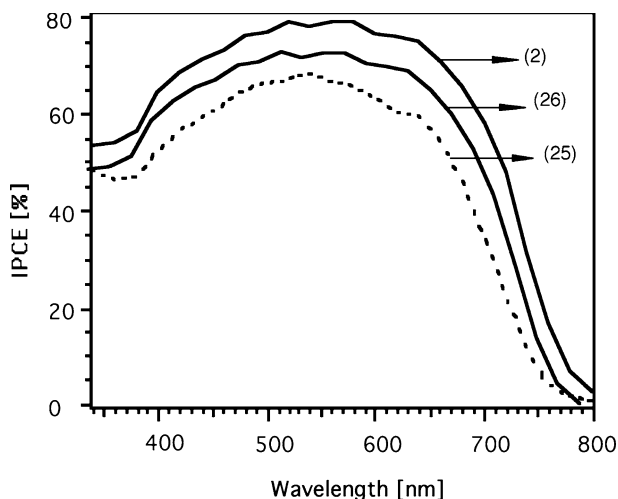


**Fig. 15** Photocurrent action spectra of nanocrystalline TiO<sub>2</sub> films sensitized by complexes **2**, **25**, and **26**. The incident photon to current conversion efficiency is plotted as a function of wavelength

photovoltaic performance of complex **26** carrying two protons is superior to that of compounds **2** and **25** that contain four or no protons, respectively. The doubly protonated form of the complex is therefore preferred over the other two sensitizers for sensitization of nanocrystalline TiO<sub>2</sub> films.

The solar to electric power conversion efficiency of dye-sensitized solar cells of laboratory scale (0.158 cm<sup>2</sup>), validated by an accredited photovoltaic calibration laboratory, has reached 11.1% under standard reporting conditions, i.e., air mass 1.5 global sunlight at 1000 W m<sup>-2</sup> intensity and 298 K temperature, rendering it a credible alternative to conventional p-n junction photovoltaic devices [68]. Photovoltaic performance data obtained with a sandwich cell under illumination by simulated AM 1.5 solar light using complex **26** are shown in Fig. 16. At 1 sun the **26**-sensitized solar cell exhibited 17.73 ± 0.5 mA current, 846 mV potential, and a fill factor of 0.75 yielding an overall conversion efficiency of 11.18%.

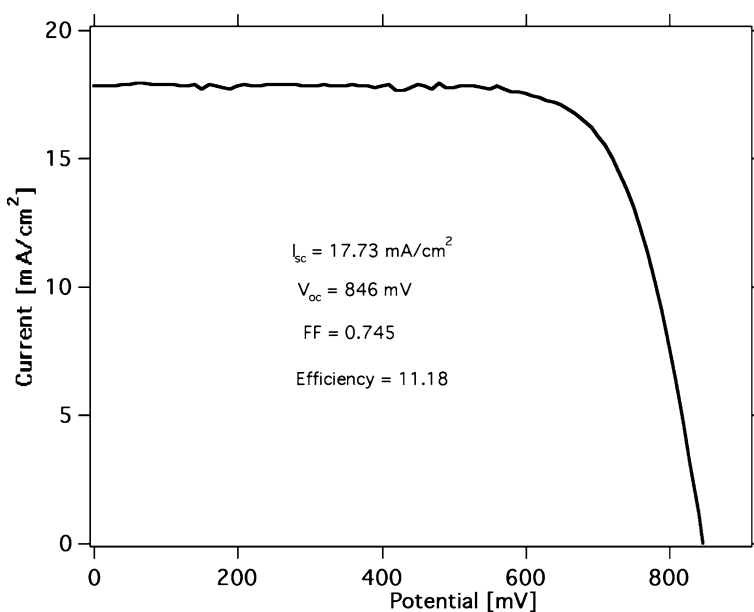


**Fig. 16** Photocurrent-voltage curve of a solar cell based on complex **26**. The cell was equipped with an anti-reflective coating. The conversion efficiency in full AM 1.5 sunlight illumination (100 mW cm<sup>-2</sup>) is 11.18%. The cell is masked with black plastic to avoid the diffusive light leaving an active cell area of 0.158 cm<sup>2</sup>

## 1.7.2

### Comparison of IPCE Obtained with Various Sensitizers

Figure 17 shows the photocurrent action spectrum of a cell containing various sensitizers. The broad feature covers the entire visible spectrum and



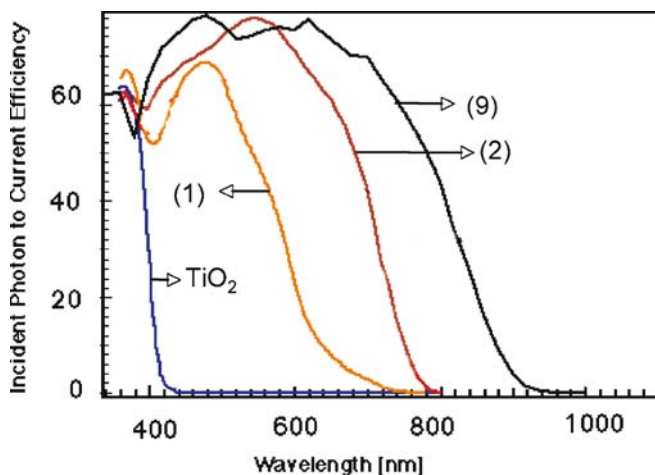


**Fig. 17** Photocurrent action spectra of bare nanocrystalline  $\text{TiO}_2$  film, and the sensitizers 1, 2, and 9 adsorbed on  $\text{TiO}_2$  films. The incident photon to current conversion efficiency is plotted as a function of wavelength

extends into the near IR region up to 920 nm for complex 9. The incident photon-to-current conversion efficiency value in the plateau region was about 80% for complex 9. Taking the light losses in the conducting glass into account, the efficiency of electric current generation is practically 95% over a broad wavelength. The overlap integral of the absorption spectrum with the standard global AM 1.5 solar emission spectrum for complex 9 yields a photocurrent density of  $20.5 \text{ mA cm}^{-2}$ . The open circuit potential is 720 mV and the fill factor is 0.7, resulting in a total power conversion efficiency of 10.5%. These results were confirmed at the National Renewable Energy Laboratory (NREL), Golden, Colorado, USA (Fig. 18). The complexes  $[\text{RuL}_3]$  (1) and  $[\text{RuL}_2(\text{NCS})_2]$  (2) under similar conditions show an IPCE value of 70–80% in the plateau region. Though the IPCE values are comparable with that of 9, the total integrated current decreased significantly due to increasing blue shift of the spectral response from 9 to 2 to 1.

### 1.7.3

#### Solid State Dye-Sensitized Solar Cells

Research on the solid state dye-sensitized solar cells (DSC) has gained considerable momentum recently as this embodiment is attractive for realizing flexible photovoltaic cells in a roll-to-roll production. The *spiro*-OMeTAD has been the most successful p-type organic conductor (hole transport material) employed. Its work function is about 4.9 eV and the hole mobility  $2 \times 10^{-4} \text{ cm}^2 \text{ s}^{-1}$ . A schematic diagram of the solid state DSC with the structure of this hole conductor is shown in Fig. 19. Reported first in 1998, the con-

## EPFL (Switzerland) nano-crystal dye sensitized cell

Sample: PL0710/2  
 Oct 30, 1998 10:41 AM  
 ASTM E 892-87 Global

Temperature = 25.0°C  
 Area = 0.1863 cm<sup>2</sup>  
 Irradiance: 1000.0 Wm<sup>-2</sup>

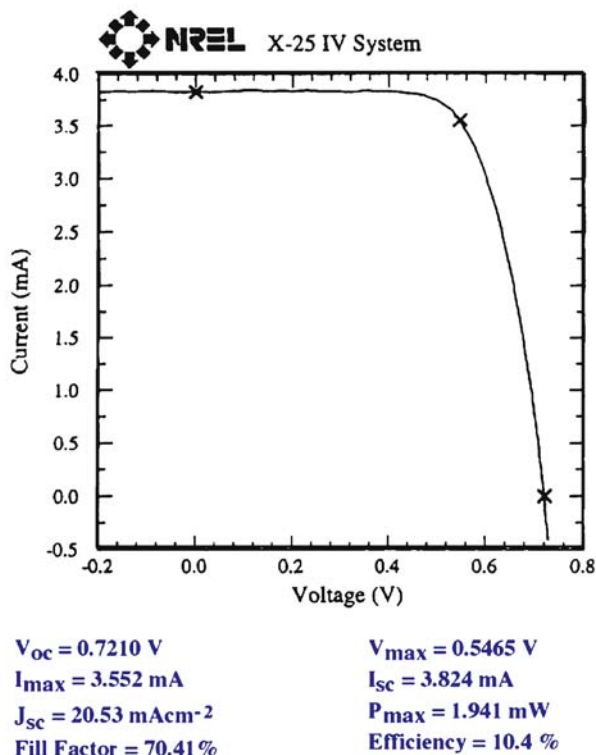


**Fig. 18** Photocurrent–voltage characteristics of complex 9 measured at the National Renewable Energy Laboratory

version yields have increased dramatically over the last few years, i.e., from a fraction of a percent to over 4% [43, 69]. The main drawback of these cells has been fast interfacial electron-hole recombination, reducing the diffusion length of the conduction band electrons to a few microns as compared to 20–100 microns for the electrolyte-based DSC. As a consequence, the film thickness employed in these cells is restricted to only 2 microns, which is insufficient to harvest the sunlight by the adsorbed sensitizer, thus reducing the resultant photocurrent. The dye monolayer itself blocks this back reaction because it is electrically insulating [70]. Hence, current efforts are being directed towards molecular engineering of the interface to improve the compactness and order of monolayer and prevent in this fashion the charge carriers from recombining.

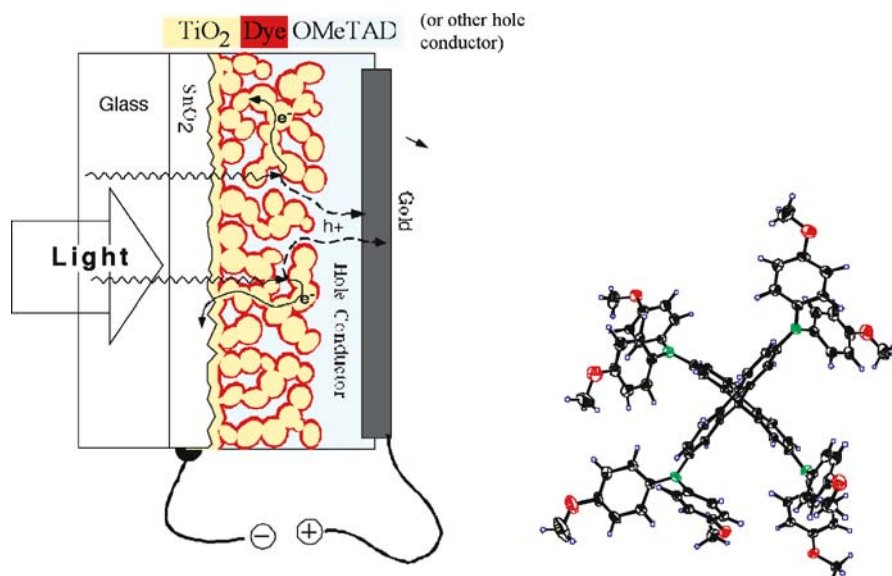


**Fig. 19** Cross-sectional view of a solid state dye-sensitized photovoltaic cell using the hole conductor spiro-OMeTAD, whose structure is indicated on the *right*

Another difficulty encountered has been the filling of the porous network with the hole conductor. This impediment may be overcome by developing oxide films having regular mesoporous channels aligned in a perpendicular direction to the current collector. On the other hand, the  $V_{OC}$  values obtained with solid state DSCs are high, reaching nearly 1 V, due to a better match of the hole conductor work function than that of the electrolyte with the redox potential of the sensitizer. The future of these solid hole conductor systems thus looks bright if the recombination and pore filling problems can be addressed.

## 1.8 Stability

In contrast to amorphous silicon, which suffers from degradation due to the well-known Staebler–Wronski effect, the intrinsic stability of the DSC has been confirmed by extensive accelerated light soaking tests carried out over the last decade. One major issue that has been settled during this period is that the sensitizers employed in the current dye-sensitized solar cell embodiments can sustain 20 years of outdoor service without significant degradation. However, as new and more advanced dye structures emerge, and in order to avoid repeating these lengthy tests every time the sensitizer is modified, kinetic criteria have been elaborated to allow prediction of long-term performance.

Figure 20 illustrates the catalytic cycle that the sensitizer undergoes during cell operation. Critical for stability are side reactions that occur from the excited state ( $S^*$ ) or the oxidized state ( $S^+$ ) of the dye. These reactions compete with electron injection from the excited dye into the conduction band of the mesoscopic oxide and with the regeneration of the sensitizer. These destructive channels are assumed to follow first or pseudo-first order kinetics and are assigned the rate constants  $k_1$  and  $k_2$ . Introducing the two branching ratios  $P_1 = k_{inj}/(k_1 + k_{inj})$  and  $P_2 = k_{reg}/(k_2 + k_{reg})$ , where  $k_{inj}$  and  $k_{reg}$  are the first order or pseudo-first order rate constants for the injection and regeneration process, respectively, the fraction of the sensitizer molecules that survives one cycle is given by the product  $P_1 \times P_2$ . A simple calculation [71] shows that the sum of the branching ratios for the two bleeding channels should not exceed  $1 \times 10^{-8}$  in order for the lifetime of the sensitizer to reach a lifetime of at least 20 years. The turnover frequency of the dye, averaged over seasons and day/night time, is about  $0.16 \text{ s}^{-1}$ .

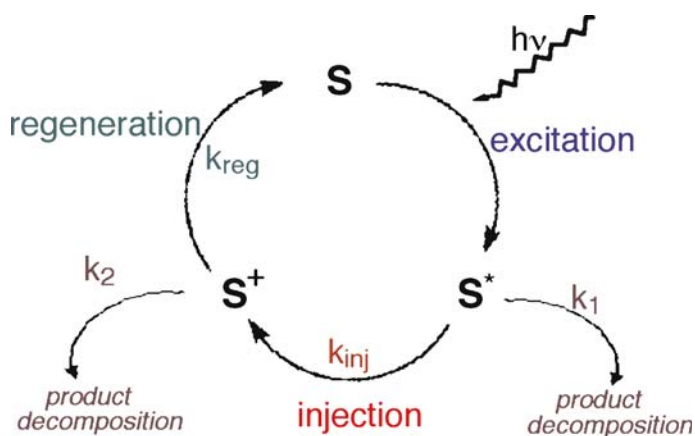


**Fig. 20** Catalytic cycle of the sensitizer during cell operation

For most of the common sensitizers, the rate constant for electron injection from the excited state to the conduction band of the  $\text{TiO}_2$  particles is in the femtosecond range. Assuming  $k_{inj} = 1 \times 10^{13} \text{ s}^{-1}$ , any destructive side reaction should have  $k_1 < 10^5 \text{ s}^{-1}$ . Ru sensitizers of the type **26** and **18** readily satisfy this condition as the decomposition from the excited state level occurs at a much lower rate than the  $10^5 \text{ s}^{-1}$  limit. Precise kinetic information has also been gathered for the second destructive channel involving the oxidized state of the sensitizer, the key parameter being the ratio  $k_2/k_{reg}$  of the rate constants for the degradation of the oxidized form of the sensitizer and its regeneration. The  $S^+$  state of the sensitizer can be readily produced by chemical or electrochemical oxidation and its lifetime determined independently

by absorption spectroscopy. A typical value of  $k_2$  is around  $10^{-4} \text{ s}^{-1}$  while the regeneration rate constant is at least in the  $10^5 \text{ s}^{-1}$  range. Hence the branching ratio is well below the limit of  $10^{-8}$ , which can be tolerated to achieve the 100 million turnovers and a 20 year lifetime for the sensitizer.

Many long-term tests have been performed with the N3-type Ru complexes, confirming the extraordinary stability of these charge transfer sensitizers. For example, a European consortium supported by the Joule program [72] has confirmed cell photocurrent stability over 8500 h of light soaking at 2.5 suns, corresponding to ca. 56 million turnovers of the dye without any significant degradation. These results corroborate the projections from the kinetic considerations made above. A more difficult task has been to reach stability under prolonged stress at higher temperatures, i.e., 80–85 °C. The recent introduction of hydrophobic sensitizers has been particularly rewarding in this regard by allowing the dye-sensitized solar cell to meet, for the first time, the specifications laid out for outdoor applications of silicon photovoltaic cells [73]. In addition, these dyes show enhanced extinction coefficients due to the extension of the  $\pi$ -conjugation on one of the bipy ligands by styrene moieties. Taking advantage of these properties and using a novel robust electrolyte formulation, a  $\geq 8\%$  efficiency dye-sensitized solar cell has been realized showing strikingly stable performance under both prolonged thermal stress and light soaking [47]

While impressive progress has been made in the development of stable, non-volatile electrolyte formulations, the conversion yields obtained with these systems are presently in the 7–10% range, i.e., below the 11.1% reached with volatile solvents. Future research efforts will be dedicated to bridge the performance gap between these systems. The focus will be on hole conductors and solvent-free electrolytes such as ionic liquids. The latter are a particularly attractive choice for the first commercial modules, due to their high stability, negligible vapor pressure and excellent compatibility with the environment.

## 1.9

### **Pilot Production of Modules, Outdoor Field Tests and Commercial DSC Development**

Figure 21 shows two prototypes of the monolithic Z-type interconnected modules, fabricated by Aisin Seiki in Japan. Note that carbon is used as a back contact to cut cost. Field tests of such modules already started several years ago and the results of these tests revealed advantages of the DSC with regards to silicon panels under realistic outdoor conditions. Thus, for equal rating under standard test conditions the DSC modules produced 20–30% more energy under real outdoor conditions than the polycrystalline silicon (pc-Si) modules. A photograph of the test station comparing the two types of photovoltaic technologies is shown in Fig. 22. The superior performance of the DSC can be ascribed to the following factors:

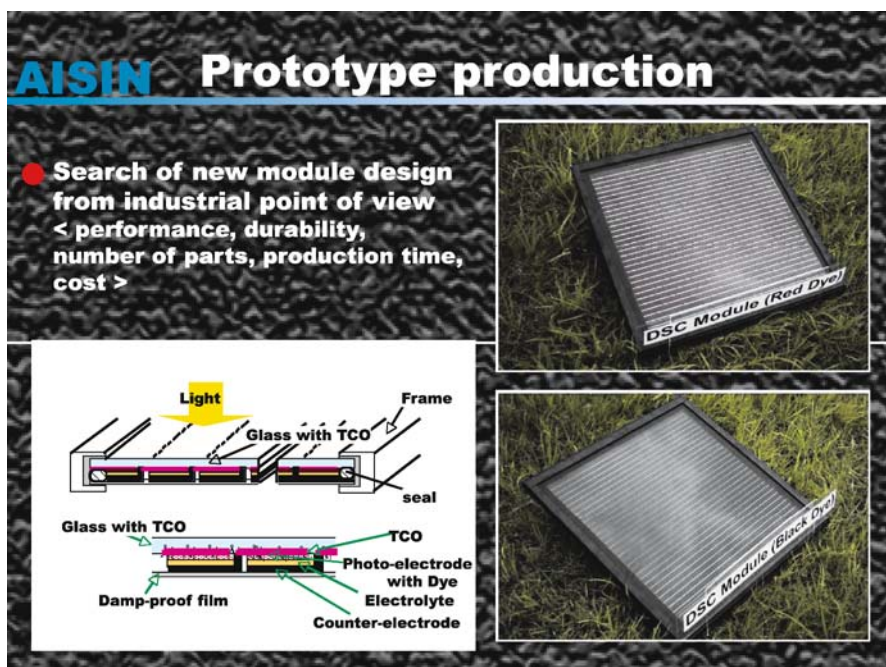


**Fig. 21** Production of DSC prototypes by Aisin Seiki in Japan. Note the monolithic design of the photovoltaic modules and the use of carbon as interconnect and counter electrode material

- The DSC efficiency is practically independent of temperature in the range 25–65 °C while that of mono- and pc-Si declines by ca. 20% over the same range
- Outdoor measurements indicate that the DSC exhibits lower sensitivity to light capture as a function of the incident angle of the radiation, although this needs to be further assessed
- The DSC shows higher conversion efficiency than pc-Si in diffuse light or cloudy conditions

While it is up to the commercial supplier to set the final price for such modules it is clear that the DSC shares the cost advantage of all thin film devices. In addition, it uses only cheap and readily available materials. Finally, in contrast to amorphous silicon and CIGS cells the DSC avoids high vacuum production steps that are very cost intensive. Given these additional advantages at comparable conversion efficiency, module costs below 1 € are realistic targets even for production plants having well below gigawatt capacity. The DSC has thus become a viable contender for large-scale future solar energy conversion systems on the bases of cost, efficiency, stability, and availability as well as environmental compatibility.



**Fig. 22** Outdoor field tests of DSC modules in Kariya City Japan at lat. 35°10'N, Azimuthal angle 0°, facing due south, tilted at 30°. Note the pc-Si modules in the *second row*



**Fig. 23** The Toyota “Dream House” featuring DSC panels made by Aisin Seiki

DSC panels have also been installed in the walls of the Toyota “Dream House” ([http://www.toyota.co.jp/jp/news/04/Dec/nt04\\_1204.html](http://www.toyota.co.jp/jp/news/04/Dec/nt04_1204.html)) shown in Fig. 23, offering a building-integrated source of solar power to the inhabitants. Very recently the British company G24I has announced the building of the first 20 MW DSC manufacturing plant in Wales (<http://www.G24I.com>).

### 1.9.1

#### Outlook

Using a principle derived from natural photosynthesis, mesoscopic injection solar cells and in particular the DSC have become a credible alternative to solid-state p-n junction devices. Conversion efficiencies over 11% and 15% have already been obtained with single junction and tandem cells, respectively, on the laboratory scale, but there is ample room for further amelioration. Future research will focus on improving the  $J_{SC}$  by extending the light response of the sensitizers in the near IR spectral region. Substantial gains in the  $V_{oc}$  are expected from introducing ordered oxide mesostructures and controlling the interfacial charge recombination by judicious engineering on the molecular level. Hybrid cells based on inorganic and organic hole conductors are an attractive option in particular for the flexible DSC embodiment. Nanostructured devices using purely inorganic components will be developed as well. The mesoscopic cells are well suited for a whole realm of applications ranging from the low power market to large-scale applications. Their excellent performance in diffuse light gives them a competitive edge over silicon in providing electric power for stand-alone electronic equipment both indoor and outdoor. Application of the DSC in building-integrated photovoltaics has already started and will become a fertile field of future commercial development. Almost 100 years ago, at the 1912 IUPAC conference in Washington, the famous Italian photochemist Professor Giacomo Ciamician from the University of Bologna predicted that mankind will unravel the secrets of photosynthesis and apply the principles used by plants to harvest solar energy in glass buildings. His visionary thoughts appear now close to becoming a reality.

## 2

### Iridium Complexes as Triplet Emitters in Organic Light-Emitting Diodes

#### 2.1

##### Introduction

Iridium(III) cyclometalated complexes are attracting widespread interest because of their unique photophysical properties and applications in organic light-emitting diodes (OLEDs). Several groups have used extensively neu-



tral Ir cyclometalated complexes in OLEDs and obtained up to 19% external quantum efficiencies, which require a complicated multilayered structure for charge injection, transport, and light emission [74–77]. An attractive alternative to the OLEDs is the light-emitting electrochemical cell (LEC) [78–82], which is particularly promising for large-area lighting applications. In these cells the use of ionic complexes facilitates electronic charge injection into the light-emitting film [78, 83, 84]. The main requirements for OLEDs and LECs are that the phosphorescent emitter should have sharp colors in the red, green and blue region, and exhibit very high phosphorescent quantum yields. Tuning phosphorescence wavelength, and enhancing phosphorescent quantum yields in these complexes in a predictable way is a daunting task, which of course is attractive for both fundamental research and practical applications [77, 85–89].

A strategy to tune the emission color in Ir(III) complexes relies on the selective HOMO stabilization and/or LUMO destabilization of the complex. Mixed ligand Ir complexes with C<sup>^</sup>N cyclometalating ligands, are particularly appealing in this respect, since the two types of ligands can be almost independently functionalized to obtain the desired color tuning [90]. In particular, electron-withdrawing substituents on the C<sup>^</sup>N ligands decrease the donation to the metal and therefore stabilize the metal-based HOMO. Electron-releasing substituents on the C<sup>^</sup>N ligand, lead, on the other hand, to destabilization of the ligand-based LUMO, ultimately leading to increased HOMO–LUMO gaps and emission energies. Much less clear are the factors that determine the emission quantum yields in mixed ligand complexes and on which parameters to act in order to increase them. It is indeed generally assumed that emission quantum yields should increase with increasing emission energy, due to the increase of the radiative rate constant and decrease of the non-radiative rate constants. These follow, respectively, the Einstein law of spontaneous emission [91] and the so-called energy gap law [92], even though exceptions to these rules are quite common.

## 2.2

### Photophysical Properties

The photophysics of polypyridyl complexes of Ir can be understood with the aid of an energy level diagram, as shown in Fig. 24. In these complexes there are three possible types of excited states: (a) metal-centered (MC) excited states, which are due to promotion of an electron from  $t_{2g}$  to  $e_g$  orbitals; (b) ligand-centered (LC) states that are  $\pi$ – $\pi^*$  transitions; (c) MLCT states. An electronic transition from metal  $t_{2g}$  orbitals to empty ligand orbitals without spin change is allowed, which is called singlet–singlet absorption. The allowed transitions are identified by large extinction coefficients. The transitions with spin change are called singlet–triplet absorption, which are forbidden and associated with small extinction coefficients. However, the ex-

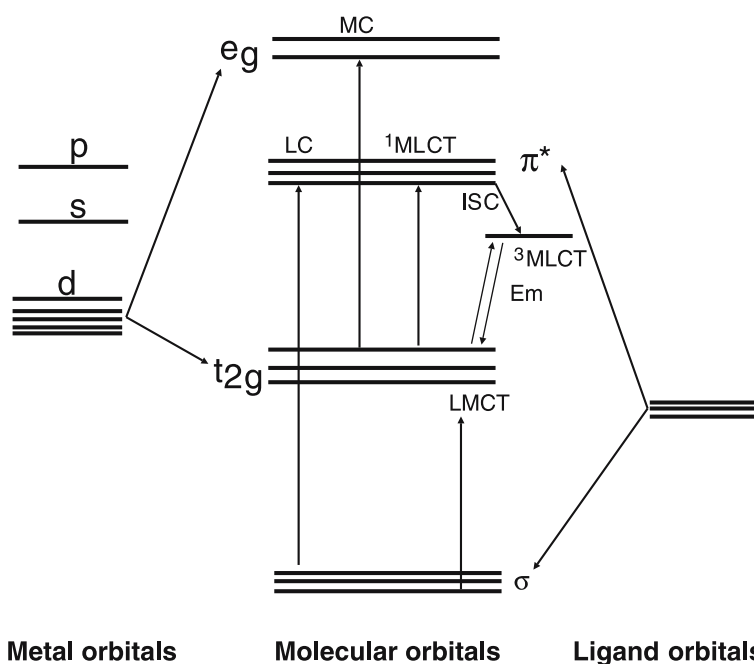


**Fig. 24** Schematic and simplified molecular orbital diagram for an octahedral  $d^6$  metal complex involving 2-phenylpyridine ( $C_3$  symmetry)-type ligands in which various possible transitions are indicated

cited singlet state may be involved in spin flip, which is called intersystem crossing (ISC), resulting in an excited triplet state. The radiative process of a singlet and triplet excited state to a singlet ground state are termed fluorescence and phosphorescence, respectively. The excited singlet states associated with LC  $\pi-\pi^*$  and MLCT transition can undergo ISC into the triplet state efficiently in Ir complexes due to spin-orbit coupling, resulting in enhanced phosphorescence quantum yields. For the cyclometalated Ir complexes, the wave function of the excited triplet state, responsible for phosphorescence, is principally expressed as a combination of the LC and the MLCT excited triplet state. However, not all the complexes are highly luminescent because of the different deactivation pathways.

### 2.3

#### Tuning of Phosphorescence Colors in Neutral Iridium Complexes

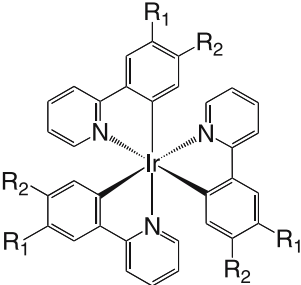
Neutral Ir complexes were obtained by an orthometalation reaction with ligands that contain a benzene ring attached to a functional group containing a donor atom such as 2-phenylpyridine (ppy) and benzo[h]-quinoline (bzq) [93]. The coordination of ppy and bzq ligands to metal is analogous to

that found in 2,2'-bipyridine except that nitrogen is replaced by carbon anion [94]. In a typical example, three ppy ligands coordinate around Ir(III) resulting in a neutral complex, in which the phenyl group carries a formal negative charge due to loss of proton and subsequent orthometalation to Ir metal. The HOMO in tris-phenylpyridine Ir(III) [Ir(ppy)<sub>3</sub>] is principally composed of orbitals of the phenyl ring and the metal d orbitals. The pyridine is formally neutral and is the major contributor to the LUMO in the [Ir(ppy)<sub>3</sub>] complex [95].

The absorption spectra of [Ir(ppy)<sub>3</sub>] display strong ligand-to-ligand (LC,  $\pi-\pi^*$ ) and MLCT transitions in the UV and the visible region, respectively. The MLCT transition bands are lower in energy than the LC  $\pi-\pi^*$  transitions. The excited triplet state shows strong phosphorescence in the green region at around 515 nm, with an excited state lifetime of 2  $\mu$ s [96].

In order to tune the phosphorescence color of [Ir(ppy)<sub>3</sub>], Watts et al. synthesized several substituted ppy-based neutral Ir complexes [96–98]. Table 1 shows the list of complexes that show strong phosphorescence from a <sup>3</sup>MLCT excited state. The phosphorescence lifetime of these complexes is in the range of 2–3  $\mu$ s in nitrogen-saturated acetonitrile at room temperature [97]. The photophysical and electrochemical data (see Table 1) demonstrate the influence of ligands bearing electron-withdrawing and the electron-donating

**Table 1** Emission, lifetime, and electrochemical data of complexes 27–34

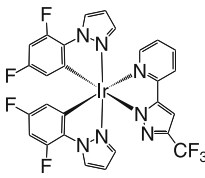
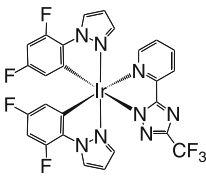
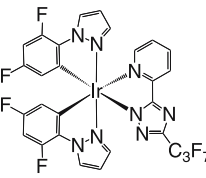
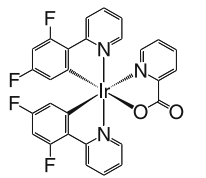
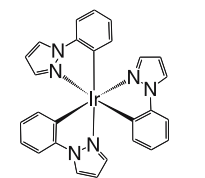
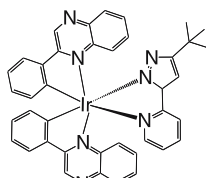
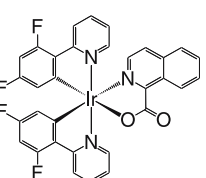
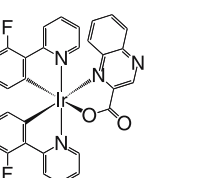


27 : R<sub>1</sub>=H ; R<sub>2</sub>=H  
 28 : R<sub>1</sub>=H ; R<sub>2</sub>=CH<sub>3</sub>  
 29 : R<sub>1</sub>=H ; R<sub>2</sub>=C<sub>3</sub>H<sub>7</sub>  
 30 : R<sub>1</sub>=H ; R<sub>2</sub>=tBu  
 31 : R<sub>1</sub>=H ; R<sub>2</sub>=F  
 32 : R<sub>1</sub>=H ; R<sub>2</sub>=CF<sub>3</sub>  
 33 : R<sub>1</sub>=H ; R<sub>2</sub>=OCH<sub>3</sub>  
 34 : R<sub>1</sub>=OCH<sub>3</sub> ; R<sub>2</sub>=H

Complex	Emission $\lambda_{\max}$ (nm)	Lifetime $\tau$ ( $\mu$ s)	Potential vs. SCE $E_{1/2ox}$ (V)	Potential vs. Fc <sup>+0</sup> (V)
27	494	1.9	0.77	0.37
28	493	1.9	0.70	0.30
29	496	1.9	0.67	0.27
30	497	2.0	0.66	0.26
31	468	2.0	0.97	0.57
32	494	2.2	1.08	0.68
33	481	2.2	0.75	0.35
34	539	2.9	0.55	0.15

substituents. It is interesting to note the difference between complexes **33** and **34** (Table 1), which is simply the effect of the position of electron-donating substitution on the phenyl ring. In complex **34** the electron-donating group is substituted at the 3-position of the phenyl ring. This destabilizes the HOMO by 0.2 V as compared to complex **33** in which the electron-donating group is substituted at 4-position. The HOMO of a ppy cyclometalated Ir complex is located primarily on the phenyl groups, therefore incorporation of an electron-donating substituent in the positions *para* to the Ir-carbon bond decreases the emission energy due to a *mesomeric* (oxygen lone pair donation to the aromatic  $\pi$  orbitals) effect. From the electrochemical data of the complexes shown in Table 1, it is evident that the less positive oxidation potential values result from ligands with electron-donating substituents, and more pos-

**Table 2** Absorption, emission, and electrochemical properties of the iridium complexes 35–42

Complex	Absorption $\lambda_{\max}$ (nm)	Emission <sup>a</sup> $\lambda_{\max}$ (nm)	Potential vs. $\text{Fc}^{+/0}$		Lifetime ( $\mu\text{s}$ )
			$E_{1/2\text{ox}}$ (V)	$E_{1/2\text{red}}$ (V)	
	295, 349	455	0.98	– 2.72	0.040
	300, 349	457	1.11	– 2.72	0.008
	302, 348	455	1.11	– 2.53	0.009
	–	468	1.00	– 1.9	–
	321	444	0.41	– 3.20	–
	359, 469	649	0.77	– 1.71	1.9
	–	581	1.00	– 1.2	–
	–	666	1.00	– 1.1	–

<sup>a</sup> Emission data were collected at 298 K

itive oxidation potential values result from ligands with electron-withdrawing substituents.

In these complexes the photophysical properties are very similar to the ppy-based Ir complexes because of substitution of electron-donating or electron-withdrawing groups on the phenyl ring. This is not surprising because the substitution of donor or acceptor groups tunes both the HOMO and LUMO levels of the metal complex to move in the same direction, leading to marginal changes in the photophysical properties.

In the mixed ligand complexes (35–38 shown in Table 2) the HOMO levels have been stabilized significantly compared to the tris(ppy)Ir(III) complex, leading to blue shifts of the emission maxima, which is also apparent from the electrochemical data [87, 99]. On the other hand, the blue shift of the emission maxima in complex 39 is due to destabilization of LUMO of the 1-phenylpyrazolyl ligand. Several other groups have developed heteroleptic Ir complexes (see Table 2), in which the LUMO levels were stabilized (see Table 2 for  $E_{\text{red}}^{1/2}$  values of complexes 40–42) compared to the tris(ppy)Ir(III) complex, leading to phosphorescent color maxima from green to red [89, 98–105]. Therefore, the compounds in Table 2 provide an exciting opportunity to tune the emission spectral properties from blue to red by simply selecting appropriate donor/acceptor ligands compared to the tris-homoleptic complexes of the type shown in Table 1.

## 2.4

### Tuning of Phosphorescence Colors in Cationic Iridium Complexes

The tuning aspect of the MLCT transitions in cationic Ir complexes is illustrated by considering the following complexes: [Ir(2-phenylpyridine)<sub>2</sub>(4,4'-*tert*-butyl-2,2'-bipyridine)]PF<sub>6</sub> (43), [Ir(2,4-difluorophenylpyridine)<sub>2</sub>(4,4'-dimethylamino-2,2'-bipyridine)]PF<sub>6</sub> (44), and [Ir(2-phenylpyridine)<sub>2</sub>(4,4'-dimethylamino-2,2'-bipyridine)]PF<sub>6</sub> (45). These complexes were synthesized in a low-boiling solvent, dichloromethane, by reacting the corresponding dichloro-bridged Ir(III) dimer with 4,4'-*tert*-butyl-2,2'-bipyridine or 4,4'-dimethylamino-2,2'-bipyridine ligands (see Table 3) [106].

The cyclic voltammogram of complex 45 (Fig. 25) measured in acetonitrile containing 0.1 M tetrabutylammonium hexafluorophosphate with 100 mV s<sup>-1</sup> scan rate shows a reversible wave at 0.72 V vs. Fc<sup>+ / 0</sup> due to oxidation of Ir(III) to Ir(IV), which is cathodically shifted by 210 mV compared to complex 43 due to the donor strength of 4,4'-dimethylamino-2,2'-bipyridine (Klein et al., unpublished data and [78, 106]). The three reversible reduction waves at -2.17 and -2.61 and -2.87 V vs. Fc<sup>+ / 0</sup> (only two waves are shown in Fig. 25) are assigned to the reduction of 4,4'-dimethylamino-2,2'-bipyridine and the two ppy ligands, respectively. It is interesting to note that the ligand-based reduction potential of 45 is significantly shifted cathodically (390 mV) compared to complex 43, demonstrating that the destabilization of

**Table 3** Absorption, emission, and electrochemical properties of cationic iridium complexes **43**, **44**, and **45**

Complex	Absorption <sup>a</sup>	Emission <sup>b</sup>	Potential <sup>c</sup>	vs. Fc <sup>+/0</sup> Lifetime <sup>d</sup>	
	$\lambda_{\max}$ (nm)	$\lambda_{\max}$ (nm)	$E_{1/2ox}$ (V)	$E_{1/2red}$ (V)	( $\mu s$ )
<b>43</b>	–	581 <sup>e</sup>	0.88 <sup>e</sup>	– 1.83 <sup>e</sup>	0.557 <sup>e</sup>
<b>44</b>	266 (8.27), 316 (2.89), 344 (2.20); 376 (1.45), 410 (0.41), 444 (0.14)	463, 493	1.0	– 2.13 – 2.49 – 2.77	4.11 ± 0.02
<b>45</b>	268 (5.62), 290 (3.49), 356 (0.95), 376 (0.85), 444 (0.19)	491, 520	0.72	– 2.17 – 2.61 – 2.87	2.43 ± 0.02

<sup>a</sup> Absorption data were measured in CH<sub>2</sub>Cl<sub>2</sub> solution. Brackets contain values for molar extinction coefficient ( $\epsilon$ ) in 10<sup>4</sup> M<sup>-1</sup> cm<sup>-1</sup>

<sup>b</sup> Emission data were collected at 298 K by exciting at 380 nm

<sup>c</sup> Electrochemical measurements were carried out in acetonitrile solution and the potentials are V vs. ferrocenium/ferrocene (Fc<sup>+/0</sup>)

<sup>d</sup> Lifetime data are collected in degassed solutions

<sup>e</sup> Data taken from [78]

the LUMO orbitals of 4,4'-dimethylamino-2,2'-bipyridine offsets more than the destabilization of the Ir HOMO orbitals caused by the electron-donating 4,4'-dimethylamino-2,2'-bipyridine ligand, ensuing an increase in the gap between the HOMO and the LUMO of **45** compared to the HOMO–LUMO gap of complex **43**.

The cyclic voltammogram of complex **44** shows a reversible couple at 1.0 V vs. Fc<sup>+/0</sup> due to oxidation of Ir(III) to Ir(IV), and two reversible reduction waves at – 2.13 and – 2.49 V vs. Fc<sup>+/0</sup> arising from the reduction of the 4,4'-dimethylamino-2,2'-bipyridine and 2-(2,4-difluorophenyl)pyridine ligand, respectively. The HOMO orbitals in **44** are stabilized upon insertion of fluoro substituents on the ppy ligands, thus ensuing an increase of the HOMO and LUMO gap of **44** compared to the HOMO and LUMO gap of **43** and **45** (Table 3) [106].

UV-Vis absorption spectra of the complexes **43**, **44**, and **45** in dichloromethane solution at 298 K display bands in the UV and the visible region

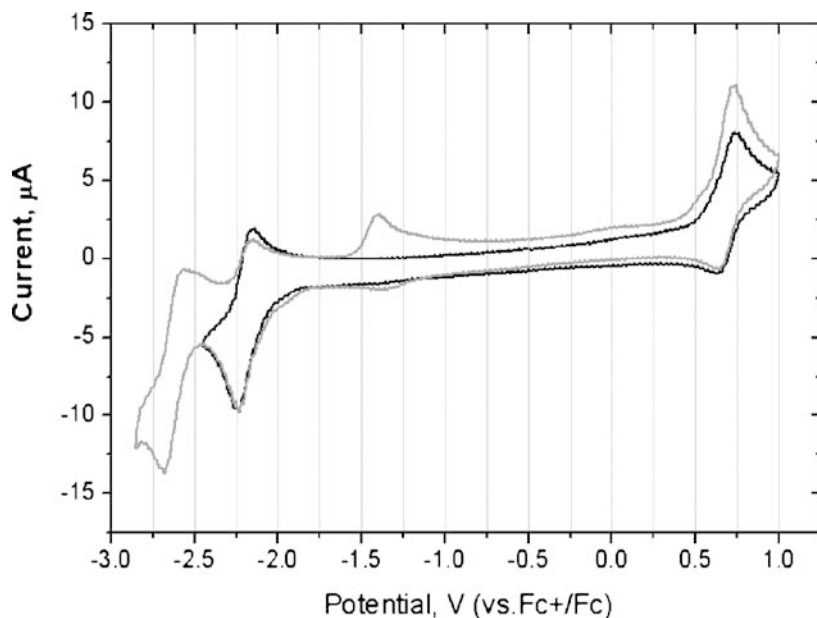


**Fig. 25** Cyclic voltammogram of complex 45 measured in acetonitrile in the presence of 0.1 M tetrabutylammonium hexafluorophosphate as supporting electrolyte with  $100 \text{ mV s}^{-1}$  scan rate. The *black line* shows the scan between  $-2.4$  to  $1 \text{ V}$ , and the *gray line* between  $-2.8$  to  $1 \text{ V}$ . The observed irreversible new wave at around  $-1.35 \text{ V}$  is due to unknown product that is formed when scanning to more negative potential

due to intraligand ( $\pi-\pi^*$ ) and MLCT transitions, respectively (Fig. 26 and Table 3) [107]. When excited at 298 K within the  $\pi-\pi^*$  or MLCT absorption bands, complex 44 shows emission maxima at 463 and 493 nm due to the 4,4'-

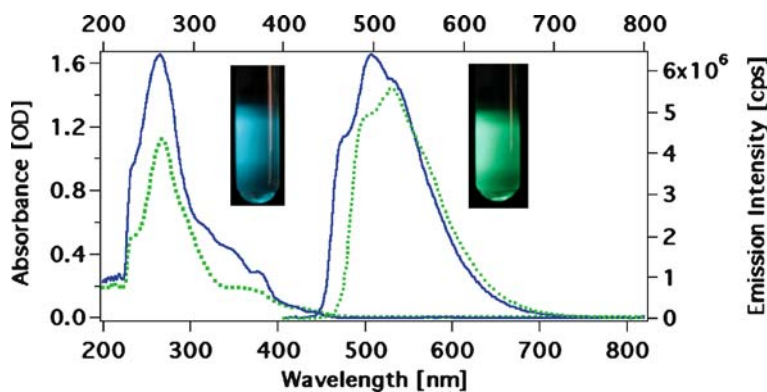


**Fig. 26** Absorption and emission spectra of 44 (*solid line*) and 45 (*dashed line*) in dichloromethane solution at 298 K

dimethylamino-2,2'-bipyridine ligand that increases the gap between LUMO of 4,4'-dimethylamino-2,2'-bipyridine and HOMO of Ir, resulting in a blue shift of the emission maxima compared to **43** [78, 96].

It is worth noting that the argon-degassed dichloromethane solutions of **44** and **45** show bright luminescence in a lighted room, and display unusual phosphorescence quantum yields of  $80 \pm 10\%$  in solution at room temperature. The emission spectral profile is independent of excitation wavelength, and the emission of **44** and **45** decayed as a single exponential with lifetimes of 2 and 4  $\mu\text{s}$  in dichloromethane solution, respectively [108].

The electronic structures of these complexes based on DFT calculations, together with plots of selected molecular orbitals are shown in Fig. 27. The HOMO in these complexes is an antibonding combination of Ir( $t_{2g}$ ) and ppy( $\pi$ ) orbitals, and is calculated at  $-5.50$  and  $-5.66$  eV for **44** and **43**, respectively (De Angelis et al., unpublished data). The LUMO of both complexes is a  $\pi^*$  orbital localized on the 4,4'-dimethylamino-2,2'-bipyridine ligand and is calculated at  $-2.49$  and  $-2.3$  eV for **43** and **44**, respectively. At higher energy, the LUMO is followed by an almost degenerate couple of ppy  $\pi^*$  orbitals, whose energies approach that of the 4,4'-dimethylamino-2,2'-bipyridine  $\pi^*$  LUMO on going from **43**, **45** to **44**.

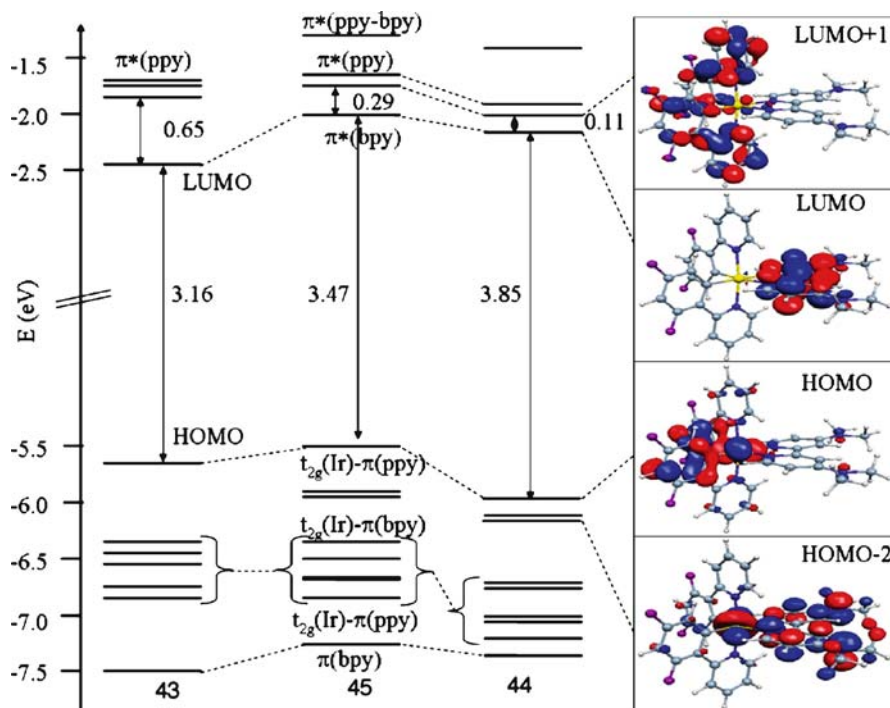


**Fig. 27** Energy and character of the frontier molecular orbitals of **43**, **45**, and **44** complexes. Also shown are isodensity plots of selected molecular orbitals



## 2.5

### Tuning of Phosphorescence Colors in Anionic Iridium Complexes

The tuning aspects of phosphorescence colors in anionic Ir complexes are illustrated using the following representative complexes: The  $(\text{C}_4\text{H}_9)_4\text{N}[\text{Ir}(\text{2-phenylpyridine})_2(\text{CN})_2]$  (**46**),  $(\text{C}_4\text{H}_9)_4\text{N}[\text{Ir}(\text{2-phenyl-4-dimethylaminopyridine})_2(\text{CN})_2]$  (**47**),  $(\text{C}_4\text{H}_9)_4\text{N}[\text{Ir}(\text{2-(2,4-difluorophenyl)-pyridine})_2(\text{CN})_2]$  (**48**),  $(\text{C}_4\text{H}_9)_4\text{N}[\text{Ir}(\text{2-(2,4-difluorophenyl)-4-dimethylaminopyridine})_2(\text{CN})_2]$  (**49**), and  $(\text{C}_4\text{H}_9)_4\text{N}[\text{Ir}(\text{2-(3,5-difluorophenyl)-4-dimethylaminopyridine})_2(\text{CN})_2]$  (**50**) (Klein et al., unpublished data). All these complexes were conveniently synthesized in low-boiling dichloromethane by reaction of the dichloro-bridged Ir(III) dimer with tetrabutylammonium cyanide. The crystal structure of complex **46** shows that the cyanide ligands coordinate through the carbon atom and adopt a *cis* configuration (Fig. 28).

Table 4 shows a comparison of the photophysical and electrochemical properties of complexes **46–50** that were measured in dichloromethane solution at 298 K. When these complexes are excited within the  $\pi-\pi^*$  and MLCT

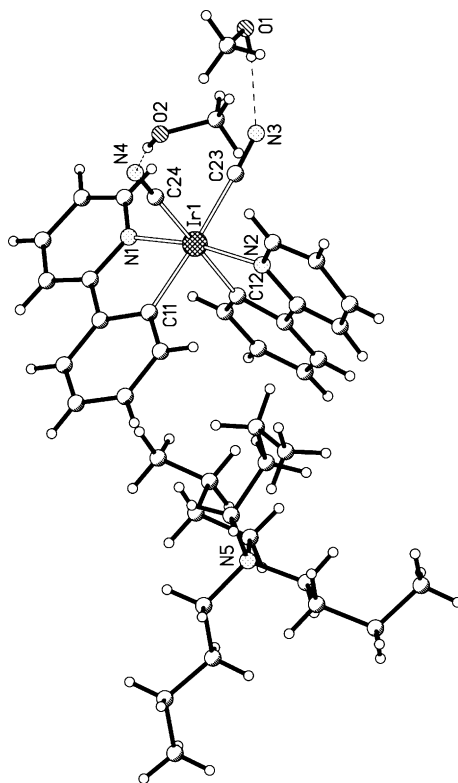


**Fig. 28** Crystal structure of  $(\text{C}_4\text{H}_9)_4\text{N}[\text{Ir}(\text{2-phenylpyridine})_2(\text{CN})_2]$  **46**

**Table 4** Structures, absorption, emission, quantum yields, lifetime, and electrochemical data of complexes **46–50** measured at 298 K in dichloromethane solution

Complex	Absorption <sup>a</sup>	Emission <sup>b</sup>	Lifetime	Potential vs. Fc <sup>+0</sup>	
	$\lambda_{\max}$ (nm)	$\lambda_{\max}$ (nm)	$E_{1/2ox}$ ( $\mu$ s)	$E_{1/2red}$ (V)	(V)
<b>46</b>	260 (41.7), 337 (0.85), 384 (0.58), 433sh (0.61) 463 (0.21)	470, 502	3.3	0.55	– 2.69
<b>47</b>	272 (3.79), 302sh (2.21), 332 (1.07), 354 (0.89), 380 (0.59)	465, 488	2.0	0.33	– 3.0
<b>48</b>	254 (6.04), 290 (2.79), 362 (0.78), 390 (0.38)	460, 485	3.3	0.96	– 2.6
<b>49</b>	266 (2.83), 290 (2.63), 302 (2.38), 338 (1.32), 360 (1.08)	451, 471	1.4	0.58	– 2.98
<b>50</b>	268 (5.25), 288 (4.20), 302sh (3.22), 356 (1.52), 378 (0.95)	468, 492	3.0	0.53	– 2.8

<sup>a</sup> Brackets contain values for molar extinction coefficient ( $\epsilon$ ) in  $10^4 \text{ M}^{-1} \text{ cm}^{-1}$

<sup>b</sup> Emission spectra were obtained from degassed solutions by exciting into the lowest MLCT band

absorption bands, they show emission maxima in the blue and yellow regions of the visible spectra. The air-equilibrated dichloromethane solutions exhibit shorter luminescence lifetimes (70–90 ns) compared to the degassed solutions (1–3  $\mu$ s). It is apparent from the photoluminescence data, which were obtained by exciting at 380 nm, that the complexes **46–50** show a color range from brilliant blue to yellow, unraveling the tuning aspect of the HOMO and the LUMO levels.

The LUMO levels of complex **47** are destabilized by incorporating dimethylamino group at the 4-position of pyridine. In complex **48** the HOMO levels are stabilized by insertion of fluoro substituents on the phenyl ring of the ppy ligand. However, in complex **49** both aspects (i.e., destabilization of the LUMO orbitals by incorporating a dimethylamino group at the 4-position of pyridine together with stabilization of HOMO orbitals by insertion of fluoro substituents on the phenyl of the ppy ligand) lead to an increase of the HOMO–LUMO gap accompanied by a blue shift of the emission spectra. Figure 29 shows a representative absorption and emission spectra of complex **49** measured in dichloromethane solution at 298 K. The complex displays bands in the UV and the visible region due to intraligand ( $\pi$ – $\pi^*$ ) and MLCT transitions, respectively [107]. When excited within the  $\pi$ – $\pi^*$  and MLCT absorption bands at 298 K, complex **49** shows emission maxima at 450 and

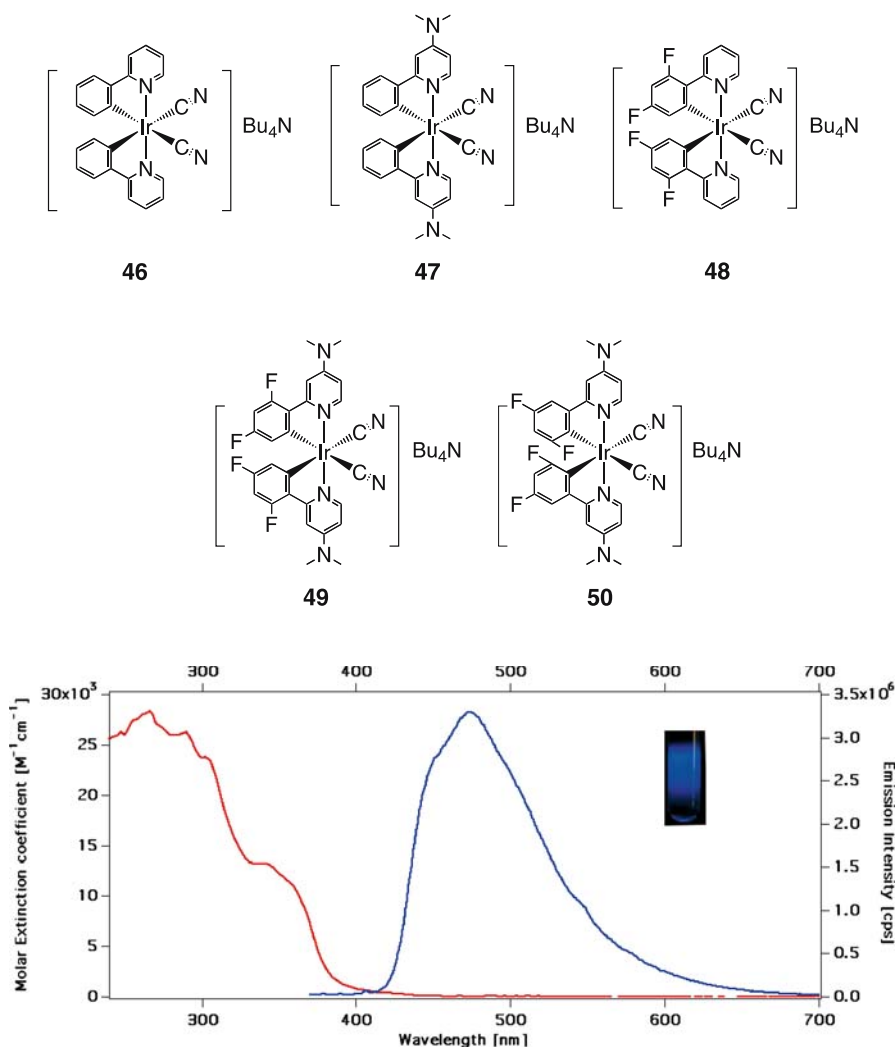


**Fig. 29** Absorption (red line) and emission (blue line) spectra of complex **49** in dichloromethane solution at 298 K. The insert shows a photo of a solution of **49** exhibiting very strong blue emission upon excitation at 380 nm

473 nm due to the 2,4-difluorophenyl-4-dimethylaminopyridine ligand that increases the HOMO–LUMO gap resulting in a blue shift of the emission maxima compared to complexes **47** and **48**.

The difference between complexes **49** and **50** is only in the position of the fluoro substituent on the phenyl ring of the ppy ligand, which are at the 2,4-position in the former and the 3,5-position in the latter. The emission maxima of complex **50** is significantly red-shifted compared to complex **49**, demon-

strating the influence of substituent position on the photophysical properties. One possible explanation for this astonishing spectral shift of complex **50** compared to complex **49** is that the fluoro groups at the 3,5-position act as electron-releasing groups, destabilizing the metal HOMO orbitals and thereby decreasing the HOMO–LUMO gap. In complex **49**, the fluoro groups are at the 2,4-positions and act as electron-withdrawing groups, resulting in stabilization of HOMO orbitals and thereby increasing the HOMO–LUMO gap.

### 2.5.1

#### Phosphorescent Color Shift in Anionic Iridium Complexes by Tuning of HOMO Levels

Figure 30 shows schematically the concept of HOMO level tuning in Ir pseudohalogen complexes of the type  $\text{TBA}[\text{Ir}(\text{ppy})_2(\text{CN})_2]$  (**46**),  $\text{TBA}[\text{Ir}(\text{ppy})_2$

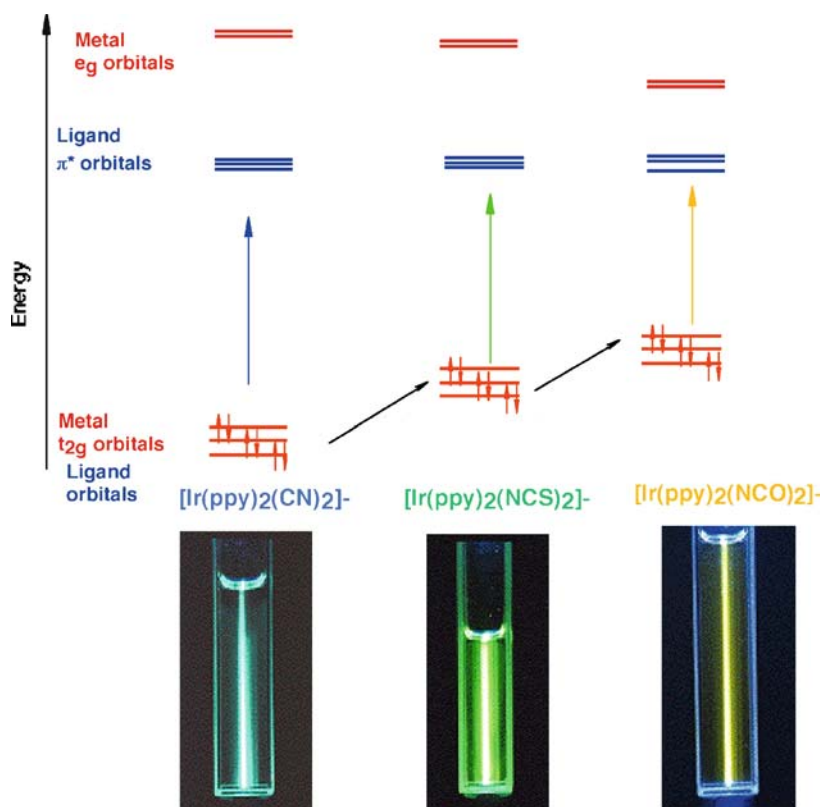


**Fig. 30** Schematic drawing of HOMO and LUMO orbitals for complexes **46**, **51**, and **52** and their phosphorescence properties, which were obtained by exciting at 415.4 nm using a krypton ion laser

(NCS)<sub>2</sub>] (**51**), and TBA[Ir(ppy)<sub>2</sub>(NCO)<sub>2</sub>] (**52**). These complexes were conveniently synthesized under inert atmosphere by reaction between the dichloro-bridged Ir dimer [Ir(ppy)<sub>2</sub>(Cl)]<sub>2</sub> in dichloromethane solvent with an excess of a pseudohalogen ligand such as tetrabutylammonium cyanide, tetrabutylammonium thiocyanate, or tetrabutylammonium isocyanate, respectively, with over 70% yields [77].

The cyclic voltammograms of **46**, **51**, and **52** show a quasi-reversible oxidation potential at 0.91, 0.45, and 0.18 V vs. ferrocenium-ferrocene, respectively. Changes in the electron-donating or electron-withdrawing nature of the ancillary ligands can result in a variation of electronic properties at the metal center. It is interesting to compare these three complexes that contain cyanide, thiocyanate, and isocyanate ligands. The 0.73 V anodic shift in oxidation potential of **46** compared to complex **52** shows the extent of  $\pi$  back-bonding to the cyanide ligand from the Ir(III) center. The enormous enhancement in  $\pi$  back-bonding leads to significant blue shift of the emission maxima of complex **46** compared to complexes **51** and **52**.

The absorption spectra of these complexes display bands in the UV and the visible region due to intraligand ( $\pi$ - $\pi^*$ ) and MLCT transitions, respectively [107]. The MLCT band in **46** (463 nm) is significantly blue-shifted compared to **51** (478 nm), and **52** (494 nm), indicating the extent of  $\pi$ -acceptor strength of the CN<sup>-</sup> ligand compared to the NCS<sup>-</sup> and NCO<sup>-</sup> ligands. The spectral shifts are consistent with the electrochemical data of these complexes. Hay has analyzed the spectral properties of Ir(III)ppy complexes using DFT, in which the low-lying transitions are categorized as MLCT transitions and the high-energy bands at above 280 nm are assigned to the intraligand

**Table 5** Emission, lifetime, and quantum yield data of complexes **46**, **51**, and **52** measured at 298 K in dichloromethane

Complex	Absorption <sup>a</sup> $\lambda_{\max}$ (nm)	Emission <sup>b</sup> $\lambda_{\max}$ (nm)	Emission $\phi_f$	Lifetime $\tau$ ( $\mu$ s)	Potential vs. Fc <sup>+0</sup> $E_{1/2ox}$ (V)
<b>46</b>	260 (41.7), 337 (0.85), 384 (0.58), 463 (0.21)	470, 502	0.94	3.1	0.91
<b>51</b>	266 (38.9), 335 (6.7), 355 (5.3), 400 (3.4), 476 (0.65),	506, 520	0.97	1.4	0.45
<b>52</b>	276 (35.1), 347 (6.62), 384 (4.22), 408 (3.41), 464 (2.36), 497 (1.26)	538, 560	0.99	0.8	0.18

<sup>a</sup> Brackets contain values for molar extinction coefficient ( $\epsilon$ ) in 10<sup>4</sup> M<sup>-1</sup> cm<sup>-1</sup>

<sup>b</sup> Emission spectra were obtained from degassed solutions by exciting into the lowest MLCT band

$\pi-\pi^*$  transitions of ppy [95]. Argon-degassed solutions of complexes **46**, **51** and **52**, when excited within the  $\pi-\pi^*$  and MLCT absorption band at 298 K, show emission maxima at 470, 506 and 538 nm, respectively with longer lifetimes (0.8–3.4  $\mu\text{s}$ ) (Table 5).

## 2.6

### Controlling Quantum Yields in Iridium Complexes

Orthometalated Ir complexes are known to have highest triplet emission quantum yields due to several factors [109, 110]:

- Ir has a large d-orbital splitting compared to other metals in the group
- Strong ligand field strength of the ppy anionic ligand increases the d-orbital splitting, leading to an enlarged gap between the  $e_g$  orbitals of Ir and the LUMO of the ligand
- Close-lying  $\pi-\pi^*$  and MLCT transitions, together with the heavy atom effect, enhance the spin-orbit coupling

However, the mixed ligand cationic Ir complexes show appreciably lower quantum yields compared to the tris-orthometalated Ir complexes because of the lower LUMO orbitals of the 2,2'-bipyridine ligand [78, 85, 96]. One strategy to increase the quantum yields of Ir complexes is to introduce F and/or  $\text{CF}_3$  substituents. This results in a stabilization of both the HOMO and the LUMO. Since the HOMO stabilization is larger than that of the LUMO, this leads to an increase in the gap between HOMO–LUMO [111]. Another strategy, however, is to decrease the gap between the lowest  $\pi^*$  orbitals of the ppy ligand and the 2,2'-bipyridine ligand by introducing donor substituents such as dimethylamino groups at the 4,4'-positions of 2,2'-bipyridine that are known to have a strong destabilization effect on the LUMO (see complexes **44** and **45**). In such type of complexes, the  $\pi-\pi^*$  and MLCT states associated with the ppy and 4,4'-dimethylamino-2,2'-bipyridine ligands are expected to be located closely together, which enhances the excited state decay through radiative pathways.

The quantum yields of complexes **44** and **45** were measured using recrystallized quinine sulfate in 1 N  $\text{H}_2\text{SO}_4$  and the widely referred complex  $\text{Ru}(\text{bpy})_3(\text{PF}_6)_2$  as quantum yield standards. The data obtained using both standards are in excellent agreement and indeed show yields that are remarkably high, i.e., 80%.

The quantum yields of Ir complexes can also be modulated by introducing ligands having strong ligand field stabilization energy, such as  $\text{NCS}^-$  and  $\text{CN}^-$ . In these complexes, the gap between the metal  $e_g$  and the ligand LUMO orbitals increases, resulting in a decay of the excited charge transfer states through radiative pathways [77].

## 2.7

### Application of Iridium Complexes in Organic Light Emitting Devices

Doping of the emitting layer of OLEDs with well-selected dye molecules is an established way to improve OLED performance. To clarify, in the context of this article, from what we understand doping is not the introduction of additional charges as in the classical semiconductor sense but rather the introduction of dye molecules with appropriate energy levels for color tuning. Besides this aspect, doping also leads to a change of the transport characteristics and to a considerable increase of the lifetime and of the quantum efficiency.

For a long time people thought that the luminescent dyes used since the work of Tang et al. are theoretically limited to an internal conversion efficiency of 25% [112]. This factor arises from quantum mechanics, where 75% of the charge wave functions are of the non-emissive triplet case and only 25% of the singlet case, allowing radiative recombination. Taken into account that only one-fifth of the created photons can leave the device, the external quantum efficiency was limited to 5% [113]. But, in contrast to this, the family of the so-called phosphorescent dyes (triplet emitters) permits the opening of an additional radiative recombination channel and harvesting of up to nearly 100% of the excited states to photon creation. Responsible for this is the presence of heavy metal atoms such as Pt or Ir [114], leading to a strong spin-orbit coupling. The common way of device realization is to mix small concentration of a highly phosphorescent guest into a host material with suitable charge transport abilities. Taking into account an unchanged out-coupling factor of one-fifth, the theoretical external quantum efficiency for the triplet dyes jumps up to 20%. Electrophosphorescence was shown for the first time by Hoshino et al. by mixing benzophenone into a poly(methylmethacrylate) host [115], but the quantum efficiency was still low. Meanwhile, quantum efficiencies up to the theoretical limits are reported in the literature [114].

Typical dye doping concentrations of singlet and triplet emitters are very different. For singlet emitters the efficient doping ratio is often limited to the range 0.5–2%, as for example 1.3% for Rubrene in tris(8-hydroxyquinolato)aluminum ( $\text{Alq}_3$ ) [116] or 0.7% for DEQ in  $\text{Alq}_3$  [117]. For triplet emitter dyes, doping ratios up to 10% or far above are possible without remarkable loss in quantum efficiency [118]. Increased doping concentrations of triplet emitters are desirable to prevent or reduce saturation effects at increased current densities due to the long lifetimes of the excited states [119]. But, high doping concentrations are accompanied by side effects. To have the dye molecules with appropriate behavior inside the matrix is one point; the other point is that the dye molecule should also be able to localize the exciton. In principle three techniques are discussed to get the exciton on the dye dopant: (i) endothermic energy transfer [120], (ii) exothermic energy trans-

fer [121], and (iii) charge trapping as it applies for heavily doped systems and for blue phosphorescent devices [119].

Another aspect is that large energy gap matrixes are desired to suppress both the electron and energy transfer pathways from the emissive dopant back to the host material [122]. Pai et al. observed the transition from hole hopping between host molecules to trap-controlled tunneling transport as a function of doping concentration [123]. At concentrations of the additive below 2 wt. %, the transport is dominated by the slow release of charges from the dye sites acting as charge traps. For concentrations above 2 wt. % hopping occurs via trap and host sites. As the trap concentration is further increased, the transport by tunneling via the additive sites becomes predominant.

The long lifetime of the triplet excitons enables them theoretically to diffuse significant distances. To reduce this, typical diode architectures, including phosphorescent emitters, require at least one more auxiliary layer (such as a hole blocking layer) than a fluorescent emitter containing diode. Further, the energy levels of the host should be significantly higher to localize the excitons on the dopant [119]. This approach will be discussed in the following section in more detail.

## 2.7.1

### Standard OLED Device Architecture

A typical multilayer device architecture containing triplet emitters is described in Fig. 31, and the resulting energy level scheme is shown in Fig. 32. ITO (indium tin oxide)-coated glass substrate is used as anode and on top of it a 10 nm thick CuPc (copper phthalocyanine) hole injection layer is

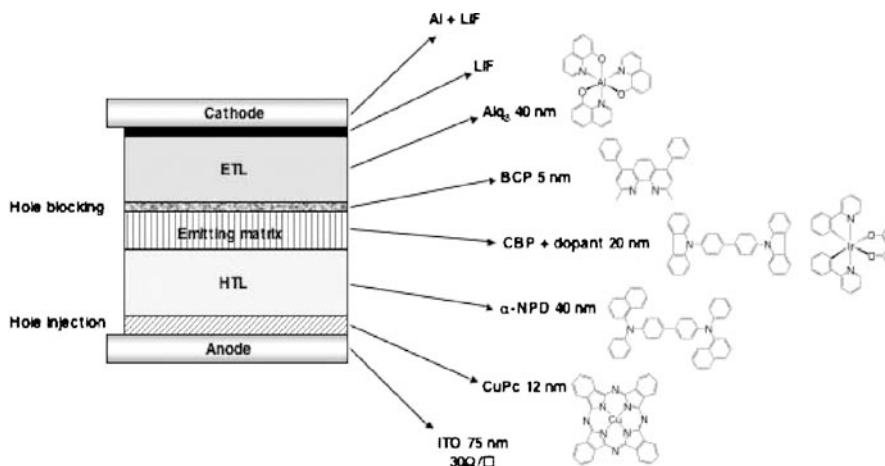


**Fig. 31** Cross-section of the OLED device



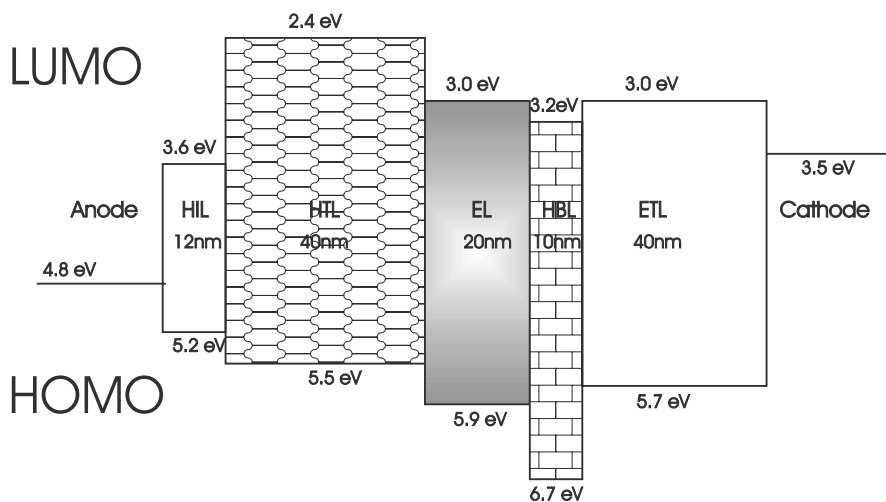


**Fig. 32** Typical electrophosphorescent multilayer device architecture composed of a hole injection layer (HIL), a hole transport layer (HTL), a emission layer (EL), a hole blocking layer (HBL), an electron blocking layer (EBL), and finally an electron transporting layer (ETL). Shown are the HOMO and LUMO energy levels of the corresponding molecules [77]. The vacuum level is assumed to be constant

deposited. Next, a 40 nm thick hole transport layer of  $\alpha$ -NPD (*N,N'*-diphenyl-*N,N'*-bis(1-naphthyl)-1,1'-biphenyl-4,4'-diamine) is evaporated, followed by a 20 nm layer of the wide energy-gap matrix of CBP (4,4'-bis(carbazol-9-yl)-biphenyl) co-evaporated with a constant rate of a phosphorescent emitter molecule. For hole blocking and resulting charge confinement in the emitting matrix layer, a 5 nm layer of BCP (2,9-dimethyl-4,7-diphenyl-phenanthroline) can be useful for quantum efficiency improvement. Finally, a 30–40 nm thick Alq<sub>3</sub> electron transport layer is deposited to improve the out-coupling efficiency [124] and to reduce exciton quenching by the metallic cathodes [114]. For performance improvement, the organics should be purified and thermally evaporated at a rate of  $1.0 \text{ \AA s}^{-1}$  at a base pressure lower than  $10^{-6}$  mbar. A well-working cathode for such architecture consists of a 0.8 nm LiF layer deposited right after the electron transporting layer (ETL) in combination with a 100 nm thick Al layer. To decrease contamination effects and impurity layers the whole fabrication should be done without breaking the vacuum. The active area of engineering segments is in the range 4–10 mm<sup>2</sup>.

The presented standard device architecture doped with different ratios of the phosphorescent emitter molecule [acetylacetonato-(bis(2-phenylpyridine) Ir(III))], labeled as complex 53, is used as a model case. Figure 33 shows the different current–voltage characteristics for complex 53 doped in CBP-host for doping concentrations ranging from zero to 12 mol %. The voltage region below  $\approx 2.5$ –3 V is characterized by a single carrier-type transport, and

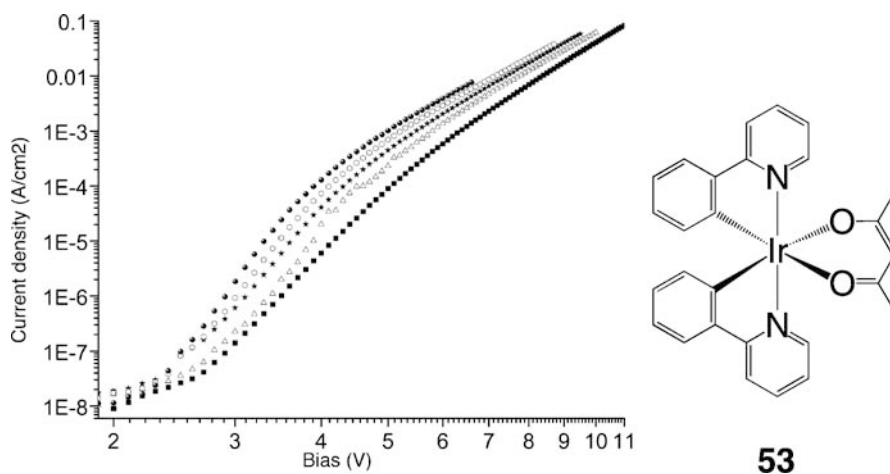
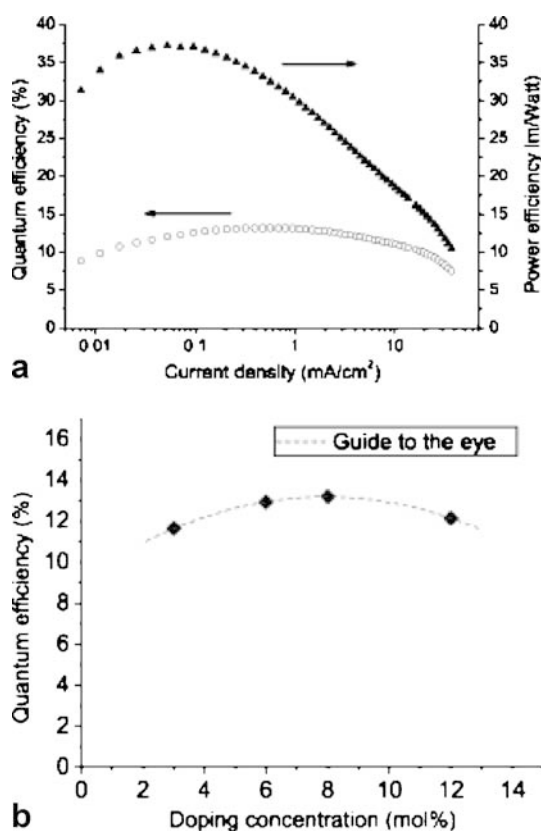


**Fig. 33** Current versus voltage characteristics for different doping concentrations of phosphorescent dye **53** in a CBP matrix

the exact value depends on the doping concentration. Above this threshold voltage, a steep increase in the diode current corresponding to two-carrier injection is observed, which leads to light generation. The lower current threshold field ( $U_{th1}$ ), here defined as the voltage for a current of  $1 \mu\text{A cm}^{-2}$ , decreases monotonously from 3.5 V for the undoped case to 2.9 V for maximum doping of 12 mol %. This indicates that the dye molecules seem to improve carrier injection into the matrix layer. The energy barrier for holes at the  $\alpha$ -NPD/CBP interface is 0.43 eV (HOMO–HOMO barrier). However, the energy barrier from  $\alpha$ -NPD to complex **53** is negligible, i.e., less than 0.1 eV [HOMOs of  $\alpha$ -NPD = 5.53 eV, CBP = 5.96 eV and of complex **53** = 5.6 eV] [77]. For higher doping concentrations this injection and transport mechanism is even improved. The energy barriers for the electrons are less important for all organic/organic interfaces ( $\leq 0.2$  eV).

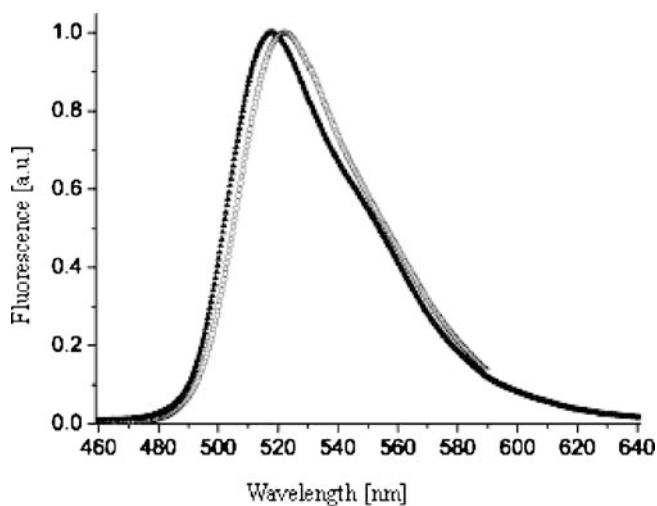
Furthermore, by direct charge injection from the adjacent hole and electron transport layers onto the phosphor molecule doped into the wide energy-gap matrix, exciton formation occurs directly on the dopant. In other words, in this image it is not the efficiency of the energy transfer from the host to the dye dopant, it is rather injection of the holes onto the dopant where they have “only” to wait for the electron. As already pointed out, it is a function of dye concentration if the charge jumps from dye to dye or if it is energetically favorable for the charge to detrapp by jumping from the dye to the host [125].

Figure 34 shows the variation of the quantum efficiency as a function of the doping concentration. We see a slight variation for concentrations between 3 and 12% with its maximum at 9% and 13.2% of external quantum efficiency. For comparison, in the undoped case the quantum efficiency is only 0.94%.



**Fig. 34** **a** External quantum and power efficiencies versus current. **b** External quantum efficiency as a function of the doping concentration

This corresponds to an improvement of around one and a half orders of magnitude. Still more impressive is the improvement in the power efficiency, which increases from  $0.65 \text{ lm W}^{-1}$  for the undoped case (not presented) up to  $37 \text{ lm W}^{-1}$  for the 9% doped case, which represents an improvement factor of 56. These values are close to the values cited in the recent literature [76]. However, they are lower than the best values achieved with triplet emitters in a TAZ-host [126]. A reason could be that the very low TAZ HOMO level of  $-6.6 \text{ eV}$  favors direct injection and transport at the dopant level and therefore the exciton escaping rate from the dopant to the host becomes negligible. This impressive value of quantum efficiency is based on a well-balanced charge ratio inside the emission layer, without any leaking current to the anode nor to the cathode side. Other experiments by Berner et al. [127] have shown how to get nearly equalized charge balance by using ITO/CuPc on the anode side and LiF/Al on the cathode side, taking into account the hole-blocking capabilities of BCP and the electron-blocking capabilities of  $\alpha$ -NPD [128–131].



**Fig. 35** Electrophosphorescence of complex 53 in a CBP matrix for the 3% (*black line*) and 12% (*gray line*) doped cases are shown. Additionally, the luminance versus voltage is presented for the 9% doped case

For the 6 mol % doped device the number of dopant molecules inside the doped volume can be calculated with the hypothesis of homogeneous distribution of the molecules. With 12  $\mu\text{s}$  of the averaged lifetime of the excited state of complex 53 and the additional assumption of homogeneous distribution of excited molecules, the upper level of the effective distance between excited molecules as a function of the current density can be estimated. Thereby, the charge density distribution was admitted to half of the doped zone, which is a reasonable assumption as demonstrated by model calculations [127]. This effective distance is directly related to the current-dependent quantum efficiency  $\eta_{(1)}$  of the device.

Figure 35 shows the electrophosphorescence spectra of complex 53 for 3% and 12% doped in CBP. A slight red shift for increasing doping concentration is seen, but the emission spectra were independent of current densities up to 150  $\text{mA cm}^{-2}$ . The same emission peak is found from a solution phosphorescence spectra of complex 53. The emission peaks of  $\alpha$ -NPD and the host, which are located in the blue at around 440–450 nm and around 480 nm, or intermediate exciplexes are not present. Another characteristic of phosphorescent dyes is the considerable reduction of the linewidth of the emission spectra compared to standard luminescence materials like Alq<sub>3</sub>. In the case of complex 53, the line width is only 52 nm (compared to an undoped Alq<sub>3</sub> emission where the line width is 83 nm), which leads to the saturated color that is necessary for high-performance color displays, assuming that the emission maximum is well located around one of the primary colors green, blue, or red.

## 2.8 Light-Emitting Electrochemical Cell Device Architecture

Another type of organic light emitting device is the light-emitting electrochemical cell (LEC), which makes use of ionic charges to facilitate electronic charge injection from the electrodes into the organic molecular semiconductor, eliminating the need for extra layers [78–82, 132]. This is a promising alternative to OLED, particularly for large-area lighting applications [82, 133–135]. In these cells a thicker organic active layer can be used, while keeping the operating voltage low, and a low-workfunction metal electrode is not needed. Recently, cationic Ir complexes **43** and **45** were incorporated in LECs leading to yellow [136] and blue-green [49, 111] electroluminescence.

To investigate the electroluminescence properties of the cationic complex **45**  $[\text{Ir}(\text{2-phenylpyridine})_2(4,4'\text{-dimethylamino-2,2'-bipyridine})]\text{PF}_6$ , LECs were fabricated in a nitrogen atmosphere glovebox [82]. They consisted of a 100 nm spin-coated layer of pristine **45** sandwiched between an ITO and an evaporated Ag electrode [106].

It is well known that solid-state LECs exhibit a significant response time since electroluminescence can only occur after the ionic double-layers have been built up at the electrode interfaces [79, 82]. Since in this case only the  $\text{PF}_6^-$  anion is mobile, the double-layers are formed by accumulation and depletion of  $\text{PF}_6^-$  at the anode and cathode, respectively. The LEC device with **45** started to emit blue-green light at a bias of 5 V after several minutes. The electroluminescence spectrum, as shown in Fig. 36 (trace a), is very similar to the photoluminescence spectrum recorded for a spin-coated film on glass and of a solution of the complex. For comparison, the electroluminescence

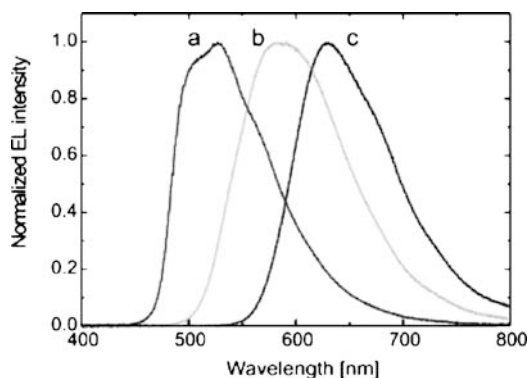


**Fig. 36** Electroluminescence spectra of ITO/EL layer/Ag devices, where the EL layer consists of  $[\text{Ir}(\text{ppy})_2(\text{dma-bpy})]\text{PF}_6$  (a),  $[\text{Ir}(\text{ppy})_2(\text{bpy})]\text{PF}_6 + \text{PMMA}$  (b), and  $[\text{Ru}(\text{bpy})_3](\text{PF}_6)_2 + \text{PMMA}$  (c)

spectra recorded for similar devices with  $[\text{Ir}(\text{ppy})_2(\text{bpy})]\text{PF}_6$  (trace b, yellow emission) and  $[\text{Ru}(\text{bpy})_3](\text{PF}_6)_2$  (trace c, orange/red emission) as active material are also shown [82]. The fact that blue-green emission is obtained with an Ag cathode at a voltage as low as 2.5 V indicates the power of the LEC behavior.

**Acknowledgements** Financial support from the Swiss Federal Office for Energy (OFEN) is greatly appreciated. We thank Dr. F. De Angelis, and Dr. D. Berner for their time and discussion.

## References

1. Hagfeldt A, Grätzel M (2000) *Acc Chem Res* 33:269
2. West W (1974) *Proc Vogel Cent Symp Photogr Sci Eng* 18:35
3. Moser J (1887) *Notiz über die Verstärkung photoelektrischer Ströme durch optische Sensibilisierung*, *Monatsh Chemie* 8:373
4. Namba S, Hishiki Y (1965) *J Phys Chem* 69:774
5. Gerischer H, Tributsch H (1968) *Phys Chem* 72:437
6. Dare-Edwards MP, Goodenough JB, Hamnett A, Seddon KR, Wright RD (1981) *Faraday Discuss Chem Soc* 70:285
7. Tsubomura H, Matsumura M, Nomura Y, Amamiya T (1976) *Nature* 261:402
8. Dunghong D, Serpone N, Graetzel M (1984) *Helv Chim Acta* 67:1012
9. Desilvestro J, Graetzel M, Kavan L, Moser J, Augustynski J (1985) *J Am Chem Soc* 107:2988
10. O'Regan B, Grätzel M (1991) *Nature* 353:737
11. Nazeeruddin MK, Wang Q, Cevey L, Aranyos V, Liska P, Figgemeier E, Klein C, Hirata N, Koops S, Haque SA, Durrant JR, Hagfeldt A, Lever ABP, Grätzel M (2006) *Inorg Chem* 45:787
12. Barbé CJ, Arendse F, Comte P, Jirousek M, Lenzenmann F, Shklover V, Grätzel M (1997) *J Am Ceram Soc* 80:3157
13. Rothenberger G, Comte P, Graetzel M (1999) *Solar Energ Mater Solar Cells* 58:321
14. Burnside SD, Shklover V, Barbe CJ, Comte P, Arendse F, Brooks K, Grätzel M (1998) *Chem Mater* 10:2419
15. Hagfeldt A, Grätzel M (1995) *Chem Rev* 95:49
16. Cahen D, Hodes G, Grätzel M, Guilemoles JF, Riess I (2000) *J Phys Chem B* 104:2053
17. Ferber J, Luther J (2001) *J Phys Chem B* 105:4895
18. van de Lagemaat J, Park N-G, Frank AJ (2000) *J Phys Chem B* 104:2044
19. Nazeeruddin MK, Kay A, Rodicio I, Humphry-Baker R, Muller E, Liska P, Vlachopoulos N, Grätzel M (1993) *J Am Chem Soc* 115:6382
20. Grätzel M (2001) *Nature* 414:338
21. Nazeeruddin MK, Grätzel M (2003) In: Ramamurthy V, Schanze KS (eds) *Molecular and supramolecular photochemistry*, vol 10. Dekker, New York, p 301
22. Nazeeruddin MK (2004) In: Nazeeruddin MK (ed) *Special issue: Michael Graetzel Festschrift, A tribute for his 60th birthday: Dye sensitized solar cells*. *Coord Chem Rev* 248:1161
23. Grätzel M (2000) In: Nalwa HS (ed) *Handbook of nanostructured materials and nanotechnology*, vol 3. Academic, New York, p 527

24. Haught AF (1984) *J Solar Energ Eng* 106:3
25. De Vos A (1992) *Endoreversible thermodynamics of solar energy conversion*. Oxford Science, Oxford, chap 6
26. Nazeeruddin MK, Zakeeruddin SM, Humphry-Baker R, Jirousek M, Liska P, Vlachopoulos N, Shklover V, Fischer CH, Grätzel M (1999) *Inorg Chem* 38:6298
27. Anderson S, Constable EC, Dare-Edwards MP, Goodenough JB, Hamnett A, Seddon KR, Wright RD (1979) *Nature* 280:571
28. Anderson PA, Strouse GF, Treadway JA, Keene FR, Meyer TJ (1994) *Inorg Chem* 33:3863
29. Hara S, Sugihara H, Tachibana Y, Islam A, Yanagida M, Sayama K, Arakawa H (2001) *Langmuir* 17:5992
30. Nazeeruddin MK, Graetzel M (2002) In: Licht S (ed) *Semiconductor electrodes and photoelectrochemistry*. Encyclopedia of electrochemistry, vol 6. Wiley, Weinheim (pp 407–431)
31. Balzani V, Juris A, Venturi M, Campagna S, Serroni S (1996) *Chem Rev* 96:759
32. Kalyanasundaram K, Nazeeruddin MK (1992) *Chem Phys Lett* 193:292
33. Nazeeruddin MK, Muller E, Humphry-Baker R, Vlachopoulos N, Grätzel M (1997) *J Chem Soc, Dalton Trans*, p 4571
34. Nazeeruddin MK, Grätzel M, Kalyanasundaram K, Girling RB, Hester RE (1993) *J Chem Soc, Dalton Trans*, p 323
35. Zakeeruddin SM, Nazeeruddin MK, Pechy P, Rotzinger FP, Humphry-Baker R, Kalyanasundaram K, Grätzel M (1997) *Inorg Chem* 36:5937
36. Nazeeruddin MK, Pe'chy P, Renouard T, Zakeeruddin SM, Humphry-Baker R, Comte P, Liska P, Le C, Costa E, Shklover V, Spiccia L, Deacon GB, Bignozzi CA, Grätzel M (2001) *J Am Chem Soc* 123:1613
37. Nazeeruddin MK, Zakeeruddin SM, Humphry-Baker R, Gorelsky SI, Lever ABP, Graetzel M (2000) *Coord Chem Rev* 208:213
38. Masood MA, Sullivan BP, Hodges DJ (1994) *Inorg Chem* 33:5360
39. Durham B, Wilson SR, Hodges DJ, Meyer TJ (1980) *J Am Chem Soc* 102:600
40. Tennakone K, Kumara GRR, Kottegoda IRM, Perera VPS (1999) *Chem Commun*, p 15
41. Chandrasekharan N, Kamat PV (2000) *J Phys Chem B* 104:10851
42. Gregg BA, Pichot F, Ferrere S, Fields CL (2001) *J Phys Chem B* 105:1422
43. Schmidt-Mende L, Kroeze J, Durrant JR, Nazeeruddin MK, Grätzel M (2005) *NANO-LETTERS* 5:1315
44. Nazeeruddin MK, Klein C, Liska P, Grätzel M (2005) *Coord Chem Rev* 248:1317
45. Nazeeruddin MK, De Angelis F, Fantacci S, Selloni A, Viscardi G, Liska P, Ito S, Bessho T, Grätzel M (2005) *J Am Chem Soc* 127:16835
46. Nazeeruddin MK, Wang Q, Cevey L, Aranyos V, Liska P, Figgemeier E, Klein C, Hirata N, Koops S, Haque SA, Durrant JR, Hagfeldt A, Lever ABP, Grätzel M (2006) *Inorg Chem* 45:787
47. Wang P, Klein C, Humphry-Baker R, Zakeeruddin SM, Grätzel M (2005) *Appl Phys Lett* 86:123508
48. Renouard T, Fallahpour R-A, Nazeeruddin MK, Humphry-Baker R, Gorelsky SI, Lever ABP, Grätzel M (2002) *Inorg Chem* 41:367
49. Barolo C, Nazeeruddin MK, Fantacci S, Di Censo D, Ito S, Comte P, Liska P, Viscardi G, Quagliotto P, De Angelis F, Grätzel M (2006) *Inorg Chem* 45:4642
50. Lever ABP (1990) *Inorg Chem* 29:1271
51. Wolfbauer G, Bond AM, Deacon GB, MacFarlane DR, Spiccia L (2000) *J Am Chem Soc* 122:130

52. Bignozzi CA, Aragazzi R, Kleverlaan CJ (2000) *Chem Soc Rev* 29:87
53. Trammell SA, Moss JA, Yang JC, Nakhle BM, Slate CA, Odobel F, Sykora M, Erickson BW, Meyer TJ (1999) *Inorg Chem* 38:3665
54. Tennakone K, Kumara GRRR, Wijayantha KGU (1996) *Semicond Sci Technol* 11:1737
55. Yan SG, Hupp JT (1996) *J Phys Chem* 100:6867
56. Yanagi H, Chen S, Lee PA, Nebesny KW, Armstrong NR, Fujishima A (1996) *J Phys Chem* 100:5447
57. Yanagi H, Fujishima A, Chen S, Lee PE, Nebesny KW, Armstrong NR (1996) *J Phys Chem* 100:5447
58. Will G, Boschloo G, Nagaraja Rao S, Fitzmaurice D (1999) *J Phys Chem B* 103:8067
59. Lemon B, Hupp JT (1999) *J Phys Chem B* 103:3797
60. Jing B, Zhang H, Zhang M, Lu Z, Shen T (1998) *J Mater Chem* 8:2055
61. Rice CR, Ward MD, Nazeeruddin MK, Grätzel M (2000) *New J Chem* 24:651
62. Murakoshi K, Kano G, Wada Y, Yanagida S, Miyazaki H, Matsumoto M, Murasawa S (1995) *J Electroanal Chem* 396:27
63. Fennie KS, Bartlett JR, Woolfrey JL (1998) *Langmuir* 14:2744
64. Fillinger A, Parkinson BA (1999) *J Electrochem Soc* 146:4559
65. Shklover V, Ovehinnikov YE, Braginsky LS, Zakeeruddin SM, Grätzel M (1998) *Chem Mater* 10:2533
66. Nazeeruddin MK, Humphry-Baker R, Liska P, Grätzel M (2003) *J Phys Chem B* 107:8981
67. Tachibana Y, Haque SA, Mercer IP, Moser JE, Klug DR, Durrant JR (2001) *J Phys Chem B* 105:7424
68. Chiba Y, Islam A, Watanabe Y, Komiya R, Koide N, Han L (2006) *Japan J Appl Phys* 2: Lett Expr Lett 45:24
69. Bach U, Lupo D, Compte P, Moser JE, Weissörtel F, Salbeck J, Spreitzer H, Grätzel M (1998) *Nature* 395:583
70. Ito S, Zakeeruddin SM, Humphry-Baker R, Liska P, Charvet R, Comte P, Nazeeruddin MK, Pechy P, Takata M, Miura H, Uchida S, Grätzel M (2006) *Adv Mater* 18:1202
71. Grätzel M (2006) *Comptes Rendus Chimie* 9:578
72. Hinsch A (2000) In: Scheel HJ (ed) *Proc 16th Eur PV Solar Energ Conf, Glasgow, Vol. 32*. James & James, London
73. Wang P, Zakeeruddin SM, Moser J, Nazeeruddin MK, Sekiguchi T, Graetzel M (2003) *Nat Mater* 2:402
74. Adachi C, Baldo MA, Thompson ME, Forrest SR (2001) *J Appl Phys* 90:5048
75. Baldo MA, Lamansky S, Burrows PE, Thompson ME, Forrest SR (1999) *Appl Phys Lett* 75:4
76. Ikai M, Tokito S, Sakamoto Y, Suzuki T, Taga Y (2001) *Appl Phys Lett* 79:156
77. Nazeeruddin MK, Humphry-Baker R (2003) *J Am Chem Soc* 125:8790
78. Slinker JD, Gorodetsky AA, Lowry MS, Wang J, Parker S, Rohl R, Bernhard S, Malliaras GG (2004) *J Am Chem Soc* 126:2763
79. Slinker J, Bernards D, Houston PL, Abruna HD, Bernhard S, Malliaras GG (2003) *Chem Commun*, p 2392
80. Rudmann H, Shimida S, Rubner MF (2002) *J Am Chem Soc* 124:4918
81. Bernhard S, Barron JA, Houston PL, Abruna HD, Ruglovksy JL, Gao X, Malliaras GG (2002) *J Am Chem Soc* 124:13624
82. Wegh RT, Meijer EJ, Plummer EA, De Cola L, Brunner K, van Dijken A, Hofstraat JW (2004) *Proc SPIE* 5519:48
83. Handy ES, Pal AJ, Rubner MF (1999) *J Am Chem Soc* 121:3525



84. Gao FG, Bard AJ (2000) *J Am Chem Soc* 122:7426
85. Yang C-H, Li S-W, Chi Y, Cheng Y-M, Yeh Y-S, Chou P-T, Lee G-H (2005) *Inorg Chem* 44:7770
86. Coppo P, Plummer EA, De Cola L (2004) *Chem Commun*, p 1774
87. Sajoto T, Djurovich PI, Tamayo A, Yousufuddin M, Bau R, Thompson ME, Holmes RH, Forrest SR (2005) *Inorg Chem* 44:7992
88. Lowry MS, Hudson WR, Pascal RAJ, Bernhard S (2004) *J Am Chem Soc* 126:14129
89. You Y, Park SY (2005) *J Am Chem Soc* 127:12438
90. Tmayo AB, Garon S, Sajoto T, Djurovich PI, Tsyba IM, Bau R, Thompson ME (2005) *Inorg Chem* 44:8723
91. Strickler SJ, Berg RA (1962) *J Chem Phys* 37:814
92. Kober EM, Caspar JV, Lumpkin RS, Meyer TJ (1986) *J Phys Chem* 90:3722
93. Juris A, Balzani V, Barigelletti F, Campagna S, Belser P, von Zelewsky A (1988) *Coord Chem Rev* 84:85
94. Nonoyama M (1975) *Bull Chem Soc Jpn* 47:767
95. Hay PJ (2002) *J Phys Chem B* 106:1634
96. King KA, Watts RJ (1987) *J Am Chem Soc* 109:1589
97. Dedeian K, Djurovich PI, Garces FO, Carlson C, Watts RJ (1991) *Inorg Chem* 30:1685
98. Sprouse S, King KA, Spellane PJ, Watts RJ (1984) *J Am Chem Soc* 6647
99. Yang CH, Li SW, Chi Y, Cheng YM, Yeh YS, Chou PT, Lee GH, Wang CH, Shu CF (2005) *Inorg Chem* 44:7770
100. Tsuboyama A, Iwawaki H, Furugori M, Mukaide T, Kamatani J, Igawa S, Moriyama T, Miura S, Takiguchi T, Okada S, Hoshino M, Ueno K (2003) *J Am Chem Soc* 125:12971
101. You Y, Park SY (2005) *J Am Chem Soc* 127:12438
102. Yeh S-J, Wu M-F, Chen C-T, Song Y-H, Chi Y, Ho M-H, Hsu S-F, Chen C-H (2005) *Adv Mater* 17:285
103. Hwang FM, Chen HY, Chen PS, Liu CS, Chi Y, Shu CF, Wu FL, Chou PT, Peng SM, Lee GH (2005) *Inorg Chem* 44:1344
104. Laskar IR, Hsu SF, Chen TM (2005) *Polyhedron* 24:189
105. Fang K-H, Wu L-L, Huang Y-T, Yang C-H, Sun IW (2006) *Inorg Chem Acta* 359:441
106. Nazeeruddin MK, Weh RT, Zhou Z, Klein C, Wang Q, Fantacci S, De Angelis F, Graetzel M (2006) *Inorg Chem* 45:9245
107. Schmid B, Garces FO, Watts RJ (1994) *Inorg Chem* 33:9
108. Ichimura K, Kobayashi T, King KA, Watts RJ (1987) *J Phys Chem* 91:6104
109. Ohsawa Y, Sprouse S, King KA, DeArmond MK, Hanck KW, Watts RJ (1987) *J Phys Chem* 91:1047
110. Garces FO, King KA, Watts RJ (1988) *Inorg Chem* 27:3464
111. Lowry MS, Goldsmith JI, Slinker JD, Rohl R, Pascal RA, Malliaras GG, Bernhard S (2005) *Chem Mater* 17:5712
112. VanSlyke SA, Tang CW (1987) *Appl Phys Lett* 51:913
113. Kim JS, Ho PKH, Greenham NC, Friend RH (2000) *J Appl Phys* 88:1073
114. Baldo MA, Adachi C, Forrest SR (2000) *Phys Rev B* 62:10967
115. Hoshino S, Suzuki H (1996) *Appl Phys Lett* 69:224
116. Mattoussi H, Murata H, Merritt CD, Kafafi ZH (1998) *SPIE Proc* 3476:49
117. Murata H, Merritt CD, Mattoussi H, Kafafi ZH (1998) *SPIE Proc* 3476:88
118. Bulovi V, Shoustikov A, Baldo MA, Bose E, Kozlov VG, Thompson ME, Forrest SR (1998) *Chem Phys Lett* 287:455
119. Lamansky S, Thompson ME, Adamovich V, Djurovich PI, Adachi C, Baldo MA, Forrest SR, Kwong R (2005) Organometallic compounds and emission-shifting organic electrophosphorescence. US Patent 6 939 624

120. Kalinowski J, Stampor W, Cocchi M, Virgili D, Fattori V, Marco P (2004) *ChemPhys* 39:297
121. Cleave V, Yahioğlu G, Le Barny P, Friend R, Tessler N (1999) *Adv Mater* 11:285
122. Ren X, Li J, Holmes RJ, Djurovich PI, Forrest SR, Thompson ME (2004) *Chem Mater* 16:4743
123. Pai DM, Yanus JF, Stolka M (1984) *J Phys Chem* 88:4714
124. Riess W, Beierlein TS, Riel H (2005) In: Brütting W (ed) *Physics of organic semiconductors*. Wiley, Weinheim (pp 511–527, ISBN 3-527-40550-X)
125. Yersin H (2004) *Top Curr Chem* 1:241
126. Adachi C, Baldo MA, Forrest SR, Thompson ME (2000) *Appl Phys Lett* 77:904
127. Berner D, Houili H, Leo W, Zuppiroli L (2005) *Phys Stat Sol* 9:202
128. Masenelli B, Berner D, Bussac MN, Zuppiroli L (2001) *Appl Phys Lett* 79:4438
129. Tutis E, Bussac MN, Masenelli B, Carrard M, Zuppiroli L (2001) *J Appl Phys* 89:430
130. Masenelli JB, Tutis E, Bussac MN, Zuppiroli L (2001) *Synth Met* 122:141
131. Masenelli JB, Tutis E, Bussac MN, Zuppiroli L (2000) *Synth Met* 121:1513
132. Pei Q, Yu G, Zhang C, Yang Y, Heeger AJ (1995) *Science* 269:1086
133. Holder E, Langeveld BMW, Schubert US (2005) *Adv Mater* 17:1109
134. Pei Q, Yu G, Zhang YC, Yang Y, Heeger AJ (1995) *Science* 269:1086
135. Chuah BS, Hwang DH, Chang SM, Davies JE, Moratti SC, Li XC, Holmes AB, De Mello JC, Tessler N, Friend RH (1997) *SPIE Proc* 132:3148
136. Slinker JD, Koh CY, Malliaras GG, Lowry MS, Bernhard S (2005) *Appl Phys Lett* 86:173506

## Conjugates of Heme-Thiolate Enzymes with Photoactive Metal-Diimine Wires

Stephen M. Contakes<sup>1</sup> · Yen Hoang Le Nguyen<sup>1</sup> · Harry B. Gray<sup>1</sup> (✉) · Edith C. Glazer<sup>2</sup> · Anna-Maria Hays<sup>3</sup> · David B. Goodin<sup>2</sup>

<sup>1</sup>Beckman Institute, California Institute of Technology, 1200 E. California Blvd., Pasadena, CA 91125, USA  
*hbgray@caltech.edu*

<sup>2</sup>Department of Molecular Biology, The Scripps Research Institute, 10550 N. Torrey Pines Rd., La Jolla, CA 92037, USA

<sup>3</sup>AMBRX, 10975 N. Torrey Pines Rd., La Jolla, CA 92037, USA

1	Probing Enzymes with Molecular Wires . . . . .	178
2	Molecular Wires for Cytochromes P450 . . . . .	180
2.1	Binding . . . . .	181
2.2	Probing Open States . . . . .	187
2.3	Sensing . . . . .	193
3	Molecular Wires for Inducible Nitric Oxide Synthase . . . . .	195
3.1	Binding . . . . .	196
3.2	Sensing . . . . .	199
4	Conclusions . . . . .	200
	References . . . . .	201

**Abstract** Heme-thiolate enzymes, notably cytochromes P450 and nitric oxide synthases, use dioxygen to oxygenate substrates. Photoactive metal-diimine molecular wires that are capable of effecting rapid redox state changes at buried active sites have been developed to generate intermediates in the catalytic cycles of these enzymes. Wires that feature a photoactive head group tethered to an active-site ligand bind P450CAM and inducible nitric oxide synthase (iNOS) primarily by hydrophobic interactions. The wire-binding specificity of each enzyme is critically dependent on the structural flexibility of the protein. P450CAM:wire conjugates can adopt open or partially open conformations, thereby accommodating a wide range of wires, whereas only long wires with smaller  $[\text{Re}(\text{CO})_3(\text{bpy})\text{Im}]^+$  head groups are able to bind tightly in the rigid active-site channel of iNOS. Dansyl-terminated molecular wires function as highly sensitive and isoform specific fluorescent sensors for P450CAM.

**Keywords** Molecular Wires · Cytochromes P450 · Nitric Oxide Synthase · Photochemistry · Electron Transfer

### Abbreviations

Ad adamantyl  
BH<sub>4</sub> tetrahydrobiopterin

CPR	cytochrome P450 reductase
EB	ethylbenzene
eNOS	endothelial nitric oxide synthase
ET	electron transfer
FAD	flavin adenosine dinucleotide
FET	fluorescence energy transfer
FMN	flavin mononucleotide
iNOS	inducible nitric oxide synthase
iNOS <sub>oxy</sub>	oxygenase domain of inducible NOS
NADPH	nicotinamide adenosine dinucleotide hydride
NHE	normal hydrogen electrode
nNOS	neuronal nitric oxide synthase
NOS	nitric oxide synthase
P450	cytochrome P450
P450BM3	cytochrome P450 from <i>Bacillus megaterium</i>
P450CAM	cytochrome P450 from <i>Pseudomonas putida</i>
pdx	putidaredoxin
tm	tetramethyl

## 1

### Probing Enzymes with Molecular Wires

The definitive characterization of catalytically relevant metalloenzyme redox states is a major challenge in bioinorganic chemistry research, as many redox-active intermediates are formed after the rate-determining steps in catalytic cycles. High-valent compound I and II ferryl species, such as those postulated to effect substrate oxidation in cytochrome P450 and nitric oxide synthase (NOS) reaction cycles, are particularly prominent examples. Both P450 and NOS employ a cysteine-coordinated heme oxygenase domain to activate oxygen through multiple electron transfer (ET) processes: in class I P450CAM systems, a terminal oxygenase domain receives its electrons from NADPH via a FAD containing cytochrome P450 reductase (CPR) domain; in class II drug metabolizing P450 [1, 2] systems, the NADPH reducing equivalents are delivered to an unusual diflavin (FAD and FMN) containing CPR module fused onto its oxygenase domain [3, 4]. NOS isoforms employ fused diflavin containing domains similar to those of the class II P450s [4].

Although ferryl intermediates of horseradish peroxidase and microperoxidase-8 have been produced in reactions with photogenerated  $[\text{Ru}(\text{bpy})_3]^{3+}$  [5], analogous experiments with P450s were unsuccessful, presumably due to the inefficiency of electron transfer from the buried heme active site through the protein backbone [6]. Photoactive molecular wires (sometimes referred to as metal-diimine wires, sensitizer-tethered substrates, or electron tunneling wires) were developed to circumvent this problem by providing a direct ET pathway between  $[\text{Ru}(\text{bpy})_3]^{3+}$  and the heme. These molecular wires, which combine the excellent photophysical properties of metal-diimine complexes

with the facile electron tunneling properties of molecular chains, can be used to generate reactive redox states associated with buried enzyme active sites: a case in point is work in which we successfully generated several novel cytochrome P450 redox states using flash-quench methods [6]. Our investigations also have revealed key factors that contribute to the binding of molecular wires to several different metalloenzymes, including cytochrome P450CAM [7–11], inducible nitric oxide synthase [12, 13], *Arthrobacter globiformis* amine oxidase [14, 15], myeloperoxidase [16], and lipoxygenase [17]; and crystallographic analyses of enzyme:wire conjugates have shed light on conformational changes associated with substrate binding and product egress [7–9]. Importantly, we have demonstrated that molecular wires can function as enzyme inhibitors [15], fluorescent sensors [10, 11], and electrochemical sensors [14].

Molecular wires consist of a ligand with affinity for a buried active site tethered to a head group that binds at the active-site channel surface (Fig. 1). The head group is optimized for the desired functionality: electron tunneling wires employ  $\text{Ru}^{\text{II}}$  or  $\text{Re}^{\text{I}}$  diimine complexes; certain other fluorescent sensors use dyes such as dansyl [10, 11] or fluorescein [16], and electrochemical wire sensors contain thiol or pyrene groups that can be attached to electrode surfaces [14]. The tether, which connects the ligand and head groups and resides in the substrate access channel, provides an electron tunneling pathway for injection or abstraction of electrons to and from the active site. The head group, tether, and ligand can be optimized to bind the enzyme of interest. In favorable cases, studies of enzyme:wire complexes reveal the factors that govern substrate specificity for a given enzyme.

We turn our attention now to cytochromes P450 and inducible nitric oxide synthase, where certain key features of wire:protein interactions have been elucidated.

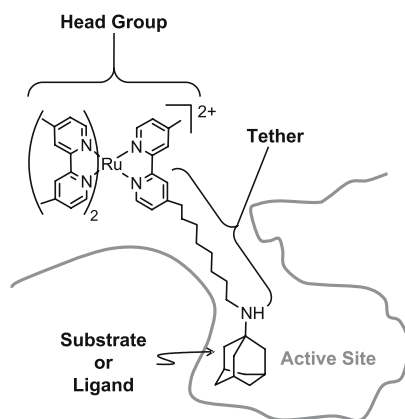
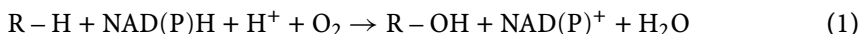


**Fig. 1** Electron tunneling wires consist of a substrate or ligand tethered to a redox-active head group

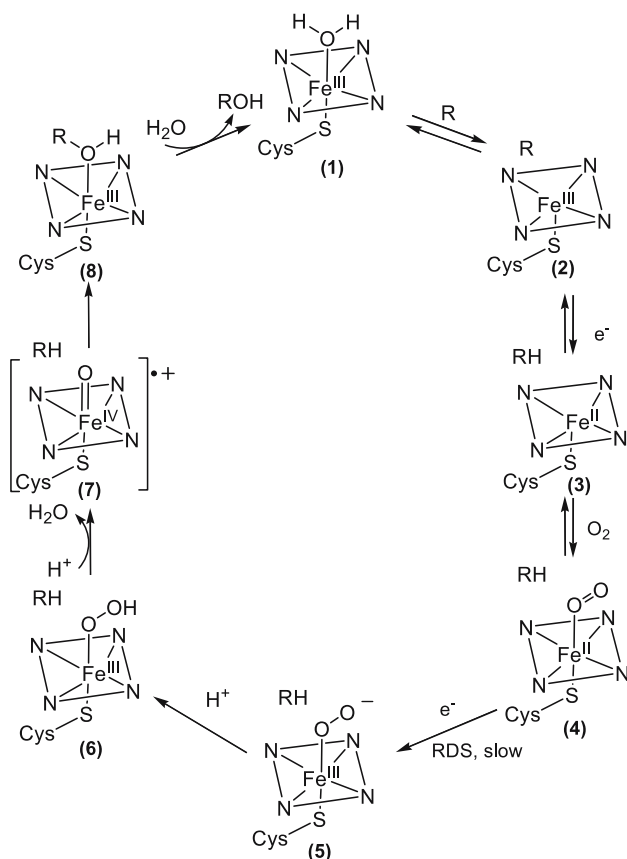
## 2 Molecular Wires for Cytochromes P450

The heme-thiolate cytochromes P450 (P450) catalyze regio- and stereospecific reactions under physiological conditions [18–20], including the hydroxylation of hydrocarbons (Equation Eq. 1), alkene epoxidation, heteroatom (N,S) oxidation, dealkylation, and (anaerobic) dehalogenation [21].



*In vivo* activities include hormone biosynthesis, xenobiotic elimination, drug (de-)activation, and carcinogenesis [22], while potential *in vitro* applications range from chemical synthesis [23] to biosensing [24].

Central to P450 catalysis is electron transfer. The catalytic cycle (Scheme 1) involves two one-electron reductions: catalysis is initiated with the first, while



**Scheme 1** P450 catalytic cycle

the overall rate is limited by the second. Much effort has been expended to investigate the factors that govern ET to and from P450 heme centers in order to understand the catalytic mechanism and ultimately harness P450 oxidation chemistry for *in vitro* applications. The ability to access and characterize compound I is central to the understanding of P450 function. While several heroic attempts have been made to observe such high-valent species in the catalytic cycle [25–28], none has led to definitive characterization of compound I.

We developed molecular wires with the goal of generating P450-I and II by direct photooxidation of the P450 heme. Although our work with electron tunneling wires has demonstrated the feasibility of photochemically inducing P450 redox reactions, definitive characterization of catalytically relevant intermediates has yet to be realized [29]. Nevertheless, our work has illuminated several features of P450 catalysis. P450 wire binding profiles illustrate the factors that govern substrate binding in the active site and its channel. Crystallographic studies of P450:wire complexes reveal novel open conformations that provide insight into the role of low-lying conformational states in P450's ability to oxygenate a wide range of substrates under conditions that require exclusion of water from the active-site channel. Wires also have been developed for use as highly selective isoform-specific fluorescent sensors for P450CAM.

## 2.1 Binding

The molecular wires developed for use with P450 isoforms are shown in Fig. 2. The structures, binding affinities, and ET properties of P450-wire conjugates vary widely, depending on the nature of the tethers and terminal groups, although all employ neutral or positively charged head groups (Table 1).

All of the molecular wires in Fig. 2 are isoform specific: they reversibly bind P450CAM to form conjugates with micromolar to nanomolar dissociation constants; but they do not bind P450BM3 [30]. This selectivity parallels the substrate profiles of the two enzymes: while P450CAM shows maximal activity with adamantyl-like substrates, P450BM3 prefers long chain fatty acids. P450BM3 has an arginine (Arg<sup>47</sup>) at the mouth of the putative substrate access channel, which has been proposed to stabilize the carboxylate group of bound fatty acid substrates [31]. Since positively charged head groups interact unfavorably with this Arg residue, we have designed wires with negatively charged sensitizers to probe P450BM3 [32].

All of our P450CAM molecular wires bind in the active-site channel, as established by the Ru–Fe heme distances ( $\leq 22.1$  Å) determined by fluorescence energy transfer (FET), crystallographic analyses, and competition experiments with the natural substrate (camphor). Imidazole-terminated

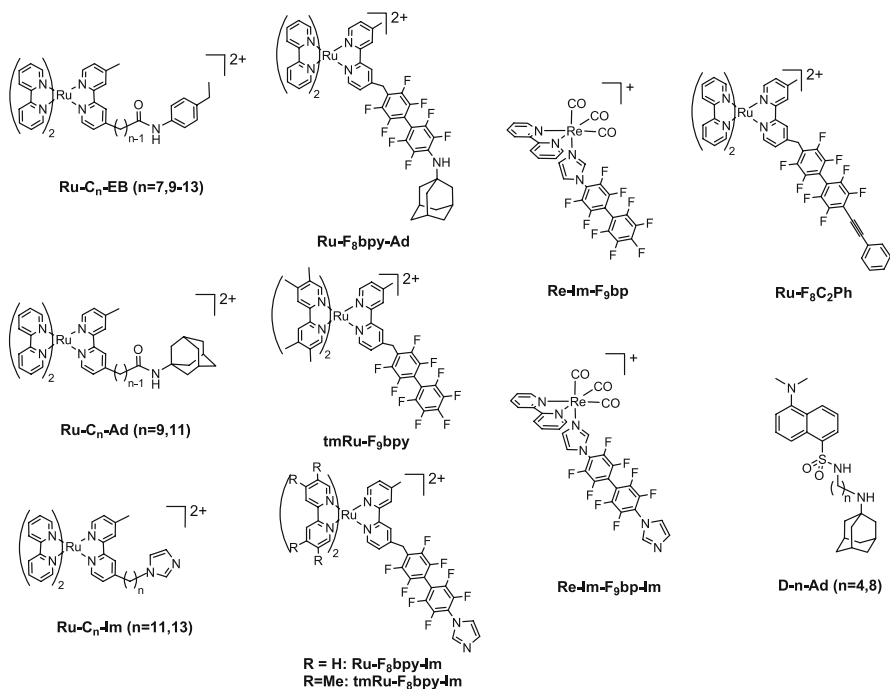


**Fig. 2** Molecular wires that bind cytochrome P450CAM

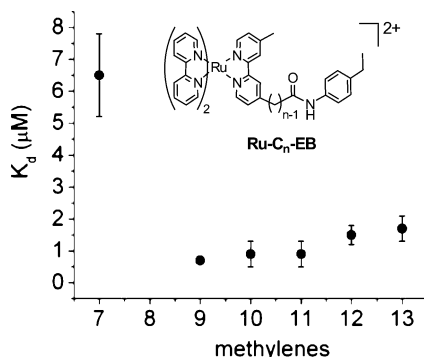


**Fig. 3** Dependence of  $K_d$  on tether length for P450:  $[\text{Ru} - \text{C}_n - \text{EB}]^{2+}$  complexes

metal-diimine wires directly ligate the heme Fe, as evidenced by a shift in the Soret peak from 416 to 420 nm [6, 33]. Notably, the spectral shift indicates that water is not fully displaced from the active site [34–36], a result that differs from the complete heme ligation observed with imidazole, suggesting that there is greater accessibility of water to the heme in the open



**Table 1** P450CAM-wire conjugates

Wire <sup>a</sup>	$K_d$ ( $\mu\text{M}$ )	$d_{\text{M-Fe}}$ ( $\text{\AA}$ )	Comments <sup>b</sup>	Refs.
[Ru - F <sub>8</sub> bpy - Ad] <sup>2+</sup>	0.077 ± 0.001 <sup>f</sup>	22.1 <sup>b</sup> 21.8 <sup>c</sup>	d	[8, 33]
[tmRu - F <sub>9</sub> bpy] <sup>2+</sup>	2.1 ± 0.5 <sup>f</sup>	17.0 <sup>b</sup>	d	[33]
[Ru - F <sub>8</sub> bpy - Im] <sup>2+</sup>	3.7 ± 0.5 <sup>f</sup>	18.1 <sup>b</sup>	Direct photoreduction 30% Fe <sup>II</sup> produced $k_f = 4.4 \times 10^6 \text{ s}^{-1}$ ; $k_b \sim$ undetermined	[33]
[tmRu - F <sub>8</sub> bpy - Im] <sup>2+</sup>	0.48 ± 0.18 <sup>f</sup>	18.1 <sup>b</sup>	Direct photoreduction 74% Fe <sup>II</sup> produced $k_f = 2.8 \times 10^7 \text{ s}^{-1}$ ; $k_b \sim 1.7 \times 10^8 \text{ s}^{-1}$	[33]
[Ru - C <sub>11</sub> - Im] <sup>2+</sup>	> 50 <sup>f</sup>		e	[11, 35]
[Ru - C <sub>13</sub> - Im] <sup>2+</sup>	4.1 <sup>f</sup>	21.2 <sup>b</sup>	d	[6, 11, 35]
[Ru - C <sub>9</sub> - Ad] <sup>2+</sup>	0.4 <sup>f</sup> 0.24 ± 0.2 <sup>g</sup> 0.09( $\Delta$ ) <sup>g</sup> , 0.19( $\Delta$ ) <sup>g</sup> 0.20 ± 0.5( $\Delta$ ) <sup>h</sup> 0.30 ± 0.5( $\Delta$ ) <sup>h</sup>	21.4 <sup>b</sup>	ET after reductive quench $k_f = 2 \times 10^4 \text{ s}^{-1}$ e	[11, 35, 39]
[Ru - C <sub>11</sub> - Ad] <sup>2+</sup>	0.6 <sup>f</sup>	21.0 <sup>b</sup>	d	[6, 11, 35, 39]
			ET after reductive quench with <i>p</i> -MDMA yields [P <sub>Cys</sub> - Fe <sup>II</sup> (H <sub>2</sub> O)] <sup>-</sup> $k_f = 2 \times 10^4 \text{ s}^{-1}$	

Table 1 continued

Wire <sup>a</sup>	$K_d$ ( $\mu\text{M}$ )	$d_{\text{M-Fe}}$ ( $\text{\AA}$ )	Comments <sup>b</sup>	Refs.
[Ru - C <sub>7</sub> - EB] <sup>2+</sup>	6.5 <sup>f</sup>	19.5 <sup>b</sup>	d ET after reductive quench with <i>p</i> -MDMA yields [P <sub>Cys</sub> - Fe <sup>II</sup> (H <sub>2</sub> O)] <sup>-</sup> $k_f \sim 10^3 \text{ s}^{-1}$	[11, 35]
[Ru - C <sub>9</sub> - EB] <sup>2+</sup>	0.7 <sup>f</sup>	19.4 <sup>b</sup>	d ET after reductive quench with <i>p</i> -MDMA yields [P <sub>Cys</sub> - Fe <sup>II</sup> (H <sub>2</sub> O)] <sup>-</sup>	[11, 35]
[Ru - C <sub>10</sub> - EB] <sup>2+</sup>	0.9 <sup>f</sup>	19.9 <sup>b</sup>	d ET after reductive quench with <i>p</i> -MDMA yields [P <sub>Cys</sub> - Fe <sup>II</sup> (H <sub>2</sub> O)] <sup>-</sup>	[11, 35]
[Ru - C <sub>11</sub> - EB] <sup>2+</sup>	0.9 <sup>f</sup>	20.1 <sup>b</sup>	d ET after reductive quench with <i>p</i> -MDMA yields [P <sub>Cys</sub> - Fe <sup>II</sup> (H <sub>2</sub> O)] <sup>-</sup> $k_f = 2 \times 10^4 \text{ s}^{-1}$	[6, 11, 35]
[Ru - C <sub>12</sub> - EB] <sup>2+</sup>	1.5 <sup>f</sup>	20.5 <sup>b</sup>	d ET after oxidative quench with [Co(NH <sub>3</sub> ) <sub>5</sub> Cl] <sup>2+</sup> gives [P <sub>Cys</sub> - Fe <sup>IV</sup> (HO)]? or a porphyrin radical $k_f = 6 \times 10^3 \text{ s}^{-1}$	[11, 35]
[Ru - C <sub>13</sub> - EB] <sup>2+</sup>	1.7 <sup>f</sup>	20.6 <sup>b</sup>	d ET after reductive quench with <i>p</i> -MDMA yields [P <sub>Cys</sub> - Fe <sup>II</sup> (H <sub>2</sub> O)] <sup>-</sup>	[11, 35]
[Re - Im - F <sub>8</sub> bp - Im] <sup>+</sup>	0.6 ± 0.5		d ET after reductive quench with <i>p</i> -MDMA yields [P <sub>Cys</sub> - Fe <sup>II</sup> (H <sub>2</sub> O)] <sup>-</sup>	[36]

**Table 1** continued

Wire <sup>a</sup>	$K_d$ ( $\mu\text{M}$ )	$d_{\text{M-Fe}}$ ( $\text{\AA}$ )	Comments <sup>b</sup>	Refs.
[Re - Im - F <sub>9</sub> bp] <sup>+</sup>	22 ± 8		d	[36]
[Ru - F <sub>8</sub> - C <sub>2</sub> Ph]	0.75	23.1 <sup>c</sup>	d	[16]
D - 8 - Ad	~ 0.02 h	N/A	N/A	[9, 10]

<sup>a</sup> See Fig. 11

<sup>b</sup> Distances were determined from time-resolved emission experiments using the Förster relationship

<sup>c</sup> Distance was determined by X-ray crystallography

<sup>d</sup> Direct photoinduced ET was not observed

<sup>e</sup> Photochemical data are not available

<sup>f</sup> Dissociation constants determined by deconvolution of transient emission spectra

<sup>g</sup> Dissociation constants determined by UV-titrations with camphor

<sup>h</sup> Value represents an upper-limit estimate of the dissociation constant

P450:wire complex (Sect. 2.2) [35]. Perhaps not surprisingly, full ligation of the heme can be achieved for ferrous P450, for which water is a poor ligand [35].

Wires terminated by hydrophobic substrates are incapable of coordinating the heme directly. When these wires bind P450CAM, water may or may not be displaced from the active site. Alkyl-tethered wires with ethylbenzene substrates do not produce significant changes in heme ligation or spin state on binding [35], whereas alkyl and perfluorobiphenyl-tethered adamantyl wires cause partial displacement of coordinated water from the active site [34–36].

The dissociation constants for P450CAM:wire complexes depend on the nature of the substrate, tether, and head group (Table 1); they reflect the neutral hydrophobic character of the P450CAM active-site channel. The highest binding constants are observed for wires containing hydrophobic substrates such as adamantyl and ethylbenzene. Interestingly, wires terminated with imidazole groups ligate the heme but bind ca. 4–20 times more weakly; for example,  $[\text{Ru} - \text{F}_9\text{bpy}]^{2+}$  binds more tightly than  $[\text{Ru} - \text{F}_8\text{bpy} - \text{Im}]^{2+}$ , suggesting that the imidazole actually destabilizes the P450:wire complex, consistent with an energetic penalty associated with desolvation of imidazole on binding in the hydrophobic active site [35]. Evidence also indicates that there is greater accessibility of water to the active site in the open P450 conformation of the P450CAM:wire complex [9], as P450CAM displays 100-fold discrimination between 1-phenyl imidazole ( $K_d = 0.4 \mu\text{M}$ ) and 4-phenyl imidazole ( $K_d = 40 \mu\text{M}$ ) [37, 38]. Hydrophobic linker and head groups promote tight binding, as can be seen by the lower dissociation constants in P450:wire complexes containing perfluorobiphenyl linkers and the 10-fold decrease in  $K_d$  observed for  $[\text{tmRu} - \text{F}_8\text{bpy} - \text{Im}]^{2+}$  vs.  $[\text{Ru} - \text{F}_8\text{bpy} - \text{Im}]^{2+}$ . The tether length also is a factor (Fig. 3):  $K_d$  values exhibit a slight tether length dependence in wires where the tether is long enough to permit access of the substrate group to the heme, whereas wires with shorter tethers bind much more weakly or not at all.

The  $\Lambda$  and  $\Delta$  enantiomers of wires with metal tris-chelate head groups interact differently with the chiral P450CAM active-site channel. Experiments with enantiopure  $\Lambda$ - and  $\Delta$ - $[\text{Ru} - \text{C}_9 - \text{Ad}]\text{Cl}_2$  wires indicate that the  $\lambda$  enantiomer binds  $\sim 1.5$ – $2$  times more tightly even though the Ru–Fe distances are indistinguishable [39]. The small difference in  $K_d$ s for the two enantiomers suggests that hydrophobic interactions with the adamantyl substrate are more important than induced fit of the head group at the mouth of the active-site channel. The slight preferential binding of  $\Lambda$ - $[\text{Ru} - \text{C}_9 - \text{Ad}]\text{Cl}_2$  may be due to more favorable hydrophobic  $\pi$ -stacking interactions between the bpy groups and Phe<sup>193</sup> and Tyr<sup>29</sup>, a proposal consistent with the P450CAM: $[\text{Ru} - \text{C}_9 - \text{Ad}]^{2+}$  crystal structure (Sect. 2.2) [39].

## 2.2

### Probing Open States

Crystal structures have been reported for conjugates between P450CAM and  $[\text{Ru} - \text{C}_9 - \text{Ad}]^{2+}$  [11],  $[\text{Ru} - \text{F}_8\text{bpy} - \text{Ad}]^{2+}$  [8], D-4-Ad [9], and D-8-Ad [9, 10]. Several of the P450CAM:wire structures are shown in Fig. 4 along with that of P450CAM: camphor [9, 33]. In the camphor complex (Fig. 4a), P450CAM possesses a native closed structure in which there is no clear path to the buried heme. In the P450:wire conjugates, the adamantyl substrate groups are bound in the active site and occupy similar positions to that observed in the P450:adamantane complex [40]. The tether/head group traces a path to the enzyme surface and forces P450CAM into an open conformation with a ca. 11 Å wide and 22 Å deep channel [8, 9]. In the P450CAM open conformation, the F and G helices are displaced ca. 1 helical turn across the I helix so that the F/G domain moves away from the P450CAM  $\beta$ -sheet domain (Fig. 5) [8, 9]. The F/G loop and certain other residues along the E, F, and G helices function as hinges to facilitate this movement (Fig. 6) [9], while long side chains on the F, G, and I helices allow hydrogen bonding contacts between the F/G domain and the I helix [8]. The H helix and the N-terminus of the I helix move with the G helix so as to further maintain interhelical contacts.

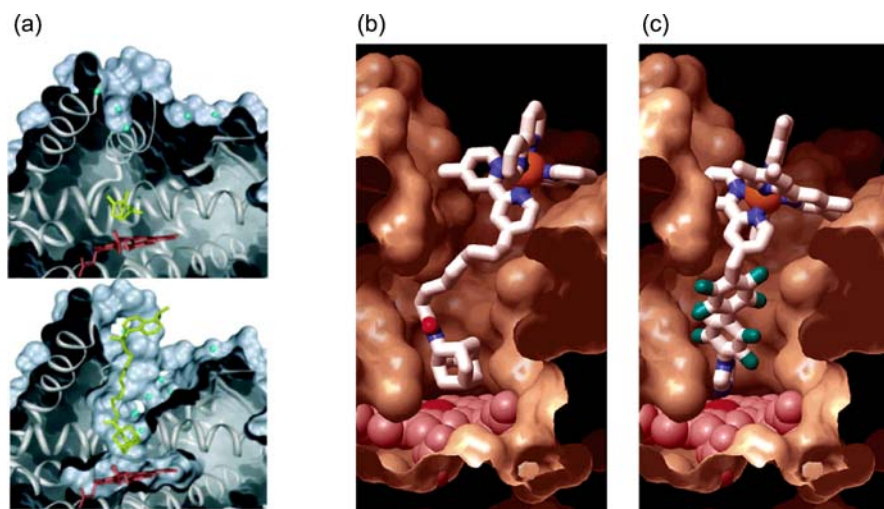


**Fig. 4** Cutaway views of the crystallographically determined structures of P450CAM wire complexes: (a) Comparison of the closed P450CAM conformation in its complex with camphor (*top*) and the open conformation adopted in its complex with D-8-Ad (*bottom*) (reproduced by permission from [9]). (b) Structure of the P450CAM:  $[\text{Ru} - \text{C}_9 - \text{Ad}]^{2+}$  complex compared with (c) a model of the P450CAM:  $[\text{tmRu} - \text{F}_8\text{bpy} - \text{Im}]^{2+}$  complex. Reproduced by permission from [33]

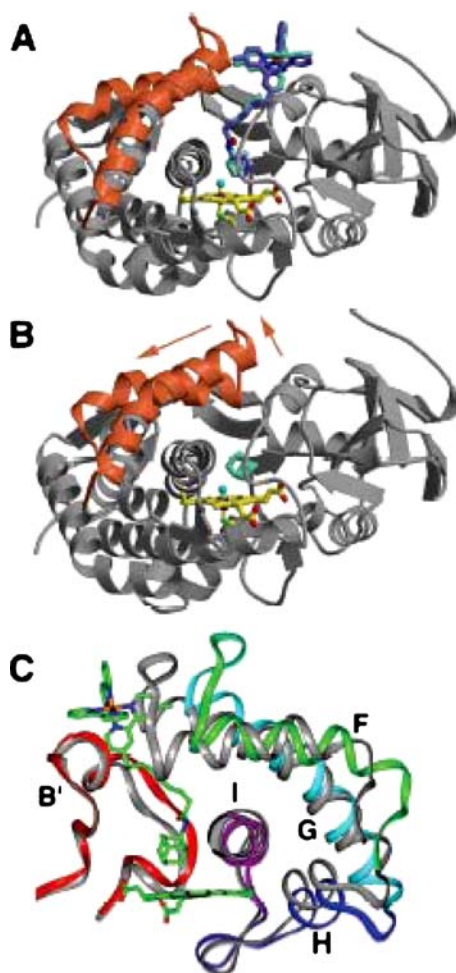


**Fig. 5** Comparison between the structure of P450CAM bound to **A**  $[\text{Ru}-\text{C}_9-\text{Ad}]^{2+}$  and **B** adamantane illustrating the displacement of the F/G subdomain across the I helix that occurs on formation of the P450CAM:  $[\text{Ru}-\text{C}_9-\text{Ad}]^{2+}$  complex. **C** Structure of the P450CAM:  $[\text{Ru}-\text{C}_9-\text{Ad}]^{2+}$  complex showing contacts between the F, G, I, and H helices. Reproduced with permission from [8]

Molecular wires with shorter tethers or more sterically demanding head groups are accommodated mainly by opening of the F/G subdomain, not by changes in substrate coordination at the active site. The extreme open conformation occurs in conjugates with  $[\text{Ru}-\text{C}_9-\text{Ad}]^{2+}$  [11] and  $[\text{Ru}-\text{F}_8\text{bpy}-\text{Ad}]^{2+}$  [8], which possess bulky  $[\text{Ru}(\text{bpy})_3]^{2+}$  head groups. Binding of the smaller D-4-Ad and D-8-Ad wires produces increasingly smaller conformational changes that involve the disruption of fewer interhelix interactions (Fig. 6) [9]. In particular, salt bridges and hydrogen bonding

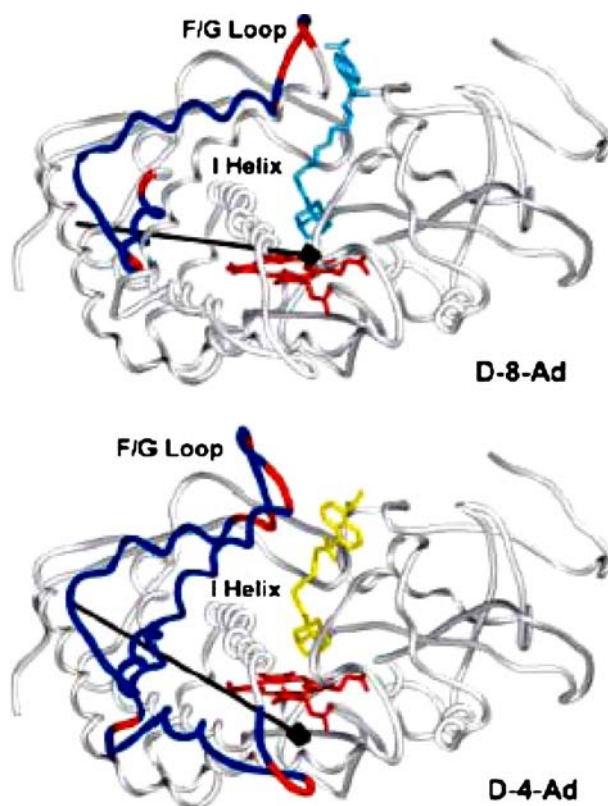


**Fig. 6** Molecular structures of the P450CAM: D-8-Ad (*top*) and P450CAM: D-4-Ad (*bottom*) complexes showing the specific domains that are significantly displaced on wire binding (*blue*) by rotational motion about hinge residues (*red*) that undergo large ( $\phi/\psi$ ) changes. The axis of the rotational motion is shown as a *black arrow*. Reproduced with permission from [9]

interactions between the F and I and B' and G helices are disrupted in the more open D-4-Ad complex, while only interactions between the F and I helices are broken in the D-8-Ad complex [9]. The overall effect of D-8-Ad binding is a more localized retraction of the F helix from the closed position, whereas D-4-Ad causes an additional retraction of the G helix. Essentially, these interactions permit the F/G subdomain to act as an adjustable clamp to hold the wire in place while excluding excess water from the active site [8].

The conformational movements associated with formation of open structures affect the positions of several catalytically important residues in the active site. The I helix bulge, which controls the water structure about the heme, and the catalytically relevant Asp<sup>251</sup> and Thr<sup>252</sup> residues are displaced into positions similar to those observed on dioxygen binding (Fig. 7) [9]. In

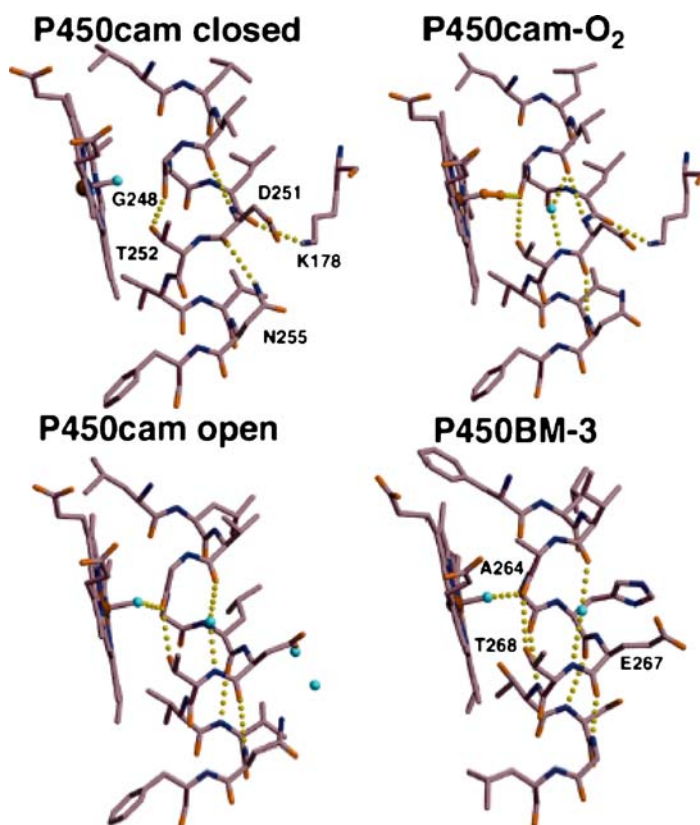


**Fig. 7** Comparison of the active-site structures of native (*closed*) P450CAM, P450CAM: O<sub>2</sub>, open P450CAM, and P450BM3. Reproduced with permission from [8]

particular, Asp<sup>251</sup>, which has been implicated in proton delivery to the active site, becomes hydrated on formation of the open conformation.

It is likely that these open conformations correspond to the structures of transient intermediates that are formed when substrates enter or products leave the active site [9]. The F/G loop occupies similar positions in other P450 isoforms, including substrate-free P450BM3 and P450NOR [41–43], and it is disordered in the crystal structures of P450terp and P4502C5 [44, 45]. The transient existence of open intermediates is supported by photoacoustic calorimetry [46, 47], cooperative substrate hydroxylation [48] and mutagenesis studies, [49] as well as computer simulations [50–52] with a variety of P450 isoforms.

Interestingly, P450:wire conjugates in the open conformation show catalytic activity. When P450:[Ru – C<sub>9</sub> – Ad]<sup>2+</sup> was treated with NADH in the presence of Pdx and Pdx reductase, the reductant was consumed at a rate of  $8 \pm 2$  mol/min/ $\mu$ mol P450, whereas product assays showed 10% formation of



the hydroxylated wire,  $[\text{Ru} - \text{C}_9 - \text{Ad} - \text{OH}]^{2+}$  [35]. Control experiments with 2-adamantylacetamide revealed a turnover rate of  $\sim 90 \pm 20 \text{ mol min}^{-1} \mu\text{mol P450}^{-1}$ . The lower rate observed for  $\text{P450}:[\text{Ru} - \text{C}_9 - \text{Ad}]^{2+}$  could be a consequence of conformational changes near  $\text{Asp}^{251}$  and  $\text{Thr}^{252}$  associated with  $[\text{Ru} - \text{C}_9 - \text{Ad}]^{2+}$  binding.

The crystallographic structures of wire:P450CAM complexes further underscore the importance of hydrophobic contacts for wire binding. The most striking results have been obtained for the complex with  $[\text{Ru} - \text{F}_8\text{bpy} - \text{Ad}]^{2+}$ , which possesses an electron-poor octafluorobiphenyl tether that is capable of forming strong parallel and perpendicular  $\pi$ -stacking interactions with electron-rich aromatic residues along the enzyme channel. As shown in Fig. 8, close contacts are made with  $\text{Tyr}^{29}$ ,  $\text{Phe}^{193}$ ,  $\text{Thr}^{87}$ , and  $\text{Tyr}^{96}$ . Of these,  $\text{Phe}^{193}$  is parallel to one of the octafluorobiphenyl rings with a 3.4 Å face-to-face distance, while  $\text{Phe}^{87}$  and  $\text{Tyr}^{96}$  are perpendicular to the biphenyl ring [8].

The results with alkyl-tethered wires further illuminate the wire:P450CAM interactions that can be exploited in inhibitor design. In these complexes, the hydrocarbon tether contacts hydrophobic residues along the active-site channel,  $\text{Ile}^{395}$ ,  $\text{Phe}^{193}$ ,  $\text{Phe}^{87}$ , and  $\text{Tyr}^{96}$ , many of which also are involved in binding the biphenyl moiety of  $[\text{Ru} - \text{F}_8\text{bpy} - \text{Ad}]^{2+}$  [8]. The flexible hydrocarbon tether permits the adamantyl moiety to adopt a favorable conformation in the active-site pocket, making extensive hydrophobic contacts with  $\text{Leu}^{244}$ ,  $\text{Thr}^{101}$ ,  $\text{Ile}^{395}$ ,  $\text{Val}^{295}$ ,  $\text{Thr}^{252}$ , and  $\text{Gly}^{248}$ . Complexes with hydrocarbon-tethered wires also make hydrogen bonding contacts between the adamantyl amide carbonyl and  $\text{Tyr}^{96}$  that are analogous to those observed between  $\text{Tyr}^{96}$  and the camphor ketone in the native enzyme [53]. In the  $[\text{Ru} - \text{C}_9 - \text{Ad}]^{2+}$  [11] and  $[\text{Ru} - \text{F}_8\text{bpy} - \text{Ad}]^{2+}$  [8] structures, the

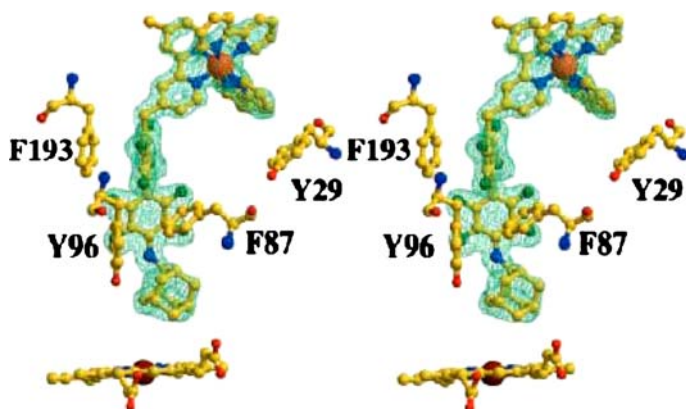


**Fig. 8** Structure of  $[\text{Ru} - \text{F}_8\text{bpy} - \text{Ad}]^{2+}$  bound to P450CAM showing interaction of the  $[\text{Ru}(\text{bpy})_3]^{2+}$  head group and octafluorobiphenyl tether with aromatic residues lining the active-site channel

[Ru(bpy)<sub>3</sub>]<sup>2+</sup> head groups of the  $\Lambda$  and  $\Delta$  enantiomers occupy different positions, making hydrophobic contacts with Tyr<sup>29</sup> and Pro<sup>187</sup>. These interactions at the mouth of the active-site channel contribute to substrate binding and serve to anchor the head group in place. Indeed, the hydrocarbon tether in the [Ru – F<sub>8</sub>bpy – Ad]<sup>2+</sup> complex is not fully extended and FET measurements (Table 1) indicate that the Ru-heme distance does not vary with tether length in other alkyl-tethered P450CAM:wire complexes.

Consistent with the above findings, multiple binding modes have been observed in the external portion of the D-8-Ad wire bound to P450CAM. The dansyl group is found in different conformations on the surface of the protein in two separate crystals of D-8-Ad bound to P450CAM, whereas the inner portions of the wire are bound identically (Fig. 9). Interestingly, the interactions of the dansyl groups with the protein are very similar in each of these conformations, owing to the rather symmetric disposition of Pro<sup>89</sup> on the B' helix and Pro<sup>187</sup> in the F/G loop.

Even after extensive structural characterization, one aspect of P450CAM binding to D-8-Ad remains puzzling. Addition of either D-8-Ad or D-4-Ad to P450CAM causes a partial spin-state shift (as judged by changes in the heme Soret absorbance) and efficient quenching of dansyl fluorescence (FET to the heme) [10]. Titration of camphor into samples of either complex causes a spin-state shift, consistent with binding of camphor at the enzyme active site. However, while camphor addition to the P450CAM:D-4-Ad complex

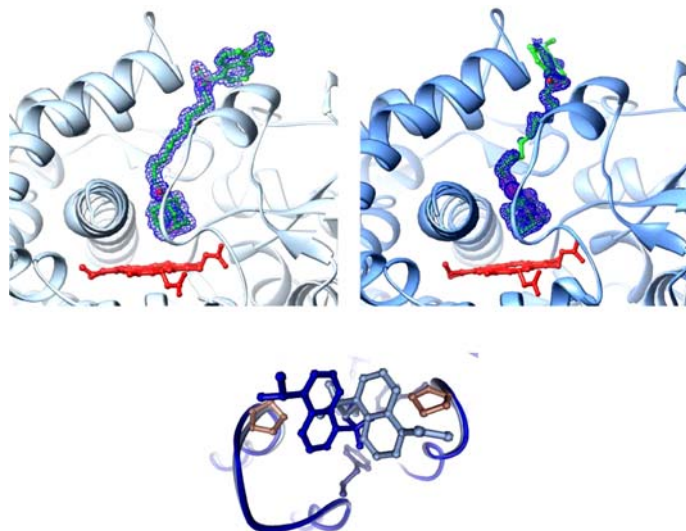


**Fig. 9** Crystal structures of two separate crystals of P450CAM bound to D-8-Ad at 1.45 Å (*left*) and 2.2 Å (*right*) resolution. In the higher resolution structure the dansyl group is found to make an interaction with Pro187 in the F/G loop while in the other crystal the dansyl is packed in a similar way against Pro89 of the B' helix

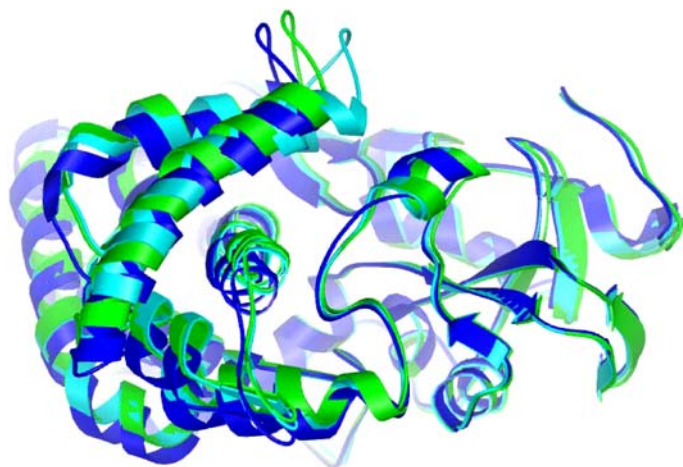


**Fig. 10** Comparison of the refined protein backbone ribbons for P450CAM complexed with D-8-Ad (*cyan*), D-4-Ad (*green*), and D-8-Ad with camphor (*blue*)

causes a recovery of fluorescence, indicating camphor induced release of the wire, no fluorescence recovery is observed when camphor is added to the P450CAM:D-8-Ad complex. This finding suggests that camphor binding to the protein does not lead to displacement of the D-8-Ad wire.

The 1.9 Å crystal structure of P450CAM in the presence of both D-8-Ad and camphor reveals that the F/G region is in a more open conformation than either D-8-Ad or D-4-Ad alone (Fig. 10). In addition, a segment of the B' helix is more disordered than in the absence of camphor and significant movement is seen in the I helix. Further, the wire electron density occupies the approximate location observed in the camphor-free P450CAM: wire structure, but it is not as well resolved. Unfortunately, because of the possible presence of D-8-Ad and/or camphor in the substrate channel, the camphor position in this structure could not be unambiguously defined, although solution measurements suggest that camphor binds at the active site, but does not completely displace the D-8-Ad wire from the channel. Apparently, P450CAM can simultaneously bind wire and camphor by further opening of the flexible active-site channel.

### 2.3 Sensing

The photophysical and selective binding properties of molecular wires have been exploited to develop highly sensitive and selective fluorescent probes of active sites (Fig. 11). Initial work using alkyl-tethered  $[\text{Ru}(\text{bpy})_3]^{2+}$ -based wires established the feasibility of selectively detecting P450CAM at sub-micromolar concentrations by monitoring the decrease in emission life-

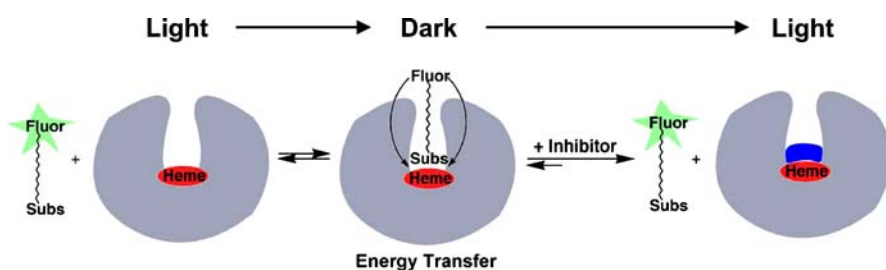


**Fig. 11** Principle of FET detection with P450: wires showing the “light to dark” method for enzyme detection and “dark to light” method for inhibitor screening

time on binding [11]. These assays were found to be highly specific for P450CAM: no change in wire lifetime was observed for other heme proteins, including yeast cytochrome c, horse skeletal muscle myoglobin, bovine lipase, cytochrome b<sub>5</sub>, bovine liver catalase, recombinant yeast cytochrome c peroxidase, and horseradish peroxidase [11]. Based on these results, wires consisting of a dansyl fluorophore tethered to an adamantyl substrate via an  $\alpha, \omega$ -diaminoalkane tether were developed as highly sensitive optical probes for inhibitor screening [10]. These wires bind P450CAM tightly ( $K_d \sim 0.02\text{--}0.83 \mu\text{M}$ ) and exhibit greatly decreased fluorescence in the presence of P450CAM which, in the case of D-4-Ad, can be restored by competition with other substrates, such as camphor (Fig. 12).

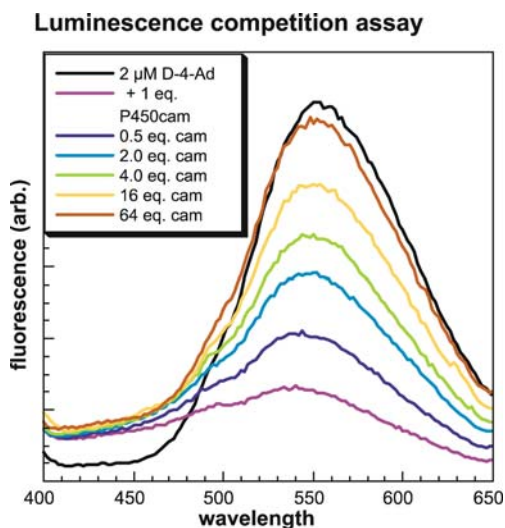


**Fig. 12** Fluorescence spectra of D-4-Ad showing the loss of emission on addition of one equivalent of P450CAM and recovery of emission on addition of camphor

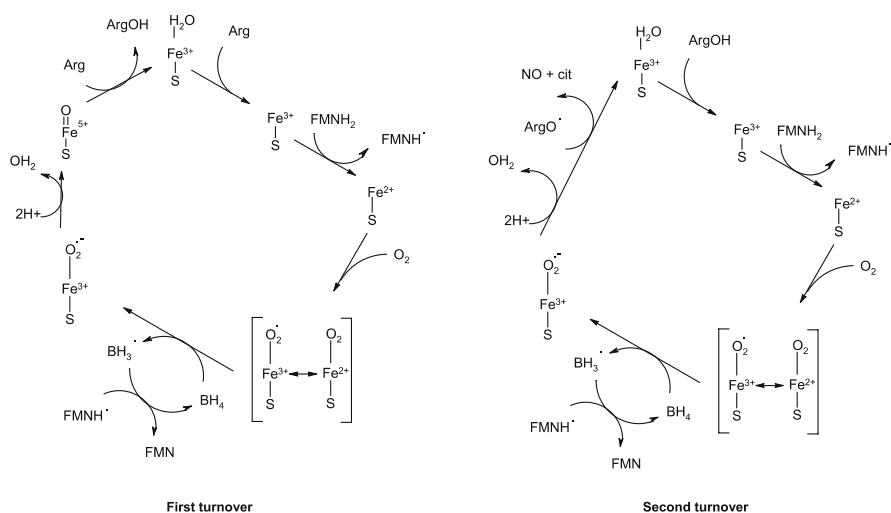
### 3 Molecular Wires for Inducible Nitric Oxide Synthase

NOS is an important signaling enzyme that synthesizes L-citrulline and nitric oxide (NO) from L-arginine and  $O_2$  via two turnovers in a P450-like catalytic cycle (Scheme 2). NOS participates in physiological processes such as neurotransmission, vasodilation, and immune response [54, 55]. Improper regulation of NO production can lead to diseases such as septic shock, heart disease, arthritis, and diabetes.

Three isoforms of NOS are produced in mammalian cells: neuronal (nNOS), endothelial (eNOS), and inducible (iNOS) [55]. All NOS isoforms exist as homodimers with a C-terminal FMN-FAD fused reductase domain, an N-terminal oxygenase domain, and a calmodulin binding sequence at the interface of the two domains. The NOS catalytic mechanism is complicated and requires  $O_2$ , NADPH, FMN, FAD,  $Ca^{2+}$ , calmodulin, tetrahydrobiopterin ( $BH_4$ ), and heme to effect the five-electron oxidation of L-arginine to L-citrulline and NO. Consumed in this process are 1.5 equivalents of NADPH and 2 equivalents of  $O_2$ .

The differences in structures and redox partners between the two classes of P450 and NOS enzymes give rise to differences in reduction potentials and electron transfer mechanisms. The fusion of the oxygenase domain to its di-flavin reductase domain facilitates ET (of relevance here is that P450 BM3 has the highest mono-oxygenase activity of all P450s [56]).

We have employed molecular wire complexes to probe the ET mechanisms of iNOS. Although we have yet to definitively characterize an iNOS:wire con-



**Scheme 2** Proposed NOS catalytic cycle

jugate by X-ray diffraction, our work has elucidated the factors that govern substrate binding in the iNOS active-site channel and on the enzyme surface. Furthermore, comparison of these results with those obtained with P450CAM has shed light on the energetics of wire-enzyme complexation.

### 3.1 Binding

Given the mechanistic similarities between P450 and NOS, our initial work with iNOS focused on molecular wires that are structurally similar to those employed with P450CAM [12, 57]. In addition, most experiments involved the oxygenase domain of inducible NOS (iNOS<sub>oxy</sub>), with N-terminal truncations at amino acid residue 65 (NOS  $\Delta$ 65) and residue 114 (NOS  $\Delta$ 114). Structural differences between the two truncated iNOS species play an important role in wire inhibition and binding: NOS  $\Delta$ 114 exists mainly in monomeric form, whereas NOS  $\Delta$ 65 exists in equilibrium between monomeric and dimeric states and forms tight dimers in the presence of L-arginine and tetrahydrobiopterin (BH<sub>4</sub>) [58]. The NOS monomer has an exposed active site, while NOS dimer has a more constricted access channel.

Molecular wires with [Ru(bpy)<sub>3</sub>]<sup>2+</sup> head groups that bind  $\Delta$ 65 and  $\Delta$ 114 iNOS<sub>oxy</sub> are shown in Fig. 13. Most of these wires are extremely hydropho-

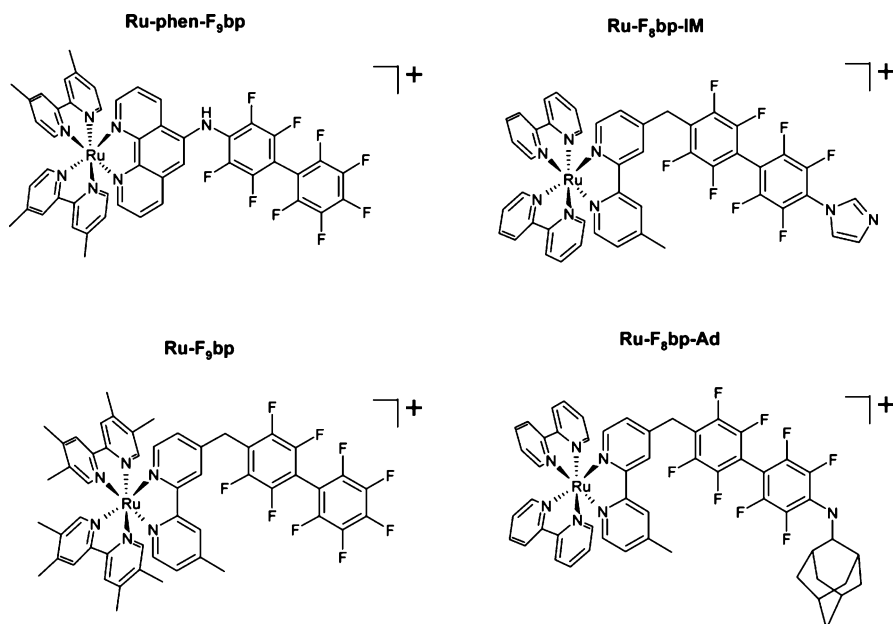


**Fig. 13** Ruthenium wires that bind iNOS<sub>oxy</sub>

bic, owing in part to a decafluorobiphenyl tether. The hydrophobicity of these complexes is further increased by addition of adamantyl groups to the decafluorobiphenyl ring and/or the use of 4,4',5,5'-tetramethylbipyridine co-ligands at the ruthenium center.

Wire binding to iNOS was quantified in work involving both time-resolved and steady-state emission experiments. The results confirm that iNOS:wire conjugates have nanomolar or low micromolar dissociation constants (Table 2) and that the wire binding interactions are not significantly affected by co-binding of L-arginine and BH<sub>4</sub>. In each truncated form ( $\Delta 65$  and  $\Delta 114$  iNOS<sub>oxy</sub>), there is substantial energy transfer quenching of the Ru(II) MLCT excited state. FET kinetics indicate that the wires bind the protein such that the head group is positioned within ca. 18–21 Å of the heme active site. Our analyses of the absorption spectra of iNOS:wire conjugates suggest that the steric bulk of the substrate group and the tether length govern the mode of wire binding. Interestingly, only the weakest binding wire, [Ru – F<sub>8</sub>bp – Im]<sup>2+</sup>, which ligates the heme Fe, displaces L-arginine from the active site.

Based on modeling work, it is not likely that [Ru – F<sub>9</sub>bp]<sup>2+</sup> and [Ru – phen – F<sub>9</sub>bp]<sup>2+</sup> will fit in the active-site channel of  $\Delta 65$ , owing to the bulk of the [Ru(bpy)<sub>3</sub>]<sup>2+</sup> head group (Fig. 14b) [13, 36, 59]. Examination of the FET-determined distances suggests that these wires bind either to the iNOS surface or the mouth of active-site channel but are too short to reach the deeply buried active site. Modeling indicates that [Ru – F<sub>8</sub>bp – Ad]<sup>2+</sup> cannot reach the active sites of  $\Delta 65$  or  $\Delta 114$  iNOS<sub>oxy</sub>, owing to the steric bulk of the adamantyl group, although [Ru – F<sub>8</sub>bp – Im]<sup>2+</sup> should be able to bind to the more open active site of monomeric  $\Delta 114$  iNOS<sub>oxy</sub> (Fig. 14). In addition, the presence of excess electron density at a concave hydrophobic patch on the oxygenase-reductase interface surface in a partial crystal structure of iNOS:[Ru – F<sub>8</sub>bp – Ad]<sup>2+</sup> is consistent with wire binding at this surface position [36, 59].

Our results confirm that the iNOS active-site channel is considerably less plastic than that of P450CAM. In addition, they suggest that ruthenium wires could inhibit iNOS activity by blocking electron transfer between the reductase and oxygenase domains.

**Table 2** iNOS:wire conjugates

Wire	$\Delta 114$ (K <sub>d</sub> , $\mu$ M)	$\Delta 65$ (K <sub>d</sub> , $\mu$ M)	$\Delta 65 + \text{arg} + \text{BH}_4$ (K <sub>d</sub> , $\mu$ M)	Refs.
[Ru – phen – F <sub>9</sub> bp] <sup>2+</sup>	–	0.5 ± 0.15	–	[59]
[Ru – F <sub>9</sub> bp] <sup>2+</sup>	0.71 ± 0.09	0.54 ± 0.04	1.7 ± 0.4	[57]
[Ru – F <sub>8</sub> bp – Im] <sup>2+</sup>	7.1 ± 0.4	6.5 ± 2.4	7.2 ± 3.4	[57]
[Ru – F <sub>8</sub> bp – Ad] <sup>2+</sup>	0.88 ± 0.15	0.58 ± 0.16	0.89 ± 0.15	[57]

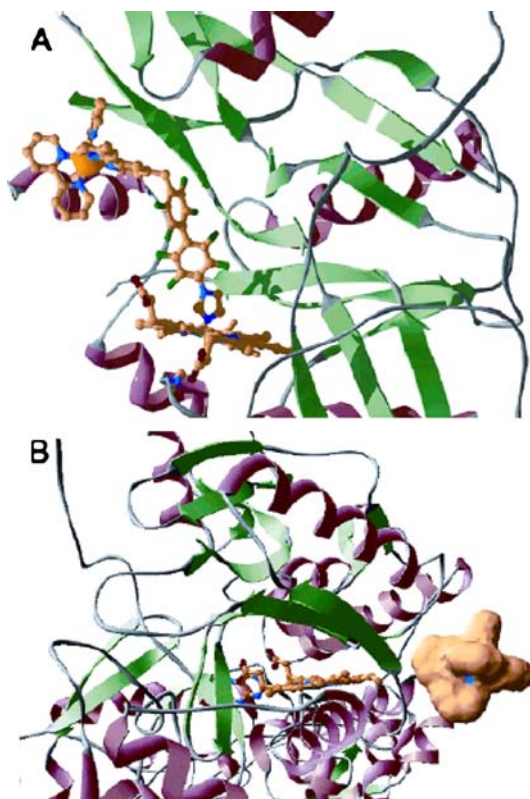


**Fig. 14** **A** Model of  $[\text{Ru}-\text{F}_8\text{bp}-\text{Im}]^{2+}$  bound to the exposed heme of NOS  $\Delta 114$ . **B** Model of  $[\text{Ru}(\text{bpy})_3]^{2+}$  docked at the proposed oxygenase-reductase interface. Reproduced from [13]

In related work, we found that use of a smaller head group,  $[\text{Re}(\text{CO})_3(\text{bpy})(\text{Im})]^+$  [60], promotes wire binding to the deeply buried iNOS active site. The four rhenium wires that have been investigated most extensively as probes of iNOS<sub>oxy</sub> are shown in Fig. 15 [12, 36].

All four wires bind in the active-site channel of the enzyme with low micromolar or nanomolar dissociation constants (Table 3). Analysis of the heme Soret suggests that the active-site structure converts from six-coordinate low-spin to five-coordinate high-spin in complexes with  $[\text{Re}-\text{Im}-\text{F}_9\text{bp}]^+$  and  $[\text{Re}-\text{Im}-\text{C}_3-\text{F}_9\text{bp}]^+$ , indicative of water displacement from the heme region. The two imidazole-terminated wires,  $[\text{Re}-\text{Im}-\text{F}_8\text{bp}-\text{Im}]^+$  and  $[\text{Re}-\text{Im}-\text{C}_3-\text{F}_8\text{bp}-\text{Im}]^+$ , both displace water and ligate the heme, as judged by observation of the characteristic “low-spin shift” of the heme Soret band.

In summary, our results show that wires with sterically demanding  $[\text{Ru}(\text{bpy})_3]^{2+}$  head groups bind with low-micromolar to nanomolar disso-



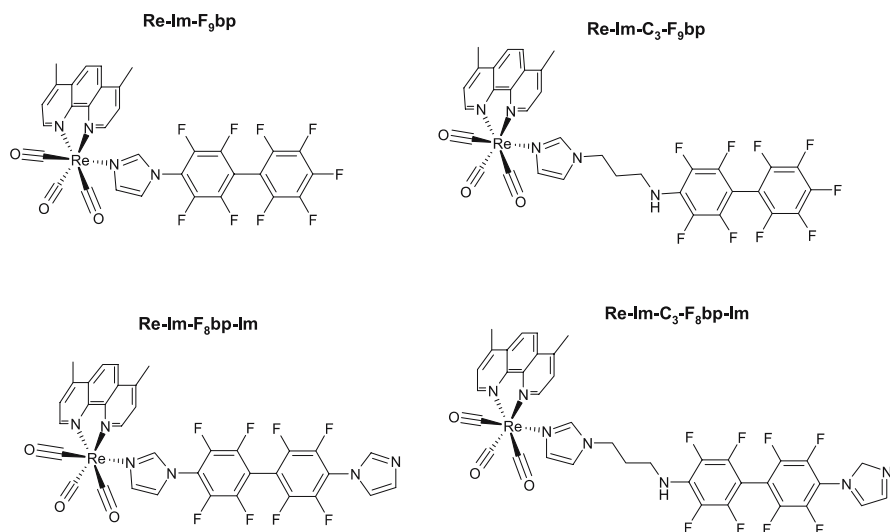


**Fig. 15** Rhenium wires that bind iNOS<sub>oxy</sub>

**Table 3** Dissociation constants for Re wires with  $\Delta 65$  iNOS<sub>oxy</sub>

Wire	$\Delta 65$ , $K_d$ ( $\mu\text{M}$ )	Wire	$\Delta 65$ , $K_d$ ( $\mu\text{M}$ )
$[\text{Re} - \text{Im} - \text{F}_9\text{bp}]^+$	1.4	$[\text{Re} - \text{Im} - \text{C}_3 - \text{F}_9\text{bp}]^+$	< 10
$[\text{Re} - \text{Im} - \text{F}_8\text{bp} - \text{Im}]^+$	0.13	$[\text{Re} - \text{Im} - \text{C}_3 - \text{F}_8\text{bp} - \text{Im}]^+$	< 10

ciation constants to the iNOS surface, presumably at the oxygenase and reductase interface, whereas wires with  $[\text{Re}(\text{CO})_3(\text{bpy})(\text{Im})]^+$  head groups bind in the active-site channel with similar affinities [13]. When compared to the remarkable indifference of P450CAM:wire stability to the steric bulk of the head group, these results underscore the importance of protein plasticity in wire binding. Additionally, the remarkable disparity in structure between the rhenium channel-binding wires and the natural substrate, L-arginine, suggests that binding is driven principally by hydrophobic interactions with active-site channel residues [13].

### 3.2 Sensing

While we have not aggressively attempted to develop fluorescent sensors for iNOS, FET and ET quenching by the heme of the MLCT excited states of  $[\text{Ru}(\text{bpy})_3]^{2+}$  and  $[\text{Re}(\text{CO})_3(\text{bpy})(\text{Im})]^+$  head groups enable the wires shown in Fig. 13 and 15 to function as effective “light-to-dark” probes of the en-

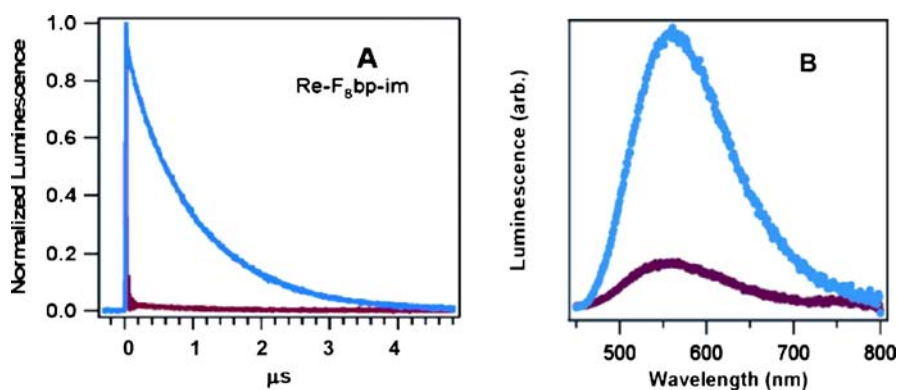


**Fig. 16** **A** Time-resolved and **B** steady-state luminescence of  $[\text{Re} - \text{Im} - \text{F}_8\text{bp} - \text{Im}]^+$  in the presence of  $\text{iNOS}_{\text{oxy}}$ . Reproduced from [12]

zyme. The most promising of these are the rhenium-based wires, whose MLCT excited states are strongly quenched by ultrafast ET to the iNOS heme (Fig. 16) [12, 13, 36]. Given the ability of iNOS to form wire complexes with nanomolar dissociation constants, it should be possible to develop extremely sensitive dansyl or fluorescein-based FET wire sensors for the enzyme.

#### 4

### Conclusions

Photoactive wire probes are powerful tools for studying protein mechanism and function, enabling rapid photogeneration of reactive enzyme redox states and systematic study of the structural factors that govern substrate binding and promiscuity. Additionally, they show promise as high affinity and isoform specific fluorescent protein sensors, electrochemical probes, and crystallographic tools for studying the open states of enzymes.

Through an understanding of the structure of the native enzyme, we have designed selective probes that successfully target and interrogate P450CAM and iNOS. In turn, structural studies of wire-enzyme complexes have provided a wealth of information. They have elucidated the chemical features that dictate the binding mode and affinity for the enzyme, and have revealed the conformational flexibility of the protein, trapping structures that mimic transient intermediates associated with substrate binding through catalysis to product release.

Working at the interface of chemistry and biology, we are exploiting techniques at the two extremes of the time scale for protein research: ultrafast photoreduction of the enzyme by these metal-diimine wires affords access to catalytic intermediates on the time scale of electron transfer, while X-ray crys-

tallography of enzyme:wire conjugates provides complementary snapshots of *static* structures. The goal of fast reduction of a deeply buried heme via a wire has been accomplished with iNOS, while detailed structural analyses with a variety of wires have provided new information about the conformational states of P450CAM, and has offered clues for creating inhibitors that take advantage of its structural flexibility.

**Acknowledgements** Figure 11 was adopted from a version prepared by Alex Dunn. We thank him and others in the Caltech molecular wires group (Ivan Dmochowski, Jon Wilker, Corinna Hess, Wendy Belliston-Bittner, Nick Halpern-Manners) for contributions that are summarized in this chapter. Our work is supported by NIH, NSF, the Ellison Medical Foundation Senior Scholar Award in Aging (to HBG), and the Arnold and Mabel Beckman Foundation.

## References

1. Roberts GA, Grogan G, Greter A, Flitsch SL, Turner NJ (2002) *J Bacteriol* 184:3898
2. Boddupalli SS, Oster T, Estabrook RW, Peterson JA (1992) *J Biol Chem* 267:10375
3. Warman AJ, Roitel O, Neeli R, Girvan HM, Seward HE, Murray SA, McLean KJ, Joyce MG, Toogood H, Holt RA, Leys D, Scrutton NS, Munro AW (2005) *Biochem Soc Trans* 33:747
4. Fuziwara S, Sagami I, Rozhkova E, Craig D, Noble MA, Munro AW, Chapman SK, Shimizu T (2002) *J Inorg Biochem* 91:515
5. Low DW, Winkler JR, Gray HB (1996) *J Am Chem Soc* 118:117
6. Wilker JJ, Dmochowski IJ, Dawson JH, Winkler JR, Gray HB (1999) *Angew Chem Int Ed* 38:90
7. Dmochowski IJ, Dunn AR, Wilker JJ, Crane BR, Green MT, Dawson JH, Sligar SG, Winkler JR, Gray HB (2002) *Method Enzymol* 357:120
8. Dunn AR, Dmochowski IJ, Bilwes AM, Gray HB, Crane BR (2001) *Proc Natl Acad Sci USA* 98:12420 x
9. Hays A-MA, Dunn AR, Chiu R, Gray HB, Stout CD, Goodin DB (2004) *J Mol Biol* 344:455
10. Dunn AR, Hays A-MA, Goodin DB, Stout CD, Chiu R, Winkler JR, Gray HB (2002) *J Am Chem Soc* 124:10254
11. Dmochowski IJ, Crane BR, Wilker JJ, Winkler JR, Gray HB (1999) *Proc Natl Acad Sci USA* 96:12987
12. Belliston-Bittner W, Dunn AR, Nguyen YHL, Stuehr DJ, Winkler JR, Gray HB (2005) *J Am Chem Soc* 127:15907
13. Dunn AR, Belliston-Bittner W, Winkler JR, Getzoff ED, Stuehr DJ, Gray HB (2005) *J Am Chem Soc* 127:5169
14. Hess CR, Juda GA, Dooley DM, Amii RN, Hill MG, Winkler JR, Gray HB (2003) *J Am Chem Soc* 125(24):7156
15. Contakes SM, Juda GA, Langley DB, Halpern-Manners NW, Duff AP, Dunn AR, Gray HB, Dooley DM, Guss JM, Freeman HC (2005) *Proc Natl Acad Sci USA* 102:13451
16. Gray HB, Dunn AR, Belliston W, Leigh BS, Contakes SM, Winkler JR (2003) 225th ACS National Meeting, New Orleans, LA, USA
17. Kenyon V, Chorny I, Carvaja SW, Holman TR, Jacobson MP (2006) *J Med Chem* 49:1356

18. Lewis DFV (2001) *Guide to Cytochromes P450: Structure and Function*. CRC Press, New York
19. Ortiz de Montellano PR (1995) *Cytochrome P450: Structure, Mechanism, and Biochemistry*. Plenum Press, New York, p 652
20. Phillips IR, Shephard EA (1998) *Methods in Molecular Biology*, vol 107. Humana Press, Totowa, p 482
21. Sono M, Roach MP, Coulter ED, Dawson JH (1996) *Chem Rev* 96:2842
22. Guengerich FP (2003) *Mol Interv* 3:194
23. Glieder A, Farinas ET, Arnold FH (2002) *Nat Biotechnol* 20:1135
24. Joseph S, Rusling JF, Lvov YM, Friedberg T, Fuhr U (2003) *Biochem Pharmacol* 65:1817
25. Davydov R, Markris TM, Kofman V, Werst DE, Sligar SG, Hoffman BM (2001) *J Am Chem Soc* 123:1403
26. Egawa T, Shimada H, Ishimura Y (1994) *Biochem Biophys Res Commun* 201:1464
27. Schlichting I, Berendzen J, Chu K, Stock AM, Maves SA, Benson DE, Sweet RM, Ringe D, Petsko GA, Sligar SG (2000) *Science* 287:1615
28. Glascock MC, Ballou DP, Dawson JH (2005) *J Biol Chem* 280:42134
29. Udit A, Contakes SM, Gray HB (2007) *Met Ions Life Sci* 3:in press
30. Udit A (2005) P450 BM3 electrochemistry and electrocatalysis. PhD, California Institute of Technology
31. Noble M, Miles C, Chapman S, Lysek D, Mackay A, Reid G, Hanzlik R, Munro A (1999) *Biochem J* 339:371
32. Sevrioukova IF, Li H, Zhang H, Petersson JA, Poulos TL (1999) *Proc Natl Acad Sci USA* 96:1863
33. Dunn AR, Dmochowski IJ, Winkler JR, Gray HB (2003) *J Am Chem Soc* 125:12450
34. Dunn AR (2003) Sensitizer-linked substrates as probes of heme enzyme structure and catalysis. PhD, California Institute of Technology
35. Dmochowski IJ (2000) Probing Cytochrome P450 with Sensitizer-linked Substrates. Ph.D., California Institute of Technology
36. Belliston Bittner W (2005) Ultrafast Photoreduction of Nitric Oxide Synthase by Electron Tunneling Wires. PhD, California Institute of Technology
37. Lipscomb JD (1980) *Biochemistry* 19:3590
38. Poulos TL, Howard AJ (1987) *Biochemistry* 26:8165
39. Dmochowski IJ, Winkler JR, Gray HB (2000) *J Inorg Biochem* 81:221
40. Raag R, Poulos TL (1991) *Biochemistry* 30:2674
41. Ravichandran KG, Boddupalli SS, Hasemann CA, Peterson JA, Deisenhofer J (1993) *Science* 261:731
42. Li H, Poulos TL (1997) *Nat Struct Biol* 4:140
43. Park SY, Shimizu H, Adachi S, Nakagawa A, Tanaka I, Nakahara K, Shoun H, Obayashi E, Nakamura H, Iizuka T, Shiro Y (1997) *Nat Struct Biol* 4:827
44. Hasemann CA, Kurumbail RG, Boddupalli SS, Peterson JA, Deisenhofer J (1995) *Structure* 2:41
45. Williams PA, Cosme J, Sridhar V, Johnson EF, McRee DE (2000) *Molec Cell* 5:121
46. DiPrimo C, Hoa GHB, Deprez E, Douzou P, Sligar SG (1993) *Biochemistry* 32:3671
47. DiPrimo C, Deprez E, Sligar SG, Hoa GHB (1997) *Biochemistry* 36:112
48. Ueng Y-F, Kuwabara T, Chun Y-J, Guengerich FP (1997) *Biochemistry* 36:371
49. Podust LM, Poulos TL, Waterman MR (2001) *Proc Natl Acad Sci USA* 98:3068
50. Paulsen MD, Ornstein RL (1995) *Proteins* 21:237
51. Poulos TL (1995) *Curr Opin Struct Biol* 5:767
52. Ludemann SK, Lounnas V, Wade RC (2000) *J Mol Biol* 303:797

53. Poulos TL, Finzel BC, Gunsalus IC, Wagner GC, Kraut J (1985) *J Biol Chem* 260:16122
54. Marletta MA, Hurshman AR, Rusche KM (1998) *Curr Opin Chem Biol* 2:656
55. Stuehr DJ (1999) *Biochim Biophys Acta-Bioenerget* 1411:217
56. Daff S, Chapman S, Turner K, Holt R, Govindaraj S, Poulos T, Munro A (1997) *Biochemistry* 36:13816
57. Dunn AR, Belliston-Bittner W, Winkler JR, Getzoff ED, Stuehr DJ, Gray HB (2005) *J Am Chem Soc* 127:5169
58. Ghosh DK, Wu CQ, Pitters E, Moloney M, Werner ER, Mayer B, Stuehr DJ (1997) *Biochemistry* 36:10609
59. Nguyen YHL (2006) Wiring inducible nitric oxide synthase. PhD, California Institute of Technology
60. Gerstein M (1992) *Acta Cryst Sec A* 48:271

# Luminescent Transition Metal Complexes as Biological Labels and Probes

Kenneth Kam-Wing Lo

Department of Biology and Chemistry, City University of Hong Kong, Tat Chee Avenue,  
Kowloon, Hong Kong, China  
*bhkenlo@cityu.edu.hk*

<b>1</b>	<b>Introduction</b> . . . . .	207
<b>2</b>	<b>DNA Labels</b> . . . . .	210
2.1	Luminescent Linkers and Nucleosides . . . . .	210
2.2	Post-modification of Oligonucleotides . . . . .	214
<b>3</b>	<b>Protein Labels</b> . . . . .	218
3.1	Electron Transfer in Metalloproteins . . . . .	218
3.2	Anisotropy Probes . . . . .	220
3.3	Luminescent Labels . . . . .	223
<b>4</b>	<b>Protein Probes</b> . . . . .	229
4.1	Luminescent Wires for Metalloproteins . . . . .	229
4.2	Platinum-Based Probes . . . . .	231
4.3	Luminescent Biotin Derivatives . . . . .	233
4.4	Probes for Indole-Binding Proteins . . . . .	240
<b>5</b>	<b>Conclusion</b> . . . . .	243
	<b>References</b> . . . . .	243

**Abstract** This review article summarises recent examples of luminescent transition metal complexes that have been employed as labelling reagents and probes for biomolecules. Two major types of biomolecules, DNA (oligonucleotides) and proteins, are focussed on here. Emphasis is placed on the structural design of the metal complexes, the labelling and probing strategies, the spectroscopic and photophysical properties of the complexes and the labelled biomolecules, and the utilisation of the conjugates in understanding biological systems and specific analytical applications.

**Keywords** DNA · Labels · Luminescence · Probes · Proteins

## Abbreviations

Az	Azurin
bpy	2,2'-Bipyridine
bpy-CH <sub>2</sub> – NH – C <sub>2</sub> – NH-biotin	4- <i>N</i> -[(2-Biotinamido)ethyl]aminomethyl-4'-methyl-2,2'-bipyridine
bpy-CO – NH – C <sub>6</sub> – NH-biotin	4- <i>N</i> -[(6-Biotinamido)hexyl]amido-4'-methyl-2,2'-bipyridine

bpy-indole	4-[ <i>N</i> -(2-Indol-3-ylethyl)amido]-4'-methyl-2,2'-bipyridine
bpy-NCS	4-Isothiocyanato-2,2'-bipyridine
bpy-NH <sub>2</sub>	4-Amino-2,2'-bipyridine
bpy-NHCOCH <sub>2</sub> I	4-Iodoacetamido-2,2'-bipyridine
BSA	Bovine serum albumin
dcbpy	4,4'-Dicarboxy-2,2'-bipyridine
dcsbpy	4,4'-Dicarboxy-2,2'-bipyridine <i>N</i> -hydroxysuccinimide ester
DFT	Density functional theory
DMT	Dimethoxytrityl
dppn	Benzo[ <i>i</i> ]dipyrido[3,2- <i>a</i> :2',3'- <i>c</i> ]phenazine
dppz	Dipyrido[3,2- <i>a</i> :2',3'- <i>c</i> ]phenazine
dppz-biotin	11-[(2-Biotinamido)ethyl]amidodipyrido[3,2- <i>a</i> :2',3'- <i>c</i> ]phenazine
dpq	Dipyrido[3,2- <i>f</i> :2',3'- <i>h</i> ]quinoxaline
dpqa	2-( <i>n</i> -Butylamido)dipyrido[3,2- <i>f</i> :2',3'- <i>h</i> ]quinoxaline
dpq-biotin	2-[(2-Biotinamido)ethyl]amidodipyrido[3,2- <i>f</i> :2',3'- <i>h</i> ]quinoxaline
FPR	Formyl peptide receptor
HABA	2-(4'-Hydroxyazobenzene)benzoic acid
Hacac	Acetylacetone
Hbsb	2-[(1,1'-Biphenyl)-4-yl]benzothiazole
Hbsn	2-(1-Naphthyl)benzothiazole
Hbt	2-Phenylbenzothiazole
Hbtth	2-(2-Thienyl)benzothiazole
HC ≡ C - C <sub>6</sub> H <sub>4</sub> - NCS- <i>p</i>	4-Isothiocyanatophenylacetylene
HC ≡ C - C <sub>6</sub> H <sub>4</sub> - NH <sub>2</sub> - <i>p</i>	4-Aminophenylacetylene
HC ≡ C - C <sub>6</sub> H <sub>4</sub> - NHCO - CH <sub>2</sub> I- <i>p</i>	4-Iodoacetamidophenylacetylene
Hmppz	3-Methyl-1-phenylpyrazole
Hpba	4-(2-Pyridyl)benzaldehyde
Hppbpy	4-(4-Hydroxyphenyl)-6-phenyl-2,2'-bipyridine
Hppy	2-Phenylpyridine
Hpq	2-Phenylquinoline
HSA	Human serum albumin
IgG	Immunoglobulin G
IL	Intra-ligand
LLCT	Ligand-to-ligand charge transfer
mcsbpy	4-Carboxy-4'-methyl-2,2'-bipyridine <i>N</i> -hydroxysuccinimide ester
Me <sub>2</sub> -Ph <sub>2</sub> -phen	2,9-Dimethyl-4,7-diphenyl-1,10-phenanthroline
Me <sub>2</sub> -phen	2,9-Dimethyl-1,10-phenanthroline
Me <sub>4</sub> -bpy	4,4',5,5'-Tetramethyl-2,2'-bipyridine
Me <sub>4</sub> -phen	3,4,7,8-Tetramethyl-1,10-phenanthroline
MLCT	Metal-to-ligand charge transfer
MMLCT	Metal-metal-to-ligand charge transfer
N <sup>-</sup> C	Anionic cyclometallating ligands
NHE	Normal hydrogen electrode
NHS	<i>N</i> -Hydroxysuccinimide
N <sup>-</sup> N	Diimine ligands

OVA	Ovalbumin
Ph <sub>2</sub> -phen	4,7-Diphenyl-1,10-phenanthroline
phen	1,10-Phenanthroline
phen-NCS	5-Isothiocyanato-1,10-phenanthroline
phen-NH <sub>2</sub>	5-Amino-1,10-phenanthroline
phen-NHCOCH <sub>2</sub> I	5-Iodoacetamido-1,10-phenanthroline
PEG	Poly(ethylene glycol)
py-3-CONHC <sub>2</sub> H <sub>4</sub> -indole	<i>N</i> -(3-Pyridoyl)tryptamine
py-3-mal	<i>N</i> -(3-Pyridyl)maleimide
py-3-NCS	<i>N</i> -(3-Pyridyl)isothiocyanate
py-4-CH <sub>2</sub> – NH-biotin	<i>N</i> -[(4-Pyridyl)methyl]biotinamide
py-4-CH <sub>2</sub> – NH – C <sub>6</sub> – NH-biotin	4- <i>N</i> -[(6-Biotinamido)hexanoyl]aminomethyl- pyridine
py-4-COOH	Isonicotinic acid
RET	Resonance energy transfer
SCE	Standard calomel electrode
TAP	1,4,5,8-Tetraazaphenanthrene
<sup>t</sup> Bu <sub>3</sub> tpy	4,4',4''-Tri- <i>tert</i> -butyl-2,2':6',2''-terpyridine

## 1

### Introduction

Luminescent transition metal complexes possess many useful photophysical and photochemical properties that enable them to serve as unique biological labels and probes. First, many transition metal complexes, especially those with a charge-transfer excited state, show intense and long-lived emission in the visible region [1–6], which is an advantage for detection and imaging studies. Although numerous organic compounds also exhibit intense emission in the visible region, their lifetimes are very short due to their singlet excited state. Thus, background interference in the samples cannot be easily removed by time-resolved detection [7]. Förster-type RET quenching is commonly employed to study interactions between biological molecules because the range of usual Förster distances is similar to the dimensions of common biomolecules. Fluorescent organic labels in these studies rely essentially on steady-state emission measurements. The longer excited-state lifetimes of transition metal complexes mean that RET quenching can be readily examined by lifetime measurements as an additional monitoring method [8]. Furthermore, metal complexes of long excited-state lifetimes are attractive candidates in the development of new anisotropic probes to study the hydrodynamics of proteins and new assays involving high-molecular antigens and antibodies [9].

A number of transition metal complexes exhibit rich photoredox properties, which allow studies of photocleavage of DNA via guanine oxidation [10], photoinduced electron-transfer reactions in metalloproteins [11], and the use



of various redox-active quenchers in the design of new bioassays [12]. Most importantly, the choice of various metal centres and a wide range of ligands renders it possible to fine-tune the ground-state and excited-state redox potentials of transition metal complexes, which facilitates the development of new photoredox-active biological labelling reagents and probes in specific investigations. Additionally, many transition metal complexes respond sensitively to their local environment, and can thus serve as luminescent reporters of their surroundings. In particular, complexes with a charge-transfer excited state usually show significant changes in their emission energy, intensities and lifetimes in different media [13]. These favourable properties enable the complexes to act as luminescent molecular probes to report biomolecular recognitions that are associated with a change of hydrophobicity. Furthermore, owing to the phosphorescent nature of most luminescent transition metal complexes, their Stokes shifts are much larger than those of the organic fluorophores. Thus, biological molecules can be multiply labelled with metal complexes without reduced fluorescence intensities due to self-quenching, which often occurs in organic fluorophores [14].

This review article summarises recent examples of luminescent transition metal complexes that have been employed as labelling reagents and probes for biomolecules. The terms “label” and “probe” refer to complexes that are *with* and *without* covalent bonding with the biomolecular targets, respectively. Two major types of biomolecules, DNA (oligonucleotides) and proteins, are the main focus of this article. In fact, a large number of metal complexes with extended planar ligands have been designed as DNA metallointercalators; many of them show interesting changes of photophysical properties upon binding to DNA molecules. Since some excellent review articles are available [15–18], these examples as “probes for DNA” are omitted here.

Since earlier work on the introduction of metal complexes to oligonucleotides [19–21], there has been much interest in this area. Section 2 describes the employment of luminescent transition metal complexes as DNA labels, which can be divided into two types: (1) the labels that are introduced before the oligonucleotides are synthesised, and (2) the labels that react with oligonucleotides that have been modified with a reactive group, usually a primary amine or a sulfhydryl group. Complexes of the first type act as a linker between two nucleosides, or they are linked to a nucleoside which is then incorporated into a growing oligonucleotide strand. Complexes of the second type are equipped with reactive functional groups that react readily with a primary amine or a sulfhydryl group. Thus, they also serve as labelling reagents for protein molecules as they can react with the amines of lysine residues and the N-terminus, or the sulfhydryl, of cysteine residues.

Different strategies have been used to attach transition metal complexes to proteins; for example, the imidazole moiety of histidine can be coordinated to metal centres such as ruthenium(II), osmium(II) and rhenium(I). Many studies have utilised the imidazole of a histidine residue as a ligand for

various metal centres [22]. Alternatively, the lysine residue can be modified by a bipyridine ligand containing an NHS ester, and metal precursor complexes can react with this ligand to form luminescent bioconjugates [23]. In general, NHS ester, isothiocyanate and aldehyde react readily with amines, and iodoacetamide and maleimide with sulfhydryls (Fig. 1) [24]. Different transition metal complexes have been functionalised with these groups to form biological labelling reagents [25, 26]; selected examples are discussed in Sect. 3.

The design of most protein probes involves the incorporation of a molecular substrate as a pendant into a metal complex. The recognition of the substrate by the protein host is then revealed by changes of the photophysical properties of the probe. However, metal complexes without a specific molecular substrate have also been employed; the recognition is usually on the basis of hydrophobic interactions. As can be seen in the examples mentioned in Sect. 4, the hydrophobic nature of protein matrix, in particular the substrate-binding sites, provides opportunities in the development of new probes.

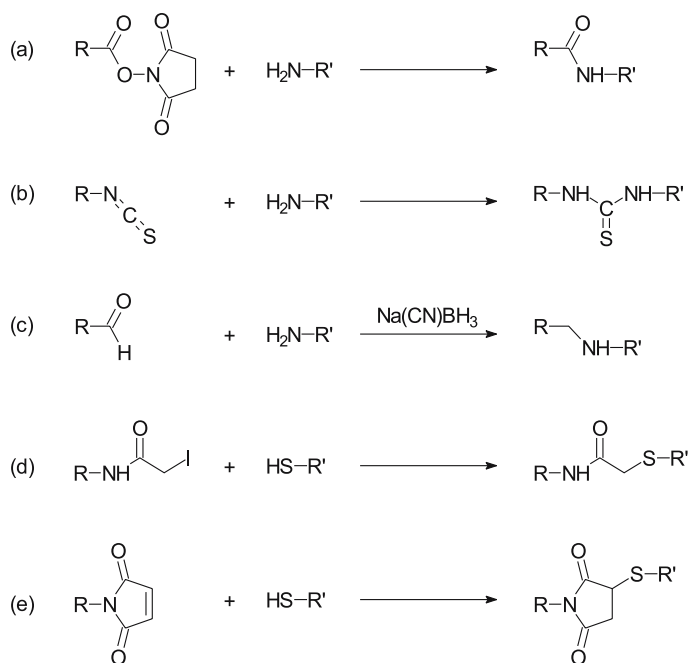


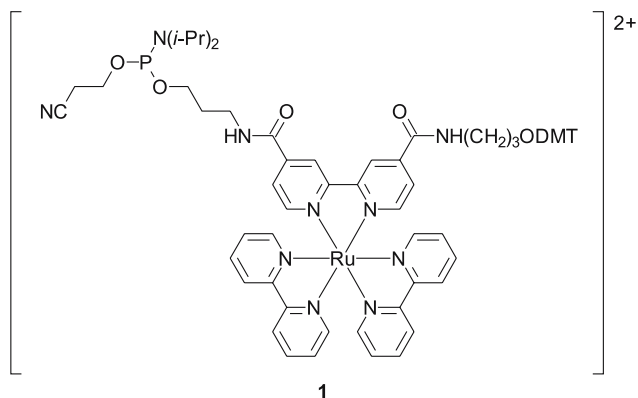
**Fig. 1** Reactions of **a** NHS ester, **b** isothiocyanate and **c** aldehyde with amines, and **d** iodoacetamide and **e** maleimide with sulfhydryls

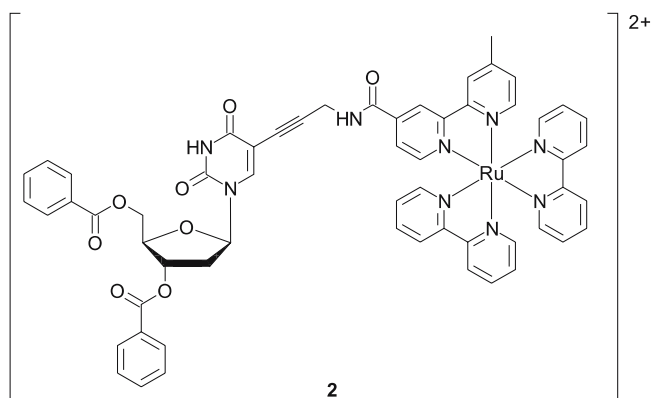
## 2 DNA Labels

### 2.1 Luminescent Linkers and Nucleosides

Lewis and Letsinger functionalised 4,4'-dicarboxy-2,2'-bipyridine and equipped it with a  $[\text{Ru}(\text{bpy})_2]^{2+}$  moiety to produce a luminescent and reactive building block (1) for oligonucleotide synthesis [27]. Three oligonucleotides including 5'-dT<sub>4</sub>-Ru-dA<sub>4</sub>-3', 5'-dG<sub>3</sub>-Ru-dC<sub>3</sub>-3' and 5'-dGCAATTGC-Ru-dGCAATTGC-3' have been isolated and purified. These ruthenium-modified DNA molecules exhibit a <sup>1</sup>MLCT ( $d\pi(\text{Ru}) \rightarrow \pi^*(\text{N}^{\wedge}\text{N})$ ) absorption band at ca. 468 nm and a <sup>3</sup>MLCT emission band at ca. 665 nm with a lifetime of ca. 0.6 to 0.8  $\mu\text{s}$  in aqueous buffer. Modelling studies showed that these oligonucleotides can adopt low-energy hairpin conformations, with the ruthenium(II) complex occupying the loop locations.

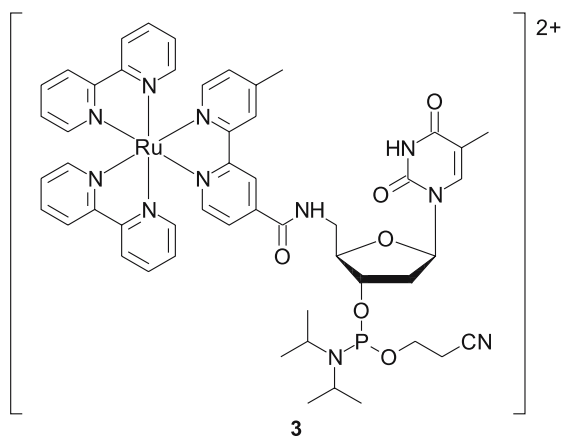
Grinstaff and co-workers reported the incorporation of an alkynyl-functionalised ruthenium(II) polypyridine complex into a 5-iodo-2'-deoxyuridine unit to give a luminescent nucleoside (2) [28]. This modified nucleoside shows a typical <sup>1</sup>MLCT ( $d\pi(\text{Ru}) \rightarrow \pi^*(\text{N}^{\wedge}\text{N})$ ) absorption band at ca. 450 nm in CH<sub>3</sub>CN. Excitation of the complex leads to <sup>3</sup>MLCT emission at ca. 640 nm in the same solvent. The deprotected complex emits at 675 nm in phosphate buffer. Time-resolved step-scan Fourier-transform infrared spectroscopic studies revealed a relatively large decrease in  $\nu(\text{C}=\text{O})$  (ca. 33  $\text{cm}^{-1}$ ) in the excited state, implying the localisation of the excited electron in the modified bipyridine unit that is directly linked to the uridine. This modified uridine has been incorporated into oligonucleotides by solid-phase synthesis [29]. The photophysical properties of the ruthenium(II)-labelled oligonucleotides and the duplexes formed with their complementary strands are similar to those of the original ruthenium(II) polypyridine complex. The incorporation

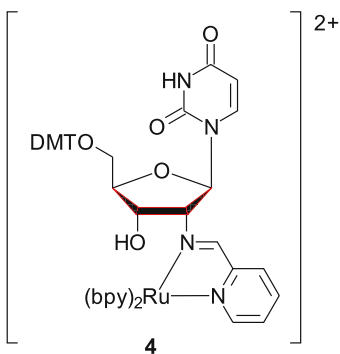




of a ruthenium(II) polypyridine complex into a thymidine phosphoramidite to give the building block (3) has also been reported by the same research group [30]. The photophysical properties of the ruthenium(II) complex are retained after the covalent attachment.

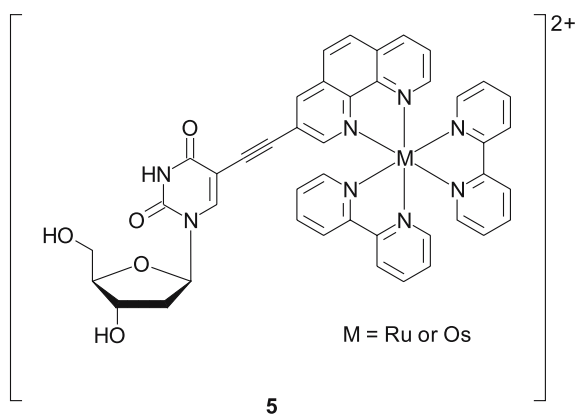
Meade and co-workers designed a chelating nucleoside that contains a diimine moiety formed from the reaction of an amine and 2-pyridinecarboxaldehyde [31, 32]. This uridine-based nucleoside has been coordinated to the low-potential  $[\text{Ru}(\text{acac})_2]$  and high-potential  $[\text{Ru}(\text{bpy})_2]^{2+}$  moieties, respectively, to form metallonucleosides. The  $[\text{Ru}(\text{bpy})_2]$ -containing nucleoside (4) displays  $^1\text{MLCT}$  ( $d\pi(\text{Ru}) \rightarrow \pi^*(\text{N}^{\wedge}\text{N})$ ) absorption at ca. 480 nm and very low-energy  $^3\text{MLCT}$  emission at ca. 730 nm ( $\tau_0 = 44$  ns,  $\Phi_{\text{em}} = 0.53 \times 10^{-3}$ ) in methanol. This nucleoside has been further derivatised and linked to a solid support to afford a precursor for oligonucleotide synthesis. An 11-mer oligonucleotide  $5'\text{-TCTCCTACACU}_{\text{Ru}}\text{-3}'$  has been prepared. It displays similar emission properties in aqueous buffer ( $\lambda_{\text{em}} = 725$  nm,  $\tau_0 = 42$  ns,





$\Phi_{em} = 0.11 \times 10^{-3}$ ), indicating that the adenine, cytosine and thymine do not quench the emission of the ruthenium(II) complex. The oligonucleotide has been hybridised with its complementary strand, and the duplex formed shows similar luminescence properties. It is evident that the photoexcited complex does not oxidise guanine, which is the most easily oxidised base. Also, the addition of quenchers such as  $[\text{Ru}(\text{NH}_3)_6]^{3+}$ , which are known to generate potent ruthenium(III) oxidant from excited ruthenium(II) polypyridine species, does not lead to detectable guanine oxidation. These interesting properties render this ruthenium label a valuable probe for DNA-mediated electron-transfer studies.

Tor modified a 2'-deoxyuridine with an alkynyl moiety at the 5-position of the base, and coupled it to ruthenium(II) and osmium(II) complexes with a 3-bromo-1,10-phenanthroline ligand to produce nucleosides (5) [33]. The ruthenium(II) nucleoside emits at 633 nm with a lifetime of 1.1  $\mu\text{s}$  and a luminescence quantum yield of 0.051 in degassed aqueous solutions, while the osmium(II) analogue shows lower-energy and much weaker emission ( $\lambda_{em} = 754 \text{ nm}$ ,  $\tau_0 = 0.027 \mu\text{s}$ ,  $\Phi_{em} = 0.0001$ ). Phosphoramidites equipped with these



metal complexes with a predetermined absolute configuration have been employed to synthesise diastereomerically pure oligonucleotides. Due to the pre-designed modification of the uridine, the complexes are located at the major groove of the double helix. The ruthenium(II) and osmium(II) oligonucleotides display  $^3\text{MLCT}$  emission at 632 and 740 nm, respectively. The emission decays are biphasic and the average lifetimes are slightly longer than those of their respective nucleosides, suggestive of a certain degree of protection of the excited complexes by the neighbouring nucleobases. Double-stranded 19-mer DNA molecules containing such a ruthenium label at the 5'-terminus of one strand, and an osmium label at various positions on the other strand, have been synthesised [34]. The  $^3\text{MLCT}$  emission of the ruthenium label is quenched as the osmium label approaches; for example, at a separation of about 16 Å, 90% of the ruthenium emission is quenched (Fig. 2). Analysis of the quenching efficiency and the Ru–Os distance reveals that the quenching can be accounted for by the Förster dipole–dipole mechanism. Deviation from the ideal system is ascribed to uncertainty of the orientation factor  $\kappa^2$ , which is assumed to be  $2/3$ . To verify this, similar double-stranded DNA molecules with the replacement of the more rigid ethynyl linker by a more flexible ethylene spacer have been synthesised. The Förster distance determined from emission quenching of these molecules is in excellent agreement with the ideal system, indicative of the key role of the dipole–dipole quenching mechanism.

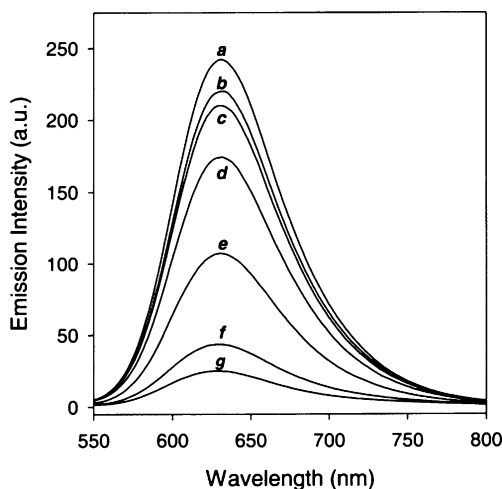
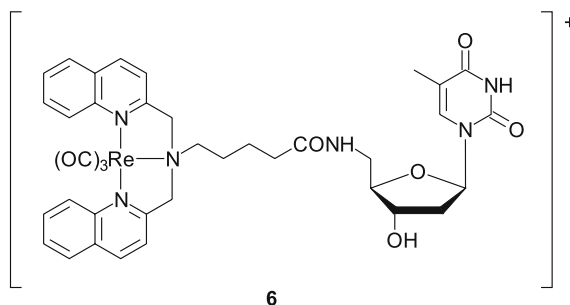


**Fig. 2** Emission spectra of double-stranded DNA molecules composed of an oligonucleotide modified at its 5'-end with ruthenium(II) nucleoside 5 and its complementary strand **a** without modification, and with a related osmium(II) label at a distance of **b** 61, **c** 52, **d** 43, **e** 31, **f** 21 and **g** 16 Å. The Ru–Os distances are based on a helical DNA model [34]

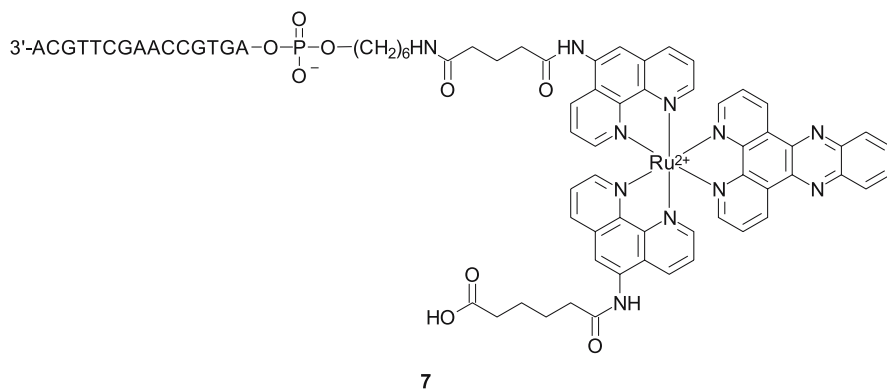


Recently, Zubieta and co-workers modified the C2' and C5' of thymidine and uridine with an amine and reacted it with 2-pyridinecarboxaldehyde and 2-quinolinecarboxaldehyde, respectively, to form chelating nucleosides [35]. These chelates have been coordinated to a  $[\text{Re}(\text{CO})_3]^+$  unit to give new metalonucleosides such as 6. The quinoline-containing complexes absorb strongly in the UV and visible region. The absorption bands at 225 to 290 nm are assigned to  $^1\text{IL} (\pi \rightarrow \pi^*)$  transitions, while those at 300 to 380 nm are  $^1\text{MLCT} (d\pi(\text{Re}) \rightarrow \pi^*(\text{ligand}))$  transitions. These nucleosides are luminescent under ambient conditions upon irradiation. The  $^3\text{MLCT}$  emission occurs at ca. 552 to 570 nm with very long lifetimes (15 to 19  $\mu\text{s}$ ) in various solvents.

## 2.2

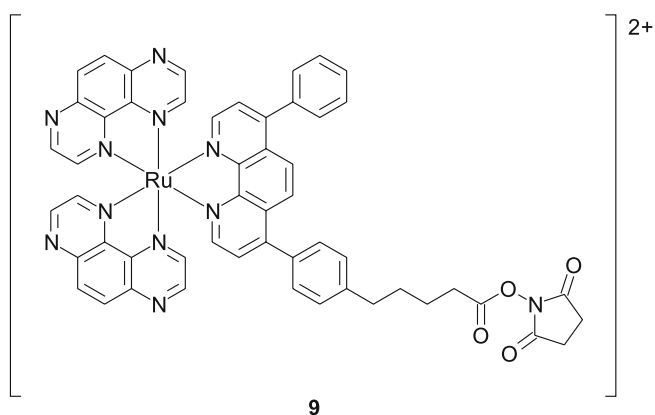
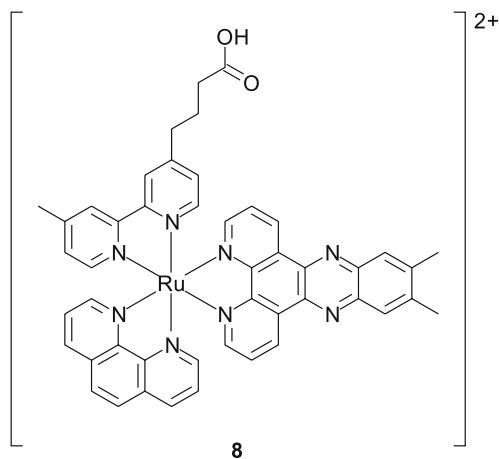
### Post-modification of Oligonucleotides

In 1992, Barton reported the coupling of a ruthenium(II) dppz complex to the 5'-end of a 15-mer oligonucleotide to form a DNA probe (7) [36]. Since the complex binds to double-stranded DNA with a high affinity and shows substantial emission enhancement after the binding, the ruthenium(II) dppz oligonucleotide has been used as a probe for single-stranded DNA molecules



of various numbers of mismatches. The emission intensities of the duplexes decrease with an increasing number of mismatches between the two DNA strands. The emission intensity is particularly weak if the mismatch is near the 3'-terminus of the ruthenated strand, because intramolecular intercalation of the complex (which balances the destabilisation caused by the mismatch) is less likely to occur near that end of the double helix. Another ruthenium(II) dppz complex (**8**) has been linked to the 5'-end of a 16-mer oligonucleotide and the DNA has been annealed to a series of complementary strands whose 5'-ends have been labelled with an osmium(II) complex [37]. The emission quenching of the ruthenium(II) complex relies on intercalation of both complexes. The quenching mechanism is assigned to triplet energy transfer between the metal complexes facilitated by the intervening base stack.

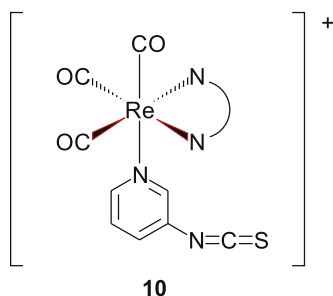
Kirsch-De Mesmaeker and co-workers linked a ruthenium(II) complex  $[\text{Ru}(\text{TAP})_2(\text{Ph}_2\text{-phen})]^{2+}$  containing an NHS ester moiety (**9**) to oligonu-

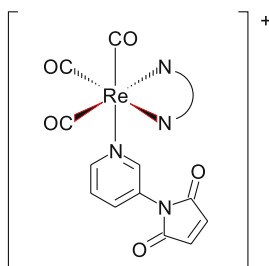




cleotides with a central uracil residue that had been modified with a propylamine at the 5-position [38]. The ruthenium(II)-derivatised oligonucleotides show similar absorption and emission properties compared to the original complex. The oligonucleotides have been hybridised with their complementary strands, and the duplexes do not show substantial changes in the melting temperature. Most remarkably, the ruthenium(II) complex of the probe strand experiences emission quenching after hybridisation with a target DNA strand containing nearby guanine bases. Similar quenching is not observed when the guanines are replaced by adenines and thymines. Thus, the emission quenching is evidently a result of photoinduced electron transfer from the guanines of the target strand to the excited complex. Photoadduct formation between the guanine and the ruthenium label means that cross-linking of the two DNA strands occurs upon irradiation; the results have been confirmed by gel electrophoresis experiments. In another study, 17-mer single-stranded DNA molecules labelled with the same ruthenium(II) complex have been synthesised [39]. Some of these oligonucleotides possess a sequence that allows the formation of secondary structures (self-structuration). Since the luminescence properties of the ruthenium(II) complex are very sensitive to its microenvironment, the luminescence decay provides a measure of the degree of self-structuration of the single-stranded DNA molecules. The oligonucleotides that show secondary structures display significant reduction in excited-state lifetimes in the presence of urea due to denaturing of the biomolecules. In addition, the emission quenching of these ruthenium(II)-modified oligonucleotides by oxygen is less sensitive compared to that of their unstructured counterparts. This leads to the conclusion that the self-structuration could protect the excited ruthenium(II) complexes from quenching by oxygen.

Lo and co-workers reported the synthesis and characterisation of rhenium(I) polypyridine isothiocyanate  $[\text{Re}(\text{N}^{\wedge}\text{N})(\text{CO})_3(\text{py-3-NCS})]^+$  (**10**) [40] and maleimide  $[\text{Re}(\text{N}^{\wedge}\text{N})(\text{CO})_3(\text{py-3-mal})]^+$  (**11**) [41] complexes. Photoexcitation of all the complexes results in intense and long-lived  $^3\text{MLCT}$  ( $d\pi(\text{Re}) \rightarrow \pi^*(\text{N}^{\wedge}\text{N})$ ) emission under ambient conditions. A universal M13 reverse sequencing primer modified with an aminohexyl group at the 5'-





11

end, 5'-H<sub>2</sub>N-(CH<sub>2</sub>)<sub>6</sub>-AACAGCTATGACCATG-3', has been labelled with [Re(phen)(CO)<sub>3</sub>(py-3-NCS)]<sup>+</sup>. The labelled primer has been isolated, purified and shown to exhibit yellow luminescence ( $\lambda_{em} = 548 \text{ nm}$ ,  $\tau_0 = 0.52 \mu\text{s}$ ) in degassed Tris-Cl buffer (50 mM) at pH 7.4 and 298 K upon irradiation. The melting temperature (40 °C) of the duplex formed between this primer and its complementary DNA strand shows a decrease of only 2 °C compared to the unmodified double-stranded DNA molecule, suggesting that no substantial changes occur in the tertiary structure of the duplex after conjugation. The labelled primer has been used as a luminescent probe to target unmodified oligonucleotides (Fig. 3). Since the maleimide moiety can react with

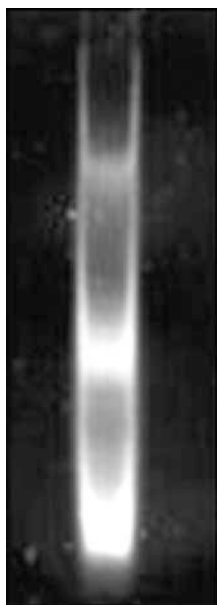
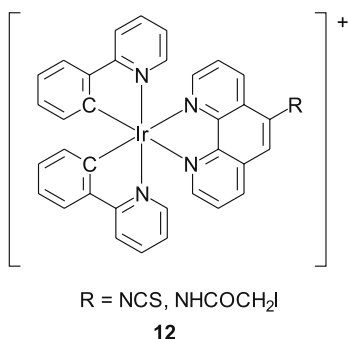


**Fig. 3** Polyacrylamide gel electrophoresis result of a hybridisation mixture of an M13 reverse sequencing primer labelled with [Re(phen)(CO)<sub>3</sub>(py-3-NCS)]<sup>+</sup> and three unmodified oligonucleotides of various lengths [40]



the sulfhydryl group to form a stable thioether, the rhenium(I) polypyridine maleimide complexes have been used to label a thiolated oligonucleotide. All the labelled oligonucleotides display intense and long-lived  $^3\text{MLCT}$  emission upon photoexcitation.

The use of luminescent cyclometallated iridium(III) polypyridine complexes as biological labels was first reported in 2001 [42]. Two luminescent cyclometallated iridium(III) complexes  $[\text{Ir}(\text{ppy})_2(\text{phen-R})]^+$  (R = NCS, NHCOCH<sub>2</sub>I) (**12**) that can specifically react with primary amine and sulfhydryl groups, respectively, have been prepared and characterised. Upon irradiation, the complexes exhibit intense and long-lived orange-yellow  $^3\text{MLCT}$  ( $d\pi(\text{Ir}) \rightarrow \pi^*(\text{N}^{\wedge}\text{N})$ ) luminescence in fluid solutions at room temperature and in low-temperature glass. These isothiocyanate and iodoacetamide complexes have been used to label a universal M13 reverse sequencing primer modified with an amine and a sulfhydryl group, respectively, at the 5'-end. The labelled DNA molecules exhibit intense and long-lived orange-yellow luminescence upon excitation. In degassed buffer solutions, the oligonucleotides emit at ca. 572 to 580 nm, with lifetimes in the sub-microsecond range. These labelled oligonucleotides have been hybridised with their unmodified complementary oligonucleotides to give luminescent double-stranded DNA molecules. The photophysical properties of these duplexes are similar to those of the labelled probes; the emission is derived from a  $^3\text{MLCT}$  ( $d\pi(\text{Ir}) \rightarrow \pi^*(\text{N}^{\wedge}\text{N})$ ) excited state.

### 3

## Protein Labels

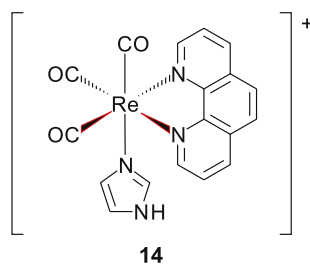
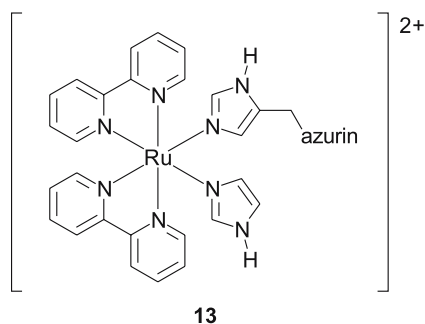
### 3.1

#### Electron Transfer in Metalloproteins

Since their first report of long-ranged electron-transfer reactions in ruthenium-modified cytochrome *c* [43], Gray and co-workers have studied re-

lated electron-transfer reactions of a number of transition metal-labelled proteins [11, 22, 44]. The ruthenium-azurin system is particularly important because it serves as a reference point for electron-transfer reactions in proteins [45, 46]. An H83Q base mutant of azurin from *Pseudomonas aeruginosa* has been prepared and additional mutations performed to give the K122H, T124H, T126H, Q107H and M109H mutants, all of which have been modified by a ruthenium complex to give the proteins  $[\text{Ru}(\text{bpy})_2(\text{imidazole})(\text{HisX-azurin})]^{2+}$  (13). Excitation of the ruthenium(II) complex at 480 nm induces electron transfer from the excited complex to the external quencher  $[\text{Ru}(\text{NH}_3)_6]^{3+}$ . Transient absorption spectroscopic measurements of the resultant  $\text{Cu}(\text{I}) \rightarrow \text{Ru}(\text{III})$  electron transfer ( $-\Delta G^\circ = 0.75 \text{ eV}$ ) in these ruthenium-azurins establish the distance dependence of electron transfer along the  $\beta$  strands. The tunnelling timetable reveals a nearly perfect exponential distance dependence, with a decay constant ( $\beta$ ) of  $1.1 \text{ \AA}^{-1}$  and an intercept at close contact ( $r_0 = 3 \text{ \AA}$ ) of  $10^{13} \text{ s}^{-1}$ . Interestingly, the distance-decay constant is similar to that found for superexchange-mediated tunnelling across saturated alkane bridges ( $\beta = \text{ca. } 1.0 \text{ \AA}^{-1}$ ), strongly indicating that a similar coupling mechanism operates in the polypeptide.

In view of the strong photooxidising properties of  $[\text{Re}(\text{phen})(\text{CO})_3(\text{imidazole})]^+$  (14) ( $\text{Re}(\text{I}^*)/\text{Re}(\text{0}) = \text{ca. } +1.3 \text{ V}$  vs NHE in  $\text{CH}_3\text{CN}$ ),  $[\text{Re}(\text{phen})(\text{CO})_3(\text{H}_2\text{O})]^+$  has been reacted with azurin to give  $[\text{Re}(\text{phen})(\text{CO})_3(\text{His83})]^+ - \text{AzCu}^+$ , which has been used to study photoinduced electron-transfer reactions [47]. In the absence of quenchers, excitation of the rhenium(I) complex

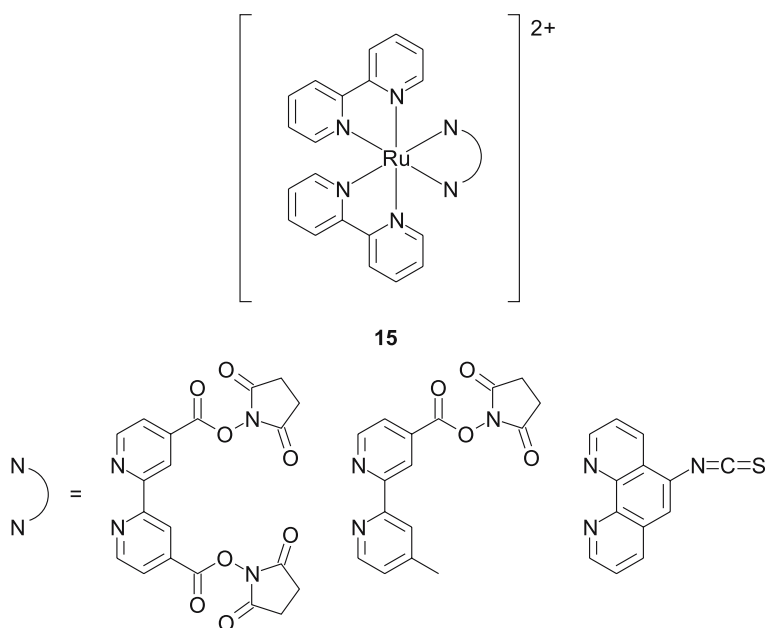


leads to direct oxidation of Cu(I) to Cu(II). Using the flash–quench technique, photogeneration of tryptophan and tyrosine radicals in these rhenium(I)-azurin conjugates has been demonstrated [48]. The EPR spectra of frozen solutions of irradiated  $[\text{Re}(\text{phen})(\text{CO})_3(\text{H83})]^+ - \text{AzZn}^{2+} / [\text{Co}(\text{NH}_3)_5\text{Cl}]^{2+}$  and  $[\text{Re}(\text{phen})(\text{CO})_3(\text{H107})]^+ - \text{AzZn}^{2+} / [\text{Co}(\text{NH}_3)_5\text{Cl}]^{2+}$  (Y72F mutant, leaving only one tyrosine, Y108, in the protein) reveals the appearance of tryptophan and tyrosine radicals, respectively. The tryptophan signal is attributable to a W48 radical, while the tyrosine signal could originate from a Y108 radical. In a related study, rhenium(I)-modified azurin mutants have been examined [49]. Interestingly, the rates of electron tunnelling through these rhenium-azurins are much higher compared to those for their ruthenium counterparts. To test the idea that Y108<sup>\*</sup> is an active intermediate in the Cu(I)  $\rightarrow$  Re(II)(H107) reaction, two rhenium-modified mutants H83Q/Q107H<sub>Re</sub>/W48F/Y72F/Y108F and H83Q/Q107H<sub>Re</sub>/W48F/Y72F/Y108F/F110W have been prepared. Transient absorption spectroscopic measurements on both mutants reveal that the electron-transfer rate constants are ca.  $10^4 \text{ s}^{-1}$ , indicating that Y108 is not involved in the rapid Cu(I) to Re(II) tunnelling. It is suggested that the tunnelling occurs directly from copper(I) to the rhenium-coordinated histidine radical. In fact, DFT calculations show that the unpaired electron in the “rhenium(II)” species, generated from the electron-transfer reaction between  $[\text{Re}(\text{phen})(\text{CO})_3(\text{imidazole})]^{+*}$  and cobalt(III) acceptor, resides on both the imidazole and the metal centre. When the imidazole is deprotonated, as would be the case at pH 7, the spin density is largely on the imidazole (71%). Remarkably, when the copper(I) oxidation rates are plotted against distances measured from C $\gamma$  of all tunnelling-mutant surface histidines, an excellent agreement with those predicted based on the standard distance-decay constant  $\beta$  of  $1.1 \text{ \AA}^{-1}$  is observed, concluding the involvement of the metal-coordinated histidine in the electron-transfer reactions.

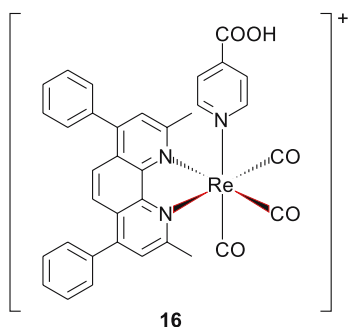
### 3.2

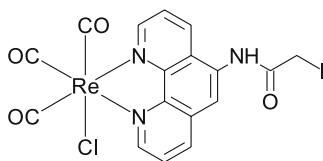
#### Anisotropy Probes

Lakowicz and co-workers attached reactive functional groups such as NHS ester and isothiocyanate to ruthenium(II) polypyridine complexes to produce labels including  $[\text{Ru}(\text{bpy})_2(\text{N}^{\wedge}\text{N})]^{2+}$  ( $\text{N}^{\wedge}\text{N} = \text{dcsbpy}, \text{mcsbpy}, \text{phen-NCS}$ ) (15) and conjugated these complexes to biomolecules such as HSA [50]. The <sup>3</sup>MLCT emission of these conjugates in buffer occurs at 655, 643 and 610 nm, respectively. The highest values for the initial anisotropy ( $r_0$ ) of these conjugates are 0.23, 0.17 and 0.14, respectively, in glycerol/water (6 : 4 v/v) at  $-55^\circ\text{C}$ . Upon binding to polyclonal anti-HSA, the labelled HSA molecules exhibit a change of the rotational correlation time, resulting in a change in anisotropy. The anisotropy of the Ru(dcsbpy) and Ru(mcsbpy) conjugates increases by about 80% while that of the Ru(phen-NCS) conjugate

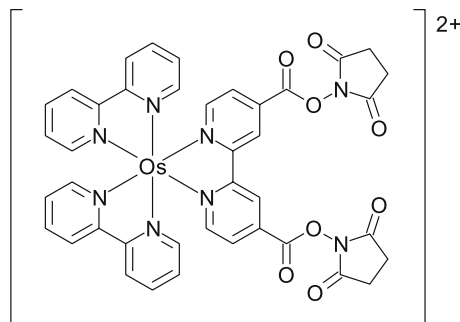


increases by 96%, rendering these complexes useful probes for competitive homogeneous immunoassays. Related rhenium(I) complexes  $[\text{Re}(\text{Me}_2\text{-Ph}_2\text{-phen})(\text{CO})_3(\text{py-4-COOH})]^+$  (**16**) [51] and  $[\text{Re}(\text{phen-NHCOCH}_2\text{I})(\text{CO})_3\text{Cl}]$  (**17**) [52] and osmium(II) complexes such as  $[\text{Os}(\text{bpy})_2(\text{dcsbpy})]^{2+}$  (**18**) have also been studied [53, 54]. The excitation and emission spectra of complex **16** in different solvents are shown in Fig. 4. This complex has been activated by NHS and coupled to various biomolecules such as HSA and IgG. The conjugates show intense and long-lived emission at ca. 550 nm ( $\tau_0 = \text{ca. } 4.1 \text{ to } 2.8 \mu\text{s}$ ). The rhenium(I) iodoacetamide complex is reactive towards the sulfhydryl group of biomolecules. The HSA conjugate of this complex emits with a lifetime of ca. 1  $\mu\text{s}$ . The potential of both rhenium(I) conjugates as





17



18

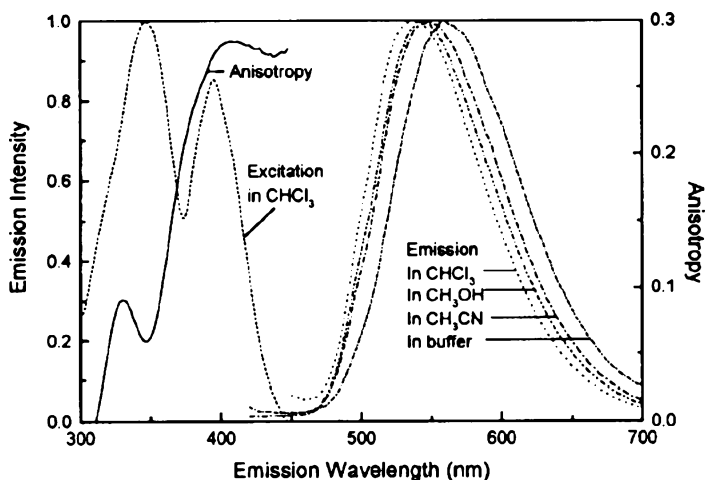


**Fig. 4** Excitation and emission spectra of complex **16** in  $\text{CHCl}_3$ ,  $\text{CH}_3\text{CN}$ ,  $\text{CH}_3\text{OH}$  and buffer at room temperature ( $\lambda_{\text{ex}} = 400 \text{ nm}$ ). The *solid line* shows the excitation anisotropy spectrum in 100% glycerol at  $-60^\circ\text{C}$  with the emission wavelength tuned to  $550 \text{ nm}$  [51]

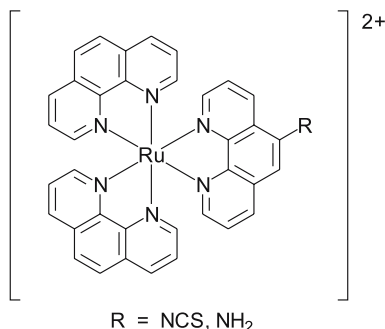
anisotropic probes has been investigated. The employment of osmium(II) polypyridine complexes allows low-energy excitation with visible to near-IR wavelengths. The serum albumin conjugate of complex **18** shows  $^3\text{MLCT}$  emission at  $770 \text{ nm}$ . The anisotropy of this conjugate increases by about 60% in the presence of an eightfold excess of monoclonal or polyclonal anti-HSA.

### 3.3

#### Luminescent Labels

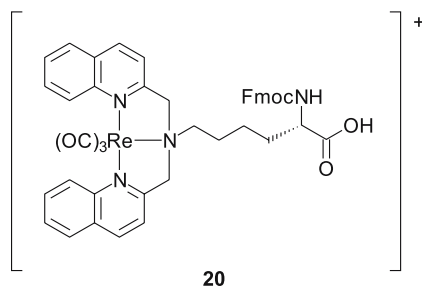
In 1992, Vos and co-workers reported the covalent linkage of ruthenium(II) polypyridine isothiocyanate and amine complexes such as  $[\text{Ru}(\text{phen})_2(\text{N}^{\wedge}\text{N})]^{2+}$  ( $\text{N}^{\wedge}\text{N} = \text{phen-NCS}, \text{phen-NH}_2$ ) (**19**) and their analogues to poly(L-lysine), BSA, HSA, OVA and IgG [55]. While the isothiocyanate complexes react with the  $\epsilon$ -amine groups of lysine residues in carbonate buffer at pH 9.6, conjugation of the amine complexes requires the periodate oxidation of the carbohydrates of the albumins to produce active aldehyde moieties and subsequent reduction of the imine linkages by sodium borohydride. Conjugation of the active ester of the dicarboxylate complexes  $[\text{Ru}(\text{N}^{\wedge}\text{N})_2(\text{dcbpy})]^{2+}$  to the same biomolecules has also been performed. All the isothiocyanate conjugates show intense  $^1\text{MLCT}$  ( $d\pi(\text{Ru}) \rightarrow \pi^*(\text{N}^{\wedge}\text{N})$ ) absorption at ca. 449 to 455 nm and  $^3\text{MLCT}$  emission bands at ca. 600 to 614 nm in buffer. The dicarboxylate conjugates show lower-energy absorption (ca. 465 to 467 nm) and emission (ca. 655 to 660 nm) bands due to the two electron-withdrawing amide moieties. The decay data of most of the conjugates could be fitted well to a double-exponential function. In degassed solution, analysis of the data from the BSA conjugates shows dual emission with lifetimes of ca. 1.2 and 0.5  $\mu\text{s}$ , respectively. The longer components are expected for molecules in a more hydrophobic environment; the shorter components are attributed to electron transfer between the excited labels and certain amino acid residues.

Zubieta, Valliant and co-workers recently reported the synthesis of an amino acid containing a  $(\text{quinoline-CH}_2)_2\text{-NR}$  chelate that can react with  $[\text{Re}(\text{CO})_3\text{Br}_3]^{2-}$  to form a luminescent complex (**20**) [56]. This complex shows dual emission at 425 and 580 nm with a lifetime of ca. 4.3 to 9.8  $\mu\text{s}$  in various solvents. The presence of an amino acid in this complex enables its incorporation into a peptide using a conventional automated synthesiser. A short peptide fMLF has been labelled with this luminescent complex and the conjugate has been used to probe the biological target human FPR studied by flow



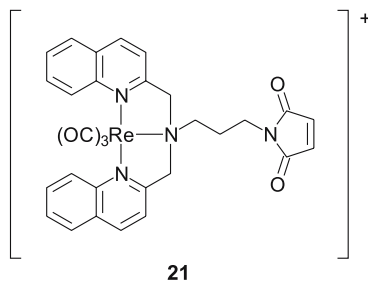
**19**





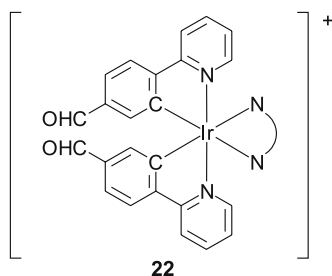
cytometry and fluorescence microscopy. Other (quinoline-CH<sub>2</sub>)<sub>2</sub>-NR chelates that contain a maleimide moiety have also been reported [57]. The tricarbonylrhenium(I) complexes of these chelates are luminescent; for example, complex **21** emits at 550 nm ( $\tau_0 = 16 \mu\text{s}$ ) in ethylene glycol at room temperature. These labels have been reacted with sulfhydryl-containing biomolecules to give luminescent conjugates.

The rhenium(I) polypyridine isothiocyanate and maleimide complexes [Re(N<sup>^</sup>N)(CO)<sub>3</sub>(py-3-NCS)]<sup>+</sup> (**10**) [40] and [Re(N<sup>^</sup>N)(CO)<sub>3</sub>(py-3-mal)]<sup>+</sup> (**11**) [41] reported by Lo and co-workers have been used to label various proteins. For example, [Re(phen)(CO)<sub>3</sub>(py-3-NCS)]<sup>+</sup> has been coupled to HSA to give a luminescent conjugate. The polyacrylamide gel electrophoresis result reveals an intense yellow luminescent band corresponding to a molecular weight of 66 kDa, which is attributable to the labelled protein. The isolated and purified bioconjugate in aqueous buffer displays intense and long-lived yellow <sup>3</sup>MLCT (dπ(Re) → π\*(phen)) emission ( $\lambda_{\text{em}} = 534 \text{ nm}$ , bi-exponential decay:  $\tau_1 = 0.79 \mu\text{s}$ ,  $\tau_2 = 0.13 \mu\text{s}$ ) upon irradiation. The rhenium(I) polypyridine maleimide complex [Re(phen)(CO)<sub>3</sub>(py-3-mal)]<sup>+</sup> has been covalently linked to a cysteine-containing peptide, glutathione (γ-Glu-Cys-Gly), and the proteins BSA and HSA. Upon photoexcitation, the bioconjugates display intense and long-lived yellow <sup>3</sup>MLCT (dπ(Re) → π\*(phen)) luminescence in buffer solutions. While the glutathione bioconjugate exhibits a single-exponential decay, both labelled serum conjugates show double-exponential decays with emission-lifetime components of ca. 1.1 and 0.2 μs. Oxygen



quenches the emission of the glutathione conjugate more effectively than that of the labelled serum albumins. It is likely that the labels coupled to BSA and HSA are located in a relatively hydrophobic environment, and a lower exposure to the solvent surroundings could account for the less efficient quenching by the oxygen molecules. The observations of long emission lifetimes of these bioconjugates indicate that these rhenium(I) maleimide labels and their isothiocyanate counterparts are promising candidates for time-resolved bioassays.

Luminescent cyclometallated iridium(III) complexes have been coupled to various biomolecules to form new conjugates. The complexes  $[\text{Ir}(\text{pba})_2(\text{N}^{\wedge}\text{N})]^+$  (22) coordinated with different diimine ligands ( $\text{N}^{\wedge}\text{N}$ ) and the aldehyde-containing cyclometallating ligand  $\text{pba}^-$  can react with the primary amine of biomolecules to form an imine that can be readily reduced to a stable secondary amine [58]. X-ray crystallographic studies of the bipyridine complex reveal a separation of ca. 9 Å between the two aldehyde oxygen atoms, which is sufficiently long to enable the complexes to function as luminescent biological cross-linkers. In fluid solutions at room temperature, the complexes show a similar vibronically structured emission band (ca. 530, 565 (sh) nm) with a very long emissive lifetime (ca. 5 μs). It is conceivable that the emissive state is  $^3\text{IL} (\pi \rightarrow \pi^*(\text{pba}^-))$  in nature. The complexes have been exploited to cross-link L-alanine and the glycoprotein avidin, respectively. Interestingly, the four cross-linked alanine conjugates show various emission colours depending on the identity of the diimine ligands. Specifically, the  $\text{Me}_4$ -phen conjugate emits with a green colour ( $\lambda_{\text{em}} = 480, 510, 550$  (sh) nm) while the  $\text{Ph}_2$ -phen analogue shows orange-yellow emission ( $\lambda_{\text{em}} = 570$  nm) (Fig. 5). The conversion of the aldehyde moiety to a secondary amine apparently changes the emissive-state character from  $^3\text{IL} (\pi \rightarrow \pi^*(\text{pba}^-))$  to  $^3\text{MLCT} (d\pi(\text{Ir}) \rightarrow \pi^*(\text{N}^{\wedge}\text{N}))$ . However, given the structured emission spectrum and the very long lifetime of the  $\text{Ir}(\text{Me}_4\text{-phen})$ -alanine conjugate, the emissive state of this labelled alanine should possess a high parentage of  $^3\text{IL} (\pi \rightarrow \pi^*(\text{Me}_4\text{-phen}))$  character. The cross-linked avidin conjugates also show long-lived and intense luminescence at an energy similar to that of their alanine counterparts. Given the intense photoluminescence of the avidin conjugates, a simple heterogeneous competitive assay for biotin using one of the con-



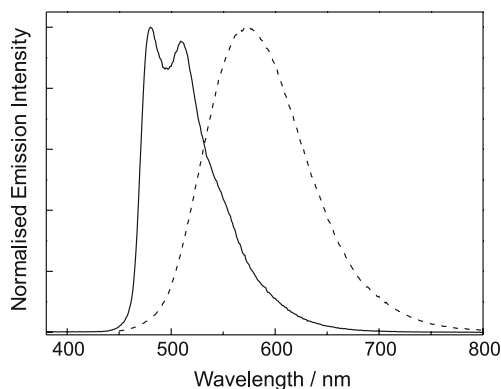


**Fig. 5** Emission spectra of bioconjugates  $[\text{Ir}(\text{pba})_2(\text{Me}_4\text{-phen})]^+(\text{alanine})_2$  (—) and  $[\text{Ir}(\text{pba})_2(\text{Ph}_2\text{-phen})]^+(\text{alanine})_2$  (---) in degassed water at 298 K [58]

jugates and biotinylated microspheres has been developed. In the assay, immobilised biotin molecules compete with free biotin analyte on binding to the luminescent avidin conjugate. After the recognition reaction, the emission intensity of the supernatant containing the mobile luminescent conjugate is measured. Under the optimised conditions, biotin of a concentration from  $1 \times 10^{-4.5}$  to  $1 \times 10^{-6}$  M could be measured by this assay. Furthermore, related rhodium(III)-pba complexes have been isolated and used as labelling reagents for biomolecules [59]. The emission bands of the BSA conjugates show rich vibronic structures, indicative of a  $^3\text{IL}$  emission origin.

Amine, aldehyde, isothiocyanate and iodoacetamide groups have been incorporated into the diimine ligands ( $\text{N}^{\wedge}\text{N}$ ) of the cyclometallated iridium(III) complexes  $[\text{Ir}(\text{N}^{\wedge}\text{C})_2(\text{N}^{\wedge}\text{N-R})]^+$  ( $\text{R} = \text{NH}_2, \text{CHO}, \text{NCS}$  and  $\text{NHCOCH}_2\text{I}$ ) (23) [42, 60, 61]. Upon irradiation, all the complexes display intense and long-lived orange-red to greenish-yellow luminescence under ambient conditions and in alcohol glass at 77 K. The emission of  $[\text{Ir}(\text{N}^{\wedge}\text{C})_2(\text{N}^{\wedge}\text{N-R})]^+$  is generally assigned to a triplet MLCT ( $d\pi(\text{Ir}) \rightarrow \pi^*(\text{N}^{\wedge}\text{N-R})$ ) excited state. The assignment is supported by the findings that the amine-containing complexes emit at the highest energy, followed by their aldehyde and iodoacetamide counterparts, while the isothiocyanate complexes emit at the lowest energy. The emission spectra of  $[\text{Ir}(\text{mppz})_2(\text{bpy-R})]^+$  ( $\text{R} = \text{NH}_2, \text{NHCOCH}_2\text{I}$  and  $\text{NCS}$ ) are shown in Fig. 6 as an example. In some cases,  $^3\text{IL}$  emissive states associated with the phen- $\text{NH}_2$  and  $\text{pq}^-$  ligands have been identified. Amine- and sulfhydryl-containing biological molecules have been labelled with a selection of the luminescent iridium(III) aldehyde, isothiocyanate and iodoacetamide complexes. Upon photoexcitation, all the bioconjugates display intense and long-lived emission in aqueous buffer at 298 K. The emission origins of most of the conjugates have been identified as  $^3\text{MLCT}$  ( $d\pi(\text{Ir}) \rightarrow \pi^*(\text{N}^{\wedge}\text{N})$ ) in nature. A new bioassay for the cardiac drug digoxin has been

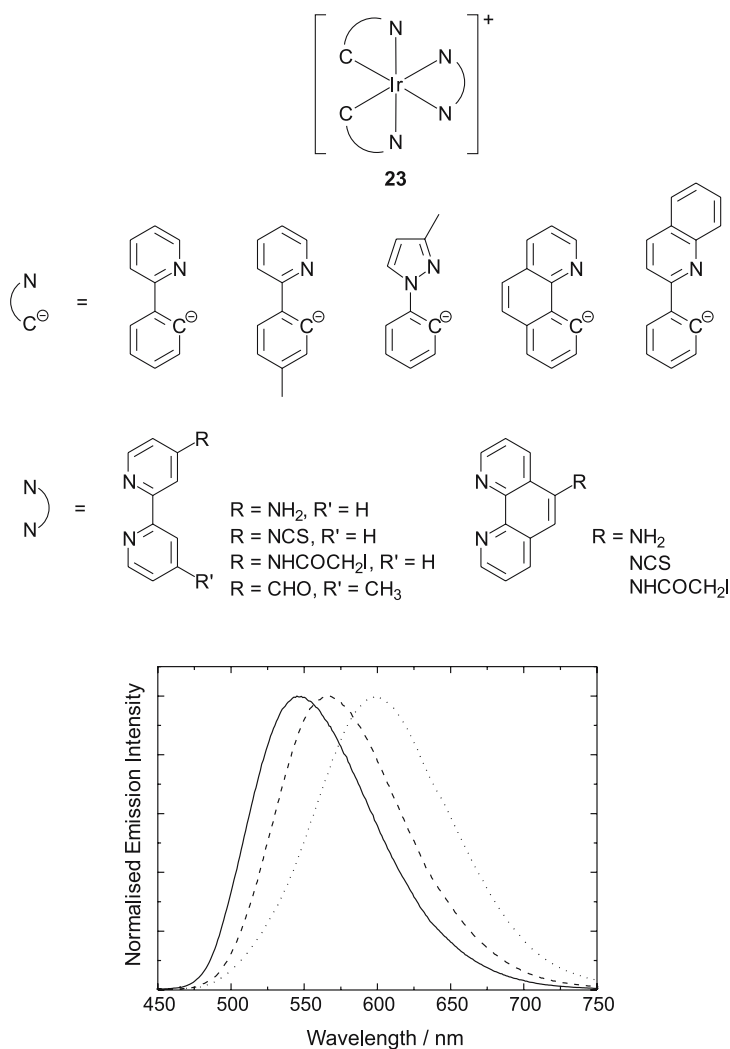
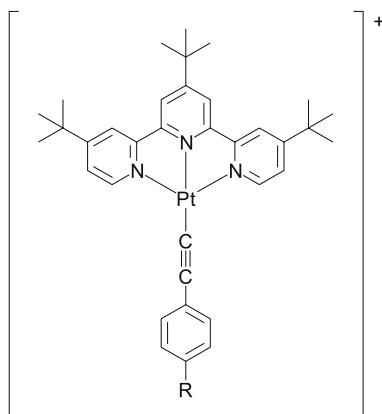


**Fig. 6** Emission spectra of  $[\text{Ir}(\text{mppz})_2(\text{bpy-R})]^+$  (R = NH<sub>2</sub> (—), NHCOCH<sub>2</sub>I (---) and NCS (···)) [60]

developed using one of the luminescent iridium(III)-avidin conjugates [60]. Under the optimised conditions, the concentration range of digoxin that can be measured by the assay is between ca.  $6.4 \times 10^{-8}$  and  $2.6 \times 10^{-5}$  M.

Yam and co-workers reported the synthesis and characterisation of three platinum(II) terpyridine complexes  $[\text{Pt}(^t\text{Bu}_3\text{tpy})(\text{C} \equiv \text{C} - \text{C}_6\text{H}_4 - \text{R} - p)]$  (R = NH<sub>2</sub>, NCS, NHCOCH<sub>2</sub>I) (24) [62]. The isothiocyanate and iodoacetamide complexes show orange-yellow <sup>3</sup>MLCT ( $d\pi(\text{Pt}) \rightarrow \pi^*(^t\text{Bu}_3\text{tpy})$ )/<sup>3</sup>LLCT ( $\pi(\text{C} \equiv \text{CR}) \rightarrow \pi^*(^t\text{Bu}_3\text{tpy})$ ) emission in various media. For example, in CH<sub>3</sub>CN



R = NH<sub>2</sub>, NCS, NHCOCH<sub>2</sub>I

24

at 298 K, these complexes emit at 586 and 638 nm, respectively, with a lifetime of ca. 0.6  $\mu$ s. The excitation and emission spectra of the isothiocyanate and iodoacetamide complexes are shown in Fig. 7. Both complexes have been coupled to HSA via the formation of a thiourea and thioether linkage, respectively. The emission of the conjugates occurs at ca. 630 to 650 nm in Tris-Cl buffer (50 mM) at pH 7.4 under ambient conditions. The emission is assigned to a <sup>3</sup>MLCT ( $d\pi(\text{Pt}) \rightarrow \pi^*({}^t\text{Bu}_3\text{tpy})$ )/<sup>3</sup>LLCT ( $\pi(\text{C} \equiv \text{CR}) \rightarrow \pi^*({}^t\text{Bu}_3\text{tpy})$ ) state.

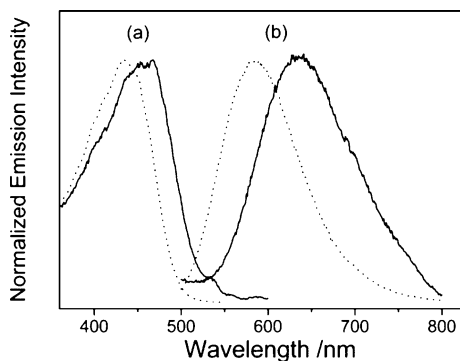
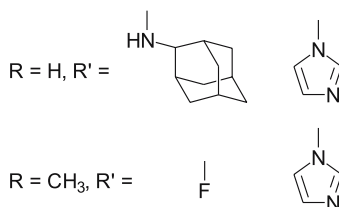
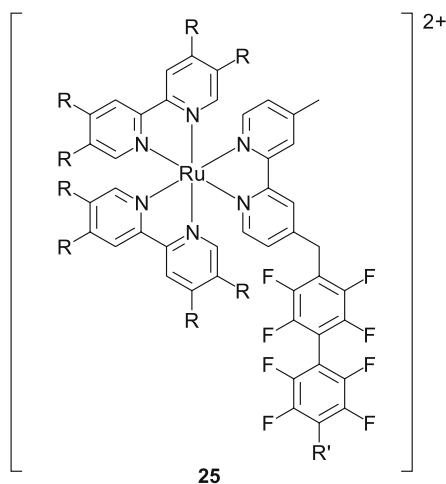


**Fig. 7** Excitation (a) and emission (b) spectra of  $[\text{Pt}({}^t\text{Bu}_3\text{tpy})(\text{C} \equiv \text{C} - \text{C}_6\text{H}_4 - \text{R}-p)]$  (R = NCS (-) and NHCOCH<sub>2</sub>I (···)) in CH<sub>3</sub>CN at 298 K [62]

## 4 Protein Probes

### 4.1 Luminescent Wires for Metalloproteins

Winkler, Gray and co-workers designed ruthenium(II) diimine adamantane and imidazole complexes containing a perfluorobiphenyl linker (**25**) [63]. These complexes bind tightly to cytochrome P450cam with dissociation constants of 0.077 to 3.7  $\mu\text{M}$ . The binding results from hydrophobic interactions between the complexes and the substrate access channel of the protein. The emission of these ruthenium(II) complexes is partially quenched upon the protein-binding event. Transient absorption spectroscopic studies on the Ru(Me<sub>4</sub>-bpy)-imidazole complex and P450cam indicate electron transfer from the excited metal complex to the haem (Fig. 8), and a forward electron-transfer rate constant ( $k_f$ ) of  $2.8 \times 10^7 \text{ s}^{-1}$  has been determined. This rate is near the coupling-limited rate, and is significantly faster than the electron transfer from the natural redox partner of P450cam, putidaredoxin, to the haemoprotein ( $k_{\text{red}} \approx 50 \text{ s}^{-1}$ ). Related rhenium(I) perfluorobiphenyl diimine complexes (**26**) have been synthesised to study photoinduced electron



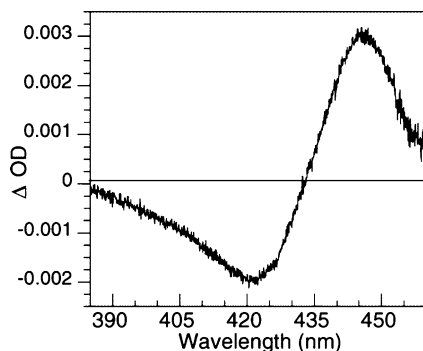
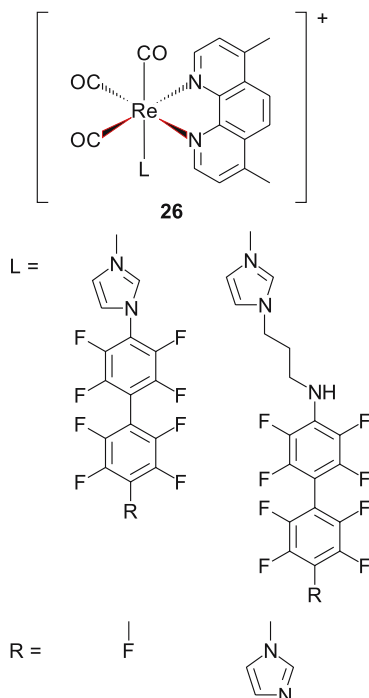


**Fig. 8** Transient absorption spectrum measured 20  $\mu$ s after 470-nm excitation of equimolar Ru(Me<sub>4</sub>-bpy)-imidazole complex and P450cam (9.6  $\mu$ M). Observed changes in optical density are chiefly due to the conversion of ferric to ferrous haem, with comparatively minor contributions from Ru(II) to Ru(III) [63]



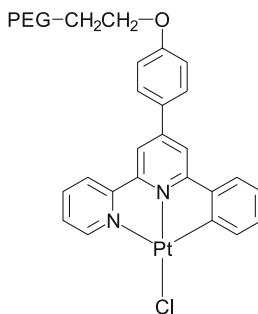
transfer to the haem of nitric oxide synthase [64]. All these complexes bind tightly to the oxidase domain of the protein. Interestingly, the complexes containing an imidazole pendant ligate the haem iron. Upon photoexcitation, the conjugates containing these complexes show bleaching at about 420 nm owing to the disappearance of iron(III) and a new optical density increase at about 445 nm due to the appearance of iron(II), indicating that the ex-

cited rhenium(I) complexes are capable of reducing the haem centres of the proteins. The electron-transfer rate is very fast, and the active-site iron(III) is reduced to iron(II) within 300 ps, which is almost 10 orders of magnitude faster than the initial reduction of nitric oxide synthase by its reductase module. It is proposed that a neighbouring tryptophan residue reductively quenches the excited rhenium(I) complex to generate a tryptophan radical and a rhenium(0) species. Electron transfer from the rhenium(0) species to the iron(III) of the haem occurs with a rate constant of about  $6 \times 10^8 \text{ s}^{-1}$ . It is likely that this very fast reduction involves electron hopping through the per-fluorobiphenyl bridge or possibly through a tyrosine residue near the haem.

## 4.2

### Platinum-Based Probes

Che and co-workers attached a poly(ethylene glycol) substituent to [Pt(hppbpy)Cl] to produce a luminescent platinum(II)-PEG complex (27) and used it as a probe for proteins [65]. The complex emits weakly in aqueous solution and the emission spectra are concentration-dependent. At  $5 \mu\text{M}$ , a weak  $^3\text{MLCT}$  ( $d\pi(\text{Pt}) \rightarrow \pi^*(\text{hppbpy}^-)$ ) emission band at 543 nm is observed. At higher concentrations ( $\geq 10^{-4} \text{ M}$ ), the complex displays a new lower-energy emission feature at 710 nm, whose origin is assigned to an MMLCT state. Upon addition of BSA, the emission intensity of the complex is enhanced (Fig. 9). A binding constant of  $2.7 \times 10^4 \text{ M}^{-1}$  and a binding stoichiometry of 1 : 1 have been determined. Addition of urea to a solution of this complex and BSA reveals small emission enhancement ([urea] from 0.5 to 2.0 M), followed by quenching ([urea] > 4.5 M). The enhancement is ascribed to the urea-induced rearrangement in domain II of the protein which leads to tighter binding of the complex. The emission quenching observed at higher urea concentration is due to unfolding of the protein. The same research group recently reported the protein-binding properties of luminescent cyclometallated platinum(II) amino acid complexes (28) [66]. The absorption band





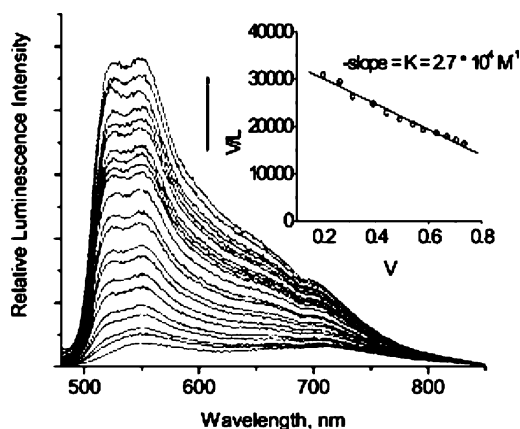
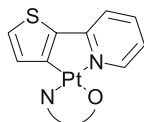
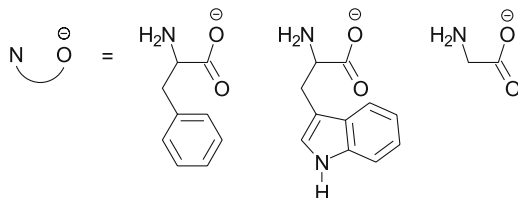


**Fig. 9** Emission spectra of complex 27 in BSA aqueous solution (pH = 7.40, 100 mM  $\text{Na}_2\text{HPO}_4 - \text{NaH}_2\text{PO}_4$  with 0.9% NaCl). From bottom to top: [BSA] ( $\mu\text{M}$ ), 0.00 to 3.15; step, 0.15 (insert: the Scatchard plot) [65]

of the phenylalanine complex at 395 nm exhibits hypochromism (11%) and a red shift (10 nm) upon addition of HSA. The changes are attributed to binding of the complex to the protein. A fairly large binding constant of  $1 \times 10^6 \text{ M}^{-1}$  (binding stoichiometry = 1.1) is determined from the spectral data. The complex exhibits weak emission in phosphate-buffered saline solution. However, addition of HSA induces emission enhancement and the emission intensity at 562 nm increases tenfold at  $[\text{HSA}]:[\text{Pt}] \geq 3$ . Polyacrylamide gel electrophoresis results indicate that this complex binds preferentially to HSA over other plasma proteins such as human  $\alpha$ -,  $\beta$ - and  $\gamma$ -globulins. It is proposed that the amino acid auxiliary ligand could direct the binding or recognition of the complex towards biomolecules through complementary hydrogen bonding.



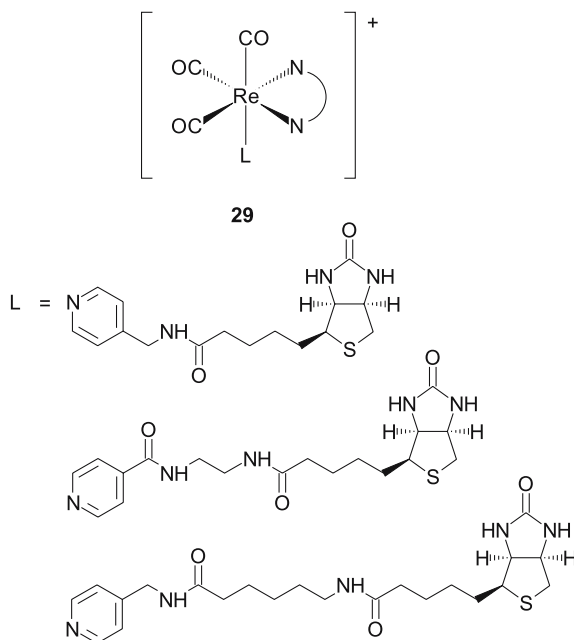
28



### 4.3

#### Luminescent Biotin Derivatives

Lo and co-workers synthesised a family of luminescent rhenium(I) polypyridine biotin complexes  $[\text{Re}(\text{N}^{\wedge}\text{N})(\text{CO})_3(\text{py-spacer-biotin})]^+$  (**29**) [67, 68]. Upon irradiation, the complexes display orange to green triplet MLCT ( $d\pi(\text{Re}) \rightarrow \pi^*(\text{N}^{\wedge}\text{N})$ ) emission in fluid solutions at 298 K. The binding of the complexes to avidin has been studied by the standard HABA assay. The assay is based on the binding of HABA to avidin that gives rise to an absorption feature at ca. 500 nm. Since the affinity of HABA to avidin ( $K_d = 6 \times 10^{-6}$  M) is much weaker than that of biotin ( $K_d = \text{ca. } 10^{-15}$  M), addition of biotin will replace the bound HABA molecules from the protein, leading to a decrease in the absorbance at 500 nm. Addition of the rhenium(I) biotin complexes to a mixture of HABA and avidin results in a decrease in the absorbance at 500 nm, indicating that the bound HABA molecules are replaced by the rhenium(I) biotin complexes. All these rhenium(I) complexes bind to avidin with the same stoichiometry as unmodified biotin ( $[\text{Re}] : [\text{avidin}] = 4 : 1$ ). Remarkably, all the complexes display enhanced emission intensities and extended lifetimes upon binding to avidin. The emission titration curves for  $[\text{Re}(\text{Me}_2\text{-Ph}_2\text{-phen})(\text{CO})_3(\text{py-4-CH}_2\text{-NH-C}_6\text{-NH-biotin})]^+$  are shown in Fig. 10. At  $[\text{Re}] : [\text{avidin}] = 4 : 1$ , the emission intensities of this class of complexes are enhanced by ca. 3.0- to 1.2-fold and the emission lifetimes are extended by



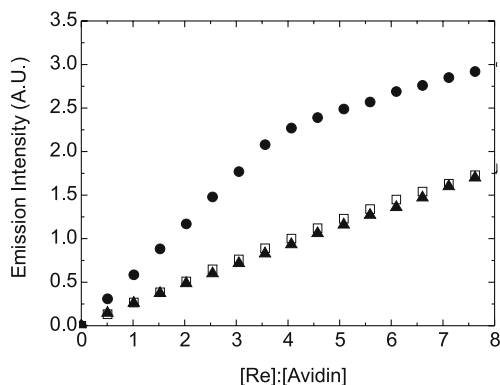
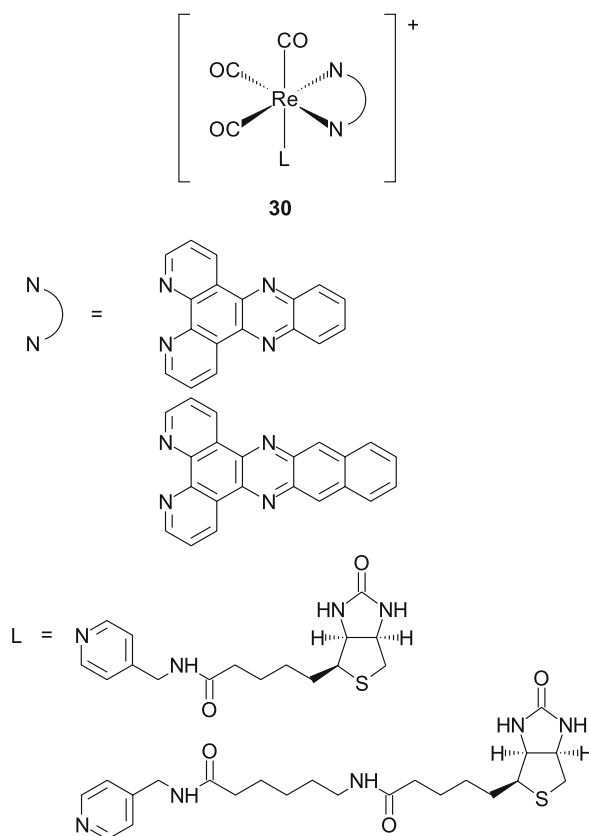


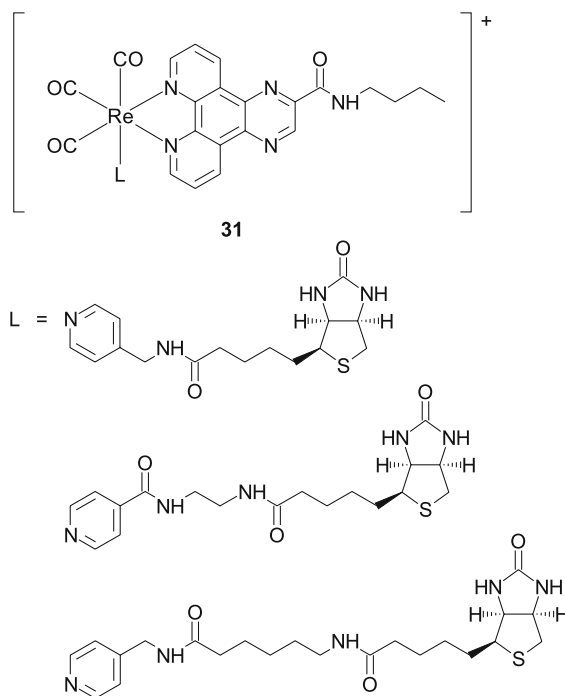
**Fig. 10** Luminescence titration curves for the titrations of (1) 3.8  $\mu\text{M}$  avidin ( $\bullet$ ), (2) 3.8  $\mu\text{M}$  avidin and 380.0  $\mu\text{M}$  unmodified biotin ( $\blacktriangle$ ), and (3) a blank phosphate buffer solution ( $\square$ ) with  $[\text{Re}(\text{Me}_2\text{-Ph}_2\text{-phen})(\text{CO})_3(\text{py-4-CH}_2\text{-NH-C}_6\text{-NH-biotin})]^+$  [68]

ca. 2.4- to 1.3-fold. Since no similar changes are observed when excess biotin is initially present, the increase in emission intensities and lifetimes is a consequence of the specific binding of the complexes to the biotin-binding sites of avidin. These observations are in contrast to most fluorophore-biotin conjugates, which suffer from severe emission quenching upon binding to avidin due to RET. The absence of emission quenching for these rhenium(I) biotin complexes is because of the insignificant overlap between their absorption and emission spectra, which disfavours RET quenching. It is conceivable that the enhancement results from (1) the hydrophobicity associated with the biotin-binding pockets of avidin and (2) the increased rigidity of the surroundings of the complexes upon the binding event. Complexes with longer spacer arms exhibit less significant emission intensity enhancement because they remain more exposed to the polar buffer after binding to the protein. Additionally, the effects of increased rigidity resulting from avidin binding are smaller for these complexes due to their longer and more flexible spacer arms. The first dissociation constants  $K_d$  of the rhenium-avidin adducts are estimated from the on-rates and off-rates of the rhenium-avidin adducts from kinetic experiments. The  $K_d$  values range from ca.  $5.5 \times 10^{-11}$  to  $3.4 \times 10^{-9}$  M, which are about 4 to 6 orders of magnitude larger than that of the native biotin-avidin system ( $K_d = \text{ca. } 10^{-15}$  M). The intrinsic emission intensity enhancement ( $I/I_0$ ) of the complexes upon binding to avidin varied from ca. 3.0- to 1.2-fold. To develop sensitive assays for avidin and biotin, one strategy is to use a quencher to selectively suppress the emission of the free rhenium(I) biotin complex by distance-dependent RET quenching. With a water-soluble negatively charged polypeptide (poly(D-Glu:D-Lys) 6:4) modified with the non-fluorescent energy-acceptor dye QSY-7 NHS ester as the quencher, the emission enhancement factor of one of the complexes increases from ca. 4.0 to 1.5 upon binding to avidin [68].

To explore bifunctional biological probes, new rhenium(I) biotin complexes containing the extended planar diimine ligands dppz and dppn (30) have been prepared [69]. Absorption and emission titration results reveal that all the complexes bind to double-stranded calf thymus DNA by intercalation. The HABA assays show that all the complexes bind to avidin with a stoichiometry of 4 : 1 ( $[\text{Re}] : [\text{avidin}]$ ). Similar to other rhenium(I) biotin complexes described above, the emission intensities and lifetimes of these complexes also increase in the presence of avidin. In particular, the complex  $[\text{Re}(\text{dppz})(\text{CO})_3(\text{py-4-CH}_2 - \text{NH-biotin})]^+$  exhibits a large emission enhancement factor of ca. 40. The avidin-induced emission enhancement has been exploited in the design of a simple homogeneous assay for biotin, which is based on the competition between the complex and biotin analyte on binding to avidin. The concentration of biotin that could be determined by this assay is between ca.  $1 \times 10^{-7.5}$  and  $1 \times 10^{-5}$  M.

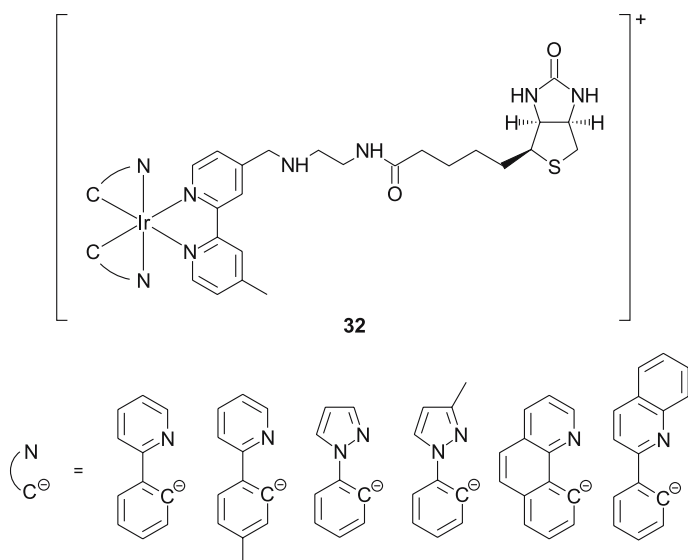
Another approach to increasing the emission enhancement factors is to identify a system that inherently shows very weak emission in aqueous buffer,





but intense emission in more hydrophobic media. New rhenium(I) biotin complexes  $[\text{Re}(\text{dpqa})(\text{CO})_3(\text{py-spacer-biotin})]^+$  (**31**) have been designed to achieve this goal [70]. The amide substituent of the diimine ligand renders the complexes very weakly emissive in aqueous buffer. Binding of these complexes to avidin has been confirmed by the HABA assays. All the complexes show increased emission intensity and lifetimes upon binding to avidin. Importantly, the emission intensity enhancement factors vary from ca. 8.1 to 3.1, which are more pronounced compared to those of the dpq analogues (ca. 1.8 to 1.2). The binding interactions of these rhenium(I) biotin complexes with avidin modified by anthracene have also been investigated.

Luminescent cyclometallated iridium(III) polypyridine biotin complexes  $[\text{Ir}(\text{N}^{\wedge}\text{C})_2(\text{bpy-CH}_2\text{-NH-C}_2\text{-NH-biotin})]^+$  (**32**) have been designed [71]. Upon excitation, all the complexes show intense and long-lived orange to greenish-yellow luminescence in fluid solutions under ambient conditions and in low-temperature glass. An excited-state assignment of  ${}^3\text{MLCT}$  ( $d\pi(\text{Ir}) \rightarrow \pi^*(\text{N}^{\wedge}\text{N})$ ) is made on the basis of the observations that the complex  $[\text{Ir}(\text{ppy})_2(\text{bpy-CH}_2\text{-NH-C}_2\text{-NH-biotin})]^+$ , which contains electron-donating substituents on its diimine ligand, emits at higher energy than the model complex  $[\text{Ir}(\text{ppy})_2(\text{bpy})]^+$ . The complex  $[\text{Ir}(\text{pq})_2(\text{bpy-CH}_2\text{-NH-C}_2\text{-NH-biotin})]^+$  shows structured emission spectra and very long emission lifetimes ( $\tau_0 = \text{ca. } 3 \text{ to } 2 \mu\text{s}$ ) in fluid solutions at 298 K, suggestive of sub-



stantial  ${}^3\text{IL}$  ( $\pi \rightarrow \pi^*(\text{pq}^-)$ ) character in its emissive state. Binding of these iridium(III) biotin complexes to avidin is confirmed by the HABA assays. Luminescence titrations using the complexes as titrants show that all the complexes display enhanced emission intensities upon binding to avidin. At the equivalence points, the emission intensities and lifetimes of the complexes increase by factors of ca. 3.3 to 1.5. It is noteworthy that the  $\text{pq}^-$  complex, being more hydrophobic than the other complexes, exhibits a higher degree of emission enhancement (ca. 3.3) after binding to avidin. Although these iridium(III) biotin complexes function as luminescent probes for avidin, their emission maxima are somewhat confined to ca. 550 to 590 nm, limiting their use as multi-colour probes. The reason is that the emissive states are essentially  ${}^3\text{MLCT}$  ( $d\pi(\text{Ir}) \rightarrow \pi^*(\text{N}^{\wedge}\text{N})$ ) in nature. Thus, a new series of luminescent cyclometallated iridium(III) arylbenzothiazole biotin complexes  $[\text{Ir}(\text{N}^{\wedge}\text{C})_2(\text{bpy-CO-NH-C}_6\text{-NH-biotin})]^+$  (**33**) of higher hydrophobicity have been synthesised [72]. In solutions at 298 K, these complexes exhibit intense and long-lived (in the microsecond timescale) emission with a much wider range of emission wavelengths ( $\lambda_{\text{em}} = 528$  to 712 nm) (Fig. 11). In view of very long emission lifetimes and rich structural features of the emission bands, the emission is assigned to a  ${}^3\text{IL}$  ( $\pi \rightarrow \pi^*(\text{N}^{\wedge}\text{C})$ ) excited state, perhaps with mixing of some  ${}^3\text{MLCT}$  ( $d\pi(\text{Ir}) \rightarrow \pi^*(\text{N}^{\wedge}\text{C})$ ) character. As expected, all the iridium(III) biotin complexes display enhanced emission intensities and extended emission lifetimes in the presence of avidin. Importantly, the more hydrophobic biphenyl and naphthyl complexes show very significant emission enhancement factors (8.1 and 5.8, respectively), providing higher detection sensitivity. The  $K_{\text{d}}$  values of the adducts formed from avidin and

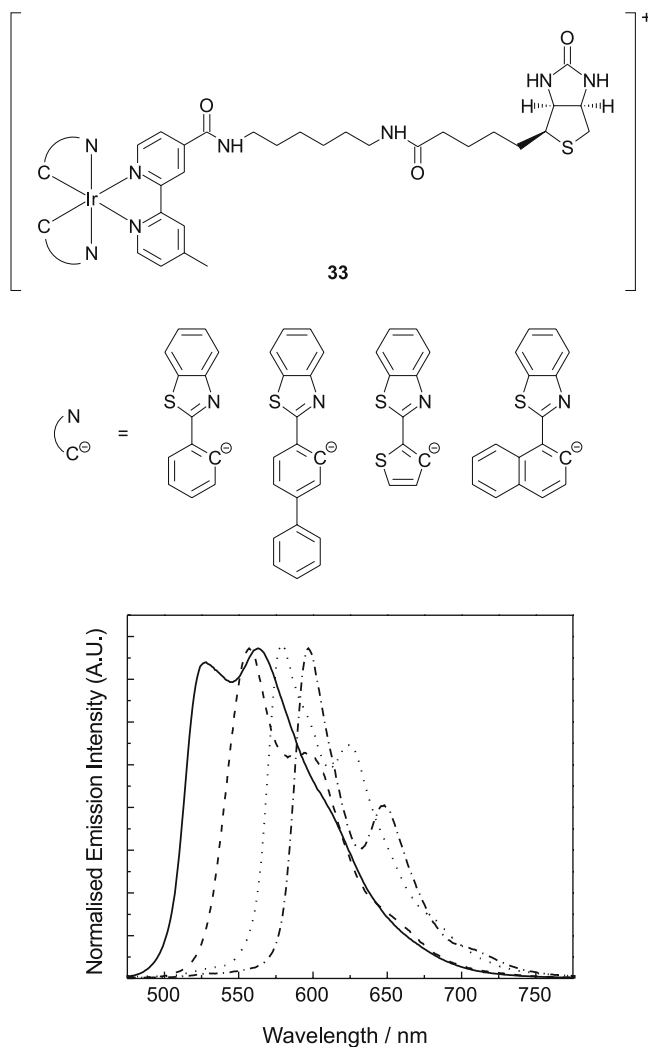
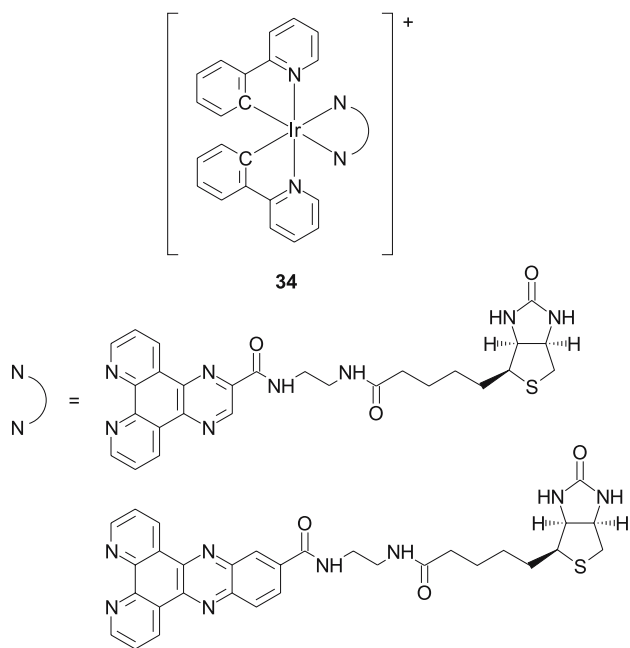


**Fig. 11** Emission spectra of  $[\text{Ir}(\text{N}^-\text{C}^-)_2(\text{bpy}-\text{CO}-\text{NH}-\text{C}_6-\text{NH}-\text{biotin})]^+$  ( $\text{N}^-\text{C}^- = \text{bt}^-$  (—),  $\text{bsb}^-$  (---),  $\text{btth}^-$  (···) and  $\text{bsn}^-$  (-·-·-)) in degassed  $\text{CH}_2\text{Cl}_2$  at 298 K [72]

all the iridium(III) biotin complexes vary from ca.  $10^{-10}$  to  $10^{-8}$  M, which are about 5 to 7 orders of magnitude larger than that of the native biotin-avidin system. It is likely that the lack of a long spacer arm and/or the bulky  $[\text{Ir}(\text{N}^-\text{C}^-)_2]$  moieties lead to the diminished avidin-binding strength.

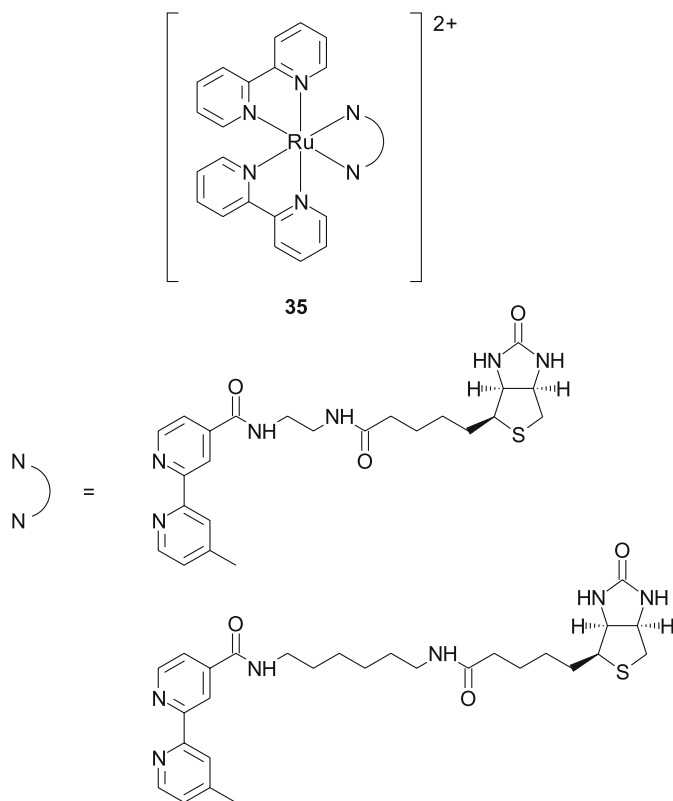
Recently, two cyclometallated iridium(III) biotin complexes with extended planar diimine ligands  $[\text{Ir}(\text{ppy})_2(\text{N}^-\text{N}-\text{biotin})]^+$  ( $\text{N}^-\text{N}-\text{biotin} = \text{dpq}-\text{biotin}$ ,  $\text{dppz}-\text{biotin}$ ) (34) have been isolated [73]. The complexes show typical  $^3\text{MLCT}$  ( $d\pi(\text{Ir}) \rightarrow \pi^*(\text{N}^-\text{N}-\text{biotin})$ ) emission at ca. 600 nm in aprotic solvents. In



aqueous buffer, the complexes are non-emissive, probably due to hydrogen-bonding interactions of the amide substituents with the water molecules. Both complexes bind to avidin as revealed by the HABA assays. Interestingly, in the presence of avidin, the complexes exhibit a new structured emission band at ca. 490, 520 (sh) nm ( $\tau_0 = \text{ca. } 2 \mu\text{s}$ ), which is much higher in energy than the  $^3\text{MLCT}$  emission of the complexes. The emissive state of the avidin-bound complexes is tentatively assigned to  $^3\text{IL} (\pi \rightarrow \pi^*(\text{N}^-\text{N-biotin}))$ .

Two ruthenium(II) polypyridine biotin complexes  $[\text{Ru}(\text{bpy})_2(\text{bpy-spacer-biotin})]^{2+}$  (**35**) have been synthesised and characterised [74]. The complexes exhibit intense and long-lived orange-red  $^3\text{MLCT} (d\pi(\text{Ru}) \rightarrow \pi^*(\text{N}^-\text{N}))$  luminescence upon irradiation in fluid solutions at 298 K and in alcohol glass at 77 K. Since the emission energy of these complexes is slightly lower than that of  $[\text{Ru}(\text{bpy})_3]^{2+}$ , the acceptor orbitals should possess predominant  $\pi^*(\text{bpy-spacer-biotin})$  character, given the lower-lying  $\pi^*$  orbitals of the biotin-containing diimine ligands due to the electron-withdrawing amide substituents. The binding of both complexes to avidin is confirmed by the HABA assays. The  $K_d$  values for these two complexes are determined to be  $4.8 \times 10^{-10}$  and  $3.1 \times 10^{-11}$  M, respectively. Luminescence titration results show that at  $[\text{Ru}]:[\text{avidin}] = 4:1$ , the emission intensities and lifetimes of the complexes are increased by ca. 1.4- to 1.2-fold only. These enhancement factors could be amplified by addition of a quencher that can preferentially reduce the luminescence of the free form of the complexes compared to the avidin-bound form. Methyl viologen,  $\text{MV}^{2+}$ , has been used because it can



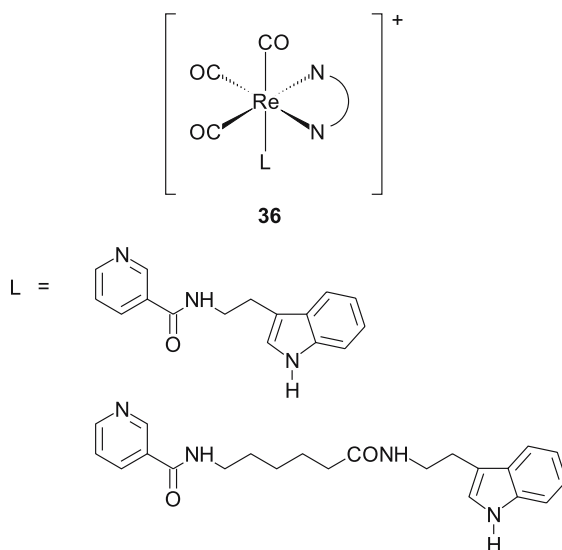


effectively quench the emission of common ruthenium(II) polypyridine complexes and its positive charge could render quenching of the avidin-bound complex less effective, given the high positive charge of the protein molecule ( $pI = \text{ca. } 10$ ). Under low-salt conditions and in the presence of  $MV^{2+}$ , both complexes display a more significant avidin-induced emission enhancement ( $I/I_0 = 2.4$  and  $2.0$ ;  $\tau/\tau_0 = 2.5$  and  $2.1$ , respectively). Under high-salt conditions, due to the more efficient quenching of the emission of the free complexes by  $MV^{2+}$ , higher emission intensity amplification factors (ca. 3.2 and 3.0) and emission lifetime elongation factors (ca. 2.8 and 2.5) are achieved.

#### 4.4

##### Probes for Indole-Binding Proteins

Lo and co-workers reported the synthesis, characterisation, photophysical and electrochemical properties of luminescent rhenium(I) diimine indole complexes  $[\text{Re}(\text{N}^{\wedge}\text{N})(\text{CO})_3(\text{py-indole})]^+$  (**36**) [75, 76]. Upon visible-light irradiation, the complexes exhibited  $^3\text{MLCT}$  ( $d\pi(\text{Re}) \rightarrow \pi^*(\text{N}^{\wedge}\text{N})$ ) emission in fluid solutions at 298 K and in low-temperature glass. When these com-



plexes are excited in the ultraviolet region ( $\lambda_{\text{ex}} = 250 \text{ nm}$ ), they exhibit an additional emission band at ca. 365 nm that originates from the indole moiety. These rhenium(I) indole complexes exhibit much lower luminescence quantum yields and shorter emission lifetimes than those of their indole-free counterparts due to self-quenching. The excited-state reduction potentials,  $E^0[\text{Re}^{+*/0}]$ , of the rhenium(I) complexes are estimated to be ca. +1.25 to +1.49 V vs SCE. On the basis of these potentials and the redox potential of indole ( $E^0[\text{indole}^{+/0}] < +1.06 \text{ V vs SCE}$ ), reductive quenching of the excited complexes by indole is favoured by > 0.2 to 0.4 eV. This, together with the results from transient absorption spectroscopic studies, leads to the conclusion that the mechanism of the emission quenching of the indole-containing complexes is electron transfer in nature. The interactions of these rhenium(I) indole complexes with indole-binding proteins such as BSA have been studied by emission titrations. The emission titration curve for  $[\text{Re}(\text{Me}_2\text{-phen})(\text{CO})_3(\text{py-3-CONHC}_2\text{H}_4\text{-indole})]^+$  is shown in Fig. 12. The emission intensities of the indole-containing complexes are enhanced by up to 17-fold in the presence of BSA. The binding constants ( $K_a$ ) for the complexes with BSA have been determined to be ca.  $10^4 \text{ M}^{-1}$  from Scatchard analysis. These values are comparable to those observed for the albumin binding of tryptamine ( $K_a = 1.1 \times 10^4 \text{ M}^{-1}$ ,  $n = 1$ ), indole-3-acetic acid ( $K_a = 1.7 \times 10^4 \text{ M}^{-1}$ ,  $n = 1$ ) and 5-hydroxyindole-3-acetic acid ( $K_a = 2.0 \times 10^4 \text{ M}^{-1}$ ,  $n = 1$ ). The rhenium(I) indole complexes can inhibit another indole-binding protein, tryptophanase. A standard assay, which is on the basis of the conversion of L-serine to pyruvate by the enzyme, has been carried out. Under the standard experimental conditions, at  $[\text{L-serine}] = 800 \text{ mM}$ , free indole inhibit 53% of the enzyme activity, while the indole-containing complexes

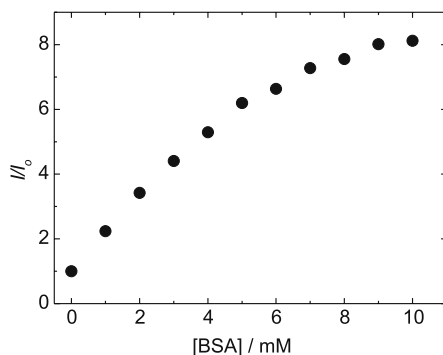
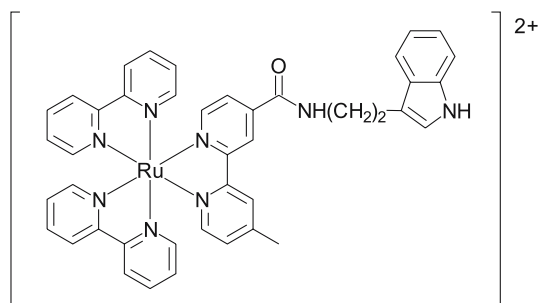


**Fig. 12** Emission titration curve of  $[\text{Re}(\text{Me}_2\text{-phen})(\text{CO})_3(\text{py-3-CONHC}_2\text{H}_4\text{-indole})]^+$  with BSA.  $I_0$  and  $I$  are the emission intensities of the complex in the absence and presence of BSA, respectively [76]

and their indole-free counterparts cause ca. 77 to 43 and 8 to 3% inhibition, respectively. The Michaelis constants ( $K_m$ ) for the complexes vary from 179 to 143 mM. Similar to unmodified indole, the rhenium(I) indole complexes inhibit the tryptophanase-catalysed conversion of L-serine to pyruvate in a non-competitive fashion.

Luminescent ruthenium(II) polypyridine indole complexes such as  $[\text{Ru}(\text{bpy})_2(\text{bpy-indole})]^{2+}$  (**37**) and their indole-free counterparts have been synthesised and characterised [77]. The ruthenium(II) indole complexes display typical  $^1\text{MLCT}$  ( $d\pi(\text{Ru}) \rightarrow \pi^*(\text{N}^{\wedge}\text{N})$ ) absorption bands, and intense and long-lived orange-red  $^3\text{MLCT}$  ( $d\pi(\text{Ru}) \rightarrow \pi^*(\text{bpy-indole})$ ) luminescence upon visible-light irradiation in fluid solutions at 298 K and in alcohol glass at 77 K. In contrast to the rhenium(I) indole complexes, the indole moiety does not quench the emission of the ruthenium(II) polypyridine complexes because the excited complexes are not sufficiently oxidising to initiate electron-transfer reactions. Emission titrations show that the luminescence intensities of the ruthenium(II) indole complexes are only increased by ca. 1.38- to



**37**

1.01-fold in the presence of BSA. However, in the presence of the quencher  $[\text{Fe}(\text{CN})_6]^{4-}$ , which preferentially suppresses the emission of the free probes, the ruthenium(II) indole complexes display more significant enhancement of emission intensities upon binding to BSA (ca. 19.7- to 2.5-fold). The binding constants of the indole-containing complexes are estimated to range from ca.  $6.6 \times 10^4$  to  $9.5 \times 10^4 \text{ M}^{-1}$ .

## 5

### Conclusion

It can be seen in this review article that the most extensively studied systems as biological labels and probes are ruthenium(II) polypyridine complexes, despite their  $^3\text{MLCT}$  emission being somewhat limited in the orange-red region. Studies have shown that complexes of other metal centres such as rhenium(I), iridium(III) and platinum(II) display more favourable photophysical properties, such as a wider range of emission wavelengths and more intense and longer-lived emission, due to a variety of excited states. While these interesting properties are useful in the development of new luminescent labels and probes, the rich photochemical behaviour of some of these complexes, such as the highly photooxidising rhenium(I) polypyridine complexes and highly photoreducing tris-cyclometallated iridium(III) systems, is expected to find applications in photoinduced electron-transfer studies. By a selection of (1) transition metal centres, (2) coordinating ligands that can significantly perturb the electronic structures of the complexes, (3) reactive functional groups that can target biomolecules, and (4) specific molecular substrates as a recognition unit, we anticipate that luminescent transition metal complexes will continue to contribute to the design of new biological labels and probes for the fundamental understanding of biological systems and specific analytical applications.

**Acknowledgements** I would like to thank the Hong Kong Research Grants Council and City University of Hong Kong for financial support. I am very grateful to previous and current members of my research group for their hard work and assistance in the preparation of this article, and to my collaborators, all of whose names appear in the reference list.

### References

1. Lees AJ (1987) *Chem Rev* 87:711
2. Balzani V, Scandola F (1990) *Supramolecular photochemistry*. Ellis Horwood, New York
3. Kalyanasundaram K (1991) *Photochemistry of polypyridine and porphyrin complexes*. Academic, San Diego

4. Roundhill DM (1994) Photochemistry and photophysics of metal complexes. Plenum, New York
5. Balzani V, Juris A, Venturi M, Campagna S, Serroni S (1996) *Chem Soc Rev* 96:759
6. Vogler A, Kunkely H (2001) *Top Curr Chem* 213:143
7. Dickson EFG, Pollak A, Diamandis EP (1995) *J Photochem Photobiol B* 27:3
8. Parkhurst LJ (2004) *Methods Enzymol* 379:235
9. Terpetschnig E, Szmajcinski H, Lakowicz JR (1997) *Methods Enzymol* 278:295
10. Blasius R, Moucheron C, Kirsch-De Mesmaeker A (2004) *Eur J Inorg Chem* 3971
11. Gray HB, Winkler JR (1996) *Annu Rev Biochem* 65:537
12. Chen L, McBranch DW, Wang HL, Helgeson R, Wudl F, Whitten DG (1999) *Proc Natl Acad Sci USA* 96:12287
13. Lees AJ (1998) *Coord Chem Rev* 177:3
14. Hemmila IA (1991) *Applications of fluorescence in immunoassays*. Wiley, New York, p 133
15. McMillin DR, McNett KM (1998) *Chem Rev* 98:1201
16. Erkkila KE, Odom DT, Barton JK (1999) *Chem Rev* 99:2777
17. Metcalfe C, Thomas JA (2003) *Chem Soc Rev* 32:215
18. Pierard F, Kirsch-De Mesmaeker A (2006) *Inorg Chem Commun* 9:111
19. Dreyer GB, Dervan PB (1985) *Proc Natl Acad Sci USA* 82:968
20. Le Doan T, Perrouault L, Chassignol M, Thuong NT, Helene C (1987) *Nucleic Acids Res* 15:8643
21. Telser J, Cruickshank KA, Schanze KS, Netzel TL (1989) *J Am Chem Soc* 111:7221
22. Winkler JR, Gray HB (1992) *Chem Rev* 92:369
23. Pan LP, Durham B, Wolinska J, Millett F (1988) *Biochemistry* 27:7180
24. Hermanson GT (1996) *Bioconjugate techniques*. Academic, San Diego, p 137
25. Lakowicz JR (1999) *Principles of fluorescence spectroscopy*, 2nd edn. Kluwer Academic/Plenum, New York, p 573
26. Lo KKW, Hui WK, Chung CK, Tsang KHK, Ng DCM, Zhu N, Cheung KK (2005) *Coord Chem Rev* 249:1434
27. Lewis FD, Helvoigt SA, Letsinger RL (1999) *Chem Commun* 327
28. Khan SI, Beilstein AE, Smith GD, Sykora M, Grinstaff MW (1999) *Inorg Chem* 38:2411
29. Khan SI, Beilstein AE, Tierney MT, Sykora M, Grinstaff MW (1999) *Inorg Chem* 38:5999
30. Hu X, Smith GD, Sykora M, Lee SJ, Grinstaff MW (2000) *Inorg Chem* 39:2500
31. Rack JJ, Krider ES, Meade TJ (2000) *J Am Chem Soc* 122:6287
32. Krider ES, Rack JJ, Frank NL, Meade TJ (2001) *Inorg Chem* 40:4002
33. Hurley DJ, Tor Y (2002) *J Am Chem Soc* 124:3749
34. Hurley DJ, Tor Y (2002) *J Am Chem Soc* 124:13231
35. Wei L, Babich J, Eckelman WC, Zubieta J (2005) *Inorg Chem* 44:2198
36. Jenkins Y, Barton JK (1992) *J Am Chem Soc* 114:8736
37. Holmlin RE, Tong RT, Barton JK (1998) *J Am Chem Soc* 120:9724
38. Ortmans I, Content S, Boutonnet N, Kirsch-De Mesmaeker A, Bannwarth W, Constant JF, Defrancq E, Lhomme J (1999) *Chem Eur J* 5:2712
39. García-Fresnadillo D, Lentzen O, Ortmans I, Defrancq E, Kirsch-De Mesmaeker A (2005) *Dalton Trans* 852
40. Lo KKW, Ng DCM, Hui WK, Cheung KK (2001) *J Chem Soc Dalton Trans* 2634
41. Lo KKW, Hui WK, Ng DCM, Cheung KK (2002) *Inorg Chem* 41:40
42. Lo KKW, Ng DCM, Chung CK (2001) *Organometallics* 20:4999
43. Winkler JR, Nocera DG, Yocom KM, Bordignon E, Gray HB (1982) *J Am Chem Soc* 104:5798

44. Gray HB, Winkler JR (2005) *Proc Natl Acad Sci USA* 102:3534
45. Langen R, Chang IJ, Germanas JP, Richards JH, Winkler JR, Gray HB (1995) *Science* 268:1733
46. Regan JJ, Di Bilio AJ, Langen R, Skov LK, Winkler JR, Gray HB, Onuchic JN (1995) *Chem Biol* 2:489
47. Connick WB, Di Bilio AJ, Hill MG, Winkler JR, Gray HB (1995) *Inorg Chim Acta* 240:169
48. Di Bilio AJ, Crane BR, Wehbi WA, Kiser CN, Abu-Omar MM, Carlos RM, Richards JH, Winkler JR, Gray HB (2001) *J Am Chem Soc* 123:3181
49. Miller JE, Di Bilio AJ, Wehbi WA, Green MT, Museth AK, Richards JH, Winkler JR, Gray HB (2004) *Biochim Biophys Acta* 1655:59
50. Szmecinski H, Terpetschnig E, Lakowicz JR (1996) *Biophys Chem* 62:109
51. Guo XQ, Castellano FN, Li L, Szmecinski H, Lakowicz JR, Sipior J (1997) *Anal Biochem* 254:179
52. Dattelbaum JD, Abugo OO, Lakowicz JR (2000) *Bioconjug Chem* 11:533
53. Terpetschnig E, Szmecinski H, Lakowicz JR (1996) *Anal Biochem* 240:54
54. Murtaza Z, Herman P, Lakowicz JR (1999) *Biophys Chem* 80:143
55. Ryan EM, O'Kennedy R, Feeney MM, Kelly JM, Vos JG (1992) *Bioconjug Chem* 3:285
56. Stephenson KA, Banerjee SR, Besanger T, Sogbein OO, Levalada MK, McFarlane N, Lemon JA, Boreham DR, Maresca KP, Brennan JD, Babich JW, Valliant JF (2004) *J Am Chem Soc* 126:8598
57. Banerjee SR, Schaffer P, Babich JW, Valliant JF, Zubieta J (2005) *Dalton Trans* 3886
58. Lo KKW, Chung CK, Zhu N (2003) *Chem Eur J* 9:475
59. Lo KKW, Li CK, Lau KW, Zhu N (2003) *Dalton Trans* 4682
60. Lo KKW, Chung CK, Lee TKM, Lui LH, Tsang KHK, Zhu N (2003) *Inorg Chem* 42:6886
61. Lo KKW, Chan JSW, Chung CK, Tsang VWH, Zhu N (2004) *Inorg Chim Acta* 357:3109
62. Wong KMC, Tang WS, Chu BWK, Zhu N, Yam VWW (2004) *Organometallics* 23:3459
63. Dunn AR, Dmochowski IJ, Winkler JR, Gray HB (2003) *J Am Chem Soc* 125:12450
64. Belliston-Bittner W, Dunn AR, Nguyen YHL, Stuehr DJ, Winkler JR, Gray HB (2005) *J Am Chem Soc* 127:15907
65. Che CM, Zhang JL, Lin LR (2002) *Chem Commun* 2556
66. Siu PKM, Ma DL, Che CM (2005) *Chem Commun* 1025
67. Lo KKW, Hui WK, Ng DCM (2002) *J Am Chem Soc* 124:9344
68. Lo KKW, Hui WK (2004) *Inorg Chem* 43:5275
69. Lo KKW, Tsang KHK (2004) *Organometallics* 23:3062
70. Lo KKW, Tsang KHK, Sze KS (2006) *Inorg Chem* 45:1714
71. Lo KKW, Chan JSW, Lui LH, Chung CK (2004) *Organometallics* 23:3108
72. Lo KKW, Li CK, Lau JSY (2005) *Organometallics* 24:4594
73. Lo KKW, Chung CK, Zhu N (2006) *Chem Eur J* 12:1500
74. Lo KKW, Lee TKM (2004) *Inorg Chem* 43:5275
75. Lo KKW, Tsang KHK, Hui WK, Zhu N (2003) *Chem Commun* 2704
76. Lo KKW, Tsang KHK, Hui WK, Zhu N (2005) *Inorg Chem* 44:6100
77. Lo KKW, Lee TKM, Zhang KY (2006) *Inorg Chim Acta* 359:1845

---

## Author Index Volumes 101–124

Author Index Vols. 1–100 see Vol. 100

*The volume numbers are printed in italics*

- Alajarin M, see Turner DR (2004) *108*: 97–168
- Aldinger F, see Seifert HJ (2002) *101*: 1–58
- Alessio E, see Iengo E (2006) *121*: 105–143
- Alfredsson M, see Corà F (2004) *113*: 171–232
- Aliev AE, Harris KDM (2004) Probing Hydrogen Bonding in Solids Using State NMR Spectroscopy *108*: 1–54
- Alloul H, see Brouet V (2004) *109*: 165–199
- Amstutz N, see Hauser A (2003) *106*: 81–96
- Anitha S, Rao KSJ (2003) The Complexity of Aluminium-DNA Interactions: Relevance to Alzheimer's and Other Neurological Diseases *104*: 79–98
- Anthon C, Bendix J, Schäffer CE (2004) Elucidation of Ligand-Field Theory. Reformulation and Revival by Density Functional Theory *107*: 207–302
- Aramburu JA, see Moreno M (2003) *106*: 127–152
- Arçon D, Blinc R (2004) The Jahn-Teller Effect and Fullerene Ferromagnets *109*: 231–276
- Aromí G, Brechin EK (2006) Synthesis of 3d Metallic Single-Molecule Magnets. *122*: 1–67
- Atanasov M, Daul CA, Rauzy C (2003) A DFT Based Ligand Field Theory *106*: 97–125
- Atanasov M, see Reinen D (2004) *107*: 159–178
- Atwood DA, see Conley B (2003) *104*: 181–193
- Atwood DA, Hutchison AR, Zhang Y (2003) Compounds Containing Five-Coordinate Group 13 Elements *105*: 167–201
- Atwood DA, Zaman MK (2006) Mercury Removal from Water *120*: 163–182
- Autschbach J (2004) The Calculation of NMR Parameters in Transition Metal Complexes *112*: 1–48
- Baerends EJ, see Rosa A (2004) *112*: 49–116
- Balch AL (2007) Remarkable Luminescence Behaviors and Structural Variations of Two-Coordinate Gold(I) Complexes. *123*: 1–40
- Baranoff E, Barigelletti F, Bonnet S, Collin J-P, Flamigni L, Mobian P, Sauvage J-P (2007) From Photoinduced Charge Separation to Light-Driven Molecular Machines. *123*: 41–78
- Barbara B, see Curély J (2006) *122*: 207–250
- Bard AJ, Ding Z, Myung N (2005) Electrochemistry and Electrogenerated Chemiluminescence of Semiconductor Nanocrystals in Solutions and in Films *118*: 1–57
- Barigelletti F, see Baranoff E (2007) *123*: 41–78
- Barriuso MT, see Moreno M (2003) *106*: 127–152
- Beaulac R, see Nolet MC (2004) *107*: 145–158
- Bebout DC, Berry SM (2006) Probing Mercury Complex Speciation with Multinuclear NMR *120*: 81–105

- Bellandi F, see Contreras RR (2003) *106*: 71–79
- Bendix J, see Anthon C (2004) *107*: 207–302
- Berend K, van der Voet GB, de Wolff FA (2003) Acute Aluminium Intoxication *104*: 1–58
- Berry SM, see Bebout DC (2006) *120*: 81–105
- Bianconi A, Saini NL (2005) Nanoscale Lattice Fluctuations in Cuprates and Manganites *114*: 287–330
- Blinic R, see Arcčon D (2004) *109*: 231–276
- Blinic R (2007) Order and Disorder in Perovskites and Relaxor Ferroelectrics. *124*: 51–67
- Boča R (2005) Magnetic Parameters and Magnetic Functions in Mononuclear Complexes Beyond the Spin-Hamiltonian Formalism *117*: 1–268
- Bohrer D, see Schetinger MRC (2003) *104*: 99–138
- Bonnet S, see Baranoff E (2007) *123*: 41–78
- Bouamaied I, Coskun T, Stulz E (2006) Axial Coordination to Metalloporphyrins Leading to Multinuclear Assemblies *121*: 1–47
- Boulanger AM, see Nolet MC (2004) *107*: 145–158
- Boulon G (2004) Optical Transitions of Trivalent Neodymium and Chromium Centres in LiNbO<sub>3</sub> Crystal Host Material *107*: 1–25
- Bowlby BE, Di Bartolo B (2003) Spectroscopy of Trivalent Praseodymium in Barium Yttrium Fluoride *106*: 193–208
- Braga D, Maini L, Polito M, Grepioni F (2004) Hydrogen Bonding Interactions Between Ions: A Powerful Tool in Molecular Crystal Engineering *111*: 1–32
- Brechin EK, see Aromí G (2006) *122*: 1–67
- Brouet V, Allouf H, Gàràj S, Forró L (2004) NMR Studies of Insulating, Metallic, and Superconducting Fullerenes: Importance of Correlations and Jahn-Teller Distortions *109*: 165–199
- Buddhudu S, see Morita M (2004) *107*: 115–144
- Budzelaar PHM, Talarico G (2003) Insertion and  $\beta$ -Hydrogen Transfer at Aluminium *105*: 141–165
- Burrows AD (2004) Crystal Engineering Using Multiple Hydrogen Bonds *108*: 55–96
- Bussmann-Holder A, Dalal NS (2007) Order/Disorder Versus or with Displacive Dynamics in Ferroelectric Systems. *124*: 1–21
- Bussmann-Holder A, Keller H, Müller KA (2005) Evidences for Polaron Formation in Cuprates *114*: 367–386
- Bussmann-Holder A, see Dalal NS (2007) *124*: 23–50
- Bussmann-Holder A, see Micnas R (2005) *114*: 13–69
- Canadell E, see Sánchez-Portal D (2004) *113*: 103–170
- Cancines P, see Contreras RR (2003) *106*: 71–79
- Caneschi A, see Cornia A (2006) *122*: 133–161
- Cartwright HM (2004) An Introduction to Evolutionary Computation and Evolutionary Algorithms *110*: 1–32
- Christie RA, Jordan KD (2005)  $n$ -Body Decomposition Approach to the Calculation of Interaction Energies of Water Clusters *116*: 27–41
- Clérac R, see Coulon C (2006) *122*: 163–206
- Clot E, Eisenstein O (2004) Agostic Interactions from a Computational Perspective: One Name, Many Interpretations *113*: 1–36
- Collin J-P, see Baranoff E (2007) *123*: 41–78
- Conley B, Atwood DA (2003) Fluoroaluminate Chemistry *104*: 181–193
- Contakes SM, Nguyen YHL, Gray HB, Glazer EC, Hays A-M, Goodin DB (2007) Conjugates of Heme-Thiolate Enzymes with Photoactive Metal-Diimine Wires. *123*: 177–203



- Contreras RR, Suárez T, Reyes M, Bellandi F, Cancines P, Moreno J, Shahgholi M, Di Bilio AJ, Gray HB, Fontal B (2003) Electronic Structures and Reduction Potentials of Cu(II) Complexes of [N,N'-Alkyl-bis(ethyl-2-amino-1-cyclopentencarbothioate)] (Alkyl = Ethyl, Propyl, and Butyl) *106*: 71–79
- Cooke Andrews J (2006) Mercury Speciation in the Environment Using X-ray Absorption Spectroscopy *120*: 1–35
- Corà F, Alfredsson M, Mallia G, Middlemiss DS, Mackrodt WC, Dovesi R, Orlando R (2004) The Performance of Hybrid Density Functionals in Solid State Chemistry *113*: 171–232
- Cornia A, Costantino AF, Zobbi L, Caneschi A, Gatteschi D, Mannini M, Sessoli R (2006) Preparation of Novel Materials Using SMMs. *122*: 133–161
- Coskun T, see Bouamaied I (2006) *121*: 1–47
- Costantino AF, see Cornia A (2006) *122*: 133–161
- Coulon C, Miyasaka H, Clérac R (2006) Single-Chain Magnets: Theoretical Approach and Experimental Systems. *122*: 163–206
- Crespi VH, see Gunnarson O (2005) *114*: 71–101
- Curély J, Barbara B (2006) General Theory of Superexchange in Molecules. *122*: 207–250
- Dalal NS, Gunaydin-Sen O, Bussmann-Holder A (2007) Experimental Evidence for the Coexistence of Order/Disorder and Displacive Behavior of Hydrogen-Bonded Ferroelectrics and Antiferroelectrics. *124*: 23–50
- Dalal NS, see Bussmann-Holder A (2007) *124*: 1–21
- Daul CA, see Atanasov M (2003) *106*: 97–125
- Day P (2003) Whereof Man Cannot Speak: Some Scientific Vocabulary of Michael Faraday and Klixbüll Jørgensen *106*: 7–18
- Deeth RJ (2004) Computational Bioinorganic Chemistry *113*: 37–69
- Delahaye S, see Hauser A (2003) *106*: 81–96
- Deng S, Simon A, Köhler J (2005) Pairing Mechanisms Viewed from Physics and Chemistry *114*: 103–141
- Di Bartolo B, see Bowlby BE (2003) *106*: 191–208
- Di Bilio AJ, see Contreras RR (2003) *106*: 71–79
- Ding Z, see Bard AJ (2005) *118*: 1–57
- Dovesi R, see Corà F (2004) *113*: 171–232
- Duan X, see He J (2005) *119*: 89–119
- Duan X, see Li F (2005) *119*: 193–223
- Egami T (2005) Electron-Phonon Coupling in High- $T_c$  Superconductors *114*: 267–286
- Egami T (2007) Local Structure and Dynamics of Ferroelectric Solids. *124*: 69–88
- Eisenstein O, see Clot E (2004) *113*: 1–36
- Ercolani G (2006) Thermodynamics of Metal-Mediated Assemblies of Porphyrins *121*: 167–215
- Evans DG, see He J (2005) *119*: 89–119
- Evans DG, Slade RCT (2005) Structural Aspects of Layered Double Hydroxides *119*: 1–87
- Ewing GE (2005) H<sub>2</sub>O on NaCl: From Single Molecule, to Clusters, to Monolayer, to Thin Film, to Deliquescence *116*: 1–25
- Flamigni L, Heitz V, Sauvage J-P (2006) Porphyrin Rotaxanes and Catenanes: Copper(I)-Templated Synthesis and Photoinduced Processes *121*: 217–261
- Flamigni L, see Baranoff E (2007) *123*: 41–78
- Fontal B, see Contreras RR (2003) *106*: 71–79
- Forrò L, see Brouet V (2004) *109*: 165–199

- Fowler PW, see Soncini A (2005) *115*: 57–79
- Frenking G, see Lein M (2003) *106*: 181–191
- Frühauf S, see Roewer G (2002) *101*: 59–136
- Frunzke J, see Lein M (2003) *106*: 181–191
- Furrer A (2005) Neutron Scattering Investigations of Charge Inhomogeneities and the Pseudogap State in High-Temperature Superconductors *114*: 171–204
- Gàràs S, see Brouet V (2004) *109*: 165–199
- Gatteschi D, see Cornia A (2006) *122*: 133–161
- Gillet VJ (2004) Applications of Evolutionary Computation in Drug Design *110*: 133–152
- Glazer EC, see Contakes SM (2007) *123*: 177–203
- Golden MS, Pichler T, Rudolf P (2004) Charge Transfer and Bonding in Endohedral Fullerenes from High-Energy Spectroscopy *109*: 201–229
- Goodin DB, see Contakes SM (2007) *123*: 177–203
- Gorelesky SI, Lever ABP (2004) *107*: 77–114
- Grant GJ (2006) Mercury(II) Complexes with Thiocrowns and Related Macrocyclic Ligands *120*: 107–141
- Grätzel M, see Nazeeruddin MK (2007) *123*: 113–175
- Gray HB, see Contreras RR (2003) *106*: 71–79
- Gray HB, see Contakes SM (2007) *123*: 177–203
- Grepioni F, see Braga D (2004) *111*: 1–32
- Gritsenko O, see Rosa A (2004) *112*: 49–116
- Güdel HU, see Wenger OS (2003) *106*: 59–70
- Gunnarsson O, Han JE, Koch E, Crespi VH (2005) Superconductivity in Alkali-Doped Fullerenes *114*: 71–101
- Gunter MJ (2006) Multiporphyrin Arrays Assembled Through Hydrogen Bonding *121*: 263–295
- Gunaydin-Sen O, see Dalal NS (2007) *124*: 23–50
- Gütlich P, van Koningsbruggen PJ, Renz F (2004) Recent Advances in Spin Crossover Research *107*: 27–76
- Guyot-Sionnest P (2005) Intraband Spectroscopy and Semiconductor Nanocrystals *118*: 59–77
- Habershon S, see Harris KDM (2004) *110*: 55–94
- Han JE, see Gunnarsson O (2005) *114*: 71–101
- Hardie MJ (2004) Hydrogen Bonded Network Structures Constructed from Molecular Hosts *111*: 139–174
- Harris KDM, see Aliev (2004) *108*: 1–54
- Harris KDM, Johnston RL, Habershon S (2004) Application of Evolutionary Computation in Structure Determination from Diffraction Data *110*: 55–94
- Hartke B (2004) Application of Evolutionary Algorithms to Global Cluster Geometry Optimization *110*: 33–53
- Harvey JN (2004) DFT Computation of Relative Spin-State Energetics of Transition Metal Compounds *112*: 151–183
- Haubner R, Wilhelm M, Weissenbacher R, Lux B (2002) Boron Nitrides – Properties, Synthesis and Applications *102*: 1–46
- Hauser A, Amstutz N, Delahaye S, Sadki A, Schenker S, Sieber R, Zerara M (2003) Fine Tuning the Electronic Properties of  $[M(\text{bpy})_3]^{2+}$  Complexes by Chemical Pressure ( $M = \text{Fe}^{2+}, \text{Ru}^{2+}, \text{Co}^{2+}$ , bpy = 2,2'-Bipyridine) *106*: 81–96
- Hays A-M, see Contakes SM (2007) *123*: 177–203

- He J, Wei M, Li B, Kang Y, G Evans D, Duan X (2005) Preparation of Layered Double Hydroxides *119*: 89–119
- Heitz V, see Flamigni L (2006) *121*: 217–261
- Herrmann M, see Petzow G (2002) *102*: 47–166
- Herzog U, see Roewer G (2002) *101*: 59–136
- Hoggard PE (2003) Angular Overlap Model Parameters *106*: 37–57
- Höpfel H (2002) Structure and Bonding in Boron Containing Macrocycles and Cages *103*: 1–56
- Hubberstey P, Suksangpanya U (2004) Hydrogen-Bonded Supramolecular Chain and Sheet Formation by Coordinated Guanidine Derivatives *111*: 33–83
- Hupp JT (2006) Rhenium-Linked Multiporphyrin Assemblies: Synthesis and Properties *121*: 145–165
- Hutchison AR, see Atwood DA (2003) *105*: 167–201
- Ingo E, Scandola F, Alessio E (2006) Metal-Mediated Multi-Porphyrin Discrete Assemblies and Their Photoinduced Properties *121*: 105–143
- Itoh M, Taniguchi H (2007) Ferroelectricity of SrTiO<sub>3</sub> Induced by Oxygen Isotope Exchange. *124*: 89–118
- Iwasa Y, see Margadonna S (2004) *109*: 127–164
- Jansen M, Jäschke B, Jäschke T (2002) Amorphous Multinary Ceramics in the Si-B-N-C System *101*: 137–192
- Jäschke B, see Jansen M (2002) *101*: 137–192
- Jäschke T, see Jansen M (2002) *101*: 137–192
- Jaworska M, Macyk W, Stasicka Z (2003) Structure, Spectroscopy and Photochemistry of the [M( $\eta^5$ -C<sub>5</sub>H<sub>5</sub>)(CO)<sub>2</sub>]<sub>2</sub> Complexes (M = Fe, Ru) *106*: 153–172
- Jenneskens LW, see Soncini A (2005) *115*: 57–79
- Jeziorski B, see Szalewicz K (2005) *116*: 43–117
- Johnston RL, see Harris KDM (2004) *110*: 55–94
- Jordan KD, see Christie RA (2005) *116*: 27–41
- Kabanov VV, see Mihailovic D (2005) *114*: 331–365
- Kang Y, see He J (2005) *119*: 89–119
- Keller H (2005) Unconventional Isotope Effects in Cuprate Superconductors *114*: 143–169
- Keller H, see Bussmann-Holder A (2005) *114*: 367–386
- Khan AI, see Williams GR (2005) *119*: 161–192
- Kind R (2007) Evidence for Ferroelectric Nucleation Centres in the Pseudo-spin Glass System Rb<sub>1-x</sub>(ND<sub>4</sub>)<sub>x</sub>D<sub>2</sub>PO<sub>4</sub>: A <sup>87</sup>Rb NMR Study. *124*: 119–147
- Kobuke Y (2006) Porphyrin Supramolecules by Self-Complementary Coordination *121*: 49–104
- Koch E, see Gunnarson O (2005) *114*: 71–101
- Kochelaev BI, Teitelbaum GB (2005) Nanoscale Properties of Superconducting Cuprates Probed by the Electron Paramagnetic Resonance *114*: 205–266
- Köhler J, see Deng (2005) *114*: 103–141
- van Koningsbruggen, see Gütlich P (2004) *107*: 27–76
- Kume S, Nishihara H (2007) Metal-Based Photoswitches Derived from Photoisomerization. *123*: 79–112
- Lein M, Frunzke J, Frenking G (2003) Christian Klíxbüll Jørgensen and the Nature of the Chemical Bond in HARF *106*: 181–191

- Leroux F, see Taviot-Gueho C (2005) *119*: 121–159
- Lever ABP, Gorelesky SI (2004) Ruthenium Complexes of Non-Innocent Ligands; Aspects of Charge Transfer Spectroscopy *107*: 77–114
- Li B, see He J (2005) *119*: 89–119
- Li F, Duan X (2005) Applications of Layered Double Hydroxides *119*: 193–223
- Liebau F, see Santamaría-Pérez D (2005) *118*: 79–135
- Linton DJ, Wheatley AEH (2003) The Synthesis and Structural Properties of Aluminium Oxide, Hydroxide and Organooxide Compounds *105*: 67–139
- Lo KK-W (2007) Luminescent Transition Metal Complexes as Biological Labels and Probes. *123*: 205–245
- Lux B, see Haubner R (2002) *102*: 1–46
- Mackrodt WC, see Corà F (2004) *113*: 171–232
- Macyk W, see Jaworska M (2003) *106*: 153–172
- Mahalakshmi L, Stalke D (2002) The R<sub>2</sub>M<sup>+</sup> Group 13 Organometallic Fragment Chelated by P-centered Ligands *103*: 85–116
- Maini L, see Braga D (2004) *111*: 1–32
- Mallah T, see Rebilly J-N (2006) *122*: 103–131
- Mallia G, see Corà F (2004) *113*: 171–232
- Mannini M, see Cornia A (2006) *122*: 133–161
- Margadonna S, Iwasa Y, Takenobu T, Prassides K (2004) Structural and Electronic Properties of Selected Fulleride Salts *109*: 127–164
- Maseras F, see Ujaque G (2004) *112*: 117–149
- McInnes EJJ (2006) Spectroscopy of Single-Molecule Magnets. *122*: 69–102
- Merunka D, Rakvin B (2007) Anharmonic and Quantum Effects in KDP-Type Ferroelectrics: Modified Strong Dipole–Proton Coupling Model. *124*: 149–198
- Micnas R, Robaszkiewicz S, Bussmann-Holder A (2005) Two-Component Scenarios for Non-Conventional (Exotic) Superconductors *114*: 13–69
- Middlemiss DS, see Corà F (2004) *113*: 171–232
- Mihailovic D, Kabanov VV (2005) Dynamic Inhomogeneity, Pairing and Superconductivity in Cuprates *114*: 331–365
- Millot C (2005) Molecular Dynamics Simulations and Intermolecular Forces *115*: 125–148
- Miyake T, see Saito (2004) *109*: 41–57
- Miyasaka H, see Coulon C (2006) *122*: 163–206
- Mobian P, see Baranoff E (2007) *123*: 41–78
- Moreno J, see Contreras RR (2003) *106*: 71–79
- Moreno M, Aramburu JA, Barriuso MT (2003) Electronic Properties and Bonding in Transition Metal Complexes: Influence of Pressure *106*: 127–152
- Morita M, Buddhudu S, Rau D, Murakami S (2004) Photoluminescence and Excitation Energy Transfer of Rare Earth Ions in Nanoporous Xerogel and Sol-Gel SiO<sub>2</sub> Glasses *107*: 115–143
- Morsch VM, see Schetinger MRC (2003) *104*: 99–138
- Mossin S, Weihe H (2003) Average One-Center Two-Electron Exchange Integrals and Exchange Interactions *106*: 173–180
- Murakami S, see Morita M (2004) *107*: 115–144
- Müller E, see Roewer G (2002) *101*: 59–136
- Müller KA (2005) Essential Heterogeneities in Hole-Doped Cuprate Superconductors *114*: 1–11
- Müller KA, see Bussmann-Holder A (2005) *114*: 367–386
- Myung N, see Bard AJ (2005) *118*: 1–57

- Nazeeruddin MK, Grätzel M (2007) Transition Metal Complexes for Photovoltaic and Light Emitting Applications. *123*: 113–175
- Nguyen YHL, see Contakes SM (2007) *123*: 177–203
- Nishibori E, see Takata M (2004) *109*: 59–84
- Nishihara H, see Kume S (2007) *123*: 79–112
- Nolet MC, Beaulac R, Boulanger AM, Reber C (2004) Allowed and Forbidden d-d Bands in Octa-hedral Coordination Compounds: Intensity Borrowing and Interference Dips in Absorption Spectra *107*: 145–158
- O'Hare D, see Williams GR (2005) *119*: 161–192
- Ordejón P, see Sánchez-Portal D (2004) *113*: 103–170
- Orlando R, see Corà F (2004) *113*: 171–232
- Oshiro S (2003) A New Effect of Aluminium on Iron Metabolism in Mammalian Cells *104*: 59–78
- Pastor A, see Turner DR (2004) *108*: 97–168
- Patkowski K, see Szalewicz K (2005) *116*: 43–117
- Patočka J, see Strunecká A (2003) *104*: 139–180
- Peng X, Thessing J (2005) Controlled Synthesis of High Quality Semiconductor Nanocrystals *118*: 137–177
- Petzow G, Hermann M (2002) Silicon Nitride Ceramics *102*: 47–166
- Pichler T, see Golden MS (2004) *109*: 201–229
- Polito M, see Braga D (2004) *111*: 1–32
- Popelier PLA (2005) Quantum Chemical Topology: on Bonds and Potentials *115*: 1–56
- Power P (2002) Multiple Bonding Between Heavier Group 13 Elements *103*: 57–84
- Prassides K, see Margadonna S (2004) *109*: 127–164
- Prato M, see Tagmatarchis N (2004) *109*: 1–39
- Price LS, see Price SSL (2005) *115*: 81–123
- Price SSL, Price LS (2005) Modelling Intermolecular Forces for Organic Crystal Structure Prediction *115*: 81–123
- Rabinovich D (2006) Poly(mercaptoimidazolyl)borate Complexes of Cadmium and Mercury *120*: 143–162
- Rakvin B, see Merunka D (2007) *124*: 149–198
- Rao KSJ, see Anitha S (2003) *104*: 79–98
- Rau D, see Morita M (2004) *107*: 115–144
- Rauzy C, see Atanasov (2003) *106*: 97–125
- Reber C, see Nolet MC (2004) *107*: 145–158
- Rebilly J-N, Mallah T (2006) Synthesis of Single-Molecule Magnets Using Metalloacyanates. *122*: 103–131
- Reinen D, Atanasov M (2004) The Angular Overlap Model and Vibronic Coupling in Treating s-p and d-s Mixing – a DFT Study *107*: 159–178
- Reisfeld R (2003) Rare Earth Ions: Their Spectroscopy of Cryptates and Related Complexes in Glasses *106*: 209–237
- Renz F, see Gütllich P (2004) *107*: 27–76
- Reyes M, see Contreras RR (2003) *106*: 71–79
- Ricciardi G, see Rosa A (2004) *112*: 49–116
- Riesen H (2004) Progress in Hole-Burning Spectroscopy of Coordination Compounds *107*: 179–205
- Robaszkiewicz S, see Micnas R (2005) *114*: 13–69

- Roewer G, Herzog U, Trommer K, Müller E, Frühauf S (2002) Silicon Carbide – A Survey of Synthetic Approaches, Properties and Applications *101*: 59–136
- Rosa A, Ricciardi G, Gritsenko O, Baerends EJ (2004) Excitation Energies of Metal Complexes with Time-dependent Density Functional Theory *112*: 49–116
- Rudolf P, see Golden MS (2004) *109*: 201–229
- Ruiz E (2004) Theoretical Study of the Exchange Coupling in Large Polynuclear Transition Metal Complexes Using DFT Methods *113*: 71–102
- Sadki A, see Hauser A (2003) *106*: 81–96
- Saini NL, see Bianconi A (2005) *114*: 287–330
- Saito S, Umemoto K, Miyake T (2004) Electronic Structure and Energetics of Fullerenes, Fullerides, and Fullerene Polymers *109*: 41–57
- Sakata M, see Takata M (2004) *109*: 59–84
- Sánchez-Portal D, Ordejón P, Canadell E (2004) Computing the Properties of Materials from First Principles with SIESTA *113*: 103–170
- Santamaría-Pérez D, Vegas A, Liebau F (2005) The Zintl–Klemm Concept Applied to Cations in Oxides II. The Structures of Silicates *118*: 79–135
- Sauvage J-P, see Flamigni L (2006) *121*: 217–261
- Sauvage J-P, see Baranoff E (2007) *123*: 41–78
- Scandola F, see Iengo E (2006) *121*: 105–143
- Schäffer CE (2003) Axel Christian Klixbüll Jørgensen (1931–2001) *106*: 1–5
- Schäffer CE, see Anthon C (2004) *107*: 207–301
- Schenker S, see Hauser A (2003) *106*: 81–96
- Scheting MRC, Morsch VM, Bohrer D (2003) Aluminium: Interaction with Nucleotides and Nucleotidases and Analytical Aspects of Determination *104*: 99–138
- Schmidtke HH (2003) The Variation of Slater-Condon Parameters  $F^k$  and Racah Parameters B and C with Chemical Bonding in Transition Group Complexes *106*: 19–35
- Schubert DM (2003) Borates in Industrial Use *105*: 1–40
- Schulz S (2002) Synthesis, Structure and Reactivity of Group 13/15 Compounds Containing the Heavier Elements of Group 15, Sb and Bi *103*: 117–166
- Scott JF (2007) A Comparison of Magnetic Random Access Memories (MRAMs) and Ferroelectric Random Access Memories (FRAMs). *124*: 199–207
- Seifert HJ, Aldinger F (2002) Phase Equilibria in the Si-B-C-N System *101*: 1–58
- Sessoli R, see Cornia A (2006) *122*: 133–161
- Shahgholi M, see Contreras RR (2003) *106*: 71–79
- Shinohara H, see Takata M (2004) *109*: 59–84
- Sieber R, see Hauser A (2003) *106*: 81–96
- Simon A, see Deng (2005) *114*: 103–141
- Slade RCT, see Evans DG (2005) *119*: 1–87
- Soncini A, Fowler PW, Jenneskens LW (2005) Angular Momentum and Spectral Decomposition of Ring Currents: Aromaticity and the Annulene Model *115*: 57–79
- Stalke D, see Mahalakshmi L (2002) *103*: 85–116
- Stasicka Z, see Jaworska M (2003) *106*: 153–172
- Steed JW, see Turner DR (2004) *108*: 97–168
- Strunecká A, Patočka J (2003) Aluminofluoride Complexes in the Etiology of Alzheimer's Disease *104*: 139–180
- Stulz E, see Bouamaied I (2006) *121*: 1–47
- Suárez T, see Contreras RR (2003) *106*: 71–79
- Suksangpanya U, see Hubberstey (2004) *111*: 33–83
- Sundqvist B (2004) Polymeric Fullerene Phases Formed Under Pressure *109*: 85–126

- Szalewicz K, Patkowski K, Jeziorski B (2005) Intermolecular Interactions via Perturbation Theory: From Diatoms to Biomolecules *116*: 43–117
- Tagmatarchis N, Prato M (2004) Organofullerene Materials *109*: 1–39
- Takata M, Nishibori E, Sakata M, Shinohara M (2004) Charge Density Level Structures of Endohedral Metallofullerenes by MEM/Rietveld Method *109*: 59–84
- Takenobu T, see Margadonna S (2004) *109*: 127–164
- Talarico G, see Budzelaar PHM (2003) *105*: 141–165
- Taniguchi H, see Itoh M (2007) *124*: 89–118
- Taviot-Gueho C, Leroux F (2005) In situ Polymerization and Intercalation of Polymers in Layered Double Hydroxides *119*: 121–159
- Teitelbaum GB, see Kochelaev BI (2005) *114*: 205–266
- Thessing J, see Peng X (2005) *118*: 137–177
- Trommer K, see Roewer G (2002) *101*: 59–136
- Tsuzuki S (2005) Interactions with Aromatic Rings *115*: 149–193
- Turner DR, Pastor A, Alajarin M, Steed JW (2004) Molecular Containers: Design Approaches and Applications *108*: 97–168
- Uhl W (2003) Aluminium and Gallium Hydrazides *105*: 41–66
- Ujaque G, Maseras F (2004) Applications of Hybrid DFT/Molecular Mechanics to Homogeneous Catalysis *112*: 117–149
- Umemoto K, see Saito S (2004) *109*: 41–57
- Unger R (2004) The Genetic Algorithm Approach to Protein Structure Prediction *110*: 153–175
- van der Voet GB, see Berend K (2003) *104*: 1–58
- Vegas A, see Santamaría-Pérez D (2005) *118*: 79–135
- Vilar R (2004) Hydrogen-Bonding Templated Assemblies *111*: 85–137
- Wei M, see He J (2005) *119*: 89–119
- Weihe H, see Mossin S (2003) *106*: 173–180
- Weissenbacher R, see Haubner R (2002) *102*: 1–46
- Wenger OS, Güdel HU (2003) Influence of Crystal Field Parameters on Near-Infrared to Visible Photon Upconversion in  $Ti^{2+}$  and  $Ni^{2+}$  Doped Halide Lattices *106*: 59–70
- Wheatley AEH, see Linton DJ (2003) *105*: 67–139
- Wilhelm M, see Haubner R (2002) *102*: 1–46
- Williams GR, Khan AI, O'Hare D (2005) Mechanistic and Kinetic Studies of Guest Ion Intercalation into Layered Double Hydroxides Using Time-resolved, In-situ X-ray Powder Diffraction *119*: 161–192
- de Wolff FA, see Berend K (2003) *104*: 1–58
- Woodley SM (2004) Prediction of Crystal Structures Using Evolutionary Algorithms and Related Techniques *110*: 95–132
- Xantheas SS (2005) Interaction Potentials for Water from Accurate Cluster Calculations *116*: 119–148
- Zaman MK, see Atwood DA (2006) *120*: 163–182
- Zerara M, see Hauser A (2003) *106*: 81–96
- Zhang H (2006) Photochemical Redox Reactions of Mercury *120*: 37–79
- Zhang Y, see Atwood DA (2003) *105*: 167–201
- Zobbi L, see Cornia A (2006) *122*: 133–161

---

## Subject Index

- Acetylide-Pt(II)-terpy centre 62  
Amine oxidase, *Arthrobacter globiformis* 179  
Anisotropy probes 220  
Au(I) centers, closed-shell 2  
Au<sub>3</sub> stacking, trimeric molecules 21  
Au<sub>3</sub><sup>+</sup>(*n*-PentN=COMe)<sub>3</sub> 11  
Aurophilic interactions 2  
Azobenzene-attached complexes 92
- Biotin derivatives, luminescent 233  
2,2'-Bipyridinium, bridged 44  
2,6-Bis(1-methylbenzimidazol-2'-yl)-pyridine 124  
2,6-Bis(4'-phenyl-2'-quinolyl)pyridine (bpqpy) 50
- Catenanes 41, 69  
-, ruthenium(II)-containing 72  
Charge separation 44  
-, photoinduced 41  
Chromene-attached complexes 81  
Citrulline 195  
Cu(I)-phen-type complexes, luminescent 60  
Cytochrome *c*, ruthenium-modified 218  
Cytochrome P450, catalysis, electron transfer 180  
-, class II drug metabolizing 178  
Cytochrome P450CAM 177  
Cytochrome P450 reductase (CPR), FAD containing 178
- Decoordination, photoinduced, catenane 72  
Di-*p*-anisylamine (DPAA) 45  
Diarylethene-attached complexes 87  
Dicyanoaurate, tunable luminescence 5
- Di-(2-(3,6-dimethoxyphenyl)ethenyl)-2,2'-bipyridine ligand 128  
4,4'-Diflavins (FAD/FMN) 178  
2,4-Difluorophenyl-4-dimethylaminopyridine ligand 160  
Dissociative excited states 64  
*cis*-Dithiocyanato bis(2,2'-bipyridine-4,4'-dicarboxylate)Ru(II) complex(2) 138  
*cis*-Dithiocyanato bis(4,4'-dicarboxy-2,2'-bipyridine)Ru(II) 130  
DNA, photocleavage, guanine oxidation 207  
DNA labels 210  
Dye sensitization 114  
Dye-sensitized solar cells 113  
-, conversion efficiency 120  
-, fabrication 117  
-, solid state 142
- Electrochemical sensors, molecular wires 179  
Electrolytes, solvent-free 146  
Electron acceptor/donor 43  
Electron tunneling wires 178  
Enzyme, wire-binding specificity 177  
Enzyme inhibitors, molecular wires 179  
Enzyme:wire conjugates 179
- Flash-quench methods 179  
Fluorescent sensors, molecular wires 179  
Förster-type RET quenching 207
- Gold(I) complexes, two-coordinate 1
- HABA, avidin 233  
Heme-thiolate enzymes, conjugates 177



- Hole conductors 146  
HOMO 121  
– levels, tuning 161  
Horseradish peroxidase, ferryl intermediates 178
- Incident monochromatic photon-to-current conversion efficiency (IPCE) 119, 140  
Indole-binding proteins, probes 240  
Iodide/triiodide redox system 116  
Ionic liquids, solvent-free electrolytes 146  
IPCE 119, 141  
Ir, electron relay 56  
–, photoactive centre 59  
Ir/Ru 41  
Ir-bis-terpyridine derivatives 45  
Ir(terpy) 53  
–, electron relay/photoactive centre 44  
Ir(III)-cyclometalated complexes 44, 225  
–, luminescent 225  
Iridium complexes, controlling quantum yields 163  
–, tuning of phosphorescence colors 151  
Iridium polypyridine complexes, cyclometalated, luminescent 218  
Iridium triplet emitters 113
- K[Au(CN)<sub>2</sub>], MCD spectra 3
- Ligand-bridged complexes 36  
Light-driven molecular machine 41  
Light-emitting electrochemical cells 113  
–, device architecture 170  
Linear two-coordinate complexes in solution, absorption/luminescence 3  
Lipoxygenase 179  
Luminescence, crystalline polymorphism 6  
–, frozen solutions 31  
–, ionic Au(I) complexes, counter ion effects 25  
Luminescent labels 223  
Luminescent linkers, nucleosides 210  
Luminescent reporters 208  
Luminescent wires, metalloproteins 229  
LUMO 121
- Magnetic circular dichroism (MCD) spectra, colorless Au(I) complexes 3
- Metal complex 79  
Metal-diimine molecular wires, photoactive 177  
Metalloenzymes 179  
Metalloproteins, electron transfer 218  
–, luminescent wires 229  
–, photoinduced electron-transfer reactions 207  
Metal-to-ligand charge transfer (MLCT) 3  
–, photoexcitation 116  
Methyl viologen (MV) electron acceptor 45  
Microperoxidase-8, ferryl intermediates 178  
Molecular machines 43  
–, light-driven 41  
–, prototypes, ruthenium-based, light-driven 64  
Molecular sensitizers 120  
Molecular wires, cytochromes P450 180  
–, dansyl-terminated, multiple electron transfer 177  
–, fluorescent sensors 179  
–, inducible nitric oxide synthase (iNOS) 195  
–, photoactive, metal-diimine 177  
–, probing enzymes 178  
Multi-mode function 79  
Myeloperoxidase 179
- N3 dye 139  
NADPH reducing equivalents 178  
Naphthalenediimide 64  
Nitric oxide synthase, inducible (iNOS) 177, 195  
–, catalytic cycle 195  
Nucleosides, luminescent linkers 210
- OLEDs 113  
–, device architecture 165  
–, iridium complexes 149, 164  
–, – triplet emitters 149  
Oligonucleotides, post-modification 214  
Organic light-emitting diodes *see* OLEDs  
Organic photochromic molecules 107  
Os(II) bis-terpyridine 45  
Oxygenase 178
- P450, catalysis, electron transfer 180  
–, class II drug metabolizing 178

- P450CAM 177  
PH<sub>2</sub>-Ir(III)-PAu<sup>4+</sup> 56  
Phenothiazine (PTZ) 44  
Phosphorescence colors, anionic Ir complexes 158  
Photoactive centre 43  
Photochemical ligand exchange 65  
Photochromism 79  
Photocurrent, action spectra 140  
-, density 120  
-, short circuit 139  
Photoisomerization 79  
Photon-to-current conversion efficiency (IPCE) 119  
Photosubstitution-isomerisation 69  
Photoswitches, metal-based 79  
Photovoltage 119  
-, open circuit 119  
Photovoltaic properties 113,139  
Platinum-based probes 231  
Platinum(II) terpyridine complexes 227  
Polypyridyl complexes, TiO<sub>2</sub> oxide surface 136  
Probing open states 187  
Protein labels 218  
Protein probes 229  
Pseudo-rotaxane 60, 70  
Putidaredoxin 229  
PZn-Ir(III)-PAu<sup>4+</sup> 56
- Reporters, luminescent 208  
RET quenching, Förster-type 207  
Rhenium wires, iNOS<sub>oxy</sub> 199  
Rhenium(I) iodoacetamide sulfhydryl groups 221  
Rhenium(I) perfluorobiphenyl diimine 229  
Rhenium(I) polypyridine biotin 233  
Rhenium(I) polypyridine isothiocyanate 216  
Rotaxane 41  
-, [Ru(diimine)<sub>3</sub>]<sup>2+</sup> core, light-driven unthreading 70
- Ru(II) bipyridyl dye, sensitizer 118  
Ru(II) bis-terpyridine complexes 45  
Ru(II) complex, scorpionate terpyridine ligand 65  
Ru(II) diimine adamantane 229  
Ru(II) polypyridine isothiocyanate 223  
Ru(II) polypyridyl complexes, 2,2'-bipyridyl-4,4'-dicarboxylic acid/thiocyanate ligands 139  
Ru(II)-tris-bidentate chromophores 62  
Ru(terpy)(phen)-incorporating ring 67  
Ruthenium-azurin 219  
Ruthenium-based light-driven molecular machine prototypes 64  
Ruthenium sensitizers 113
- Scorpionate 41  
Sensitizer, catalytic cycle 145  
-, spectral response 122  
Sensitizer-tethered substrates 178  
Short circuit photocurrent 139  
Solar cells, dye-sensitized 113, 120  
-, TiO<sub>2</sub>-based, panchromatic charge transfer sensitizers 121  
Solvoluminescence, Au<sub>3</sub><sup>I</sup>(MeN=COMe)<sub>3</sub> 16  
Spectral response 122  
Spirooxazine-attached complexes 81  
Spiropyran-attached complexes 81  
Stabler-Wronski effect 144  
Stilbene-attached complexes 92  
Surface chelation, polypyridyl complexes, TiO<sub>2</sub> oxide surface 136
- Thermal ligand exchange 65  
TiO<sub>2</sub>-based solar cells, panchromatic charge transfer sensitizers 121  
Tris-[Ru(4,4'-dicarboxy-2,2'-bipyridine)<sub>3</sub>] 122
- Zinc porphyrin 58